Mathematical Modelling of Microwave Enhanced Chemical Vapour Infiltration

Chandradeo Bokhoree

A Doctoral Thesis

submitted in partial fulfilment of the requirements
for the award of Degree of Doctor of Philosophy
of Loughborough University

April 2004

ABSTRACT

With their excellent high temperature mechanical, chemical and thermal properties, fibre reinforced ceramic matrix composites have emerged as an important class of materials having a wide range of applications in various technological fields. Microwave Enhanced Chemical Vapour Infiltration (MECVI) has been recognized as a new process route because of its ability to conserve the reliability and durability of the precursor materials. The primary advantage of using microwaves is that they cause an inverse temperature profile to be formed that prevents entrapment of accessible porosity and greatly accelerates the process. However, to develop the MECVI process further, a complete understanding of the effects of the process parameters on the infiltration mechanism and processing time is necessary. Modelling efforts can offer an insight into the critical factors in this process and suggest ways to optimize processing.

A 2-D mathematical model investigating the densification of SiC_f/SiC composites by microwave enhanced Chemical Vapour Infiltration (CVI) under forced-flow of the gaseous reactants is presented. The analysis in the model included a set of partial differential equations coupled together describing the electromagnetic heating of the SiC preform, the mass transport of the gaseous species by forced flow and the chemical reaction taking place for the deposition of SiC solid inside the porous sample. Finite Difference Method (FDM) was applied to solve the system of equation numerically. The results showed that the use of microwave energy combined with appropriate pressure gradients provided increased control over the composite quality. It was observed that the sample was infiltrated from the inside out, however, the edges of the preform remained less densified due to excessive pressure gradient being built up.

A 1-D model was developed thereafter to investigate the infiltration of a single pore inside a porous SiC preform under microwave heating, by allowing the gaseous reactants to flow through the sample by diffusion transport. The model is used to investigate the occurrence of thermal runaway during the infiltration process. An asymptotic analysis was performed to obtain averaged homogenized equations describing the microwave heating and the transport/reaction processes. The results showed that the dielectric properties of the sample greatly affected the thermal distributions, which could undergo thermal runaway during MECVI. It was also seen that the pores closed faster at the boundary due to higher gas concentration.

In general, the models gave a considerable amount of insight in understanding the MECVI process.

ACKNOWLEDGEMENT

I would like to express my sincere gratitude to Prof. J.G.P. Binner and Prof. G.A. Kriegsmann for their invaluable guidance, discussions and encouragement during my PhD study. Their instruction and support have always been a tremendous help during the course of my research project. It was a great pleasure and a great experience to conduct this thesis under their supervision, and I look forward to collaborating with them and expect more support in future research.

I am very grateful to Dr. B.S. Tilley who provided me with valuable suggestions and comments to improve my research work, and for his early collaborations.

Many people have helped me through my study years; here I would like to extend my thanks to:

- Dr. B. Vaidhyanathan and Dr. D. Jaglin for explaining the Microwave Enhanced Chemical Vapour Infiltration process and providing me with numerous references.

- The members of the Department of Mathematical Sciences at NJIT for their valuable support during my stay at NJIT. Especially, I would like to thank Mrs. R. Rowan; her kindness, help and support made my degree pursuing study a very pleasant journey.

- The members of the department of IPTME for their help and support.

- Dr. C. Prentice and Dr. R. Shatwell (QINETIQ)

A personal thanks goes to all my family and friends who supported and helped me in every aspect during my research study. Specially, I wish to express my appreciation to someone very special to me, her patient love, constant encouragement and understanding enabled me to accomplish this work. Thanks Siwani..

Finally, I would like to acknowledge Loughborough University, QINETIQ, Farnborough and NJIT, USA, for their financial support.

TABLE OF CONTENTS

CHAPTER 3: MICROWAVE ENHANCED FORCED-FLOW CHEMICAL VAPOUR INFILTRATION: - A 2-D MATHEMATICAL MODEL

NOMENCLATURE

a -   radius of the perform (m)

A -   effective specific surface area in a unit cell(m^{-1})

A_s -   surface area of the sample (m^2)

b -   half thickness of the perform (m)

B -   biot number

$\mathbf{B}_d$ -   magnetic flux density (*tesla*)

c_p -   specific heat ($JKg^{-1}K^{-1}$)

c_{p_s} -   specific heat of SiC ($JKg^{-1}K^{-1}$)

c_{p_g} -   specific heat of gaseous mixture (MTS+H$_2$) ($JKg^{-1}K^{-1}$)

c_s -   speed of light (ms^{-1})

c_v -   fibre bundle volume content in a unit cell

C -   MTS concentration ($molm^{-3}$)

C_0 -   initial inlet MTS concentration ($molm^{-3}$)

C_l -   closed loop carrying current

D -   diffusion coefficient (m^2s^{-1})

$\mathbf{D}_d$ -   displacement flux density (Cm^{-2})

Da -   Damkholer number defining the ratio of rate of the reaction to the rate of mass transport by convection

D'_a -   Damkohler number representing the ratio of the characteristic diffusion time to the characteristic reaction time

D_0 -   diffusion coefficient at T_0 and P_0 (m^2s^{-1})

D_c -   damping constant

D_{ij}^e -   effective Knudsen diffusion coefficients of species i (m^2s^{-1})

D_i^e -   effective molecular diffusion coefficients of species i (m^2s^{-1})

D_{ij}^0 -   reference diffusivities at reference temperature T_0 and pressure P_0

D_i^0 -   reference diffusivities at reference temperature T_0 and pressure P_0

e	-	thermal emissivity of SiC
$\overline{\mathbf{E}}$	-	total electric field within and around the 2-D preform (Vm^{-1})
$\overline{\mathbf{E}}_{inc}$	-	incident electric field (Vm^{-1})
$\mathbf{E}_p$	-	electric field that penetrates the 1-D laminate perform (Vm^{-1})
$\overline{\mathbf{E}}_s$	-	scattered electric field (Vm^{-1})
$\mathbf{E}^*$	-	complex conjugate of E (Vm^{-1})
E_a	-	activation energy (J)
E_0	-	incident field intensity (Vm^{-1})
E_1	-	rate of incident energy (Js^{-1})
E_2	-	rate of energy stored (Js^{-1})
E_3	-	rate at which energy is loss (Js^{-1})
f	-	frequency of radiation (Hz)
f_c	-	electrical conductivity of the SiC preform normalized by σ_0
F	-	moving solid/gas interface in 1-D model
$\mathbf{G}(\underline{x})$	-	Green's function
$\mathbf{H}$	-	magnetic field ($NsC^{-1}M^{-1}$)
$\mathbf{H}^*$	-	complex conjugate of H ($NsC^{-1}M^{-1}$)
$\hbar$	-	Lennard-Jones parameter for the pair of gases
h_e	-	heat transfer coefficient ($Wm^{-2}K^{-1}$)
i	-	defining complex number, $\sqrt{-1}$
I_{gain}	-	integral gain parameter
$\mathbf{J}_c$	-	current density (Am^{-2})
J_f	-	molar flux ($Kgmol^{-1}$)
$\mathbf{J}_i$	-	diffusive component of flux of species i
J_K	-	free-molecule flux
k	-	propagation constant
k'	-	relative permittivity (Fm^{-1})
k''	-	relative dielectric loss (Fm^{-1})
k'_s	-	relative permittivity of SiC (Fm^{-1})

k_s''	-	dielectric loss of SiC (Fm^{-1})
k_g'	-	relative permittivity of gaseous mixture (MTS+H$_2$) (Fm^{-1})
k_g''	-	dielectric loss of gaseous mixture (MTS+H$_2$) (Fm^{-1})
k_p	-	permeability of the medium (Hm^{-1})
k_t	-	thermal conductivity of the material ($Wm^{-1}K^{-1}$)
k_{ts}	-	thermal conductivity of SiC ($Wm^{-1}K^{-1}$)
k_{tg}	-	thermal conductivity of gaseous mixture (MTS+H$_2$) ($Wm^{-1}K^{-1}$)
k_B	-	Boltzmann's constant ($m^2 Kgs^{-2}K^{-1}$)
k_1	-	reaction constant
l_q	-	height of quartz tube from its centre (m)
L_1	-	length of the edges in the unit cell (m)
$\mathbf{L}_p$	-	distance moved by a fluid particle
M_{H_2}	-	molecular mass of hydrogen ($Kgmol^{-1}$)
M_{MTS}	-	molecular mass of MTS ($Kgmol^{-1}$)
M_g	-	molecular mass of the gas. ($Kgmol^{-1}$)
N_c	-	number of components in a gas phase
N_1^2	-	index of refraction
$\mathbf{n}$	-	unit outward normal vector
n_m	-	number of molecules
n_1	-	number of moles
$\mathbf{N}_T$	-	total molar flux ($Kgmol^{-1}$)
$\mathbf{N}_i$	-	molar flux of species i ($Kgmol^{-1}$)
P	-	pressure (kPa)
$P_{ab}(r)$	-	power absorbed per unit volume (kWm^{-3})
P_c	-	measure of absorbed power density (kWm^{-3})
P_d	-	power per unit surface area (kWm^{-2})
Pe	-	Peclet number

P_{inc}	-	instantaneous incident power (kW)
P_{gain}	-	proportional gain of the power controller
P_n	-	net polarization
P_t	-	total porosity
P_v	-	rate of internal energy generation (Js^{-1})
P_w	-	measure of input microwave power (kW)
P_0	-	atmospheric pressure (kPa)
$P1$	-	inlet pressure of the perform (kPa)
$P2$	-	outlet pressure of the preform(kPa)
$\mathbf{q}$	-	total heat flux vector
$\mathbf{q}_c$	-	conductive heat transfer
$\mathbf{q}_R$	-	heat loss due to radiation
Q	-	volume flow rate per unit area ($ml\,min^{-1}$)
Q_f	-	volumetric flow rate of the fluid (MTS+H_2) ($ml\,min^{-1}$)
$\mathbf{r}$	-	radial vector
r	-	radius of the bundle of fibers in a unit cell (m)
r_p	-	radius of cylindrical capillary (m)
r_0	-	initial radius of the fibres (m)
R	-	universal gas constant ($JKg^{-1}K^{-1}$)
R_m	-	total reflection coefficients
R_R	-	molar deposition rate per unit of solid surface area
$\mathbf{S}$	-	Poynting vector
S_c	-	closed surface
S_s	-	solid surface area per unit volume in the perform (m^{-1})
S_1	-	single pore structure parameter one
S_2	-	single pore structure parameter two
s_b	-	Stefan-Boltzmann constant ($Wm^{-2}K^{-4}$)
t	-	time (s)
T	-	temperature (K)

T_c	-	critical temperature for reaction to occur (K)
T_0	-	reference temperature (Ambient) (K)
T_s	-	set-point temperature (K)
U	-	gas velocity in the x-direction (ms^{-1})
u	-	solid growth rate (Kgs^{-1})
u_c	-	dummy variable
v	-	precursor velocity along the y-direction (ms^{-1})
$\bar{v}$	-	mean molecular speed (ms^{-1})
$\mathbf{V}$	-	fluid velocity vector (ms^{-1})
V_c	-	enclosed volume by S_c
w_f	-	dimensionless probability factor
x	-	preform dimension along the x-axis (m)
$\underline{x}$	-	coordinate vector ($x\hat{\mathbf{i}} + y\hat{\mathbf{j}}$)
$\underline{x}_1$	-	coordinate vector ($x_1\hat{\mathbf{i}} + y_1\hat{\mathbf{j}}$)
x_{f_i}	-	mole fraction of species i
y	-	preform dimension along the y-axis (m)
z	-	direction along the z-axis
$\hat{\mathbf{z}}$	-	unit vector along the z-axis
α	-	phase constant
α_1	-	factor determining % porosity between two ceramic sheets in 1-D model
α_t	-	thermal diffusivity of the ceramic (m^2s^{-1})
β	-	attenuation *constant*
β_m	-	propagation constants for mode m
β_r	-	radiation heat loss parameter
δ	-	phase angle
δ_f	-	delta function
$\varepsilon(\omega)$	-	permittivity of the material (Fm^{-1})
$\varepsilon^*(\omega)$	-	complex permittivity (Fm^{-1})

ε_0 -   permittivity of free space (Fm^{-1})

η_0 -   impedance of free space (Fm^{-1})

θ_i -   dimensionless time variable for *ith* process

λ_s -   wavelength of radiation in the medium,

λ_0 -   wavelength of radiation in free space

$\mu(\omega)$ -   magnetic permeability of the material (Hm^{-1})

μ_0 -   permeability of free space ($WbA^{-1}m^{-1}$)

μ_v -   viscosity of the fluid ($Kgm^{-1}s^{-1}$)

ρ_p -   material density (Kgm^{-3})

ρ_{P_s} -   density of SiC (Kgm^{-3})

ρ_{P_g} -   density of gaseous mixture (MTS+H_2) (Kgm^{-3})

ρ_f -   density of the fluid (MTS+H_2) (Kgm^{-3})

$\rho(\mathbf{r})$ -   charge density (Cm^{-3})

$\sigma(\omega)$ -   electrical conductivity (Fm^{-1})

σ_0 -   conductivity of the ceramic sheets at ambient temperature T_0, (Fm^{-1})

ϕ -   porosity of the medium

ϑ -   void fraction

ω -   angular frequency

Π^* -   collision integral

∇ -   del operator

∇^2 -   Laplacian operator

Δx -   step size along *x*-direction

Δy -   step size along the *y*-direction

Δt -   time step size

GLOSSARY

Composite	A material created from a fiber (or reinforcement) and an appropriate matrix material in order to maximize specific performance properties. The constituents do not dissolve or merge completely but retain their identities as they act in concert.
SiC$_f$/SiC	Silicon carbide fibre / silicon carbide composite
Tow	Bundle of twisted or untwisted continuous fibres. A tow may contain tens of thousands of individual continuous fibres.
Intratow	Describing the porosity existing between fibres within a tow.
Intertow	Describing the porosity existing between fibre tows.
TE polarization	A propagation mode in which the axial field component is a magnetic field vector. The axial electric field vector is zero.
TM polarization	A propagation mode in which the axial field component is an electric field vector. The axial magnetic field vector is zero.
Skin effect	The phenomenon in which the penetration depth of the electromagnetic field decreases with increase in the dielectric properties of the material.
Asymptotic-theory	Method for obtaining approximate solutions to problems involving involving a small parameter.
LU-decomposition	A procedure for decomposing a matrix into a product of a lower triangular matrix and an upper triangular matrix.

LIST OF TABLES

LIST OF FIGURES

CHAPTER 1:

INTRODUCTION

1.1   Ceramic matrix composites

Ceramic materials have excellent characteristics for use in high temperature structural materials and mechanical parts because of their heat-stability, superior strength at high temperature and relatively low density as compared to metals and polymers. However, in the monolithic state they are characterized as being brittle, weak and susceptible to catastrophic failure. This behaviour can be attributed to the ease of crack propagation, which is the result of the very low fracture toughness and poor durability of the ceramics [1,2,3]. Broad progress has been accomplished in the past three decades to alleviate these negative features through material improvement, new ceramic materials, and improved design methods. This new generation of ceramics and design methods has the potential to help the industries of the future reach their visions of increased energy efficiency, increased productivity and decreased maintenance [1,4].

Important advances have occurred in the fabrication of composite materials, particularly Ceramic Matrix Composites (CMCs) in order to prevent failure by incorporating energy-dissipating mechanisms in the fracture process [1]. CMCs combine reinforcing ceramic phases with a ceramic matrix to create materials with new and superior properties. In ceramic matrix composites, the primary goal of the ceramic reinforcement is to provide toughness to an otherwise brittle ceramic matrix (Figure 1.1). The desirable characteristics of CMCs include high-temperature stability, high thermal-shock resistance, high hardness, high corrosion resistance, light weight and flexibility in providing unique engineering solutions.

1.2   Fibre reinforced ceramic matrix composites

Ceramic reinforcements are available in a variety of forms. Typical ceramic reinforcements are presented in Table 1.1. The toughening of ceramics through discontinuous reinforcements that include whiskers, short fibres and particulates are

often performed using conventional monolithic ceramic processes such as slip casting or injection moulding followed by sintering or hot pressing [1,2,5]. These result in ceramics with better fracture toughness. However, the brittle failure problem may still persist when extremely demanding properties are required [1,6]. The use of fibres in the continuous form to incorporate high strength and high modulus in a brittle matrix has received much interest since woven fibre materials have been gaining increasing technological importance as reinforcements in the past 15-20 years [1,3,4,7,8]. With continuous fibre reinforcements, a large fraction of applied load on a ceramic matrix composite can continue to be supported by the fibres even after the matrix has been fractured. Figure 1.1 displays the mechanical behaviour of a continuous fibre reinforced ceramic matrix composites and its monolithic equivalent. Further, continuous ceramic fibres in the form of textile structures with two and three-dimensional arrangements not only provide a mechanism for structural toughening of composites but also facilitate the processing of composites into near-net shape structural parts [8]. However, the use of continuous fibres to reinforce CMCs is more expensive than discontinuous fibre reinforcements.
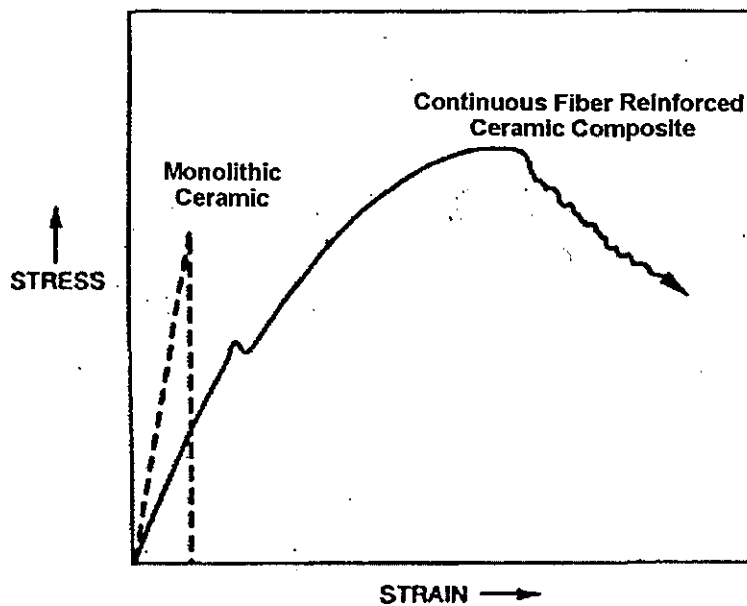
Figure 1.1: Comparison of failure modes for monolithic ceramic and continuous fibre reinforced CMCs [4].

Particles	SiC, TiC, Al_2O_3
Discontinuous fibres	
(a) whiskers	SiC, TiB_2, Al_2O_3
(b) short fibres	Glass, Al_2O_3, SiC, mullite, vapour grown
Continuous fibres	
(a) oxide	Al_2O_3, mullite, ZrO_2, silica-based glasses
(b) non-oxide	B, C, SiC, Si_3N_4, BN
Sheets/Laminates	SiC

Table 1.1: Examples of ceramic reinforcements listed by categories [1].

1.3   Applications of CMCs

It is convenient to divide the general applications of CMC's in terms of aerospace and non-aerospace applications. In the aerospace area, performance is the foremost consideration while in the non-aerospace fields cost effectiveness is the prime consideration [1].

Aerospace applications, in general, demand high thrust-to-weight ratios, faster cruising speeds, increased altitudes and improved flight performance. These goals translate into material requirements involving increased strength-to-density, stiffness-to-density and improved damage tolerance – all at significantly higher temperatures. High temperature structural composites represent a key technology for advanced aerospace systems. Continuous fibre reinforced ceramic composites potentially offer higher specific mechanical properties which can be utilized in a variety of high temperature aerospace applications. For example, silicon carbide coated carbon/carbon composites are used as a thermal protection material in the US space shuttle [1,9,10]. Carbon fibre/silicon carbide composites are candidate materials for a variety of space plane programmes [1,10]. Other aerospace applications for ceramic matrix composites include a variety of hypersonic radomes and high-temperature turbine engines.

Among the non-aerospace applications of CMCs are cutting tools inserts, wear resistant parts, engine components at high temperatures and in corrosive environments, nozzles and exhaust ducts and energy related applications such as heat-exchanger tubes.

3

For such applications, the components can range from simple to complex and tend to be similar in size. Thus, it is not surprising that for such applications, there are commercially available dense, wear-resistant, particle and whisker reinforced CMCs [1,9,10,11]. The main advantages of ceramic cutting tools include chemical stability, superior hardness and ability to operate at higher temperature, which translate into higher cutting speeds. In the area of wear resistant parts, CMCs offer high hardness, low friction, superior abrasion resistance and good mechanical performance at high speeds. Whereas, in the energy related areas involving heat transfer, storage and heat exchangers, among the major drawbacks of using monolithic ceramics is their poor thermal shock resistance. Here, continuous fibre reinforced CMCs can be used profitably to overcome these drawbacks.

In general, the use of CMCs components in a variety of applications makes economic sense because it will result in higher operating temperature, higher efficiency, benefits in the energy and environmental (reduced emission) area service life, etc. A summary of other applications plus those described above is described in table 1.2.

1.4 Worldwide market for CMCs

Applications of ceramic matrix composites that have been on the market for a number of years include cutting tools and wear parts. Other emerging applications being field-tested or still in the development stage include gas turbine seals, hot gas filters and high-pressure heat exchangers. One of the major obstacles to continued growth of the CMC market is still cost (both raw materials and manufacturing) and joint efforts between industries have been addressing this problem over the last few years. Another major obstacle is the lack of reliability in current materials.

According to a report from Business Communications Company, Inc [12], the global market for ceramic matrix composites in 1999 was $216.6 million. This was forecast to increase to $318 million by the 2004 with an average annual growth rate (AAGR) of 8% per year from 1999 to 2004, see table 1.3. In terms of market share, the U.S. has currently over 50% of the world market and is expected to increase this market share by a few percent by 2004. One of the highest growth areas in Japan is expected to

be space propulsion applications. Gas turbine components are another high growth area for this country.

Product area	Examples	Likely industrial market(s)
Advanced heat engines	Combustors, liners, wear parts, etc.	High-temperature gas turbines; possibly diesel, gas turbine combustor retrofits
Heat recovery equipment	Air preheaters, recuperators	Indirect heating uses; energy intensive industrial internal processes (e.g., aluminium remelters, steel reheaters, glass melters)
Burners and combustors	Radiant tube burners	Potentially any indirect-fired, high-temperature and/or controlled atmosphere heating/ melting/ heat treating industrial applications
	Combustors	Low-NO_x Clean fuel heating applications, including gas turbine combustors, industrial process heat
Process equipment	Reformers, reactors, HIP equipment	Chemical process industry, petroleum refining
Waste incineration systems	Handling equipment, internals, cleanup	Conventional and advanced toxic/hazardous waste facilities, with or without energy recovery
Separation/filtration	Filters, substrates, centrifuges	Gas turbine, combined cycle and other configurations; particulate traps for diesel exhausts, molten metals, sewage treatment
Refractories	Furnace linings, crucibles, flasks etc.	High-temperature / industrial heating/ melting/ heat treating processes
Structural components	Beams, panels, decking, containers	

Table 1.2: Potential industrial applications for continuous fibre reinforced ceramic matrix composites [1].

The U.S. market for ceramic matrix composites alone in 1999 was worth $115.6 million. This includes prototype and production quantities, as well as research funding. Currently, the markets are still dominated by wear parts, cutting tools and radiant burner tubes. The U.S. market is expected to reach $177.6 million by 2004 with an AAGR of 9.1% per year from 1999 to 2004 [12]. Energy-related applications in the U.S. are the fastest growing market segments from 1999 to 2004, at an AAGR of 20%. Lower growth rates are expected for defense and space applications of 6% per year. By 2005, new market segments to emerge include thermal protection systems and propulsion components for spacecraft, as well as selected aircraft applications. By 2010 widespread application of ceramic matrix composites is expected, including in the defense and industrial processing areas (chemical processing).

As with monolithic ceramics, however, ceramic matrix composites face several major obstacles to continued commercialization. Acceptance by design engineers and users is critical and difficult, since ceramics are perceived as fragile and brittle. There is also a general bias against new materials especially because of the lack of experience. Most end users want the new part to cost the same as the one being replaced. Reliability is another important issue. Another problem is that tooling and producing prototype can be time consuming and expensive.

	1999	2004	AAGR % 1999-2004	Total AAGR % 1999-2004
U.S.	115.6	177.6	20.0 - Energy related applications 6.0 - defence and space applications	9.1
Worldwide	216.6	318.0	—	8.0

Table 1.3: U.S. and World Markets for Ceramic Matrix Composites ($ Millions) [12]

1.5 State of the art processing techniques of fibre reinforced CMCs

The design and tailoring of composite microstructures to achieve improved or new properties presents processing challenges. Limited or near-zero porosity is

commonly desired, as is a substantial degree of homogeneity in the density and microstructure of the deposited material, whilst the strength of the reinforcing fibres must be retained. The fibres must be thoroughly embedded in the matrix and the matrix precursor must fill the voids between the fibres, by means of a mechanical bond with the reinforcement [13,14]. The processing route must therefore be the most appropriate or the least detrimental for the elements of the composites. Table 1.4 shows some available techniques to produce fibre reinforced ceramic matrix composites [14].

Two stages are usually involved in the fabrication of fibre reinforced CMCs:

- Incorporation of the reinforcing phase into an unconsolidated phase (e.g. slurry infiltration, in-situ chemical reaction and liquid infiltration), see table 1.4.

- Matrix consolidation (optional) or densification steps (sintering or reactive sintering).

FRCMC fabrication process	Typical processing temperatures / K	Advantages	Disadvantages
Polymer impregnation and pyrolysis	1373-1673	• Similar to resin transfer moulding in polymers • Simple tooling	• Crack formation in the matrix during fabrication • Polymer impregnation
Melt oxidation	1173-1623	• Rapid oxidation rates • Relatively thick section	• Rapid oxidation rates require other additives • Residual metal/ceramic matrix
Melt infiltration	up to 2273	• Dense matrix formation • Near net shape processing • Crystallised matrix	• High molten matrix temperatures • Restrictions on matrix choices • Variable infiltration times
Sol-gel	1273-1673	• Reasonable infiltration	• Amorphous matrix • Porous matrix • Simple geometry • Limited commercial availability
Hot-pressing	up to 2023	• Simple, stacked lay-ups • Standard set up	• Multiple heating steps • Simple geometries
Slurry infiltration	1273-1673	• Low cost manufacturing • Moulding techniques similar to polymer moulding	• Critical fibre size • Thermal expansion critical for matrix • Slurry composition • Multiple heating steps

Table 1.4: Fibre reinforced CMC fabrication processes [14].

Among the production processes cited above, chemical vapour infiltration (CVI), polymer impregnation and pyrolysis (PIP) and molten silicon infiltration are routes that do not adversely affect the fibres and result in materials with specific individual properties [15,16,17]. The demand for structural ceramics such as fibre reinforced CMCs has grown substantially in the past decade. As a result, vapour phase synthesis has emerged as a method for the preparation of near final-shape FRCMCs for advanced structural applications [16]. Among these vapour phase techniques, CVI has shown great promise in the past few years and has been increasingly recognized as one of the most successful techniques for the fabrication of FRCMCs, such as SiC_f/SiC^* [18,19,20,21]. This has led to a rapidly expanding interest in chemical vapour infiltration

Several variations of the CVI process have been developed and have led to a range of different properties. However, all are based on the use of a radiant heating source [16-25]. The reactant vapours are allowed to pass through low-density porous structures. When the temperature is high enough, vapour deposits as solid-phases on and between the fibres to form the matrix of the composite. As the deposition progresses, the fibres get larger and consequently the spaces between the fibres are reduced. The aim is to achieve a low porosity matrix without any density gradients across the preform and hence good mechanical properties.

As discussed in Chapter 2, the flow characteristics of the gaseous reactants and the heating approach used are the main characteristics differentiating each CVI process. Isothermal isobaric CVI, the easiest to achieve practically, can result in a non-uniformly densified composite and also requires long processing times [25]. The deposition of the matrix occurs preferentially near the outer surface, thus leading to the blockage of surface channels, which then prevents the gaseous reagents from penetrating the preform further. Consequently, high residual porosity remains within the centre of the preform, deleteriously affecting the mechanical properties [20,25,26]. The use of temperature and pressure gradients can overcome these drawbacks to an extent. However, as will be shown in chapter 2, when a thermal gradient is combined with a forced-gas flow, non-uniformly densified preform can also result even though a level of higher densification has been achieved [21,23,24,27].

Thus the search for more efficient methods that yield rapid and complete densification continues. The use of microwave heating in the processing of ceramic materials has recently been recognised as a promising technique [28-32]. Sintering,

---

* Silicon carbide fibre/silicon carbide composite (SiC_f/SiC)

melting, calcining, drying and joining are already some of the processes in which microwaves act as the heating source. In the CVI process, microwave heating allows an inverse temperature profile to build up across the preform [29,30,31], that is, the centre of the preform becomes hotter than the surface. Thus the reaction rate is higher in the interior of the preform and infiltration occurs from the inside out. This prevents the entrapment of accessible porosity, which constitutes a major drawback for high mechanical performance with current technology and greatly accelerates the process. Although the use of microwave heating is believed to be more efficient compared to conventional heating during the CVI process, several major negative aspects exist obstructing the development and exploitation of this emerging technology. Some of these drawbacks are outlined in chapter 2.

1.6 Research objectives

To be able to develop the microwave-enhanced CVI process further, a complete understanding of the evolution of the growing matrix in time and space as well as knowing the correlations between the process parameters is essential. This may be achieved by investigating mathematical models for the process. As with the research and development of many other advanced structural materials, modelling has always played a key role in the development of the CVI process. As the CVI technology has progressed and become the leading process for fabrication of fibre-reinforced CMCs, modelling techniques have also advanced, involving coupled partial differential equations of conservation laws. A number of mathematical models describing CVI under microwave heating have been investigated in recent years [31,32,34,35,37,38]. During the infiltration of the ceramic preform using microwave heating, both the electrical and thermal properties of the material changes. Very few of the models actually include these changes. Further, these models allow for diffusion based chemical vapour infiltration only.

The goal of the present research is to construct and investigate mathematical models describing microwave enhanced chemical vapour infiltration under pressure driven flow and diffusion of gaseous precursors. These modelling efforts can offer an insight into the critical factors in this process; help to understand the effects of the various varying parameters, plus their consequences on the infiltration mechanism and

processing time, suggest ways to optimize processing and opportunities for further advances in process technology and provide a tool for integrating the design and manufacture of advanced components. A complete understanding and a successful model of microwave enhanced CVI will pave the way to a Real-time computer simulation of the process. It will dramatically reduce the cost of scientific research on the process and the industrial fabrication of CMCs; hence enhance the fabricability – a major concern in current practice. Along with microwave enhanced CVI being used to fabricate components of increasing size and complexity, the modelling of the latter will be even more important for future developments.

1.7 Overview of the next chapters

In Chapter 2, a general survey of the literature of chemical vapour infiltration (CVI) and its different types are given in the first section. This includes a description, experimental results and theoretical models of the different types of CVI. Further, application of microwave heating to CVI and prior work conducted at Nottingham University are presented. In the second section, the fundamentals and limitations of microwave heating are discussed. The theoretical and numerical models describing microwave heating are given as well. Section three contains a general review about the modelling of porous media and the type of transport and reaction processes occurring within those porous performs. Finally, in section four, literature on the key factors of modelling of CVI under microwave heating and their limitations are discussed.

In Chapter 3, a detailed formulation of the numerical models developed during this research work is presented first. Three models are built to investigate the volumetric heating, transport/reaction and infiltration processes occurring during Microwave Enhanced Forced-flow CVI (MEFCVI):

• Microwave heating of a two-dimensional preform

• Forced-flow chemical vapour infiltration

• Combination of microwave heating and forced flow during CVI (MEFCVI)

The numerical techniques applied and the numerical results obtained for each of these models are presented and discussed in the following sections.

In Chapter 4, the formulation of a theoretical model investigating microwave enhanced chemical vapour infiltration under diffusion transport process is presented

first, followed by an asymptotic analysis producing averaged equations describing the process. The numerical results obtained are then presented and discussed at the end.

A general discussion on the models developed is given Chapter 5. This includes comparison of the numerical results with experimental and theoretical literature results, understanding the effects of the various parameters involved in the ME-FCVI and diffusion based MECVI process and suggesting ways to process optimization. In Chapter 6, a general conclusion is presented based on the models developed that contributed to the present research work. Finally Chapter 7 addresses areas where further research may be carried out to improve the models developed so far for microwave enhanced CVI. A list of appendices and references are mentioned at the end of this thesis.

CHAPTER 2:

LITERATURE SURVEY

2.1 Chemical vapour infiltration (CVI) process

The technique is derived from an older technology, chemical vapour deposition (CVD), in which a coating of a material on a substrate is deposited from an appropriate precursor gas [1,10]. During chemical vapour infiltration, gaseous reactants flowing into a furnace infiltrate a heated porous preform (generally made from fibres), penetrate the void spaces and decompose to deposit a solid phase onto the fibres surface, thereby filling the spaces within the preform, see figure 2.1. This coating forms the matrix, which along with the fibres constitutes the composite. As is known, entrapment of porosity is detrimental to the subsequent properties; therefore the deposition coating must interlock in order that the fibres are held together without leaving spaces between them [16,40]. As a rule, a fully densified preform is the desired result if good mechanical properties for the composite are to be achieved. However, CVI is relatively complex and requires detailed phenomenological knowledge of the mass and heat transfer, chemical kinetics and infiltration stages taking place within the process [20,23,41]. Different applied conditions would result in different microstructures and properties in addition to dissimilarities in deposition rate and density gradients across the preform, since inherent competition may exist between the reaction-deposition mass and heat transport processes [42,43].

(a) Initial diameter and separation between fibres

(b) Close contacts result in reduced area for deposition

(c) A few isolated pores remaining within the tow
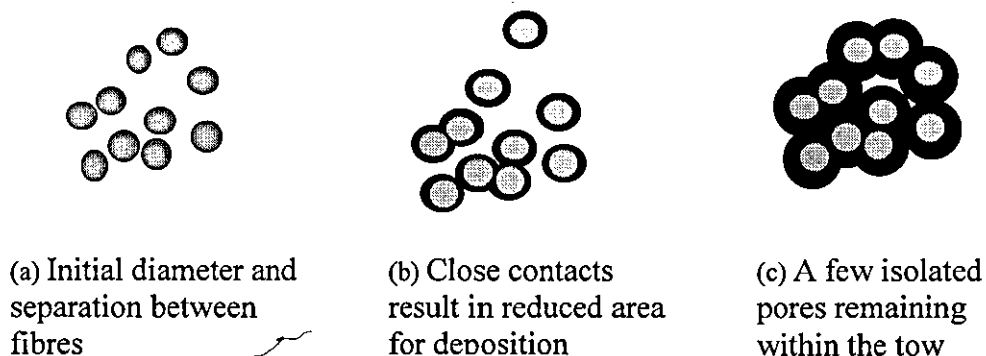
Figure 2.1: Geometric model for infiltration of oriented fibre preform.

CHAPTER 2: LITERATURE SURVEY

2.1.1 Advantages of CVI

The extensive interest in the CVI process arises for several reasons. First, CVI has the potential to fabricate fibre reinforced ceramic matrix composites that have attractive mechanical properties (fracture toughness in particular), and at relatively low temperatures (e.g. TiB_2 has its melting temperature at $3225^{\circ}C$ but can be deposited at $900^{\circ}C$). The *in situ* deposition of an interfacial layer on the fibres can also enhance the fibre pullout effect (after the fibres crack, more energy is needed to pull the fibre apart from the matrix) and the near net shape potential leads to easier production for irregular shaped components. Due to its low processing temperature, the CVI process can avoid thermal degradation of the fibre and therefore the CVI process displays low residual stresses [1,20,26,43,44] in the subsequent CMC. The capability to adjust conditions in order to control matrix microstructures can result in a highly pure and fine grained matrix material, superior to that normally obtainable with other fabrication methods and also a low composite porosity [27,44].

CVI is also useful to further infiltrate materials fabricated by other processes (internal pores or cracks can be filled) and has the advantage of not needing sintering aids [10,14]. Finally the ability to pre-coat the fibre preform using the same equipment in order to tailor the fibre bonding can improve the mechanical properties.

2.1.2 CVI processing types

Fundamentally, the characteristics of the CVI process rely principally on:
- The presence or the absence of a thermal gradient across the preform
- The pressure conditions that govern the gas flow when entering the preform: isobaric, forced flow or pressure pulse,

Varying these parameters lead to several variants of the CVI process and a wide range of results [39,44].

Conventional CVI relies on heating by a radiant heating source such as induction coils and graphite susceptors. The centre of the component is heated by the thermal conduction of energy from the surface leading to a temperature at the centre lower than at the surface of the component. Since porous structures are good thermal insulators, the temperature gradients can be quite extreme.

13

There are two main conventional CVI variations that have been studied in depth for fabricating fibre reinforced CMCs; (i) the isothermal isobaric CVI (ICVI), classified as type I in figure 2.2 and (ii) the forced-flow thermal gradient CVI (FCVI), labelled as type IV, but the four main types as seen in the figure are discussed in this section for completeness.
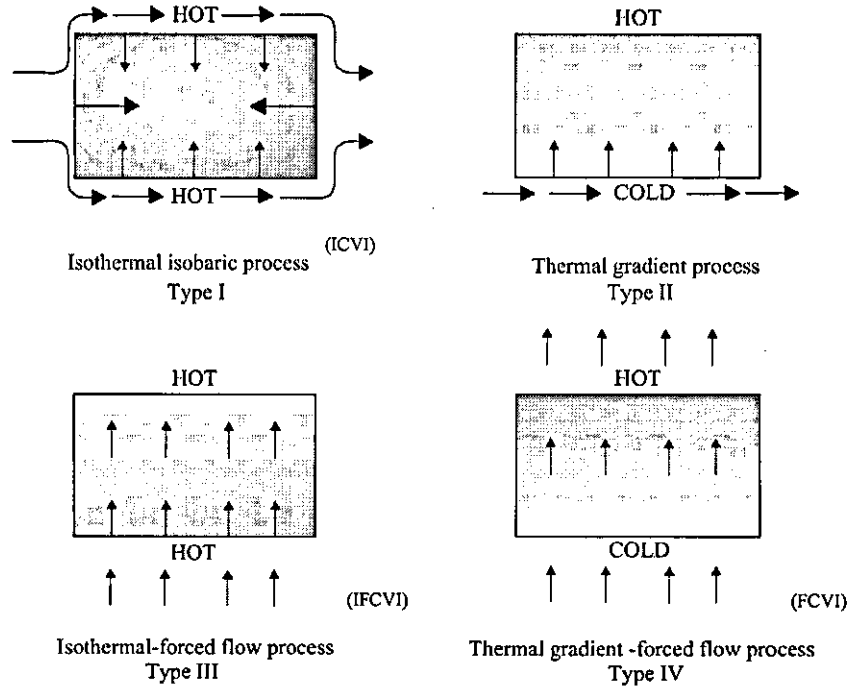
Figure 2.2: Type I to type IV CVI processes [44]. The arrows represent the flow of gaseous species. The darker regions are representative of the level of densification.

2.1.2.1 Isothermal isobaric CVI (ICVI)

ICVI is the most widely commercially used process; it involves a diffusion mechanism for the gaseous species transport [44-48]. The porous preforms are placed in a uniform-temperature zone of a hot-wall reactor under vacuum (~1 kPa). The gaseous reactants move across the preform and the delivery of molecular or atomic species onto the surfaces and internal porosities of the preform occurs through chemical diffusion in the gas phase. Similarly, gaseous reaction products must diffuse out of the preform back into the reactor, see figure 2.3.

The main difficulties of this process are the tendency to deposit preferentially near the outer surface because the concentration of the reagents decreases on progressing into the preform and the concentration of products, which tend to lag the

deposition, increases within the preform. Long processing times (several weeks are not uncommon) are thus required to reach reasonably high matrix densities [25,27,45,46,48]. The external transport conduits can also seal before any significant deposition occurs at the centre of the preform. This relatively impermeable layer then slows the rate of infiltration and accentuates the density gradient that is known to be detrimental for mechanical properties. The process has to be interrupted several times in order to permit removal by machining of the dense "crust" formed on the exterior surface of the preform. This both significantly increases the duration of the process and the production cost, which can become uneconomical for all but very high value applications.

Despite the long infiltration times, the ICVI process is, however, well suited for the fabrication of thin-walled, i.e. no more than 3 mm composites, of complex shapes [25,46,47].
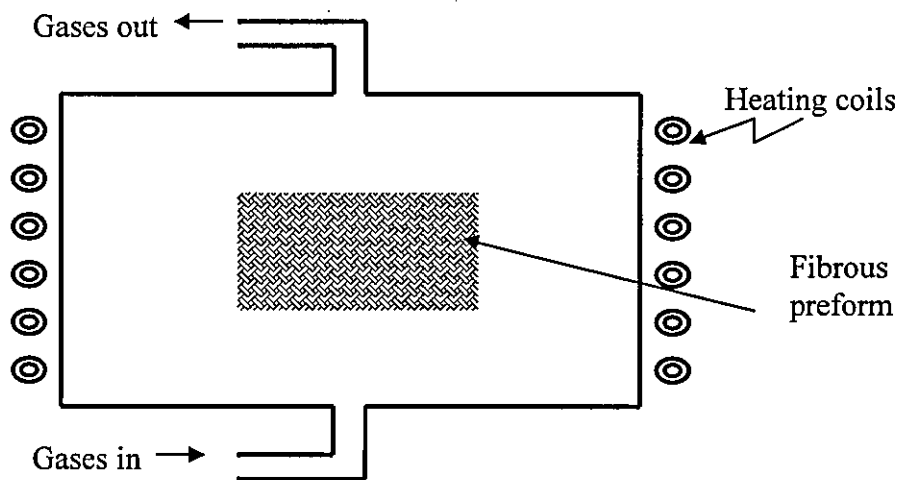
Figure 2.3: Schematic of an isothermal isobaric chemical vapour infiltration process

Isothermal chemical vapour infiltration has extensively been studied theoretically since the late 1980's and early 1990s [45,46,49-62]. A simple pore model describing the interaction between the diffusion and reaction mechanisms occurring duing ICVI was developed by Middleman [49]. Under conditions commonly used in commercial ICVI, the model showed that densification occurred directly from the surface reaction that arises from the decomposition of the precursor species. No gas phase reaction played a role in producing the composite. However, the author speculated that if a chemical scheme was found that produced the precursor species

15

through a gas-phase reaction and if the reactor was operated at a very short residence time, then it was possible to achieve densification from the inside out. This showed that the kinetics of gas-phase and surface reactions was a key factor in developing improved models for ICVI. A similar study was performed by Sheldon et al [52] for the fabrication of SiC_f/SiC via the decomposition of methyltrichlorosilane (MTS). The authors observed that more uniform infiltration was obtained in the samples when baffles were placed in the reactor and HCl was added to the inlet gases. However, this model predicted that the infiltration of the preforms should be more uniform than the results they obtained experimentally. This discrepancy can be explained by the fact that the mass transport and the deposition kinetics are more complex than the description they used. Robust numerical simulations were performed recently by Jin et al to simulate the developing fibre-matrix microstructure in two and three dimensions during ICVI [58,61,62]. However, the models do not incorporate either kinetic theory or percolation theory, which were used by previous authors [49-57] to describe the diffusion-reaction mechanisms and the preforms microstructure. Whilst the models were able to predict the residual porosity during the infiltration process and the precise locations and shapes for all pores, they were unable to predict the influence of the varying parameters on the infiltration stages. Further, significant discrepancy was observed between the numerical and experimental results.

2.1.2.2. Thermal gradient CVI (TG-CVI)

Many attempts have been made to introduce a thermal gradient across the preform via modifications to the heating system design, see figure 2.4 [63,64]. The aim is to attain high density and homogeneous ceramic composites and reduce the infiltration time.

A steep thermal gradient is created by exposing one side of the preform to the hot zone of a furnace, figure 2.2, type II. The part of the preform away from the source of heat is then cooler because of the self-insulation provided by the porous preform. Water-cooling at the bottom side of the preform can also be used to increase the temperature gradient if necessary. The gaseous reactant supplied via a flowing gas stream over the cold surface progresses axially and radially by diffusion from the cold side to the hot surface. Deposition of the matrix phase does not occur until the diffusing

reactants approach the vicinity of the hot zone of the preform. As deposition occurs at and near the hot surface, the amount of porosity decreases, causing the density and thermal conductivity to increase for the infiltrated portion. As a result, more of the preform is heated to a temperature high enough to cause significant deposition to occur. Infiltration occurs progressively from the hot surface toward the cold area. However, long infiltration times (weeks) are again necessary since the transport of reactants into the preform, and reaction products out, occurs by diffusion alone. It is usual to increase the temperature at the colder surface of the preform in order to attain sufficiently high temperatures further within the preform. The cold surface is generally machined off at the end of the process to remove material that was not sufficiently infiltrated.
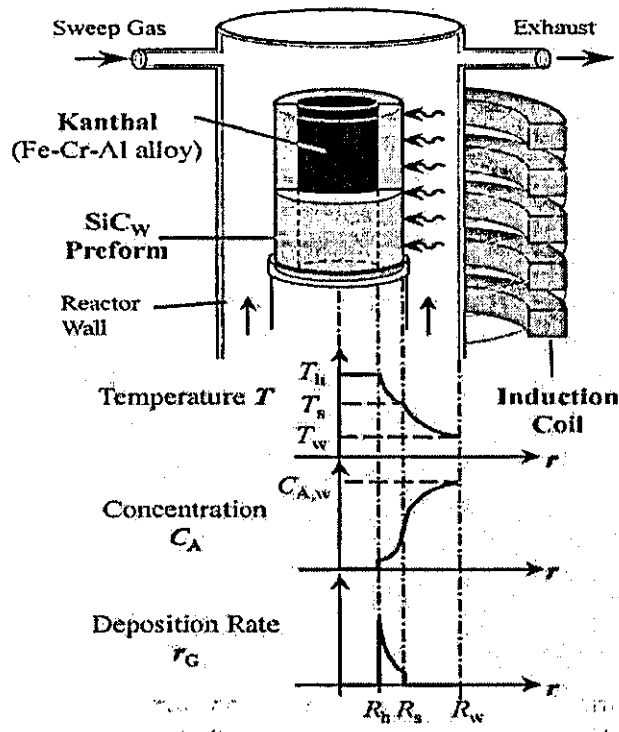
Figure 2.4: Schematic of a thermal-gradient CVI reactor, adapted from [69]

The experimental results obtained from chemical vapour infiltration using thermal gradient proved that the process was indeed not appropriate enough to limit the drawbacks obtained from ICVI. Few mathematical models [65-68] developed during the past decade describing the TG-CVI process further helped to understand the disadvantages of applying the thermal gradient alone. Gupte and Tsamopoulos [65] utilized a single pore model and later used percolation theory [66] to demonstrate the importance of the pore geometry and the imposed temperature gradients on the

17

densification process. They concluded that although the thermal gradients improved the densification to some extent, thermal gradients alone were insufficient to counterbalance the diffusion limitations. Ofori and Sotirchos [67] later developed multidimensional models to describe TG-CVI. They used a generalized form of the dusty-gas model[*] to describe the mass transport of the gaseous species in anisotropic porous structures. Their results indeed supported those obtained earlier experimentally and theoretically, however the models focused mostly on the effects of using multidimensional analysis.

2.1.2.3 Isothermal forced flow CVI (IFCVI)

To overcome the limitations imposed by diffusion, forced flow of the gaseous precursors can be used, see figure 2.2 type III. This process known as forced flow chemical vapour infiltration has been studied under isothermal conditions [45,69-72]. In general, the experimental results showed that the IFCVI process was a technique by which dense ceramic composites could be produced in a rapid way and approximately five times faster as compared to ICVI. Mass transport no longer relies significantly on diffusion phenomenon but on the flow rate used. However, whilst this works well at high porosities, when some regions of the preform reach densities greater than 85%, they become impermeable as the porosity closes [45,69,72], ending the flow of reagent even though other regions of the preform may be of much lower density. Furthermore deposition then occurs preferentially near the preform surface leading to non-uniform deposition because the reagent concentration is highest here. This fact was supported by theoretical models constructed to investigate the process [73,74]. Vignoles et al [74] showed that the IFCVI process relied on the interplay between the chemical species transport and the chemistry, both inside and outside the porous medium. Proper control of these parameters would then result in the desired densification of the preform. During the past decade, IFCVI process has been mostly used to consolidate fibrous or particulate materials.

2.1.2.4 Forced flow/ thermal gradient CVI (FCVI)

FCVI is the most well-known chemical vapour infiltration process. It takes advantage of both a thermal gradient and a forced flow of reagents, see figure 2.2 type

[*] see section 2.3.4

IV. Oak Ridge National Laboratory (ORNL) [22] and Georgia Tech Research Institute [75] developed this approach specifically to overcome the problems of slow diffusion and restricted permeability. The processing behaviour relies on the combination of type II and type III processing.

A steep thermal gradient is created by exposing one side of the preform to the hot zone of a furnace at temperatures around 1473 K, see figure 2.5. The part of the preform away from the source of heat is then cooler because of the self-insulation provided by the porous preform. Water-cooling at the bottom side of the preform may also be used to further expand the temperature gradient if necessary. Gaseous reactant supplied *via* a flowing gas stream over the cold surface progresses axially and radially from the cold side to the hot surface. Deposition of the matrix phase does not occur until the reactants approach the vicinity of the hot zone on the top side of the specimen, therefore preventing the entrance side from being sealed. As deposition occurs at, and near the hot surface, the amount of porosity decreases, causing the density and thermal conductivity to increase for the infiltrated portion. This results in more of the sample areas being heated to a temperature high enough to cause significant deposition to
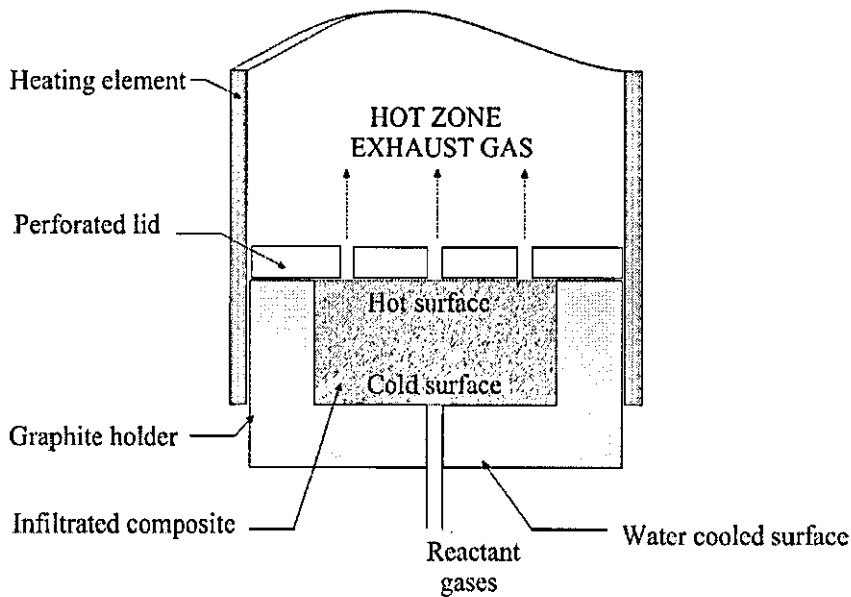
Figure 2.5: Schematic of a forced flow CVI equipment (adapted from [22].

occur; alteration of the heating and cooling leads to a similar effect. Hence, infiltration occurs progressively from the hot surface toward the cold area [22,76-80]. The cooler surface rises in temperature, causing eventual infiltration of the entire volume although

deposition quality occurring at the cold side is poor. However, the deposition times are greatly reduced compared to the ICVI process [22,76-80].

In FCVI, thermal gradients constitute an important parameter since they can lower the densification time. Any thickness can be infiltrated when a proper thermal gradient is selected [78,79] with the bottom temperature kept at temperatures high enough to avoid significant depletion of the gas and blockage in this region.

The process is terminated when the pressure gradient (also called the back pressure) across the preform becomes too large due to the closure of the flow passages through the pores. This pressure drop across the preform is often monitored in order to follow the extent of the densification [79].

Some alternative flow paths which permit continued forced flow of the reagents through the preform, even after some regions have densified to the point where they are impermeable, can be created. Figure 2.6, shows the creation of lateral exits by cooling both the bottom and the sides of the disk allowing the build-up of reactant gases to evacuate on the sides since the deposition initially occurs preferentially at the middle top of the preform.
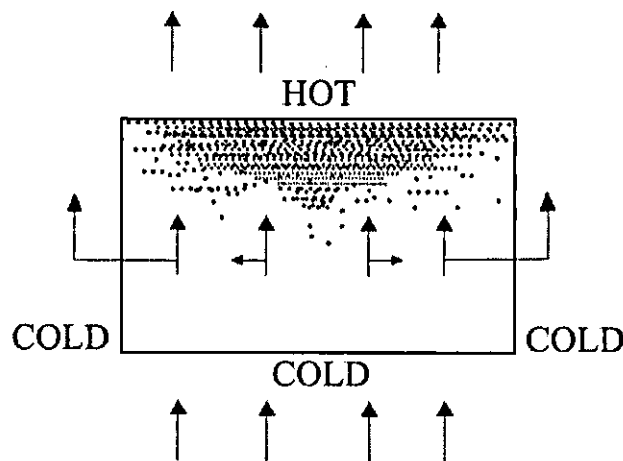
Figure 2.6: Improved thermal gradient-forced flow CVI process.

Uniformity and efficiency in the deposition across the preform are enhanced compared to ICVI. A reduction in the infiltration time to 10 - 24 h is expected when operating conditions are adequately selected [22,78,79]. However, even though the reaction is no longer kinetically controlled by diffusion, vapour deposition relying on forced flows has limitations. The composite never achieves the expected theoretical density since the reactant stream is forced to flow through the preform. The finest

porosity within the fibre bundles (tows) is only reached by diffusion. Experiments have shown that the maximum degree of deposition is achieved with the longest infiltration time [27]. Disadvantages also include more complex temperature and gas flow controls as well as greater complexity in processing multiple parts. It is only suitable for thick-walled structures (~25 mm thick) of simple geometry [78,79].

Much effort has been done in the past to investigate the FCVI process theoretically and numerically [26,41,81-86]. One of the first such studies was done by Tai and Chou [26] in 1990. The authors applied a quasi-steady-state approach to model the FCVI process. They adopted a three-dimensional unit cell to simulate the spatial arrangements of reinforcements in the fibre preform. Their analytical results indicated that the final density of the composite was highly influenced by the position of the heating elements in the reactor. A highly uniform matrix deposition could be achieved by reducing the temperature differences among the heating elements in the reactor. Further, they also observed that the forced convection flow within the preform allowed for better uniform densification and significant reduction in processing time as compared to ICVI. However, they noted that significant increase in pressure was necessary to maintain constant flow rate. Consequently, they concluded that reducing the gaseous flow rate at the end of the process was desirable for further infiltration. The same authors later studied the effects of the activation energy of the decomposition reaction of methyltrichlorosilane (MTS) vapour in excess hydrogen for the fabrication of SiC_f/SiC composites [83]. They observed that the type of reaction mechanism considered during the investigation affected the theoretical matrix decomposition.

Starr and Smith [81] developed a three-dimensional model to study FCVI. The model results suggested a self-optimizing feature of the forced flow/gradient CVI process that produced uniform density in the final composite over a range of infiltration conditions. However, the model did not consider the effect of the increasing back-pressure that is observed experimentally during the infiltration process.

Gupte et al [82] modelled the process by using a Bethe lattice and percolation theory to account for utilized, unutilized and blocked pore space (see section 2.3). They also assumed Darcy's flow in the preform. Their results clearly showed that thermal gradients, when combined with pressure gradients, quite satisfactorily overcome diffusion limitations and provide increased control over the product quality. However, their results also showed that densification was limited by early termination of the process due to excessive pressure gradients. This competing effect lead to an optimum

flow rate beyond which lower overall densification was observed, in spite of better uniformity.

Other mathematical and numerical models [41,84-86] showed similar results to those obtained from the models described above. The important fact that contributes to uniform density during FCVI, is that it is necessary to have a proper combination of flow rates and temperature gradients to avoid preferential deposition in the region close to the hot face.

2.1.3 Limitations of CVI

Although the chemical vapour infiltration process has an enormous potential for the fabrication of FRCMCs due to the advantages that it offers, see section 2.1.1, it does suffer some limitations. Some of these were discussed in section 2.1.2 and depend on the particular variant of CVI used. Since ICVI and FCVI are the two main CVI processes that have been extensively studied, some of their limitations are listed in table 2.1. Note that the reactants involved in the matrix formation can be toxic, corrosive, explosive or a combination of these [88].

	Limitations	
	ICVI	FCVI
Processing time	Up to 1000 h	As short as 10-20 h
Number of parts	Several to many	Single
Reactor	Large	Sophisticated to maintain both the thermal and pressure gradient
Cost	High due to lengthy processing time and intermittent machining operations	High to due the costly equipment and the high expenditure per part
Density	Up to 90%	Up to 90%
Uniformity	Density gradients	Relatively uniform near the hot zone
Shape/size of the part	Complex/Thin (3 mm)	Simple/Thick (25 mm)

Table 2.1: Limitations of ICVI and FCVI processes (adapted from 39)

2.1.4 CVI under microwave heating

The conventional CVI processes that have been discussed above all rely on radiant heating of the fibre preform and hence thermal conductivity to control the temperature profile in the preform. The major problem encountered here is the preferential deposition in the preform's outer regions, which results in pore blockage, a non-uniform composite density, and/or residual porosity. An alternative is the use of microwave radiation at the heating source for the processing of the ceramic composites. The advantages of using microwaves arise principally from its ability to couple energy directly into the material being processed, leading to the formation of an inverse temperature profile, which allows the preform to be infiltrated from the inside out [28,29,30,39]. As a result, it can avoid pore closure and reduce deposition times an order of magnitude shorter than can be achieved using conventional ICVI with the production of uniformly and highly densified fibre reinforced CMCs.

2.1.4.1 Prior experimental work at Nottingham Univ.

Jaglin and Binner [30,39] investigated the densification mechanisms occurring in a microwave enhanced chemical vapour infiltration process depositing a SiC matrix in a Nicalon-based fibre preform to produce a SiC_f/SiC fibre-reinforced ceramic matrix composite under pressure driven flow of the gaseous precursors. They investigated the kinetics of the SiC infiltration from hydrogen and methyltrichlorosilane. Hydrogen acting as a carrier gas in the reaction, is used not only for its lightness (reactant diffusion is then faster), but its presence is often necessary for reaction with chemical constituents such as chlorine. Optimum infiltration conditions were selected to analyse the densification process across the fibre performs. Pressure, temperature and hydrogen flow rates were the main influential parameters studied in the deposition of SiC matrix. The inverse temperature profile was successfully produced via microwave heating, resulting in preferential densification of the SiC_f/SiC composites from the inside out. An average relative density of ~55% was achieved in 24 h, representative of a gain of 26 vol.% from the initial vol.% fibre. The centre was densified up to 70%. Table 2.2 summarizes the advantages and disadvantages obtained from this study [39].

Advantages	Disadvantages
• More spatially uniform, high-density composites of complex shapes can be produced in comparison to conventional CVI processes employing radiant heating • Relatively short processing times; the infiltration proceeds more rapidly and to a greater extent with microwave heating/external cooling • No machining operations required to remove crusting, since the latter does not occur • Microwaves radiations enhance the deposition kinetics and the conversion rates.	• MECVI may remain a slow process if it relies on the diffusion of the gas species. Higher reductions in time are expected in forced flow operations where deposition reactions are not transport limited. • Only one preform per run was produced at a time. However, it was possible to overcome this situation • There may be limitations on sample size and shape. Specific cavity design may be required • Spatially non-uniform electric field (hot and cold spots) and uncontrolled microwave mode jumping inside the preform may result in non-uniform heating and deposition patterns. Thermal runaway occurs when different rates of absorption occur in different parts of the sample • Undesirable gas-phase plasma formation at low pressures, with concomitant drop in power delivered to preform

Table 2.2: Advantages and disadvantages of the microwave enhanced chemical vapour infiltration (MECVI) process [39].

2.1.4.2 Modelling of CVI under microwave heating

Modelling and numerical simulations describing this newly emerging technology, forced-flow chemical vapour infiltration process under microwave heating (ME-FCVI), can eventually reduce the time consuming experimental part. If models can successfully simulate the heating behaviour, mass transport and reaction process during ME-FCVI, then the processing parameters can be changed accordingly to produce the desired composite without the cost of sample preparation and testing. However, proper modelling of ME-FCVI is quite difficult because of the complexities involved during the process. A proper theoretical knowledge of microwave heating of ceramic materials is necessary to understand the heating stage during ME-FCVI. In the next section, the use of microwaves to process ceramic materials is described.

Accordingly, knowledge of the following physico-chemical phenomena should as well be taken into account before modelling ME-FCVI:

- Mass transport of the gaseous species in the preform (convection and diffusion mechanism)

- Chemical reactions taking place inside the preform

- Porous medium structural evolution

These phenomena are described in later sections.

2.2 Microwave processing of materials

2.2.1 Introduction

Originally, microwaves were principally used for communication and radar [88,89]. In 1950, the use of microwave energy to heat materials was discovered [90-92]. Now microwaves ovens have become common for heating food products in the home. The potential advantages of microwave heating have led researchers to design and implement new processes for industrial use. The most prominent characteristic of microwave heating is its *volumetric nature*, which is quite different from conventional heating where the heat must be conducted in from the surface of the material. Volumetric heating means that materials can absorb microwave energy directly and internally and convert it to heat. It is this characteristic that leads to advantages from using microwaves to process materials.

In the past, microwave heating had been successfully used in the following fields: tempering meat, preheating rubber slugs, vulcanizing rubber, drying crushed oranges and organic/inorganic synthesis [93]. Such industrial applications were centred on relatively low temperatures. Beginning in the late 1980s, there was growing interest in high temperature microwave processing of materials. With some successful applications both at laboratory and industrial scales, for example, in the field of ceramic processing (ceramic sintering, joining and slip casting), microwaves were justified as a potential heating mechanism to replace some conventional heating methods. These potential applications have attracted more researchers to this field [91,94-96].

However, a basic understanding of microwaves and their interaction with ceramic materials is required to realize the promise, as well as to understand the

limitations, of microwave processing. Although there is a broad range of ceramic materials that can be processed using microwaves, there are fundamental characteristics and properties that make some of these materials particularly conducive to microwave processing and others difficult. Further, while an empirical understanding of microwave processing is important in moving developmental processes into production, a more fundamental approach is required for development of optimized process cycles, equipment and controls [97-99]. For instance, repeatability of a measurement is challenging during microwave processing since the results can be affected by a number of factors, including changes in dielectric properties during processing, electromagnetic interferences with temperature measurements, sample size and placement of the sample within the cavity. The purpose of this section is to discuss, in general terms, the fundamental nature of microwaves, a mathematical description of the wave propagation and their interactions with materials and how these interactions generate heat.

2.2.2 Fundamentals of microwave heating

Fig 2.7 illustrates the electromagnetic spectrum. Radiation whose frequencies range from 300 MHz to 300 GHz, with wavelengths ranging from a few mm to 30 cm, are referred to as microwaves and heating effects that occur in this frequency range are referred to as microwave (MW) heating. Frequency bands have been specifically allocated for Industrial, Scientific and Medical (ISM) applications by the Federal Communications Commission [97] with the principal frequencies centred at 915 MHz (896 MHz in the UK) and 2.45 GHz.
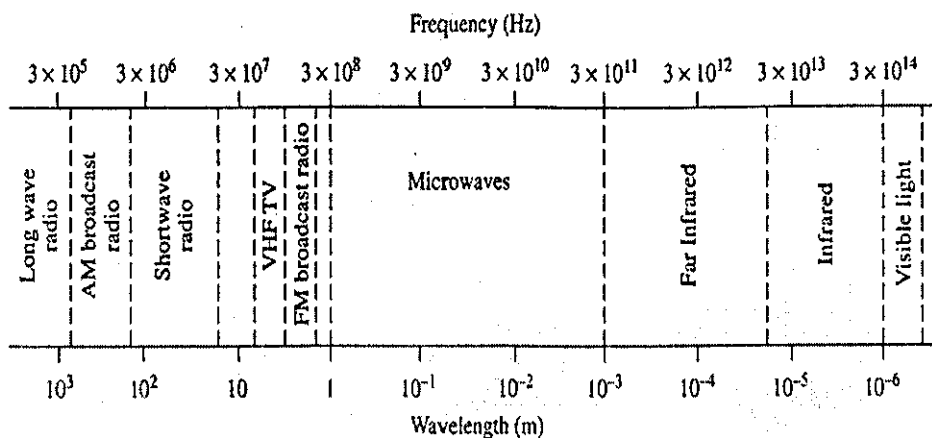
Figure: 2.7: The electromagnetic spectrum [100]

2.2.2.1 Wave propagation

Microwaves are propagating electromagnetic waves composed of an oscillating electric field $\mathbf{E}$ and magnetic field $\mathbf{H}$. These fields are perpendicular to each other and, in phase, are known as transverse electromagnetic (TEM) waves. As with all other carriers of electromagnetic energy, microwaves obey Maxwell's equations [100-102] and thus depend on interrelationships between the time-varying magnetic field and the time-changing electric field. The spatial and temporal variations of $\mathbf{E}$ and $\mathbf{H}$ are thus obtained by solving Maxwell's equations. Although the differential forms of Maxwell's equations are mostly used for obtaining solutions, the physical significance of Maxwell's equations is best understood in their *integral forms* [89,90]. The first equation is Faraday's law of induction:

$$\oint_{C_l} \mathbf{E} \cdot dl = -\frac{d}{dt} \int_{S_c} \mathbf{B}_d \cdot \mathbf{n}\, ds, \tag{2.1}$$

which states that the induced electromotive force around a closed current carrying loop C_l enclosing a surface S_c is equal to the negative of the rate of change of the magnetic flux associated with S_c. $\mathbf{B}_d$ is the magnetic flux density and the integral on the right hand side represents the magnetic flux and $\mathbf{n}$ is the unit outward vector normal to the surface S_c.

The second equation is an extension of Ampere's law:

$$\oint_{C_l} \mathbf{H} \cdot dl = \int_{S_c} \mathbf{J}_c \cdot \mathbf{n}\, ds + \frac{d}{dt} \int_{S_c} \mathbf{D}_d \cdot \mathbf{n}\, ds, \tag{2.2}$$

which states that the magnetomotive force around a closed loop C_l equals the sum of the ohmic current and the rate of change of the displacement current enclosed by the loop. In equation (2.2), $\mathbf{J}_c$ is the current density and $\mathbf{D}_d$ is the displacement flux density or electrical displacement. The original form of Ampere's law was stated only for time independent fields and did not involve the displacement current. The extension of Ampere's law to time dependent fields by Maxwell culminated for the first time in a consistent set of equations for time varying electromagnetic fields. Equation (2.2) is often referred to as the Ampere-Maxwell law.

The last two equations are Gauss's laws:

$$\int_S \mathbf{D}_d \cdot \mathbf{n} \, ds = \int_{V_c} \rho(\mathbf{r}) \, dv \,, \tag{2.3}$$

and

$$\int_{S_c} \mathbf{B}_d \cdot \mathbf{n} \, ds = 0 \,. \tag{2.4}$$

Equation (2.3), where $\rho(\mathbf{r})$ is the charge density, states that the net outward flux of the electrical displacement $\mathbf{D}_d$, from a closed surface S_c enclosing a volume V_c, is equal to the net charge contained in V_c. Equation (2.4) states that the net outward magnetic flux from a closed surface S_c is equal to zero. Equations (2.1-4) are the Maxwell's equations in integral form [90].

The constitutive equations relating $\mathbf{J}$, $\mathbf{D}$ and $\mathbf{B}$ to $\mathbf{E}$ and $\mathbf{H}$ are:

$$\mathbf{J}_c = \sigma(\omega)\mathbf{E}(t), \qquad \mathbf{D}_d = \varepsilon(\omega)\mathbf{E}(t) \qquad \mathbf{B}_d = \mu(\omega)\mathbf{H}(t), \tag{2.5}$$

where $\sigma(\omega)$ is the electrical conductivity, $\varepsilon(\omega)$ is the permittivity, $\mu(\omega)$ is the magnetic permeability of the material and $\omega = 2\pi f$, where f is the frequency of radiation. In *linear dielectric* materials, $\sigma(\omega)$, $\varepsilon(\omega)$ and $\mu(\omega)$ are independent of the field intensity. Causality between the field quantities in the constitutive equations (2.5) requires that $\sigma(\omega)$, $\varepsilon(\omega)$ and $\mu(\omega)$ be complex quantities that are functions of ω.

The differential forms of equations (2.1) and (2.2) obtained by applying Stokes theorem are:

$$\nabla \times \mathbf{E} = -\frac{\partial \mathbf{B}_d}{\partial t} \tag{2.6}$$

and

$$\nabla \times \mathbf{H} = \mathbf{J}_c + \frac{\partial \mathbf{D}_d}{\partial t}. \tag{2.7}$$

The differential forms of equations (2.3) and (2.4) obtained by applying the divergence theorem are:

$$\nabla \cdot \mathbf{D}_d = \rho(r) \tag{2.8}$$

and

$$\nabla \cdot \mathbf{B}_d = 0. \tag{2.9}$$

Equations (2.6-2.9) are Maxwell's equations in differential form. Combining these with the constitutive equations in equation (2.5) allows the electric and magnetic field distributions in an object exposed to microwaves to be obtained.

2.2.2.2 Microwave/material interactions and polarization

Important applications of microwaves result from their interaction with various types of materials. This research deals particularly with microwave interactions with ceramic materials, which are also referred to as dielectric materials in this thesis. When a dielectric material is placed in the path of microwaves, microwave/material interactions may take place and heating of the material may be initiated. The interactions take place through the electric and magnetic field. Without an electric field, the dipoles (atoms and groups of atoms) that have an unbalanced charge are randomly orientated and the net polarization is zero. However, the application of an electric field in a dielectric material results in the formation and the movement of the dipoles, which results in a net polarization of the substance. There are several mechanisms that are responsible for this occurrence, including: electronic, ionic, molecular (dipole) and interfacial (space-charge) polarization [99,103-105]. In general, the addition of an applied field to each of these mechanisms in a normal state will cause a displacement of charge, which results in a polarization in the direction of the field. This effect on each mechanism can be seen schematically in figure 2.8. For a given material, the sum of the contributions from each mechanism determines the net polarization, P_n, of the dielectric material:

$$P_n = P_{electronic} + P_{ionic} + P_{molecular} + P_{interfacial}.$$

(2.10)

1. Electronic Polarization

For a dielectric material in a normal state, electrons are bound to their parent atoms and are fixed to their equilibrium positions. This mechanism becomes apparent upon application of an electric field, under which the electrons are shifted from equilibrium with respect to the positive nuclei in the direction of the field. In this state the atom acts as a temporary induced dipole.

2. Ionic or Atomic Polarization

Ionic or atomic polarization differs from the electronic mechanism in that it occurs due to the relative motion of the atoms instead of a shift of the electron clouds surrounding atoms. Under an applied field, a separation of charge is caused which yields a displacement of the cations and anions in crystals relative to their equilibrium positions. Specifically, cations are attracted towards the negative electrode and anions are attracted towards the positive electrode.

3. Molecular Polarization

Molecules are randomly oriented in a material in a normal state so that there is no net charge present. Molecule or dipole polarization occurs when an external field aligns permanent dipoles parallel to the field. In some materials, this polarization can be retained upon removal of the field due to the need for thermal activation of molecular rotation.

4. Interfacial Polarization

In interfacial or space charge polarization, mobile charge carriers in a heterogeneous material are accelerated by an applied field until they are impeded by and pile up at physical barriers. This build up of charge dictates the polarization of the material. Grain/phase boundaries and free surfaces are common barriers.

The polarization resulting from the mechanisms above is strongly influenced by frequency [106] and the individual mechanisms have varied dependences of their polarization upon frequencies. In general the larger the size of the sample involved, the slower the response upon application or removal of a field and consequently the relaxation frequency is lower.

The origin of microwave heating lies in the ability of the electric field to polarise the charges in the material and the inability of this polarisation to follow rapid reversals of the field that, consequently, cause loss mechanisms. Polarisation in the material is thus responsible for microwave heating in dipolar materials [99].
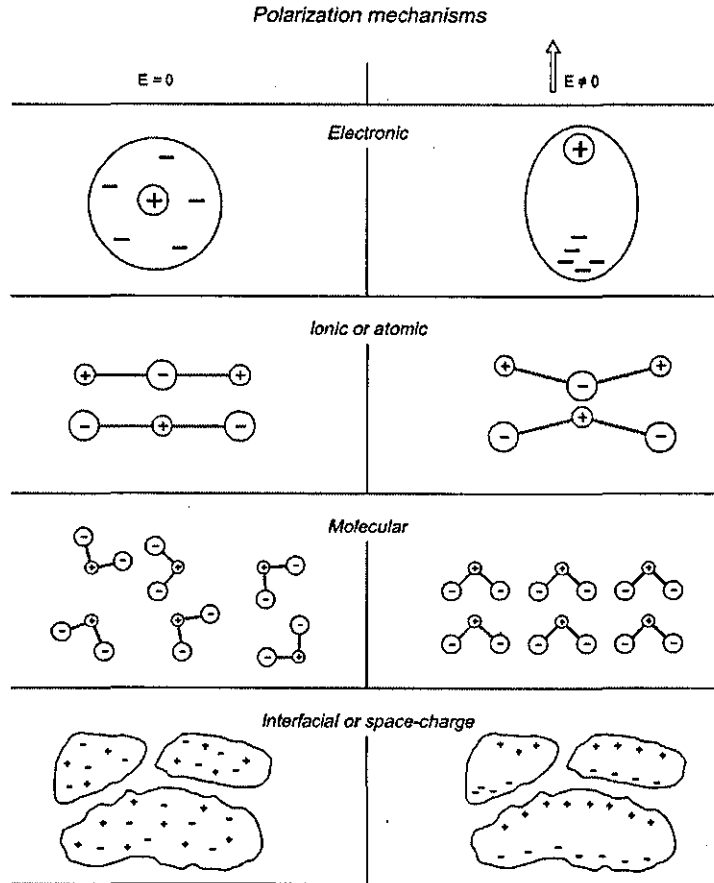
Figure 2.8: Schematic representation of the polarization mechanisms in materials [103]

2.2.2.3 Dielectric properties and dielectric loss mechanisms

The configuration of a microwave field in the presence of a material is determined by Maxwell's equations with the appropriate boundary conditions [97]. The degree of interaction or absorption of microwaves is characterised by the *complex permittivity* of the material. The expression of the complex permittivity is obtained as follows: If Maxwell's equations are solved in the frequency domain with a time-harmonic dependence of the form $e^{-i\omega t}$, then the electric and magnetic field are given by $\mathbf{E} = \overline{\mathbf{E}}e^{-i\omega t}$ and $\mathbf{H} = \overline{\mathbf{H}}e^{-i\omega t}$ respectively. t represents the time variable and ω is the angular frequency. Using the constitutive equations (2.5) to replace $\mathbf{B}_d$ and $\mathbf{D}_d$ in terms of $\mathbf{H}$ and $\mathbf{E}$, equation (2.6) can be rewritten as:

$$\nabla \times \overline{\mathbf{E}} = i\omega\mu(\omega)\overline{\mathbf{H}} \qquad (2.11)$$

and equation (2.7) as:

31

$$\nabla \times \overline{H} = [\sigma(\omega) - i\omega\varepsilon(\omega)]\overline{E} = -i\omega\varepsilon * (\omega)\overline{E}. \tag{2.12}$$

The term involving σ represents the condition currents and the term with ε represents the contribution from displacement current. In a good conductor the conduction currents dominate and in a good dielectric displacement currents are large. In most materials heated by microwaves both terms contribute to the currents. A general treatment for wave propagation in such materials is carried out by defining $\varepsilon * (\omega)$ in equation (2.12), as the *complex permittivity* where:

$$\begin{aligned} \varepsilon * (\omega) &= \varepsilon(\omega) + \frac{i\sigma(\omega)}{\omega} \\ &= \varepsilon'(\omega) + i\varepsilon''(\omega). \end{aligned} \tag{2.13}$$

In the second line of equation (2.13), $\varepsilon *$ has been split into its real part $\varepsilon'\, (= \text{Re}(\varepsilon'))$, which represents the material's ability to store electrical energy, and an imaginary part $\varepsilon''\, (= \text{Im}(\varepsilon'))$, which accounts for dielectric loss through energy dissipation. Since ε and σ are in general complex functions, $\varepsilon' = \text{Re}(\varepsilon) - \text{Im}(\sigma/\omega)$ and $\varepsilon'' = \text{Im}(\varepsilon) + \text{Re}(\sigma/\omega)$. Thus the conductivity and dielectric properties contribute to both ε' and ε'' [97,107]. This is the most general relationship for ε' and ε'' with ε and σ. Most texts prefer to ignore the complex forms of ε and σ whereby $\varepsilon' = \varepsilon$ and $\varepsilon'' = \sigma/\omega$. With such an assumption, σ is in reality an effective conductivity of the material incorporating conductive as well as dielectric losses. In either case, a proper interpretation of ε' and ε'' requires an appropriate model for the constitutive parameters ε and σ. The term lossy is commonly used in the MW literature to denote materials that dissipate electrical energy into heat.

The measured ε' and ε'' are typically reported scaled with respect to the free space permittivity ε_0. Hence the relative permittivity k' and the relative dielectric loss k'', are:

$$k' = \varepsilon'/\varepsilon_0 \text{ and } k'' = \varepsilon''/\varepsilon_0. \tag{2.14}$$

If magnetic effects are negligible, the magnetic permeability $\mu(\omega)$ is well approximated by its value μ_0 in free space. If this is true, then the relative dielectric constant k' and k'' are the two electrical properties of the material that are sufficient

for studying microwave heating. In one and two dimensional spaces, equations (2.11) and (2.12) can be coupled together to obtain:

$$\nabla^2 \mathbf{E} + k^2 \mathbf{E} = 0, \tag{2.15}$$

where

$$k^2 = \omega^2 \mu_0 \varepsilon_0 (k' + ik''). \tag{2.16}$$

Equation (2.15) is known as the wave or Helmholtz equation whose solutions represent waves travelling in opposite directions. The propagation constant k is represented as a complex quantity

$$k = \alpha + i\beta, \tag{2.17a}$$

where α and β are related to the dielectric properties of the medium and frequency of radiation by

$$\alpha = \frac{2\pi f}{c_s} \sqrt{\frac{k'\left(\sqrt{1 + \tan^2 \delta} + 1\right)}{2}}, \tag{2.17b}$$

$$\beta = \frac{2\pi f}{c_s} \sqrt{\frac{k'\left(\sqrt{1 + \tan^2 \delta} - 1\right)}{2}}, \tag{2.17c}$$

where the loss tangent, $\tan \delta = \dfrac{k''}{k'}$ and δ is the phase angle change between the electric field and the current. In equations (2.17b) and (2.17c) we have used the property $c_s = 1/\sqrt{\mu_0 \varepsilon_0}$ where c_s is the speed of light in free space. The *phase constant* α represents the change of phase of the propagating wave and is related to the wavelength of radiation in the medium, λ_s, by

$$\lambda_s = \frac{2\pi}{\alpha}, \tag{2.18}$$

which in free space reduces to $\lambda_0 = c_s/f$. The *attenuation constant* β controls the rate at which the incident field intensity E_0 decays into a sample. The quantity β^{-1} is known as the *penetration depth*, that is, the distance at which the field intensity decreases to $1/e$ of its incident value.

2.2.2.4 Poynting theorem and power dissipation

The expression for the absorbed power is obtained through the Poynting theorem [97,107]. The power flux associated with a propagating electromagnetic wave is represented by the Poynting vector $\mathbf{S}$ and the time average power flux for harmonic fields is [97]:

$$\mathbf{S} = \frac{1}{2}\mathbf{E} \times \mathbf{H}^*, \tag{2.19}$$

where $\mathbf{H}^*$ denotes the complex conjugate of $\mathbf{H}$. The Poynting theorem allows the evaluation of the power absorbed in the medium. It is expressed as:

$$\oint_{S_c} \mathbf{S} \cdot \mathbf{n} \; ds = -\frac{1}{2}\omega\varepsilon_0 k'' \int_{V_c} \mathbf{E} \cdot \mathbf{E}^* \; dv + \frac{i\omega\mu_0}{2} \int_{V_c} \mathbf{H} \cdot \mathbf{H}^* \; dv + \frac{i\omega\varepsilon_0 k'}{2} \int_{V} \mathbf{E} \cdot \mathbf{E}^* \; dv, \tag{2.20}$$

and states that the net power flow across a surface S_c enclosing a volume V_c equals the power absorbed in the medium (real part) to that stored in electric and magnetic fields (imaginary part). $\mathbf{E}^*$ denotes the complex conjugate of $\mathbf{E}$. Applying the divergence theorem to equation (2.20), the differential form of the Ponyting theorem is:

$$\nabla \cdot \mathbf{S} = -\frac{1}{2}\omega\varepsilon_0 k'' \mathbf{E} \cdot \mathbf{E}^* + i\omega\left(\frac{\mu_0}{2}\mathbf{H} \cdot \mathbf{H}^* + \frac{\varepsilon_0 k'}{2}\mathbf{E} \cdot \mathbf{E}^* \right), \tag{2.21}$$

and the power absorbed per unit volume is:

$$\begin{aligned} P_{ab}(r) &= -\mathrm{Re}(\nabla \cdot \mathbf{S}) \\ &= \frac{1}{2}\omega\varepsilon_0 k'' \mathbf{E} \cdot \mathbf{E}^*. \end{aligned} \tag{2.22}$$

Hence with a knowledge of the electric field distribution in the medium the local power absorbed is obtained from (2.22). Note that the absorbed power is only dependent the electric field intensity in the sample and k'' if the latter is dependent on temperature.

2.2.2.5 Temperature distribution

When a dielectric material is heated using microwave energy, electrical energy is converted to heat. Thus knowing how the heat propagates within the material, or in other words knowing the temperature distribution, is very important. However, the

atmosphere surrounding the material is not directly affected by the microwave energy and hence will be at a lower temperature than the surface of the dielectric. The well-known conservation law of energy states that the rate of energy incident upon a control surface, E_1 enclosing the material plus any rate of internal generation, P_v, must balance the rate at which the energy stored changes within the control volume, E_2 plus the rate at which energy leaves the control surface E_3. Therefore we can write:

$$E_1 + P_v = E_2 + E_3 \tag{2.23}$$

The internal heat generation is a volumetric process, which in microwave heating is due to the flow of displacement currents or the tendency of permanent dipoles present to re-orientate. By assuming that the material forms the control volume, the equation for the heat flow, including a volumetric source, P_v, can be written as

$$c_p \rho_p \frac{\partial T}{\partial t} = -\nabla \cdot \mathbf{q} + P_v, \tag{2.24}$$

where T represents the temperature distribution, $\mathbf{q}$ is the total heat flux vector, ρ_p is the material density and c_p is the specific heat. Here the total flux $\mathbf{q}$ incorporates heat losses due to conduction and radiation and can thus be written as

$$\mathbf{q} = \mathbf{q}_c + \mathbf{q}_R = -k\nabla T + \mathbf{q}_R, \tag{2.25}$$

where $\mathbf{q}_c$ denotes the conductive heat transfer, $\mathbf{q}_R$ represents the term due to radiation and k_t is the thermal conductivity. Hence knowing the other parameters in (2.24), the temperature distribution, T, can thus be found. The direct consequence of this volumetric heating of a dielectric by microwave radiation is the creation of an inverse temperature profile across the sample [29,30,35,37,39,99], see figure 2.9. The magnitude of the profile is controlled by the input of microwave power and the external cooling or insulation conditions [30,39].
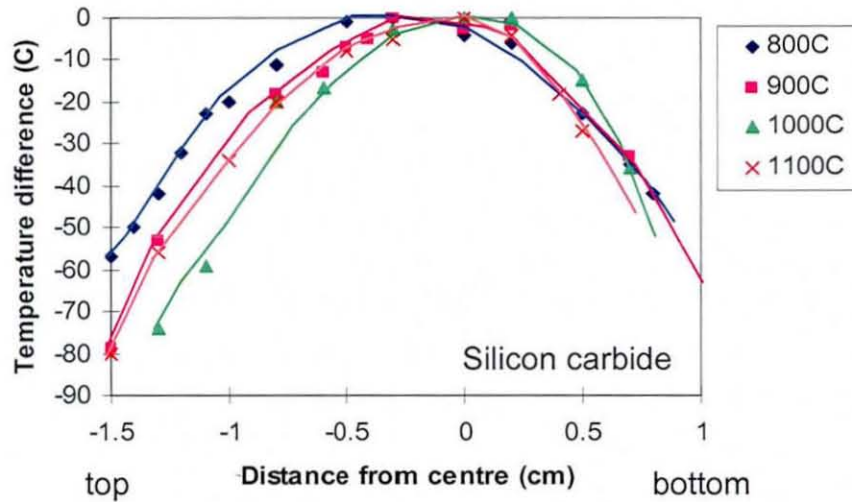
Figure 2.9: Inverse temperature profiles for silicon carbide fibres heated by microwave energy [30].

2.2.3 Limitations of the microwave heating of ceramic materials

In the past decade, microwave processing of ceramic materials has become an area of intense activity [93,97,98]. Microwave heating is attractive because of its applicability in volumetric heating at an accelerated rate (much faster than conventional methods) and with good control. Investigators in the field hope to produce efficiently high-quality materials and products. However, microwave processing has not always been as successful as proponents of the technology had hoped [97,98,108]. Due to the complexity of microwave interactions with materials, the successful application of microwave processing places a heavier demand on understanding the technique than does conventional heating. Further, there exist major drawbacks hindering the development and exploitation of this emerging technology. Among these limitations, include such phenomena like non-uniform heating, thermal spikes, hot-spots formation and thermal runaway [114,116,120,123,124] (refer to section 2.2.5), which cause the deleterious effect of non-uniform material properties. For example, Vogt et al [120] observed thermal spikes in microwave processing of ceramic oxide fibres. The heating of alumina/silica fibre tows in a single mode microwave cavity produced hot-spots that lasted for only a few seconds. The thermal spikes were triggered by a small increase in power, after which that section of the fibres became cooler than before the power increase.

These limitations of microwaves are a function of physics whereby the wavelengths of the waves are smaller than the overall materials dimensions being processed. Such difference in wavelength to material geometry is the inherent causes for non-uniform heating associated with microwaves. Moreover, they are caused by the temperature dependencies of the electrical and thermal properties of the irradiated material. For example, the dependence of the effective electrical conductivity on temperature nonlinearly couples Maxwell's equations (2.6)-(2.9) to the heat equation (2.24), while the presence of the electric and polarization fields in the source term of the heat equation couple it nonlinearly in the other direction.

2.2.4   Modelling microwave heating of ceramic materials

There has been a considerable amount of work directed at the understanding of the nonlinear microwave heating process during the early 90's and it has all dealt with one and two-dimensional models. The heating of a dielectric material in half-space has been examined in the low electrical conductivity limit [109], [110], in the low thermal conductivity limit [111-113] and in models where these parameters were taken as powers of temperature, for a variety of thermal boundary conditions applied at the interface. Spatial structures corresponding to hot spots have been discovered in the second limit and response curves relating the final steady state temperature to the incident microwave power have been given for the first. However, these curves are monotonic and do not explain phenomena such as thermal runaway.

Thomas et al [114] developed an elementary model of the heat transfer process during the sintering of ceramic oxide fibres, to observe the formation of thermal spikes and hot spots. They concluded that thermal spikes in microwave heating of these ceramic fibres are apparently caused by a reduction in dielectric loss as temperature exceeds a phase transition temperature, which lead to a new phase with smaller dielectric loss. However, this model ignores the coupling between the microwave field and power absorbed by the fibre.

Deepak and Evans [115] investigated a two-dimensional model illustrating microwave heating of ceramic bodies. They demonstrated the effects of microwave parameters, external cooling conditions and the material geometry on the temperature gradient. They concluded that the power density of the microwaves and the external

cooling could be manipulated together to control both the temperature and the temperature gradient with the specimen. They also showed that microwave heating of irregular-sized material could lead to phenomena like thermal runaway.

The models described above, however, ignore the fact that the dielectric properties strongly depend on temperature for certain ceramic materials, as explained earlier. In a systematic effort to understand the governing physics of microwave heating of ceramic materials on the macroscopic level, including the temperature dependencies of the electrical and thermal properties, Kriegsmann has conducted small Biot number asymptotic analysis of the coupled non-linear system of the time harmonic electric field and the heat equation for (1) an infinite one dimensional ceramic slab of finite thickness on the order of a slab wavelength located in free space [116] and (2) for a two dimensional slab of similar thickness situated in a TE_{103} applicator[*] with adjustable iris [117]. In case (1), he offered a plausible explanation for thermal runaway through an S-shaped response curve relating the steady state slab temperature to the incident power. This phenomenon is discussed in detail in the next sub-section. In case (2), he again obtained the S-shaped curve and demonstrated how the shape of the curve depends upon the coupling of the microwave to the cavity and upon the effect of the subsequent heating on this coupling. By considering various aperture sizes, he further showed that the shape of this response curve is strongly affected by the skin effect[**] and cavity detuning.

Booty and Kriegsmann [118] developed and analysed a mathematical model describing microwave heating and joining of ceramic cylinders. They showed the formation of hot-spots, which propagate and stabilize during the joining process. They deduced that if the temperature in the relatively warm region of the hot spot is sufficient for sintering, then ceramic fibre could be slowly pulled through the waveguide, thus insuring that the entire sample is processed. Later Kriegsmann [119] focused on the consequences of hot spots in microwave heating of ceramic fibres. He developed an analysis of the microwave heating of a thin ceramic cylinder in a single mode, highly resonant cavity to study the non-uniformity of the electric field along the axis of the cylinder. He observed that the locally elevated temperature and corresponding electrical conductivity at a hot spot affects the local structure of the electric field and consequently, this interaction had the potential to affect the heating process in turn.

[*] Transverse electric mode applicator. 1 and 0 show the number of half cycles of sinusoidal variation of intensity exiting within the applicator whose length is 3 half wavelength of the electromagnetic field.
[**] The phenomenon in which the penetration depth of the electromagnetic field decreases with increase in the dielectric properties of the material.

During microwave processing of ceramic materials, some materials of commercial interest, such as alumina, are essentially transparent to microwaves and thus require a large amount of power to be able to reach desired temperatures. Whilst others such as silicon carbide absorb microwaves readily. Investigators have explored a susceptor-based heating technique to overcome these difficulties associated with processing either type of materials [120,121]. Most susceptor-based heating schemes involve the simultaneous heating of two electrically and thermally disparate materials. When these materials are in contact, the scheme can be viewed as the heating of a ceramic laminate. The material heating of such a laminate composed of three layers was modelled and analysed successfully by Pelesko and Kriegsmann [121]. They investigated the heating of a low-loss material, i.e. microwave transparent placed in between two lossy materials, susceptors, using microwaves. They illustrated that the use of the susceptors indeed lowered the power required to heat the low-loss material. Further they showed that the maximum stable temperature varied as a function of the thickness of the suceptors and this variation could be used to control phenomena like thermal runaway.

Following a similar trend, Kriegsmann and Tilley [122] later developed a mathematical theory describing the use of microwaves to heat ceramic laminate panels that occurs in a variety of industrial processes such as chemical vapour infiltration. The model took into account the microstructure of the thin constitutive ceramic slabs that make up the laminate composite. They investigated the heating trends for a variety of porosity levels present within the composites for CVI applications. They deduced that thermal runaway could occur during the infiltration process in CVI process. In addition, they studied the effect of the incident polarization on the heating process. They concluded that the use of a *TE polarized** incident microwave is inefficient in certain CVI applications, but produces a more favourable temperature gradient as compared to *TM polarization***.

2.2.5 Thermal runaway

Among the limitations described above, thermal runaway is the major drawback hindering the widespread use of microwave energy [99,123,124]. This is due to the uncontrolled rate of rise of temperature brought about by the positive slope of the microwave loss factor (imaginary part of the dielectric property), ε'' versus the

---

* A propagation mode in which the axial field component is a magnetic field vector. The axial electric field vector is zero.
** A propagation mode in which the axial field component is an electric field vector. The axial magnetic field vector is zero.

temperature response T. This is shown qualitatively in figure 2.10. Generally the rate of rise of temperature of a material is proportional to the power dissipated, whilst heat is conducted away at a rate proportional to $\alpha_r \nabla^2 T$ (see equation 2.24), where $\alpha_r = k_t / c_p \rho_p$, is the thermal diffusivity of the ceramic and ∇^2 is the Laplacian operator [97]. An equilibrium temperature is established when the energy input is equal to the rate of loss. Most ceramics exhibit a loss factor characteristic as depicted from Figure 2.10. However, for some of them, the rate of energy input far exceeds the rate of heat loss. Therefore, after an initial absorption of the microwave energy, the temperature rise beyond T_c, the critical temperature, will cause ε'' to increase, which in turn results in a further rapid temperature rise and so on. Often, the critical temperature is near, or even below, the temperature at which the material processing occurs. Damage to the ceramic is possible at this stage; hence precise control of the material's
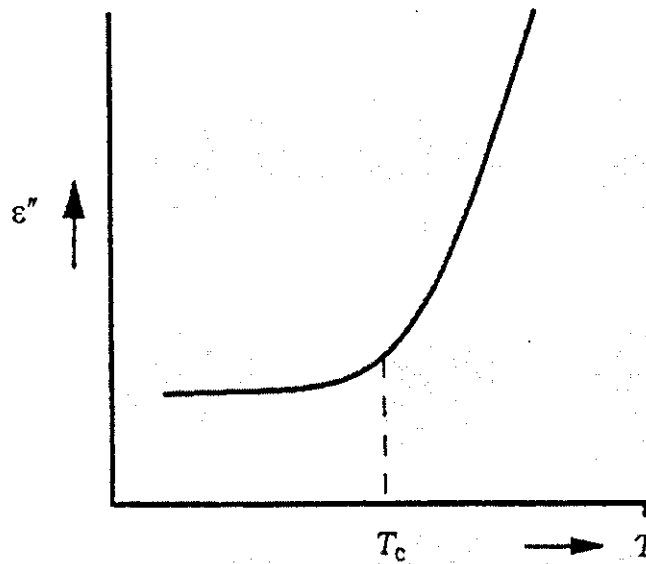
Figure 2.10: Qualitative representation of the loss factor with temperature, where T_c is the critical temperature when runaway occurs [34].

temperature profile is essential.

Although experimental reports about thermal runaway are mentioned in many papers, a systematic experimental study is rarely seen. One experimental result was given by Roussy et al [123], where the microwave heating of rubber was studied. It was found that when the incident power level was 25 W, a steady temperature could be attained; but when the power level was increased to 35 W, the temperature increased

rapidly starting from some point and finally the rubber was burned. Similar observations were made by Zhang et al [124] when studying the effect of increase power level on the heating Pt/Al_2O_3 catalyst. Two common points exist in these experimental reports. First, below a critical microwave power level, a stable temperature could be attained by the materials at the end of the process and this temperature increases with increasing power. The second point is that the temperature of the material increases rapidly with a slight increase of input microwave power from that critical power level. The experimental results show that the temperature response to the input power is not continuous; at some critical power value a temperature discontinuity exists. These observations are supported by the theoretical analysis of thermal runaway performed by Kriegsmann [116]. He found that the steady-state temperature as a function of the input microwave power gave an S-shaped response curve. A predicted curve is illustrated in figure 2.11, where different electric fields intensity represents different input power levels.
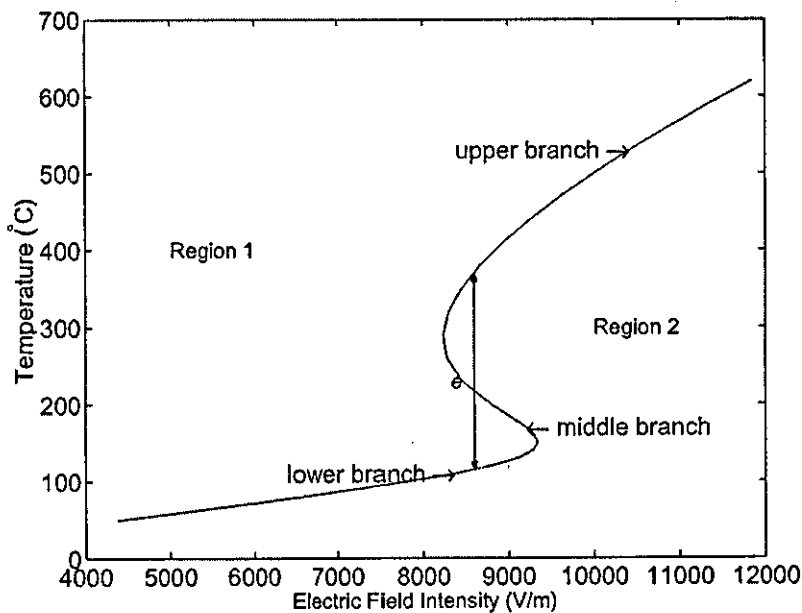
Figure 2.11: Stability analysis using S-shaped curve.

Every point on the curve represents a thermally balanced state. The S-shaped curve divides the whole electric field and temperature plane into two regions. In region 1, heat loss is larger than heat absorbed by the materials. In region 2, heat loss is less than heat absorbed by the materials. Suppose there is a point e on the middle branch of the S-shaped curve. If the temperature fluctuates slightly, the temperature will keep

increasing or decreasing until it reaches an equilibrium point on the upper or lower branch. Then from this S-shaped curve, the dynamic response for different power levels can be derived. Based on the energy balance, Kriegsmann concluded that the middle branch of the S-shaped curve was unstable. For that reason, a temperature jump is possible, suggesting a plausible mechanism for thermal runaway control problems.

After Kriegsmann's initial work, other researchers found the S-shaped curve under different conditions. For example, Jackson et al [125] developed a one-dimensional model for microwave heating of a sphere in a rectangular resonant cavity. Their results were similar to Kriegsmann's [116]. They observed that for long processing times, the surface temperature of the sphere was nearly unchanged while the centre temperature experienced thermal runaway, since only surface temperature could be measured during experiments; this result can be important for processing materials.

Later, Gupta et al [126] analysed a one-dimensional slab heated by microwaves. Following the lead of previous authors, the S-shaped curve was used to analyse the thermal stability. One interesting result was that thermal runaway could be avoided by selecting a particular thickness of the slab.

Although the models described above are different from each other, the common point is that the dielectric loss factor ε'' plays the most important role in thermal runaway.

2.2.5.1   Control of thermal runaway

Thermal runaway during microwave heating can be prevented by controlling accurately the temperature of the material. This can be achieved successfully by varying the input microwave power during the process. Experimentally, one way to achieve the latter is by using a temperature control unit with a feedback control system between the temperature output and the microwave system [39]. A schematic diagram of a system is shown in figure 2.12. A type-K thermocouple, inserted halfway through the thickness of the sample by means of a 3 mm hole drilled at the centre, is used as a sensor to measure the temperature. The temperature controller connected to the microwave unit is used as a feedback source to adjust the magnetron's output by comparing the sample temperature with the set-point temperature defined by the user. Figure 2.13 shows a typical temperature increase for a Nicalon-based preform under controlled microwave power [39]. This was done by setting an upper limit on the

microwave power level and this limit was gradually increased when more microwave energy was needed to reach higher temperatures. This approach was valuable for preventing the sample from undergoing thermal runaway.

There exist different types of feedback that are used to control the temperature of a heated system since in reality the system temperature constantly drifts above and below the set point most of the time. One of the temperature controllers that use sophisticated means of reducing these variations is a Proportional-Integral-Differential (PID) controller. It was used in the above experiment to control the temperature of the sample. The PID controller employs three basic feedback control modes: proportional (P), integral (I), and derivative (D) control. This can be expressed mathematically as

$$P_{ab} = P_{gain}\left((T_s - T) + D_c \frac{d}{dt}(T_s - T) + I_{gain} \int (T_s - T)\, dt\right), \tag{2.26}$$

where P_{ab} represents the power absorbed, P_{gain} is the proportional gain of the controller, D_c is damping constant, I_{gain} is the integral gain parameter and t represents the time. T_s and T are the set-point temperature and the temperature of the sample respectively.
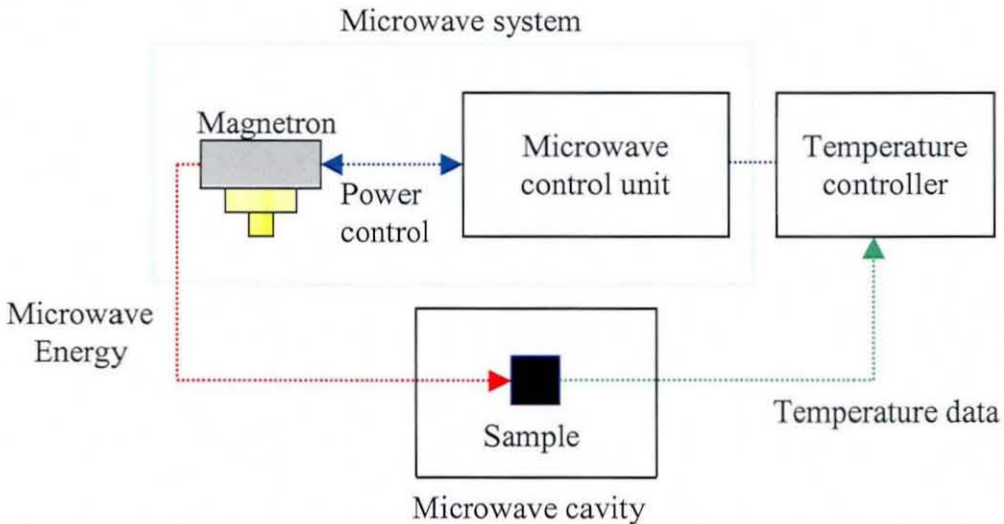
Figure 2.12: Schematic of the feedback control system between the temperature output and the microwave system
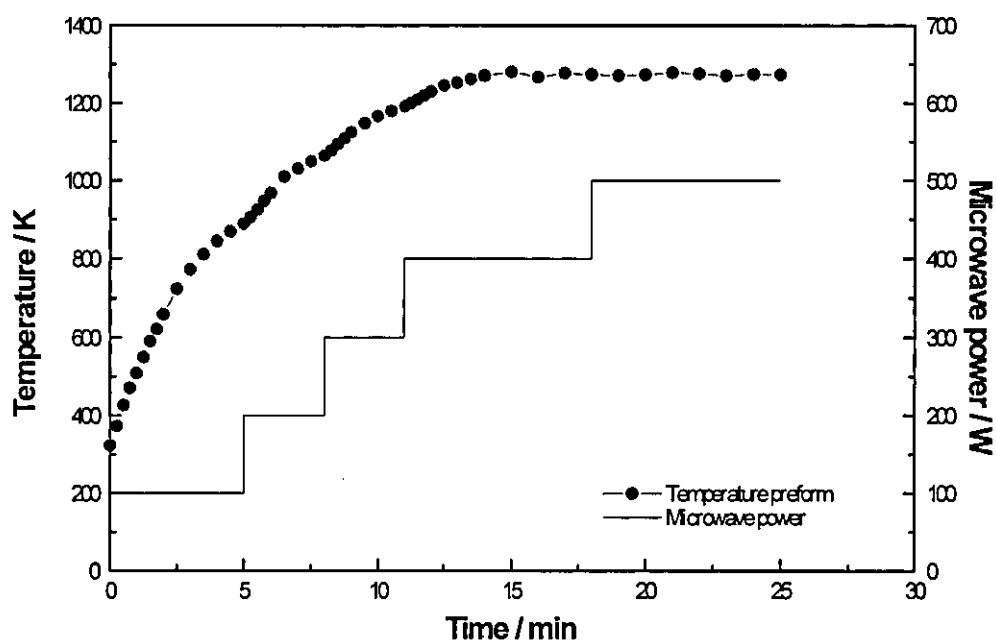
Figure 2.13: Typical temperature increases for a non-infiltrated Nicalon-based preform under an inert atmosphere [39].

Some mathematical models describing controlled microwave heating of ceramics have been developed in the past. Tian [127] numerically modelled the rapid microwave heating of a ceramic sample without destroying the material through thermal runaway. His idea was to start out at a power level greater than the critical power (power needed for thermal runaway to occur) and allow the system to evolve. Then as the process began to accelerate and temperature began to approach the critical value, the power was cut back to a level less than the critical power. If this was done correctly and at the right time, then the temperature approached a stable equilibrium, hence avoiding runaway.

Kriegsmann [116] later developed a simple control model for the microwave heating of ceramics in the small Biot number limit. This control process militated against thermal runaway and enabled the desired steady state temperature to be easily reached. In studies of a thin slab and a thin cylindrical sample the small heat loss assumption allowed the forced heat equation to be averaged. Hence an ordinary differential equation was obtained, which was coupled with the control equation to

describe the evolution of the temperature. The choice of the feedback parameters involved was shown to be important with respect to overshoot of the temperature.

Beale and Li [128] developed an automatic feedback control system for controlling the temperature of ceramic samples heated by microwave energy. The control system to manipulate the microwave power level was designed based on a linearization of a nonlinear dynamic heating model and a nonlinear equation relating the temperature at the core of the sample to that at the surface. The control system was able to regulate the temperature of the sample about a reference value with little oscillation. They have also shown that for low-loss materials, the control system was able to prevent thermal runaway, allowing regulation of the material temperatures above the runaway value.

Whilst it has been shown to be theoretically possible to control thermal runaway during the microwave heating of ceramics, in practice however, this has not always been the case. One of the reasons behind this is the lack of reliability and accuracy of the temperature measurements. This is mainly due to the occurrence of non-uniform microwave heating.

2.3   Mass transport in porous preforms during CVI

The transport of the gaseous species in the porous media can be due to several mechanisms. Three of these mechanisms are often considered most dominant – molecular diffusion, Knudsen diffusion and convection (Darcy flow) [129,130]. This section discusses these three mechanisms as applied to the transport of the gaseous precursor inside the porous preform during CVI.

2.3.1 Molecular diffusion

The gaseous precursors in the porous media can move by molecular or Fickian diffusion if the pores are large enough. In this process, the different species of the gaseous mixture move relative to each other under the influence of concentration gradients (concentration diffusion) and temperature gradients (thermal diffusion). Here the molecule-molecule collisions dominate over molecule-pore wall collisions.

Molecular diffusion is described by Fick's law:

$$J_f = -D\nabla C \,, \tag{2.27}$$

where J_f is the molar flux, D is the diffusion coefficient and C is the concentration of the precursor. Generally, the diffusion coefficient for a binary system, like hydrogen and MTS, which is used to produce SiC$_f$/SiC composite via CVI, is a function of temperature, pressure and composition. The data available on D for most binary mixtures are, however, quite limited in range and accuracy [130]. The available correlations of the molecular diffusion is thus of limited scope and are based more on theory than on experiment. For a system like hydrogen and MTS, where hydrogen is in excess, for the production of SiC$_f$/SiC [39], the mixture can be considered as dilute and according to the Kinetic theory [130], D can be expressed as

$$D = \frac{0.001858\,T^{3/2}\sqrt{\dfrac{1}{M_{MTS}} + \dfrac{1}{M_{H_2}}}}{P\hbar^2\Pi} \,, \tag{2.28}$$

where P is the pressure, $\hbar$ is the Lennard-Jones parameter for the pair of gases, Π is the collision integral and T is the temperature. M_{H_2} and M_{MTS} are the molecular mass of hydrogen and MTS respectively.

2.3.2 Knudsen diffusion

In Knudsen or free-molecule diffusion, the gaseous species densities are so low that collisions between molecules can be ignored compared to collisions of molecules with the pore walls. This occurs when the pore radius is small compared to the mean free path of the diffusing species. The flux of molecules of any species through any kind of pore is equal to the number of molecules of that species passing into the entrance of the pore per unit area per unit time multiplied by the probability that a molecule that enters the pore will eventually get all the way through and not bounce back out the entrance [129]. This probability depends only on the geometry of the pore and the law of reflection for molecules hitting the inner walls of the pore.

If there is a gas with a molecular density of n_m molecules at one end of the pore and a vacuum at the other, the free-molecule flux, J_K is then given by

$$J_K = w_f n_m \overline{v},$$ (2.29)

where w_f is a dimensionless probability factor and $\overline{v}$ is the mean molecular speed given as

$$\overline{v} = \sqrt{\frac{8k_B T}{\pi M_g}},$$ (2.30)

k_B being the Boltzmann's constant and M_g is the molecular mass of the gas.

2.3.3 Convective (Darcy's) flow

The movement of the gaseous precursor in a porous material can be described by Darcy's law [131], written as:

$$Q = -\frac{k_p}{\mu_v} \nabla P,$$ (2.31)

where Q is the volume flow rate per unit area, P is the pressure, μ_v is the viscosity of the fluid and k_p is the permeability. The gaseous species act as a continuum fluid driven by a pressure gradient and molecule-molecule collisions dominate molecule-pore wall collisions. The pore size and length are variable in a porous preform. The permeability includes an averaging of the pore size, length and shape to determine the volume flow rate.

The velocity of the fluid in the pore will be much higher than Q because the latter is based upon the volume of fluid passing through a unit area, only a small portion of which is composed of pores. Thus a fluid particle will move a distance $\mathbf{L}_p$ in a time that is much smaller than $\mathbf{L}_p / Q$, but it is the quantity Q that is observable in porous flows and that is of most practical interest.

During the early stage of CVI, the transport process of the gaseous species takes place mostly through molecular diffusion when the operating pressure is low enough. However, as the radius of the pores decreases with densification of the preform, Knudsen diffusion becomes the predominant mechanism. Similarly, under conditions with large pressure gradients (the case during forced-flow), Darcy flow of the gaseous

reactants within the pores becomes dominant. Some authors have considered the contribution of molecular and Knudsen diffusion together with viscous flow by using the Dusty Gas Model [129] to develop multi-component CVI models [32,33,45,51,67,132]. This model accounts for the contributions of all these mechanisms and it has been shown that it is suitable for simplified porous medium [45,51].

2.3.4 Description of the Dusty-Gas model

The Dusty-Gas model is a theory which describes the transport of gases through porous media. It is so called because it treats the porous medium as a component of gas mixture, consisting of giant molecules, like dust in a gas. Transport equations for the gas through the porous media are derived by applying the kinetic theory of gases. The model divides the molar flux $\mathbf{N}_i$ of species i into diffusive and convective components, given by:

$$\mathbf{N}_i = \mathbf{J}_i + x_{f_i}\mathbf{N}_T,\qquad(2.32)$$

where x_{f_i} is the mole fraction of species i and $\mathbf{N}_T$ is the total molar flux of all the gaseous species present. A gaseous phase is assumed to consist of N_c components. The Dusty-Gas model is used in the following formulation to evaluate molar fluxes of the various components present. The diffusive component of flux $\mathbf{J}_i$ is related to the gradient of its mole fraction and the total pressure by:

$$\sum \frac{x_{f_j}\mathbf{J}_i - x_{f_i}\mathbf{J}_j}{\Delta_{ij}} = \frac{-P}{RT}\nabla x_{f_i} - \frac{x_{f_i}}{RT}\left(1 - \frac{\dfrac{1}{D_i^e}}{\displaystyle\sum_{s=1}^{N_c}\dfrac{x_{f_s}}{D_s^e}}\right)\nabla P,\qquad(2.33)$$

where

$$\frac{1}{\Delta_{ij}} = \frac{1}{D_{ij}^e} + \frac{1}{D_i^e D_j^e \displaystyle\sum_{s=1}^{N_c}\dfrac{x_{f_s}}{D_s^e}}.\qquad(2.34)$$

Here p denotes the total pressure of the system, R is the universal gas constant and T is the temperature of the preform. D_{ij}^e and D_i^e are respectively the effective molecular and Knudsen diffusion coefficients of species i. Equation 2.33 provides $N_c - 1$

linearly independent relations for the diffusive fluxes of N_c components in the gaseous phase. The additional relation between the diffusive fluxes is given by:

$$\sum_{i=1}^{N_c} \mathbf{J}_i = 0,$$
(2.35)

which can be combined with Equation 2.33 to solve for the diffusive flux of each species. Once the diffusive components are known, the total flux $\mathbf{N}_T$ due to diffusion and viscous flow of the multi-component mixture is given by:

$$N_T = \frac{\displaystyle\sum_{s=1}^{N_c} \frac{\mathbf{J}_s}{D_s^e}}{\displaystyle\sum_{s=1}^{N_c} \frac{x_{f_s}}{D_s^e}} - \frac{1}{RT}\left(\frac{k_p P}{\mu_v} + \frac{1}{\displaystyle\sum_{s=1}^{N_c} \frac{x_{f_s}}{D_s^e}}\right)\nabla P,$$
(2.36)

where k_p is the permeability of the porous preform and μ is the viscosity of the gas mixture. Variations in the diffusivities due to temperature, pressure and pore structure are given by:

$$D_{ij}^e = D_{ij}^0 \left(\frac{p_0}{p}\right)\left(\frac{T}{T_0}\right)^{1.65} S_1$$
(2.37)

for molecular diffusivities and:

$$D_i^e = D_i^0 \left(\frac{T}{T_0}\right)^{1.65} S_2$$
(2.38)

for Knudsen diffusivities. D_{ij}^0 and D_i^0 are reference diffusivities at reference temperature T_0 and pressure P_0 and can be estimated using the Chapman Enskog theory [130]. S_1 and S_2 represent the pore structure parameters dependent on the particular pore structure model used. If the latter is represented by a network of uniformly sized cylindrical capillaries [45,51] then the pore structure parameters and the permeability coefficient are given by:

$$k_P = \frac{\phi}{3}\left(\frac{r_p^2}{8}\right)$$
(2.39)

$$S_1 = \frac{\phi}{3} \quad \text{and} \quad S_2 = \frac{\phi}{3}\left(\frac{r_p}{r_0}\right).$$

(2.40)

The molar fluxes for the gaseous components considered can be evaluated using the above set of equations and the results obtained can be incorporated in the mass balance conservation equations for the gaseous species. The Dusty-Gas model, however, is applicable for low-pressure systems only [33,45,67].

Considering the gas-transport and reaction aspects of the CVI process, it is a natural approach to use a minimum of two coupled partial differential equations that describe changes in the reactant concentration and the solid structure as a function of both position and time. The fundamental conservation laws lie at the heart of these CVI models developed so far. Starr's finite volume model [46] is based on the mass balance equation:

$$D\frac{d^2C}{dx^2} + U\frac{dC}{dx} = R_R \times S_s,$$

(2.41)

where C is the concentration of a chemical species, D is the diffusion coefficient, U is the gas velocity in the x-direction, R_R is the molar deposition rate per unit of solid surface area and S_s is the solid surface area per unit volume. Both Chang's [55] and Sheldon's [52] models are based on conservation of volume

$$\frac{d\vartheta}{dt} = -u \times S_v(\vartheta),$$

(2.42)

where ϑ is the void fraction (porosity), u is the solid product growth rate and $S_v(\vartheta)$ is the gas/solid surface area per unit volume of the porous preform. These two models took different functions of $S_v(\vartheta)$: $S_v(\vartheta) = 2\left(\frac{\vartheta}{\vartheta_0}\right)\frac{(1-\vartheta_0)r}{r_0}\frac{r}{r_0}$ in [52], where r_0 is the radius of the initial cylindrical fibres and r is the radius of the coated fibres, and $S_v(\vartheta) = \frac{2\sqrt{\vartheta}\sqrt{\vartheta_0}}{r_0}$ in [55], where r is the cylindrical pore radius and r_0 is the initial pore radius. In both cases ϑ_0 is the initial porosity. Mathematical models in these forms show the effect of key process variables and can be used to analyze the optimization and control of infiltration during the CVI process.

The system of equations describing the mass transport and reaction process can finally be coupled with the system of equations describing the microwave heating of the preform to describe the microwave enhanced CVI process.

2.4 Mathematical modelling of ME-FCVI

2.4.1 Process variables during ME-FCVI process

In order to build a mathematical model of the microwave enhanced forced-flow chemical vapour infiltration (ME-FCVI) process, first it is necessary to understand the key process factors, viz. temperature, pressure, precursor concentration and flow rate. Optimal choices of these variables can reduce the infiltration time, increase the deposition rate and improve the uniformity of infiltration. These variables also affect the structure of the deposited matrix and therefore the properties of the composite product. A brief qualitative description of the influence of these important process variables is given below.

Temperature. A reduction in the processing time can be achieved by using higher temperature but at the expense of steeper temperature profiles [31,35,38]. This will significantly affect the density and composition gradient across the preform. Therefore it is important to understand how the microwave heating parameters are affected by the material and electrical properties changes that occur during the process. Knowledge of the dielectric properties of the ceramic structure and their variation during processing is essential to predict the evolution of the temperature in the sample to avoid the limitations that occur during microwave heating. Further, the work carried out by Jaglin also showed that the stoichiometry of the SiC deposited on the inside the fibrous preform is affected by temperature. Thus a proper understanding of this effect is vital.

Pressure and flow rate. The total gas pressure has a strong influence on the diffusion and kinetic processes [39,78,83,86]. Chemical reaction rates typically decrease with a reduction in flow rate. Further it has been shown that applying forced-flow overcomes diffusion limitations and decreases the processing time. However, during processing the permeability of the preform decreases, which results in an increase in the pressure gradient across the sample.

Precursor concentration. A reduction in the reagent concentration typically decrease the reaction rates, hence increases the processing time. However, it has minimal effect on the uniformity of the matrix composition [38].

Reaction type. This is the nature of the reaction and it determines the deposition rate of the matrix materials. In this research, the deposition of silicon carbide (SiC) from methyltrichlorosilane (MTS) is considered as a paradigm for the production of SiC_f/SiC composites. The following equation governs SiC formation during the ME-FCVI process:

$$CH_3SiCl_3\,(g) + n_1\,H_2\,(g) \longrightarrow SiC\,(s) + 3\,HCl\,(g) + n_1\,H_2\,(g)$$

MTS is decomposed in the gas phase at high temperatures into SiC solid phase and HCl gaseous species, H_2 acting as the carrier gas in the reaction. The by-product HCl can have a strong inhibition effect on the process [46,52].

The deposition of SiC from MTS is, in fact, a very complex reaction [24,97,133] with the MTS gas phase decomposition sequence essentially completed within one second. The deposition sequence probably involves multiple steps or competing forward or reverse reactions [133,134].

Generally, the changes in the process variables that enhance uniform infiltration also unfortunately decrease the overall matrix deposition rate. Low temperature, low reagent concentration and low pressure particularly reduce the deposition rate and result in long infiltration times. The goal of process optimization is therefore often linked to the objective of achieving a balance between obtaining uniform infiltration and reducing the total processing time. However, one of the major factors that affects the processing variables described above, and which in turn affects the whole process, is the change of the pore structure and surface area. The mathematical difficulty lies in that the microscopic pore structure is too complex to be expressed in an analytic way and that during the process it may change topology and form inaccessible pores as deposition progresses. Figure 2.14a-b shows example of the densification of a SiC_f/SiC composite by CVI. In the first figure macro-pores are clearly visible between the *tows*[*] of fibres and layers of cloths. In the second figure, an infiltrated tow is indicated with some remaining inaccessible *intra-tow*[**] porosity. Systematically detecting these

---

[*] Bundle of twisted or untwisted continuous fibres. A tow may contain tens of thousands of individual continuous fibres.
[**] Describing the porosity existing between fibres within a tow.

52

changes and adjusting the temperature, gas transport and deposition accordingly impose a huge computational workload on the model.
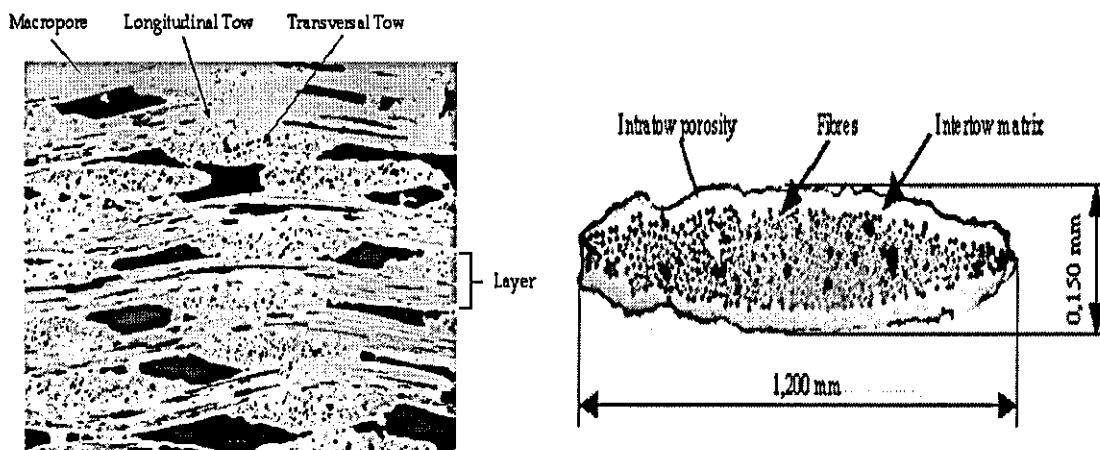
Figure 2.14: (a) Structure of a cross-sectioned woven SiC_f/SiC composite. (b) Cross-section of a tow showing SiC fibres, intra-tow porosity and SiC matrix situated on the outside of the tow (adapted from [39]).

2.4.2 Modelling of porous preform during CVI

Many mathematical models have been presented in the past to describe structure evolution in porous media undergoing morphological changes as a result of the chemical reactions and matrix deposition occurring during the CVI process [53,61,64,65,66,83,135,136,137]. Because of the mathematical difficulties involved in modelling the evolution of pore microstructure, some basic assumptions were made to simplify the problem when establishing the CVI models.

The most popular simplification was that a single cylindrical pore of a characteristic diameter representing a typical pore in the substrate. Gupte's model [65] utilizes a single pore to demonstrate the importance of the pore geometry, total gas pressure, temperature and imposed temperature gradient on the degree of densification achieved. Yu's generalized pore model [135] uses a network of cylindrical pores to represent porous structure and it also assumes uniform pore length. Sotirchos' distributed pore size and length model [136] takes the same approach but relaxes the assumption to a population of cylindrical pores with a distribution density over the size range of pores. Figure 2.15 shows a two-dimensional sketch representing a porous structure modelled as a network of cylindrical pores and the evolution of diameter $\Gamma(t)$

for a single pore. This model was adapted by Langhoff et al [61] to study isothermal chemical vapour infiltration.

Another assumption that was made implicitly or explicitly by most CVI models is that the whole internal surface area of the substrate is accessible to the reacting fluid at all porosity levels and all times, that is, inaccessible pore volume formation does not take place. In order to incorporate this phenomenon, some models take into account the percolating characteristics of the porous structure of CVI fibrous preforms and involve percolation theory to make the process stop after the porosity reaches a certain level.
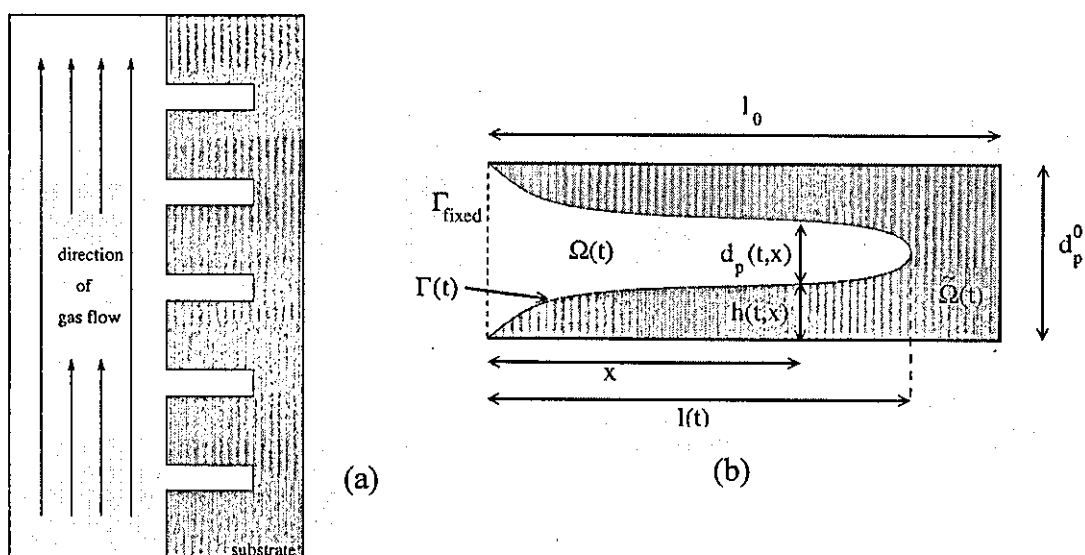
Figure 2.15: (a) Schematic view of the pores in a substrate during CVI. (b) Schematic of the evolution of a single pore (adapted from [61]).

In Gupte's effective medium approach [66], the transient porous microstructure is approximated by a Bethe lattice (see figure 2.16) and concepts of percolation theory are used to account for utilized, unutilized and filled pore space. In Starr's gas-transport model [137], a node-bond percolation model, the porosity is represented as a network of spherical "nodes" connected by cylindrical "bonds". Percolation theory is also used in Yu's [135] and Sotirchos [136] models to predict creation of trapped porosity as density increases and the smaller pores are filled.

Tago et al [64] considered a cubic array of disconnected cylinders to model the porous structure of a SiC whisker preform. In this model, the whiskers were separated at the initial time as shown in figure 2.17. As the infiltration progresses, the whiskers

54

radius R_f and the length L_f increase accordingly and the whiskers began to connect with each other.

(a)   (b)
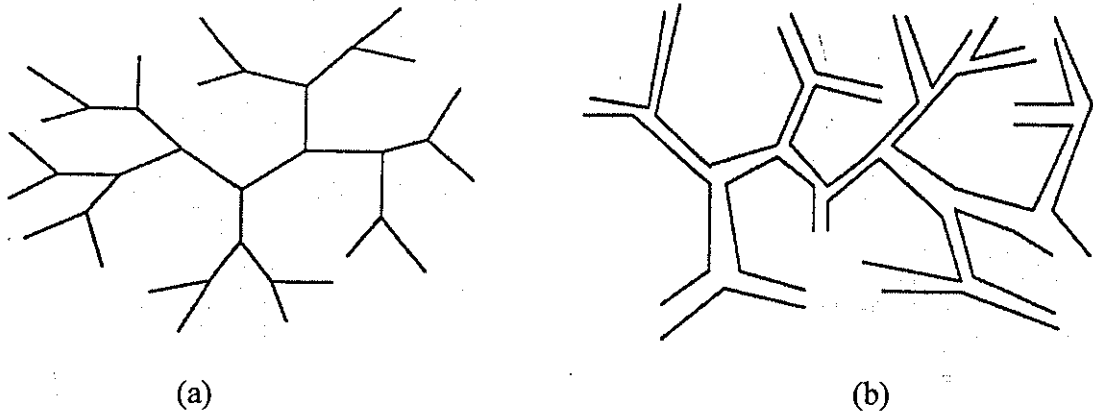
Figure 2.16: (a) Schematic of a Bethe lattice of coordination number z = 3 and (b) the corresponding pore network (adapted from [66]).

Chung and McCoy [53] represented the geometry of a woven fabric as a system of layered plies of woven tows containing bundles of filaments to obtain a non-homogeneous model. Three different regions or voids for diffusion and deposition were included in the model: holes due to weaving, spaces between plies and gaps around filaments (see figure 2.18).
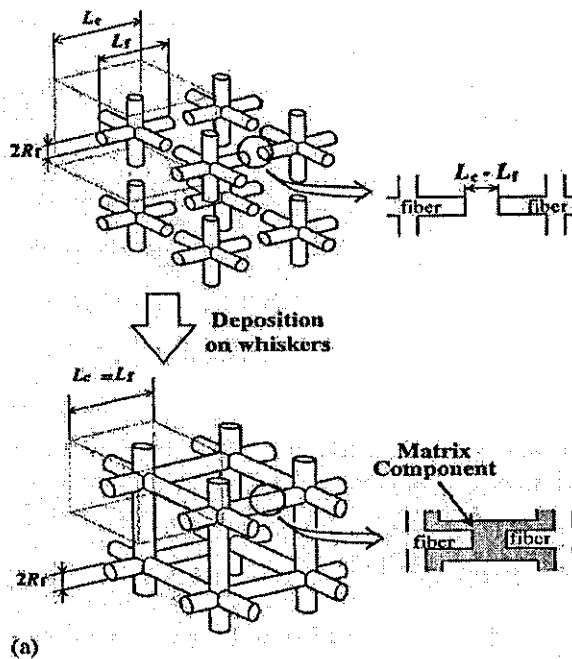
Figure 2.17: Cubic array of disconnected cylinders model describing a whisker preform [64].
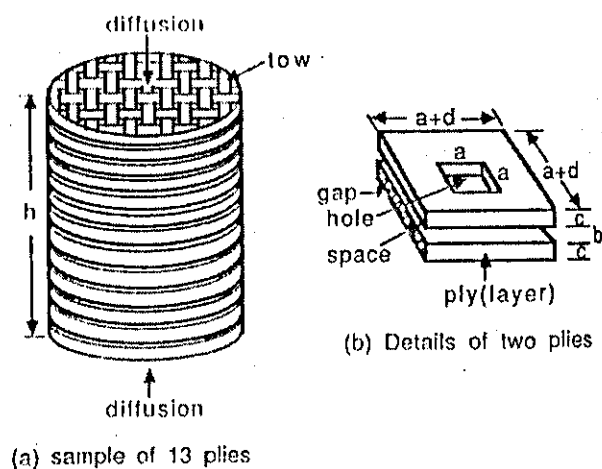
Figure 2.18: Schematic drawing of a woven fabric preform: a is the side-length of the square holes, b is the distance between plies, c is the thickness of one ply, d is the width of a tow and h is the height of the sample.

Tai and Chou [83] successfully modelled the microstructure of a fibrous preform by adopting a unit cell whose edges and diagonals represent fibre tows. The sample was divided into a finite number of unit cells with their dimensions depending on the density of the preform and the initial radius of the fibre tows.

2.4.3 Literature review of chemical vapour infiltration models under microwave heating

The use of microwave heating in the CVI process has been modelled in a variety of ways. The first such model was reported by Gupta and Evans [31]. These authors used a very simplified model of the perform structure (a single pore model) and pseudosteady-state equations to describe the processing of a SiC composite, considering diffusion transport of the gaseous precursors. Based on some further simplification the model lead to the conclusion that infiltration proceeded more rapidly and to a greater extent with microwave heating/external cooling than in isothermal infiltration. The model also suggested that infiltration could be optimized by manipulation of the microwave power and external cooling. Further, the computed extent of infiltration was seen to be very sensitive to the initial pore size. The same authors later developed a two dimensional model in which mass fluxes were expressed according to the dusty-gas model [35]. This time, the porosity of the preform was modelled by cylindrical capillaries lying parallel to the x- and y-axes. They

demonstrated that at least one dimension of the preform must be short in order for gas to diffuse through it, thus suggesting that only sheet-like, rod-like or thin walled ceramic composites could be produced using CVI technology. They also observed that a lower processing temperature yielded a more uniform deposition of the matrix material, however, the processing time was longer.

Shortly thereafter, a mathematical model describing the infiltration of a cylindrical carbon preform by representing volumetric heating as a constant heat source was proposed by Morell et al [32]. They included a detailed description of the transport reaction processes and of the evolving pore structure in their investigation; the dusty-gas model was used to describe the transport processes. The preform was envisioned as consisting of identical cylindrical fibres randomly positioned in three-dimensional space. They showed that volume heating resulted in favourable temperature profiles in the composite, which, depending on the power level, yielded an inside-out deposition and therefore complete densification, However, considering a constant applied power, they observed that accessible porosity becomes trapped inside the composite above a critical power level. They then suggested several power modulation schemes to optimize the densification process. In a follow-up study, Morell et al [33] proposed a novel technique called pulsed power volume heating CVI. In this technique the power of the volume-heating source was modulated according to a prescribed waveform. Operating conditions were identified leading to substantial improvements in deposit uniformity within the preform. These studies, however, assumed thin samples; hence microwave power attenuation was not a problem.

A chemical vapour infiltration scheme that combines pressure pulsing and a volume heating method was formulated by Ofori and Sotirchos [132]. A rigorous mass transport and reaction model for multicomponent mixtures in the porous medium, a ceramic slab, was employed to investigate the developed process. They revealed that for relatively thick performs, significant temperature gradients were encountered only close to the external surfaces. Thus, by applying rectangular wave pressure pulsing, under other appropriate operating conditions, they observed that densification proceeded from the centre toward the surface of the preform. However, since the microwave heating generated a flat temperature profile in the interior, the sinusoidal pulsing had no effect on the density gradients close to the centre. Further significant density gradients close to the centre were observed when non-zero minimum pressure

pulsing was employed. They concluded that pulsing at the optimal times became progressively less important as the densification process continued.

However, the models described above considered that the local electrical and thermal properties are independent of temperature. This eventually decoupled the electromagnetic portion of the problem from the heat transfer and reaction/diffusion parts, hence allowing a simplified analysis of the process. Further, this simplification avoided the authors from observing the occurrence of phenomena like thermal runaway during the process, which can lead to dramatic effects during the densification process.

Skamser et al [36] used a numerical model to simulate the temperature and composition distributions produced inside a specimen heated with microwave energy. The dielectric properties of the specimen were allowed to change with composition, resulting in non-uniform power absorption and steady-state temperature gradients. They observed that when the specimen became less lossy or when the changes in the microwave heating properties were gradual, the reaction proceeded relatively uniformly and the volumetric heating created an inside-out densification. However, when the changes in the properties were significant, the microwave heating resulted in high temperature gradients, which lead to hot zone formation. The formation of these hot zones, which could lead to thermal runaway, however, was not discussed in the paper.

2.4.4 Prior work at New Jersey Tech (NJIT)

The model developed by Pelesko and Kriegsmann [121], describing the heating of a ceramic laminate without any chemical reaction, was considered by Tilley and Kriegsmann [37] to develop a simple one-dimensional model of CVI into a fibrous alumina preform to fabricate a SiC/Al_2O_3 composite via the decomposition of methyltrichlorosilane. From the initial model, it was found that if the square ratio of the thermal conductivities of SiC and alumina was proportional to the ratio of their electrical conductivities, then the electric and thermal problems decoupled. In the model, a plate of SiC was placed in between two layers of alumina. The temperature in the preform (alumina) was essentially constant and the substrate (SiC plate) temperature obeyed a heat equation, with a heat flux entering the preform from the substrate that depends on the total power conversion within the substrate and the time rate-of-change of the temperature. Tilley and Kriegsmann have extended this model by

including a moving front separating the substrate from the preform [37] and have considered the dynamic version of the microwave enhanced CVI process: as the desired product fills the pores, the electrical properties change considerably from the unfilled region. Such property changes in exothermic chemical reactions have been modelled successfully using asymptotic techniques [138,139]. These rely on a thin reaction zone, a flame front, whose thickness scales on the inverse of the activation energy in which the chemical process takes place, separating the unreacted zone from the process region. Appropriate jump conditions in reactant concentration and temperature can be found by analysing the full reaction system in the reaction zone and using matched asymptotic expansions to find the appropriate boundary conditions. They found that infiltration time could be improved significantly if the preform was attached to a substrate whose electrical and thermal properties were disparate. They also found that three stages of the process exist for large activation energies; an inert heating stage during which the substrate temperature rises, a processing stage during which the reaction occurs and a terminal stage characterized by a nearly uniform preform temperature. However, in this model they have defined the reacting front as an isotherm in the material, ignoring variations in the reactant concentration. In a later work [38] they found that these effects were significant although the temperature at the interface composite material and unreacted material remained fixed during the reacting stage of the process.

CHAPTER 3

MICROWAVE ENHANCED FORCED-FLOW CHEMICAL VAPOUR INFILTRATION: - A 2-D MATHEMATICAL MODEL

3.1 Introduction

This chapter describes the two dimensional mathematical model developed in the course of this research project to study the effects of the process variables on the densification profiles and processing times occurring during Microwave Enhanced Forced-Flow Chemical Vapour Infiltration (ME-FCVI). Due to the complexities involved in developing such model, two sub-modules were first developed separately: (1) an electromagnetic (EM) module where Maxwell's equations coupled with the heat diffusion equation were solved to determine the electromagnetic and temperature distributions within a preform having a constant porosity level, and (2) a forced-flow chemical vapour infiltration (FCVI) module in which the mass balances, pressure distributions and porosity variation describing the infiltration process of the porous preform were evaluated. The first model also investigated the occurrence of thermal runaway under decreasing porosity during ME-FCVI. These two sub models were then coupled together to study the effects of altering the processing variables on the deposition profiles and processing times. Section 3.2 considers the mathematical formulation of these sub-models whilst the numerical techniques used to solve the coupled system of equations are detailed in section 3.3. The numerical results obtained for the two models from simulations are outlined and discussed in section 3.4.

3.2 Model formulation

The experimental investigation for ME-FCVI undertaken by Jaglin [39], where the densification of SiC$_f$/SiC composites was carried out, was considered here to develop the model. Figure 3.1 shows the schematic of the apparatus used during the experimental process, details outlining this work can be found in [39]. The process

chamber, consisting of a quartz tube with a porous SiC preform fixed inside it, resides inside a microwave cavity whose dimensions are much larger than the sample. Methyltrichlorosilane (MTS) in excess hydrogen was allowed to flow continuously through the tube and the sample via an inlet at a pressure P_1, as indicated by the upward arrow, and to leave the chamber via two outlets, indicated by the downward arrows. Since the process chamber was made of quartz, which is microwave transparent, it allowed electromagnetic fields to propagate inside it to heat the preform volumetrically to the desired temperature. The gaseous precursors flowing through the porous preform chemically reacted at the elevated temperatures to deposit solid SiC matrix within the pores, thus forming the composite. These different processes occurring within the quartz tube were modelled separately in the following sub sections.
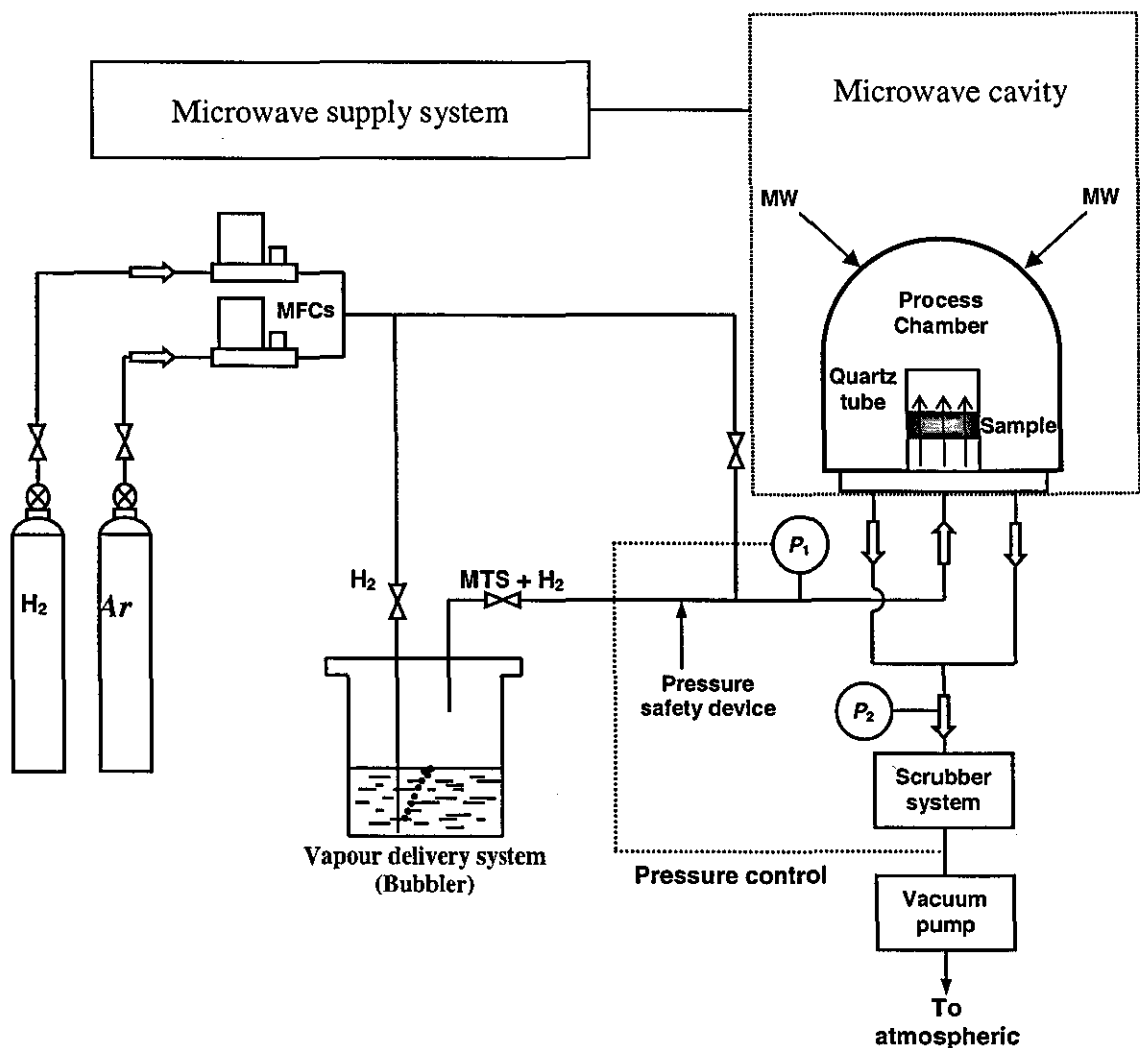
Figure 3.1: Schematic diagram of the ME-FCVI apparatus – MFCs = mass flow controllers, MW = microwave radiation.

3.2.1 Electromagnetic (EM) sub-model

In this sub section, the EM sub-model describing the microwave heating of the preform is outlined. Figure 3.2 shows the 2-D schematic diagram considered to develop the model. The quartz tube was assumed relatively long, $c \gg b$, compared to the thickness of the sample.

$$MTS + H_2 + HCl$$
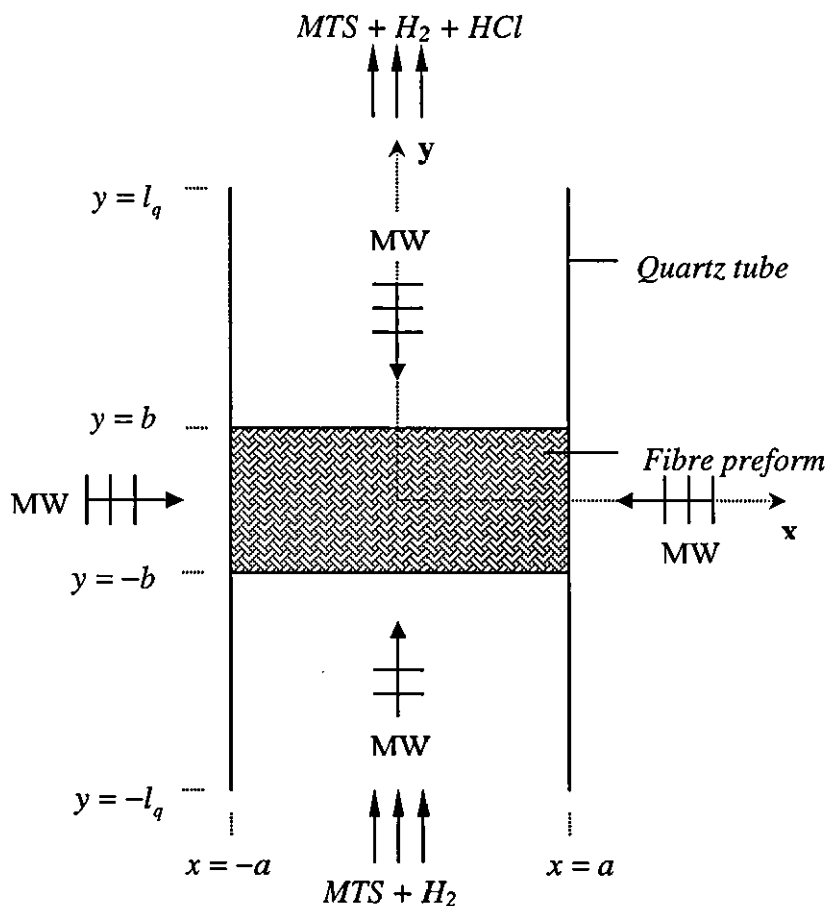
Figure 3.2: Schematic diagram considered for the mathematical model, showing the flow of precursors inside the quartz tube and through the fibre preform under microwave heating. MW – microwaves, MTS – methyltrichlorosilane, HCl – hydrochloric acid, H_2 – hydrogen gas

The following approximations are considered to solve for the electric field within the preform:

- The preform was assumed to be homogeneous and isotropic. The width of the sample was assumed to be much larger than its length and thickness.

- The sample was also assumed to be in free space occupying an arbitrary cross section, where four identical electromagnetic plane waves were allowed to propagate through it as shown in figure 3.2.

- The operating frequency of the EM fields was 2.45 GHz, thus for this high frequency, the temperature of the preform followed only the time-averaged value of the power deposited by the fields.

3.2.1.1 Governing equations for determining the electric field

Under these conditions, Maxwell's equations were solved in the frequency domain with a time-harmonic dependence of the form $e^{-i\omega t}$ and are given by:

$$\nabla \times \overline{E} = i\omega\mu\overline{H} , \tag{3.1}$$

$$\nabla \times \overline{H} = -i\omega\varepsilon\overline{E} + \sigma\overline{E} , \tag{3.2}$$

where ∇ is the del operator, ω is the angular frequency, μ is the magnetic permeability, ε is the permittivity and σ is the electrical conductivity. $\overline{E}$ and $\overline{H}$ represent the electric and magnetic fields respectively. It was further assumed that $\mu = \mu_0$, where μ_0 is the magnetic permeability of free space. Hence equations (3.1) and (3.2) were reduced to:

$$\nabla(\nabla \cdot \overline{E}) - \nabla^2\overline{E} = k_2^2 N^2 \overline{E} , \tag{3.3}$$

where $N^2 = \dfrac{\varepsilon}{\varepsilon_0} + i\dfrac{\sigma}{\omega\varepsilon_0}$ and $k_2^2 = \omega^2\mu_0\varepsilon_0$, ε_0 is the permittivity of free space. The incident fields were considered polarized linearly in the $\hat{z}$-direction and considering the fact that the problem was two dimensional, the following expression was obtained:

$$\nabla^2\overline{E} + k_2^2 N^2 \overline{E} = 0 . \tag{3.4}$$

The total electric field was actually the sum of the incident electric fields, $\overline{E}_{inc}$, and the scattered electric fields, $\overline{E}_s$ given by:

$$\overline{E} = \overline{E}_{inc} + \overline{E}_s , \tag{3.5}$$

where the incident field satisfies the Helmholtz equation (3.4), with $N^2 = 1$ in free space. Using (3.4) and (3.5) the following equation was finally obtained:

$$\nabla^2\overline{E}_s + k_2^2\overline{E}_s = k_2^2(1 - N^2)(\overline{E}_{inc} + \overline{E}_s) \tag{3.6}$$

Equation (3.6) was solved by a Green's function approach [140]. Considering the free space Green's function and using the fact that the scattered fields satisfied the radiation condition in the far field away from the sample, the following integral equation was obtained after some mathematical analysis:

$$\overline{E}(\underline{x}) = \overline{E}_{inc} + k_2^2 \iint_{Body} \left(1 - N^2(\underline{x}_1)\right)\overline{E}(\underline{x}_1)H_0^{(1)}\left(k_2|\underline{x} - \underline{x}_1|\right) \, dx_1 dy_1 , \tag{3.7}$$

where $H_0^{(1)}$ is the Hankel function of the first kind of order zero. A detailed description for converting equation (3.6) to (3.7) is provided in appendix 1. The body over which the integration in equation (3.7) was performed was actually the SiC sample. Equation (3.7) does not give an explicit solution for the electric field $\overline{E}$, since $\overline{E}$ also appears under the integral sign. However, a numerical solution to equation (3.7) was possible and is described in section 3.3. Since it was assumed the preform to be subjected to EM waves from all four sides; the electric fields of the EM waves were $E_0 e^{ik_2 x}\hat{z}$, $E_0 e^{-ik_2 x}\hat{z}$, $E_0 e^{ik_2 y}\hat{z}$, $E_0 e^{-ik_2 y}\hat{z}$. These fields were superimposed to obtain a single incident field given by:

$$\overline{E}_{inc} = E_0 \left(e^{ik_2 x} + e^{-ik_2 x} + e^{ik_2 y} + e^{-ik_2 y}\right)\hat{z}, \tag{3.8}$$

where E_0 is the amplitude of the incident fields.

It is noted at this stage that the microstructure of the porous sample was neglected, thus a uniformly dense SiC preform was assumed heated by the microwaves. However, the porosity factor ϕ can be included explicitly in the effective electrical properties, which are temperature dependent. The properties generally increase with increase in temperature T. Thus assuming these properties to be linearly dependent on the porosity (for convenience) and re-arranging N^2, the following expression was obtained:

$$N^2 = k'(\phi,T) + ik''(\phi,T), \tag{3.9a}$$

where,

$$k'(\phi,T) = k_s'(T)(1-\phi) + k_g'(T)\phi, \tag{3.9b}$$

$$k''(\phi,T) = k_s''(T)(1-\phi) + k_g''(T)\phi \tag{3.9c}$$

The subscript s corresponds to the properties of the solid material and g to the properties of the gas mixture present in the voids within the preform. k' and k'' are the relative permittivity and dielectric loss of the preform.

3.2.1.2 Governing equations determining the temperature distribution

Within the preform the electric field interacted with the solid material and increased its temperature by dipolar heating according to the equation:

$$\rho_p c_p (\phi) \frac{\partial T}{\partial t} = \nabla \cdot \left(k_t (\phi) \nabla T \right) + \frac{1}{2} \varepsilon_0 k''(\phi, T) \left| \overline{E}(\underline{x}) \right|^2 \qquad (3.10)$$

where ρ_p, c_p and k_t are the density, specific heat and thermal conductivity of the preform respectively. These thermal properties were assumed to depend linearly on ϕ as follows:

$$\rho_p c_p (\phi) = \rho_{p_s} c_{p_s} (1 - \phi) + \rho_{p_g} c_{p_g} \phi , \qquad (3.11a)$$

$$k_t (\phi) = k_{t_s} (1 - \phi) + k_{t_g} \phi . \qquad (3.11b)$$

Implicit in equation (3.10) is that the time t was much greater than an electromagnetic wave period, $\frac{2\pi}{\omega}$. By averaging the heat equation over a wave period, this wave period time scale was effectively removed to obtain the form of the source term in (3.10). The preform was initially at the ambient temperature, T_0, that is:

$$T(x, y; 0) = T_0 . \qquad (3.12a)$$

Due to the symmetry of the problem, the temperature distribution was solved only for the 1st and 4th quadrant, that is for $0 \leq x \leq a$ and $-b \leq y \leq b$. No flux boundary condition was applied on the symmetry line, $x = 0$. At the exterior surfaces of the preform, heat was lost due to convection and radiation to the surroundings. Thus the thermal boundary conditions on these interfaces, $x = a$ and $y = \pm b$, were respectively:

$$k_t (\phi) \frac{\partial T}{\partial x} + h_e (T - T_0) + s_b e (T^4 - T_0^4) = 0 , \qquad x = a \qquad (3.12b)$$

$$\pm k_t (\phi) \frac{\partial T}{\partial y} + h_e (T - T_0) + s_b e (T^4 - T_0^4) = 0 , \qquad y = \pm b \qquad (3.12c)$$

where h_c is the heat transfer coefficient, s_b is the Stefan-Boltzmann constant and e is the thermal emissivity of the preform. In general, the convection term is significant only at lower temperatures. Convective losses are quickly overpowered by radiation losses once relatively high temperatures are attained. The mass transport / reaction sub-model is formulated next.

3.2.2 Forced-flow chemical vapour infiltration (FCVI) sub-model

The configuration of the homogeneous isotropic fibrous preform under the pressure-driven flow of the gaseous precursors, shown in figure 3.2 during the chemical vapour infiltration process, was considered. The gaseous precursors, MTS and H_2, were allowed to flow through the quartz tube and the sample as indicated by the upward arrows. The unreacted MTS gas together with H_2 and HCl were assumed to flow continuously upward in the tube. As previously assumed, the width of the sample was much greater than its length and thickness. Thus a two-dimensional porous medium at the beginning of the deposition process was investigated. Figure 3.3a shows a schematic diagram of the fibrous preform used for the ME-FCVI process [39]. The preform was manufactured by stacking multiple layers of fabric, consisting of fibre tows, arranged together in random orientations.

3.2.2.1 Modelling of the porous preform

To simulate the microstructure of the fibrous preform for the mathematical model, a three-dimensional unit cell was adopted here, see figure 3.3b. The sample was divided into a finite number of unit cells and the following assumptions were made regarding the reactant properties, the preform structure and the flow phenomena:

- Fluid flow within the preform obeyed Darcy's law
- Thermal equilibrium was achieved among the matrix formed during the process, fiber bundles and reactants in a unit cell.
- Deposition was uniform throughout the unit cell.
- Heat generation by chemical reaction was neglected compared to the amount of heated generated by the microwave heating. Thus, as seen from equation (3.10), no extra heat source term is present.

66

This type of porous structure modelling has successfully been used in the past by Tai and Chou [83]. The dimension of the unit cell depends on the density of the preform and the initial radius of the bundle of fibers. Within the unit cell, knowing the bundle volume content c_v, (bundle volume in the unit cell/total unit-cell volume), the dimension of the unit cell can be mathematically deduced. Generally speaking, during the process the matrix grows radially from the surface of the bundles. The idea that the matrix grows radially from the surface of a sphere was adopted to model the matrix deposition at the centre and corner of the unit cell due to bundle entanglement.
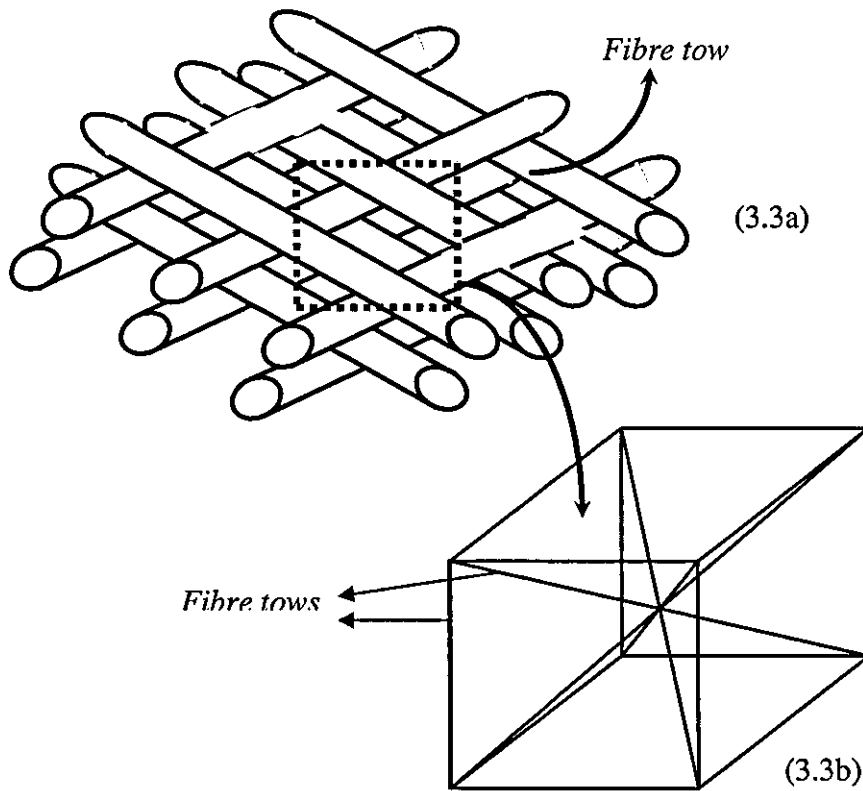
Figure 3.3a: Shows the schematic diagram of the fibrous preform used for the ME-FCVI process [39]. Figure 3.3b: Unit cell for a 3-D fibrous preform. The edges and the diagonals represent part of bundles of fibres (fibre tows) present in the preform. However, the internal porosity (intratow) present within each bundle is neglected, thus these bundles are assumed perfectly dense and cylindrical in shape.

If r denotes the radius of the bundle of fibers initially, then

$$c_v = \frac{\left((\sqrt{3}+4)L_1 + \left(((3-\sqrt{3})/27 - 14/6)(6-2\sqrt{3})-4\right)r\right)\sqrt{3}\,\pi\,r^2}{L_1^3},$$
(3.13a)

67

where L_1 is the length of the edges in the unit cell. (The derivation of equation 3.13a can be found in appendix 2).

The porosity, ϕ, of a unit cell during the process was calculated from

$$\phi = 1 - \frac{v_s}{v_b} \qquad (3.13b)$$

where v_s and v_b represent the volume of the solid and the bulk volume of the unit cell, respectively. v_s was obtained by calculating the matrix deposition within a unit cell during processing. The porosity of a unit cell was then expressed as:

$$\phi = 1 - \frac{\left((\sqrt{3}+4)L_1 + \left(((3-\sqrt{3})/27 - 14/6)(6-2\sqrt{3}) - 4\right)r\right)\sqrt{3}\,\pi r^2}{L_1^3}, \qquad (3.13c)$$

where r is the radius of the bundle of fiber in the unit cell which increased during the process.

Similarly, the effective specific surface area available for reaction to occur during the process in a unit cell is given by

$$A = \frac{\left((6+8\sqrt{3})L_1 - \left((14/3)\sqrt{18-6\sqrt{3}} + 50\sqrt{3}/3 + 14\right)r\right)\pi r}{L_1^3} \qquad (3.13d)$$

Based upon this model describing the porous preform, the pressure, porosity and MTS concentration distributions during the process were calculated and their effects on the initial input parameters like the flow rate or vice-versa was investigated.

3.2.2.2 Governing equations for the mass transport/reaction processes

The mass conservation equations for the flow of the reactants (MTS and H_2) and their composition variation are expressed as:

$$\nabla \cdot (\phi V) = -\Gamma A / \rho_f, \qquad (3.14)$$

$$\frac{\partial(\phi C)}{\partial t} + \nabla \cdot (\phi V C) = \nabla \cdot (D\phi \nabla C) - \Gamma A / \rho_f, \qquad (3.15)$$

$$\frac{\partial r}{\partial t} = \Gamma / \rho_{p_s} ,$$

(3.16)

where $\mathbf{V}$ is the fluid velocity vector, t is the time, ρ_f and ρ_{p_s} are the fluid and SiC densities respectively. D is the diffusion coefficient; C is the concentration of MTS in the fluid, Γ is the net mass transfer rate (reaction rate) during thermal deposition of MTS from fluid to solid. The densities of SiC and the fluid (average densities of MTS and H_2) were assumed constant in this analysis. Since H_2 was regarded as a carrier gas during the process, its mass conservation equation was disregarded at this stage, as it didn't take part in the reaction. Also any effect of the by-product, HCl, formed during the process was ignored at this level.

Darcy's law was used to relate the driving pressure P to the flux of the fluid:

$$\phi \mathbf{V} = -\frac{k_p}{\mu_v} \nabla P ,$$

(3.17)

where μ_v is the viscosity of the fluid and k_p is the permeability of the porous preform. Further, since the mass fraction of MTS in H_2 was relatively small, the fluid system was considered as dilute. Thus binary diffusion is appropriate to be considered whose coefficient D is given according to the kinetic theory [130] by:

$$D = \frac{0.001858 T^{3/2} \sqrt{\dfrac{1}{M_{MTS}} + \dfrac{1}{M_{H_2}}}}{P \hbar^2 \Pi^*} ,$$

(3.18)

where $\hbar$ is the Lennard-Jones parameter for the pair of gases, Π^* is the collision integral, T is the temperature and M_{H_2} and M_{MTS} are the molecular weight of H_2 and MTS respectively. The relation between the permeability and the geometry of the matrix is important for realistically modelling the non-linear processes involved here, but a clear analytical description is not obvious. Nevertheless, permeability was commonly assumed to be a power law function of porosity [83]:

$$k_p = \frac{\pi r^2 \ln(0.64/(1-\phi)^2)}{97.6} \frac{\phi}{1-\phi}$$

(3.19)

The viscosity was assumed constant in the analysis. The chemical reaction in this study was the pyrolysis of methyltrichlorosilane (MTS) gas under excess hydrogen. The decomposition reaction is expressed as:

$$CH_3Cl_3Si_{(s)} + n_1 H_{2\,(g)} \longrightarrow SiC_{(s)} + 3HCl_{(g)} + n_1 H_{2\,(g)} \tag{3.20}$$

The reaction rate was assumed to be first order in the precursor concentration and to have an Arrhenius-type dependence on the temperature, given as:

$$\Gamma = k_1 C \exp(-E_a / RT), \tag{3.21}$$

where k_1 is the reaction constant in, E_a is the activation energy and R is the universal gas constant. It is observed here that the reaction rate was considered to be proportional to the mole fraction of MTS.

Due to the symmetry of the problem, the system of equations is solved only for $0 \leq x \leq a$ and $-b \leq y \leq b$. The initial and boundary conditions are given as:

At time $t = 0$,

$$C(x, y, 0) = C_0 \tag{3.22a}$$

$$P(x, -b, 0) = P_1 \tag{3.22b}$$

$$P(x, b, 0) = P_2 \tag{3.22c}$$

$$r = r_0, \quad \phi = \phi_0 \tag{3.22d}$$

The boundary conditions are:

$$C(x, 0, t) = C_0, \qquad \frac{\partial C}{\partial y} = 0, \quad y = b \tag{3.22e}$$

$$\frac{\partial P}{\partial x} = 0, \quad \frac{\partial C}{\partial x} = 0, \qquad x = 0, \quad x = a \tag{3.22f}$$

The values $P1$ and $P2$ are maintained fixed during the process to investigate the effect of allowing a fixed pressure gradient across the sample. On the other hand, to maintain a constant mass flux of the gaseous precursor, the outlet pressure $P2$ is kept fixed and the pressure variation is calculated independently.

3.2.3 Non-dimensionalisation analysis

It was convenient in the numerical analysis to follow to deal with dimensionless variables and parameters. Accordingly, the dimensionless variables denoted by prime letters were defined:

$$(x, y) = (x', y')/b, \qquad P = P2P', \qquad V = v'V, \qquad t = t'\theta_i, \qquad C = C_0 C',$$

$$T = (T' - T_0)/T_0, \qquad D = D_0 D', \qquad A = A'/L_1, \qquad r = r'L_1, \qquad k_p = k_p' k_p^0,$$

$$k_t'(\phi) = k_{ts} k_t(\phi), \qquad \mathbf{E} = \mathbf{E}'/E_0, \qquad k_2 = k_2' b, \qquad \rho_p c_p(\phi) = \rho_{p_s} c_{p_s} g(\phi) \qquad (3.23)$$

Here k_p^0, controlled by the initial porosity ϕ_0, represents the initial permeability of the preform and the precursor velocity V along the y-direction is defined as $V = Q_f / A_p \phi_0$, Q_f being the constant volumetric flow rate of the fluid. Using the above non-dimensional variables, equations (3.8)-(3.12), which describes the EM sub-model, after dropping the primes, can be rewritten as:

$$\overline{\mathbf{E}}(\underline{x}) = \overline{\mathbf{E}}_{inc} + k_2^2 \iint\limits_{Body} \left(1 - N^2(\underline{x}_1)\right) \overline{\mathbf{E}}(\underline{x}_1) H_0^{(1)}\left(k_2 |\underline{x} - \underline{x}_1|\right) \, dx_1 dy_1, \qquad (3.24a)$$

$$\overline{\mathbf{E}}_{inc} = \left(e^{ik_2 x} + e^{-ik_2 x} + e^{ik_2 y} + e^{-ik_2 y}\right) \hat{z}, \qquad (3.24b)$$

$$\frac{\rho_{p_s} c_{p_s} b^2}{k_{ts} \theta_1} g(\phi) \frac{\partial T}{\partial t} = \nabla \cdot (k_t(\phi) \nabla T) + \frac{P_w B}{k''(\phi_0, T_0)} k''(\phi, T) |\mathbf{E}|^2, \qquad (3.24c)$$

$$k_t(\phi) \frac{\partial T}{\partial x} + B\{T + \beta_r[(T+1)^4 - 1]\} = 0, \qquad x = a/b, \qquad (3.24d)$$

$$k_t(\phi) \frac{\partial T}{\partial y} + B\{T + \beta_r[(T+1)^4 - 1]\} = 0, \qquad y = 1, \qquad (3.24e)$$

$$-K(\phi) \frac{\partial T}{\partial y} + B\{T + \beta_r[(T+1)^4 - 1]\} = 0, \qquad y = -1. \qquad (3.24f)$$

The initial condition is given by $T(x, y, 0) = 0$. Similarly, the governing equations, which describe the FCVI sub-model, can be written in the following non-dimensional form:

$$\nabla \cdot \left(k_p \nabla P \right) = \frac{C_0}{\rho_f} Da A \Gamma_1 , \tag{3.24g}$$

$$\frac{b^2 \mu_v}{k_p^0 P2\theta_2} \frac{\partial(\phi C)}{\partial t} - \nabla \cdot (Ck_p \nabla P) = \frac{1}{Pe} \nabla \cdot (D\nabla C) - Da A \Gamma_1 , \tag{3.24h}$$

$$\frac{\rho_{p_s}}{C_0 k_1 \theta_3} \frac{\partial r}{\partial t} = \Gamma_1 , \tag{3.24i}$$

$$\Gamma_1 = C \exp(-E_a / RT_0(T+1)) , \tag{3.24j}$$

$$\frac{\partial P}{\partial x} = 0, \qquad \frac{\partial C}{\partial x} = 0, \qquad x = a/b \tag{3.24k}$$

$$P = 1, \qquad \frac{\partial C}{\partial y} = 0, \qquad y = 1 \tag{3.24l}$$

$$P = P1/P2, \qquad C(x,t) = 1, \qquad y = -1 \tag{3.24m}$$

The following controlling parameters eventually emerged during the analysis:

$$P_w = k''(\phi_0, T_0) b |E_0|^2 / 2h_e T_0 , \qquad B = h_e b / k_{ts} , \qquad \beta_r = s_b e T_0^3 / h_e ,$$

$$Da = \frac{k_1 b^2 \mu_v}{k_p^0 P2L}, \qquad Pe = \frac{k_p^0 P2}{D_0 \mu_v} . \tag{3.25}$$

P_w is a measure of input microwave power, B is the Biot number, β_r is the radiation heat loss parameter, Da is the Damkholer, number which defines the ratio of the chemical reaction rate relative to the rate of mass transport by convection, and the Peclet number Pe is the ratio between the rates of mass transport by diffusion to that by convection.

Equations (3.24a-f) describe the microwave-heating model and are solved separately initially for fixed porosity to obtain the electric field and the unsteady state temperature distributions. The thermal time scale θ_1 is taken to be $\theta_1 = \rho_{p_s} c_{p_s} b^2 / k_{ts}$ in the EM-model. Equation (3.24g) is a Poisson equation for pressure and describes total fluid conservation and equation (3.24h) states that the gaseous concentration changes because of reaction, diffusion and convection processes taking place. The next equation describes the temporal evolution of porosity due to the chemical reaction and, finally, equation (3.24j) is used to evaluate the mass transfer rate. These constitute the balance

set of equations for this study of the FCVI sub-model and are solved numerically in the next section.

It is noted here that various time scales evolved in the problem. Three of them present in equations (3.24c,h,i) are θ_1 θ_2 and θ_3. It was found that the time scale at which the porosity of the medium decreases was much larger compared to the thermal diffusion and convective flow time scales, see table 3.1. Thus equations 3.24g-h were solved in the steady state form to determine the pressure and MTS concentration distributions in the FCVI model. Equation 3.24i was solved to obtain unsteady state solutions.

Table 3.1: Time scales of physical phenomena

Time scale	Represented parameter	Order of magnitude
Thermal diffusion	θ_1 $(\rho_{p_s} c_{p_s} b^2 / k_{ts})$	$O(10^{-1})$
Convective Flow	θ_2 $(b^2 \mu_v / P2k_p^0)$	$O(10^{-2})$
Porosity evolution	θ_3 $(\rho_{p_s} / C_0 k_1)$	$O(10^3)$

3.3 Numerical experimental

In this section the numerical techniques employed to solve the system of equations describing the EM and FCVI models are presented. The Finite Difference Method (FDM) [141,142] was used here to solve equations (3.24c-m) numerically. The FDM is based upon approximations, which permit replacing the differential equations by finite difference equations. These finite difference approximations are algebraic in form; they relate the value of the dependent variable, example temperature, at a point in the solution region (preform) to the values at some neighbouring points. Thus a finite difference solution basically involves three steps:

- Dividing the solution region into a grid of nodes.
- Approximating the differential equations by finite difference equivalents that relate the dependent variable at a point in the solution region to its values at the neighbouring points.
- Solving the difference equations subject to the prescribed initial and boundary conditions.

The system of equations describing the EM-model is first solved. However, before applying the FDM to solve equations (3.24c-f), the electric field distribution is first determined by solving equations (3.24a-b) for the EM-model.

3.3.1 EM-model: determining the electric field

As previously stated, equation (3.24a) does not give an explicit solution for E, since E also appears under the integral sign, thus it must be solved numerically to obtain the electric field distribution. The rectangular sample, that is the solution region, is divided in the x-y plane into equal small rectangles of sides Δx and Δy as in figure 3.4. The coordinates (x_{i_c}, y_j) of a typical grid point considered here are represented as:

$$x_{i_c} = x_0 + i_c \Delta x, \qquad i_c = 0,1,\ldots\ldots\ldots,2M \qquad\qquad x_0 = -a/b,$$

$$y_j = y_0 + j\Delta y, \qquad j = 0,1,\ldots\ldots\ldots,2N \qquad\qquad y_0 = -1.$$

The electric field and its properties within a smaller rectangle are assumed to be constant.
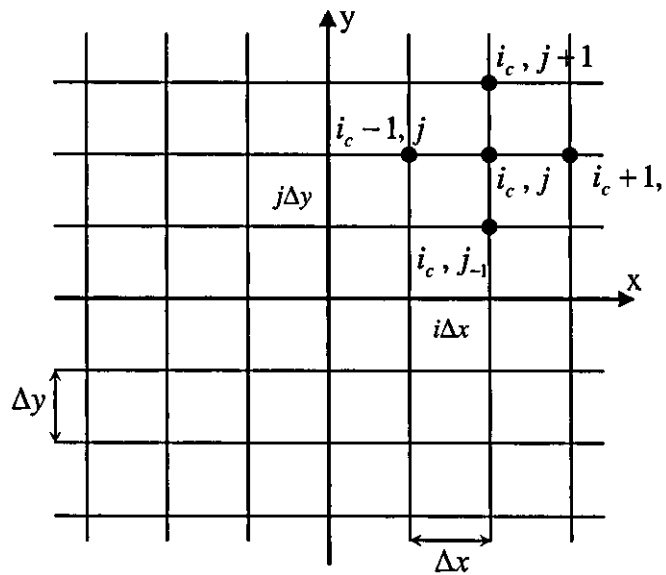
Figure 3.4: Shows part of the discretization of the fibrous preform, the solution region.

Equation (3.24a) can thus be expressed as a summation of the form:

$$E(\underline{x}_j) = E_{inc}(\underline{x}_j) + k_2^2 \sum_{\substack{m=0 \\ m \neq j}}^{p} E(\underline{x}_m)Q^j(\underline{x}_m) + R(\underline{x}_j), \quad 0 \leq j \leq p_t, \tag{3.26}$$

where,

$p_t = (2M+1)(2N+1) - 1$ and $Q^j(\underline{x}_m) = \Delta x \Delta y \left[1 - N^2(\underline{x}_m)\right] H_0^{(1)}\left(k_2 \left|\underline{x}_j - \underline{x}_m\right|\right)$. The term

$R(\underline{x}_j)$ is obtained for the case when $m = j$ and is given by:

$$R(\underline{x}_j) = \int_{y_j - \Delta y}^{y_j + \Delta y} \int_{x_j - \Delta x}^{x_j + \Delta x} \left[1 - N^2(\underline{x}_m)\right] E(\underline{x}_m) H_0^{(1)}\left(k_2 \left|\underline{x}_j - \underline{x}_m\right|\right) \, dx_j \, dy_j \tag{3.27}$$

The integration in the above equation is performed by considering the following assumption:

$x_m = x_j + \alpha'$ and $y_m = y_j + \beta'$, where α' and β' are considered as small quantities. Using these assumptions, equation (3.27) is converted to:

$$R(\underline{x}_j) = \left[1 - N^2(\underline{x}_m)\right] E(\underline{x}_m) \int_{-\Delta y}^{\Delta y} \int_{-\Delta x}^{\Delta x} H_0^{(1)}\left(k_2 \sqrt{\alpha'^2 + \beta'^2}\right) d\alpha' d\beta'. \tag{3.28}$$

For small argument u_c, the Hankel function $H_0^{(1)}$ is given by (see appendix 3):

$$H_0^{(1)}(u) \approx 1 + \frac{2i}{\pi} \ln u_c.$$

Substituting this approximation in (3.28) and performing the integration, the following expression is obtained for $R(\underline{x}_j)$:

$$R(\underline{x}_j) = \frac{8i\Delta x \Delta y}{\pi}\left(\ln\left(k_2\sqrt{\Delta x^2 + \Delta y^2}\right) + \tan^{-1}\left(\frac{\Delta x}{\Delta y}\right)\right) \\ + \frac{4i\Delta y^2}{\pi}\tan^{-1}\left(\frac{\Delta x}{\Delta y}\right) - \frac{4i\Delta x^2}{\pi}\tan^{-1}\left(\frac{\Delta y}{\Delta x}\right) \tag{3.29}$$

Thus knowing the values for $Q^j(\underline{x}_j)$ and $R(\underline{x}_j)$ for each element $\underline{x}_j$, equation (3.26) is transformed into a set of $p_t + 1$ linear equations, which are represented in matrix form as:

$$\begin{bmatrix} 1/k_2^2 - R(\underline{x}_0) & -Q^0(\underline{x}_1) & -Q^0(\underline{x}_2) \cdots & \cdots & \cdots & \cdots -Q^0(\underline{x}_p) \\ -Q^1(\underline{x}_0) & 1/k_2^2 - R(\underline{x}_1) & -Q^1(x_2) \cdots & \cdots & \cdots & \cdots -Q^0(\underline{x}_p) \\ \vdots & \ddots & & \ddots & & \vdots \\ \vdots & \ddots & \ddots & & \ddots & \vdots \\ \vdots & & \ddots & \ddots & & \vdots \\ \vdots & & & \ddots & \ddots & \vdots \\ -Q^{p-1}(\underline{x}_0) \cdots & \cdots \cdots -Q^{p-1}(\underline{x}_{p-2}) & 1/k_2^2 - R(\underline{x}_{p-1}) & -Q^{p-1}(x_p) \\ -Q^p(\underline{x}_0) \cdots & \cdots & \cdots & -Q^p(\underline{x}_{p-2}) & -Q^p(\underline{x}_{p-1}) & 1/k_2^2 - R(\underline{x}_p) \end{bmatrix} \begin{bmatrix} E(\underline{x}_0) \\ \vdots \\ \vdots \\ \vdots \\ \vdots \\ \vdots \\ \vdots \\ E(\underline{x}_p) \end{bmatrix} = \begin{bmatrix} E_{inc}(\underline{x}_0) \\ \vdots \\ \vdots \\ \vdots \\ \vdots \\ \vdots \\ \vdots \\ E_{inc}(\underline{x}_p) \end{bmatrix}$$

$$\ldots(3.30)$$

This system of linear equations is solved onward using LU Decomposition [143].

3.3.2 EM-model: determining the temperature distribution

The Finite Difference Method [141,142] is used here to solve equations 3.24c-f to obtain the unsteady state solutions describing the thermal distributions Following the steps mentioned earlier, the preform is discretized in the x-y plane as shown in figure 3.4 and the time variable t is also discretized accordingly with time step Δt:

$$t_n = n\Delta t, \quad n = 0,1,2,\ldots\ldots\ldots$$

Figure 3.5 shows the point (i_c, j) with its associated nodes discretized in time. Thus using FDM, the parabolic partial differential equation (3.24c) is converted to its equivalent finite difference approximation, given as:

$$g\frac{\left(T_{i_c,j}^{n+1} - T_{i_c,j}^n\right)}{\Delta t} = k_t(\phi)\left(\frac{T_{i_c+1,j}^{n+1} - 2T_{i_c,j}^{n+1} + T_{i_c-1,j}^{n+1}}{\Delta x^2}\right) + k_t(\phi)\left(\frac{T_{i_c,j+1}^{n+1} - 2T_{i_c,j}^{n+1} + T_{i_c,j-1}^{n+1}}{\Delta y^2}\right) + F_{i_c,j}^n, (3.31)$$

where,

$$F_{i_c,j}^n = \frac{P_w B}{k''(\phi_0, T_0)}k''(\phi^n, T_{i_c,j}^n)\left|E_{i_c,j}^n\right|, \quad i_c = 0,1,2,\ldots\ldots\ldots,M, \quad j = 0,1,2,\ldots\ldots\ldots,N.$$

However, this equation results in a pentadiagonal system of equations at each time-step Δt, which is very cumbersome and time consuming to solve. Alternatively, the equation is split into two equations with the use of Alternating Direct Implicit (ADI)

scheme [141,143]. The idea is to divide each time-step into two steps of size $\Delta t/2$. In each sub-step, a different space dimension is treated implicitly:

$$\frac{T_{i_c,j}^{n+1/2} - T_{i_c,j}^{n}}{\Delta t/2} = \frac{k_t(\phi)}{g(\phi)}\left(\frac{T_{i_c+1,j}^{n+1/2} - 2T_{i_c,j}^{n+1/2} + T_{i_c-1,j}^{n+1/2}}{\Delta x^2} + \frac{T_{i_c,j+1}^{n} - 2T_{i_c,j}^{n} + T_{i_c,j-1}^{n}}{\Delta y^2}\right) + \frac{F_{i_c,j}^{n}}{g(\phi)} \qquad (3.32a)$$

$$\frac{T_{i_c,j}^{n+1} - T_{i_c,j}^{n+1/2}}{\Delta t/2} = \frac{k_t(\phi)}{g(\phi)}\left(\frac{T_{i_c+1,j}^{n+1/2} - 2T_{i_c,j}^{n+1/2} + T_{i_c-1,j}^{n+1/2}}{\Delta x^2} + \frac{T_{i_c,j+1}^{n+1} - 2T_{i_c,j}^{n+1} + T_{i_c,j-1}^{n+1}}{\Delta y^2}\right). \qquad (3.32b)$$

Equation (3.32a) is implicit in the x-direction and explicit in the y-direction. The data for the $(n+1/2)^{th}$ time step provided by this equation upon using the values of the temperature at the nth time-step is then fed to equation (3.32b), which is implicit in the y-direction and explicit in the x-direction, to get the values of the temperature at the $(n+1)^{th}$ time step. The advantage of this implicit method is that each sub-step requires only the solution of a simple tridiagonal system.
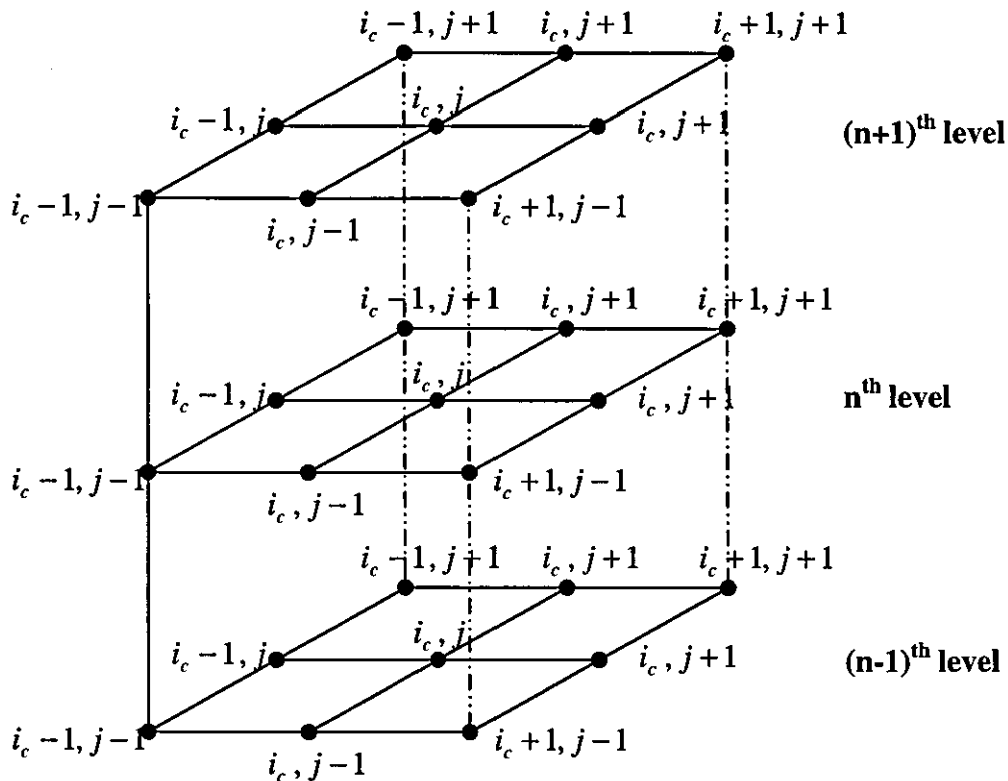
Figure 3.5: Shows the grid points in two space dimension at three different time levels

The above equations can be re-written in the following form:

$$- \lambda_1 T_{i_c-1,j}^{n+1/2} + (1+2\lambda_1)T_{i_c,j}^{n+1/2} - \lambda_1 T_{i_c+1,j}^{n+1/2} = \gamma_1 T_{i_c,j-1}^n + (1-2\gamma_1)T_{i_c,j}^n + \gamma_1 T_{i_c,j+1}^n + \frac{\Delta t}{2g(\phi)}F_{i_c,j}^n,$$

$$.....(3.33a)$$

$$- \gamma_1 T_{i_c,j-1}^{n+1} + (1+2\gamma_1)T_{i_c,j}^{n+1} - \gamma_1 T_{i_c,j+1}^{n+1} = \lambda_1 T_{i_c-1,j}^{n+1/2} + (1-2\lambda_1)T_{i_c,j}^{n+1/2} - \lambda_1 T_{i_c+1,j}^{n+1/2}, \qquad (3.33b)$$

where, $\lambda_1 = \dfrac{\Delta t k_t(\phi)}{2g(\phi)\Delta x^2}$ and $\gamma_1 = \dfrac{\Delta t k_t(\phi)}{2g(\phi)\Delta y^2}$.

The equivalent finite difference approximations for the initial and boundary conditions are expressed as:

$$T_{i_c,j}^0 = 0, \qquad (3.33c)$$

$$T_{M+1,j}^n = T_{M-1,j}^n - \frac{2\Delta xB}{k_t(\phi)}\left\{T_{M,j}^n + \beta_r\left[\left(T_{M,j}^n + 1\right)^4 - 1\right]\right\}, \qquad (3.33d)$$

$$T_{-1,j}^n = T_{1,j}^n, \qquad (3.33e)$$

$$T_{i_c,-1}^n = T_{i_c,1}^n - \frac{2\Delta yB}{k_t(\phi)}\left\{T_{i_c,0}^n + \beta_r\left[\left(T_{i_c,0}^n + 1\right)^4 - 1\right]\right\}, \qquad (3.33f)$$

$$T_{i_c,N+1}^n = T_{i_c,N-1}^n - \frac{2\Delta yB}{k_t(\phi)}\left\{T_{i_c,L}^n + \beta_r\left[\left(T_{i_c,L}^n + 1\right)^4 - 1\right]\right\}. \qquad (3.33g)$$

It is recalled here that the thermal problem is solved only for positive x values due to the symmetry property involved. By evaluating equation (3.33a) for $i_c = 0,1,2,\ldots\ldots\ldots,M$, the following two matrix equations are obtained to determine the $(n+1/2)^{th}$ time step temperature at the lower and upper boundary nodes, that is, for $j = 0, N$:

$$
\begin{bmatrix}
1+2\lambda_1 & -2\lambda_1 & & & \\
-\lambda_1 & 1+2\lambda_1 & -\lambda_1 & & \\
\ddots & \ddots & \ddots & & \\
& -\lambda_1 & 1+2\lambda_1 & -\lambda_1 & \\
& & -2\lambda_1 & 1+2\lambda_1 + \\
& & & \dfrac{2\Delta xB\lambda_1}{k_t(\phi)} &
\end{bmatrix}
\begin{bmatrix}
T_{0,0}^{n+1/2} \\ \vdots \\ \vdots \\ \vdots \\ \vdots \\ T_{M,0}^{n+1/2}
\end{bmatrix}
=
\begin{bmatrix}
1-2\gamma_1 - & 2\gamma_1 & & \\
2\Delta yB\gamma_1/k_t(\phi) & \ddots & \ddots & \\
& \ddots & \ddots & \\
& & 1-2\gamma_1 - & 2\gamma_1 \\
& & 2\Delta yB\gamma_1/k_t(\phi) &
\end{bmatrix}
\begin{bmatrix}
T_{0,0}^n \\ T_{0,1}^n \\ \vdots \\ \vdots \\ T_{M,0}^n \\ T_{M,1}^n
\end{bmatrix}
+
\begin{bmatrix}
\Omega_{0,0}^n \\ \vdots \\ \vdots \\ \vdots \\ \vdots \\ \Omega_{M,0}^n
\end{bmatrix}
$$

$$...(3.34a)$$

78

$$
\begin{bmatrix}
1+2\lambda_1 & -2\lambda_1 & & & \\
-\lambda_1 & 1+2\lambda_1 & -\lambda_1 & & \\
& \ddots & \ddots & \ddots & \\
& & -\lambda_1 & 1+2\lambda_1 & -\lambda_1 \\
& & & -2\lambda_1 & 1+2\lambda_1 + \\
& & & & \dfrac{2\Delta xB\lambda_1}{k_t(\phi)}
\end{bmatrix}
\begin{bmatrix}
T_{0,N}^{n+1/2} \\ \vdots \\ \vdots \\ \vdots \\ \vdots \\ \vdots \\ T_{M,N}^{n+1/2}
\end{bmatrix}
=
\begin{bmatrix}
2\gamma_1 & 1-2\gamma_1 - & & \\
& & 2\Delta yB\gamma_1/k_t(\phi) & \\
& \ddots & \ddots & \\
& & \ddots & \ddots \\
& & 2\gamma_1 & 1-2\gamma_1 - \\
& & & 2\Delta yB\gamma_1/k_t(\phi)
\end{bmatrix}
\begin{bmatrix}
T_{0,0}^{n} \\ T_{0,1}^{n} \\ \vdots \\ \vdots \\ \vdots \\ T_{M,0}^{n} \\ T_{M,1}^{n}
\end{bmatrix}
+
\begin{bmatrix}
\Omega_{0,N}^{n} \\ \vdots \\ \vdots \\ \vdots \\ \vdots \\ \vdots \\ \Omega_{M,N}^{n}
\end{bmatrix}
$$

$$\ldots(3.34b)$$

where $\quad \Omega_{i_c,j}^{n} = \dfrac{\Delta t}{2g(\phi)}F_{i_c,j}^{n} - \dfrac{2\Delta yB\beta_r\gamma_1}{k_t(\phi)}\left[\left(T_{i_c,j}^{n}+1\right)^4 -1\right] \quad$ for $\quad i_c = 0,1,\ldots\ldots\ldots,M-1 \quad$ and

$$\Omega_{M,j}^{n} = \dfrac{\Delta t}{2g(\phi)}F_{i_c,j}^{n} - \dfrac{2(\lambda_1\Delta x + \gamma_1\Delta y)B\beta_r}{k_t(\phi)}\left[\left(T_{M,j}^{n}+1\right)^4 -1\right] \quad .$$

The temperature at the interior nodes within the preform for the $(n+1)^{th}$ time step are obtained by solving the following matrix equations:

$$
\begin{bmatrix}
1+2\lambda_1 & -2\lambda_1 & & & \\
-\lambda_1 & 1+2\lambda_1 & -\lambda_1 & & \\
& \ddots & \ddots & \ddots & \\
& & -\lambda_1 & 1+2\lambda_1 & -\lambda_1 \\
& & & -2\lambda & 1+2\lambda_1 + \\
& & & & \dfrac{2\Delta xB\lambda_1}{k_t(\phi)}
\end{bmatrix}
\begin{bmatrix}
T_{0,j}^{n+1/2} \\ \vdots \\ \vdots \\ \vdots \\ \vdots \\ \vdots \\ T_{M,j}^{n+1/2}
\end{bmatrix}
=
\begin{bmatrix}
\gamma_1 & 1-2\gamma_1 & \gamma_1 & & \\
& \ddots & \ddots & \ddots & \\
& & \ddots & \ddots & \ddots \\
& & & \ddots & \ddots & \ddots \\
& & & & \gamma_1 & 1-2\gamma_1 & \gamma_1
\end{bmatrix}
\begin{bmatrix}
T_{0,j-1}^{n} \\ T_{0,j}^{n} \\ T_{0,j+1}^{n} \\ \vdots \\ T_{M,j-1}^{n} \\ T_{M,j}^{n} \\ T_{M,j+1}^{n}
\end{bmatrix}
+
\begin{bmatrix}
\Omega_{0,j}^{n} \\ \vdots \\ \vdots \\ \vdots \\ \vdots \\ \Omega_{M,j}^{n}
\end{bmatrix}
$$

$$\ldots(3.34c)$$

where, $\Omega_{i_c,j}^{n} = \dfrac{\Delta t}{2g(\phi)}F_{i_c,j}^{n}, \qquad i_c = 0,1,\ldots\ldots\ldots,M-1, \qquad j = 1,2,\ldots\ldots\ldots,N-1$

and $\Omega_{M,j}^{n} = \dfrac{\Delta t}{2g(\phi)}F_{M,j}^{n} - \dfrac{2\lambda_1\Delta xB\beta_r}{k_t(\phi)}\left[\left(T_{M,j}^{n}+1\right)^4 -1\right].$

Similar matrix equations are obtained while evaluating equation (3.33b) using the corresponding boundary conditions. It is noted here that the nonlinear term present in the radiation boundary conditions are evaluated using temperature values at previous time steps. This is basically done to avoid solving nonlinear system of equations that would be generated instead. The matrix equations, representing systems of linear

79

equations, are then solved together numerically using LU decomposition [143] to obtain the temperature distribution at each time-step, Δt. However, since the dielectric properties of the sample are considered temperature dependent (see equations 3.9a-c), their values are updated at every time step. Further, the heat source terms present in the system of linear equations (3.34), which contains the dielectric properties, are updated at each time step as well. Thus this causes the matrix equations (3.30) and (3.34) to be solved together at each time step, Δt. Figure 3.6 shows the flow chart describing the steps involved in solving the complete EM-model numerically.
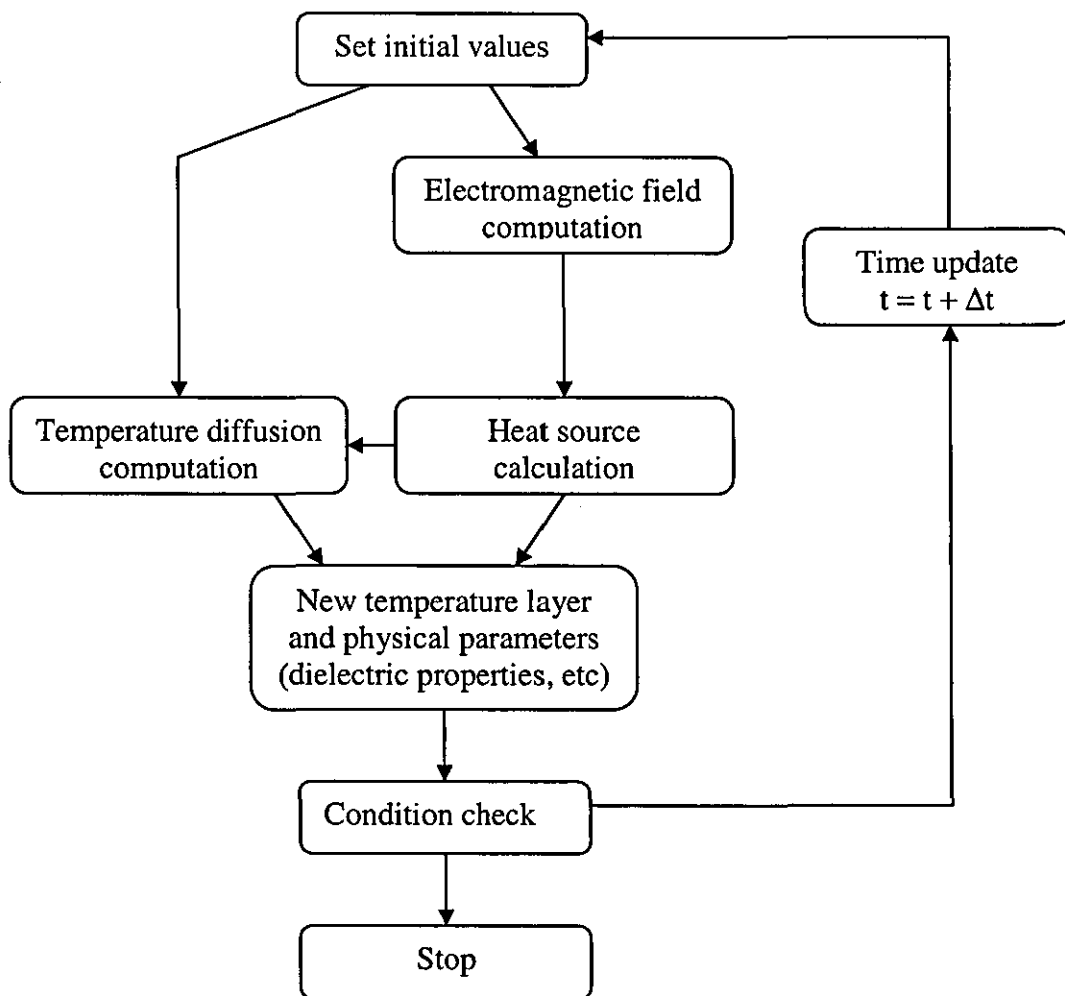
Figure 3.6: Flow chart describing the steps involved in numerically solving the EM-Model.

80

3.3.3 FCVI-model:

In this sub-section, the system of equations, (3.24g-m), describing the Forced-Flow Chemical Vapour Infiltration model is numerically solved using the Finite Difference Method. Comparing the data in Table 3.1, it is noted here that the convective flow time scale, θ_2, is much smaller than the porosity evolution time scale, θ_3. Thus, the time scale θ is taken to be $\theta = \theta_3 = \rho_{p_s}/C_0 k_1$. This causes the coefficient of the time derivative term in equation 3.24h to be very small. Hence, the time dependent term is neglected and the equation is solved to obtain steady state solutions describing the concentration distribution during the process. Equations (3.24g and 3.24h) are re-written in the following form for convenience:

$$\frac{\partial k_p}{\partial x}\frac{\partial P}{\partial x} + k_p\frac{\partial^2 P}{\partial x^2} + \frac{\partial k_p}{\partial y}\frac{\partial P}{\partial y} + k_p\frac{\partial^2 P}{\partial y^2} = \frac{C_0}{\rho_f}DaA\Gamma_1, \tag{3.35a}$$

$$Pek_p\nabla P \cdot \nabla C = -D\nabla^2 C + \left(1 - \frac{CC_0}{\rho_f}\right)D_a PeA\Gamma_1. \tag{3.35b}$$

Considering figures 3.4 and 3.5, which relates the discretization of the preform in space and time, equations (3.24i-m) and (3.35a-b) are transformed into their equivalent finite difference approximations:

$$\left(\frac{k_{P_{i_c+1,j}} - k_{P_{i_c-1,j}}}{2\Delta x}\right)\left(\frac{P_{i_c+1,j} - P_{i_c-1,j}}{2\Delta x}\right) + k_{P_{i_c,j}}\left(\frac{P_{i_c+1,j} - 2P_{i_c,j} + P_{i_c-1,j}}{\Delta x^2}\right) +$$

$$\left(\frac{k_{P_{i_c,j+1}} - k_{P_{i_c,j-1}}}{2\Delta y}\right)\left(\frac{P_{i_c,j+1} - P_{i_c,j-1}}{2\Delta y}\right) + k_{P_{i_c,j}}\left(\frac{P_{i_c,j+1} - 2P_{i_c,j} + P_{i_c,j-1}}{\Delta y^2}\right) = \frac{C_0 DaA_{i_c,j}\Gamma_{1i_c,j}}{\rho_f} \tag{3.36a}$$

$$Pek_{P_{i_c,j}}\left(\left[\frac{P_{i_c+1,j} - P_{i_c-1,j}}{2\Delta x}\right]\left[\frac{C_{i_c+1,j} - C_{i_c-1,j}}{2\Delta x}\right] + \left[\frac{P_{i_c,j+1} - P_{i_c,j-1}}{2\Delta y}\right]\left[\frac{C_{i_c,j+1} - C_{i_c,j-1}}{2\Delta y}\right]\right)$$

$$= -D(T_{avg})\left(\frac{C_{i_c+1,j} - 2C_{i_c,j} + C_{i_c-1,j}}{\Delta x^2} + \frac{C_{i_c,j+1} - 2C_{i_c,j} + C_{i_c,j-1}}{\Delta y^2}\right) - \tag{3.36b}$$

$$\left(1 - \frac{C_{i_c,j}C_0}{\rho_f}\right)D_a PeA_{i_c,j}\Gamma_{1i_c,j}$$

$$\frac{r_{i_c,j}^{n+1} - r_{i_c,j}^{n}}{\Delta t} = -\Gamma_{1i_c,j} \tag{3.36c}$$

$$\Gamma_{1i_c,j} = C_{i_c,j} \exp\left(-E_a / RT_0 (T_{i_c,j} + 1)\right) \tag{3.36d}$$

$$\phi_{i_c,j} = 1 - \frac{\left((\sqrt{3}+4)L_1 + \left(\left((3-\sqrt{3})/27 - 14/6\right)\left(6-2\sqrt{3}\right)-4\right)r_{i,j}\right)\sqrt{3}\,\pi\, r_{i_c,j}^2}{L_1^3} \tag{3.36e}$$

$$P_{-1,j} = P_{1,j}, \quad C_{-1,j} = C_{1,j}, \quad \text{at } x = a/b \tag{3.36f}$$

$$P_{M+1,j} = P_{M-1,j}, \quad C_{M+1,j} = C_{M-1,j}, \quad \text{at } x = 0 \tag{3.36g}$$

$$P_{i_c,N} = 1, \quad C_{i_c,N+1} = C_{i_c,N-1}, \quad \text{at } y = 1 \tag{3.36h}$$

$$P_{i_c,-1} = \frac{P_1}{P_2} \text{ or } P_{i_c,-1} = P_{i_c,1} - \frac{2\Delta y w_0}{k_{P_{i,0}}} \qquad C_{i_c,0} = 1, \quad \text{at } y = -1 \tag{3.36i}$$

for $i_c = 0,1,2,\ldots\ldots\ldots,M$, $j = 0,1,2,\ldots\ldots\ldots,N$ and $n = 1,2,3,\ldots\ldots\ldots$.

Equation (3.36a) and (3.36b), which determine the pressure and concentration distributions respectively, are actually elliptic equations and they are solved using similar techniques. To avoid repetitiveness, only the matrix equations obtained while solving equation (3.36b) together with the boundary conditions, (3.36f-i) are shown here.

Equation (3.36b) can be written in a simplified form as:

$$\theta_{i_c+1,j}^1 C_{i_c+1,j} + \theta_{i_c-1,j}^2 C_{i_c-1,j} + \theta_{i_c,j+1}^3 C_{i_c,j+1} + \theta_{i_c,j-1}^4 C_{i_c,j-1} + \theta_{i_c,j}^5 C_{i_c,j} = DaPeA_{i_c,j}\Gamma_{1i_c,j} \tag{3.37}$$

where,

$$\theta_{i_c+1,j}^1 = Pek_{P_{i_c,j}}\left(\frac{P_{i_c+1,j} - P_{i_c-1,j}}{4\Delta x^2}\right) + \frac{D(T_{avg})}{\Delta x^2}$$

$$\theta_{i_c-1,j}^2 = -Pek_{P_{i_c,j}}\left(\frac{P_{i_c+1,j} - P_{i_c-1,j}}{4\Delta x^2}\right) + \frac{D(T_{avg})}{\Delta x^2}$$

$$\theta_{i_c,j+1}^3 = Pek_{P_{i_c,j}}\left(\frac{P_{i_c,j+1} - P_{i_c,j-1}}{4\Delta y^2}\right) + \frac{D(T_{avg})}{\Delta y^2}$$

$$\theta_{i_c,j+1}^4 = -Pek_{P_{i_c,j}}\left(\frac{P_{i_c,j+1} - P_{i_c,j-1}}{4\Delta y^2}\right) + \frac{D(T_{avg})}{\Delta y^2}$$

$$\theta_{i_c,j}^5 = \frac{C_0 D_a Pe}{\rho_f} A_{i_c,j} \Gamma_{1_{i_c,j}} - \frac{2D(T_{avg})}{\Delta x^2} - \frac{2D(T_{avg})}{\Delta y^2}$$

A linear system of coupled equations is obtained by substituting the values of i for each value of j in (3.37). This is represented in terms of the following matrix equations:

$$M^1 C^1 + T_{**}^2 C^2 = b^1, \qquad \text{for } j = 1 \tag{3.38a}$$

$$T_*^{j-1} C^{j-1} + M^j C^j + T_{**}^{j+1} C^{j+1} = b^j, \qquad \text{for } j = 2, 3, \ldots\ldots N - 1 \tag{3.38b}$$

$$T_*^{N-1} C^{N-1} + M^N C^N = b^N, \qquad \text{for } j = N \tag{3.38c}$$

where the matrices M^j, T_*^j, and T_{**}^j and the vectors C^j and b^j are given as:

$$M^j = \begin{bmatrix} \theta_{0,j}^5 & \theta_{1,j}^1 + \theta_{-1,j}^2 & & & & \\ \theta_{0,j}^2 & \theta_{1,j}^5 & \theta_{2,j}^1 & & & \\ \ddots & \ddots & \ddots & & & \\ & \ddots & \ddots & \ddots & & \\ & & \theta_{M-2,j}^2 & \theta_{M-1,j}^5 & \theta_{M,j}^1 \\ & & & \theta_{M+1,j}^1 + \theta_{M-1,j}^2 & \theta_{M,j}^5 \end{bmatrix} \qquad C^j = \begin{bmatrix} C_{0,j} \\ \vdots \\ \vdots \\ \vdots \\ C_{M,j} \end{bmatrix} \qquad j = 1, 2, 3, \ldots\ldots, N$$

$$b^1 = \begin{bmatrix} DaPeA_{0,1}\Gamma_{1_{0,1}} - \theta_{0,0}^4 C_{0,0} \\ \vdots \\ \vdots \\ \vdots \\ DaPeA_{M,1}\Gamma_{1_{M,1}} - \theta_{M,0}^4 C_{M,0} \end{bmatrix} \qquad T_{**}^j = \begin{bmatrix} \theta_{0,j}^3 & & & \\ & \ddots & & \\ & & \ddots & \\ & & & \theta_{M,j}^3 \end{bmatrix} \qquad j = 2, 3, \ldots\ldots, N$$

$$T_*^j = \begin{bmatrix} \theta_{0,j}^4 & & & \\ & \ddots & & \\ & & \ddots & \\ & & & \theta_{M,j}^4 \end{bmatrix} \quad j = 1, 2, \ldots\ldots, N-1 \qquad b^j = \begin{bmatrix} DaPeA_{0,j}\Gamma_{1_{0,j}} \\ \vdots \\ \vdots \\ \vdots \\ DaPeA_{M,j}\Gamma_{1_{M,j}} \end{bmatrix} \quad j = 2, 3, \ldots\ldots N$$

These matrix equations can hence be embedded into a single matrix equation:

83

$$\overline{M}\,\vec{C} = \vec{b} \qquad\qquad (3.39)$$

where,

$$\overline{M} = \begin{bmatrix} M^1 & T_{**}^2 & & & \\ T_*^1 & M^2 & T_{**}^3 & & \\ & \ddots & \ddots & \ddots & \\ & & T_*^{N-2} & M^{N-1} & T_{**}^N \\ & & & T_*^{N-1} & M^N \end{bmatrix}, \qquad \vec{C} = \begin{bmatrix} C^1 \\ \vdots \\ \vdots \\ \vdots \\ C^N \end{bmatrix} \quad \text{and} \quad \vec{b} = \begin{bmatrix} b^1 \\ \vdots \\ \vdots \\ \vdots \\ b^N \end{bmatrix}$$

The same techniques were applied to equation (3.36a) to obtain similar matrix equations. These equations were finally solved using the same numerical techniques applied to solve the system of equations determining the electric and temperature distributions. To avoid extra numerical computation, the diffusion coefficient D was taken to be dependent only on the average temperature of the sample during the process. However, at this stage the FCVI-Model is solved to obtain variation of the porosity distributions under isothermal conditions during the process. At each time step Δt, the properties of the unit cells, that is the surface area available for reaction to occur, the radius of the fibre bundle, the porosity and the permeability values are calculated. These data are then used to computationally update pressure and concentration distributions. Figure 3.7 shows the flow chart describing the steps involved to determine the pressure, MTS concentration and porosity distributions at each time step numerically. Further, it is recalled here that two pressure conditions are set at the boundary $y = -1$, that is, at the lower boundary of the sample. A fixed inlet pressure of the gaseous precursor is first applied to study the porosity evolution during the Chemical Vapour Infiltration process. Secondly a fixed flow rate is maintained at the lower boundary to study the effect on the preform infiltration. During the experimental investigation undertaken by Jaglin [39], both the hydrogen flow rate and the inlet pressure of the gaseous mixture were maintained constant. Theoretically, the inlet pressure would increase under constant volume flow rate during the infiltration process. Also the volume flow rate would decrease when a constant inlet pressure was maintained. Thus it was reasonable, to study the effects on the infiltration profiles under both conditions.
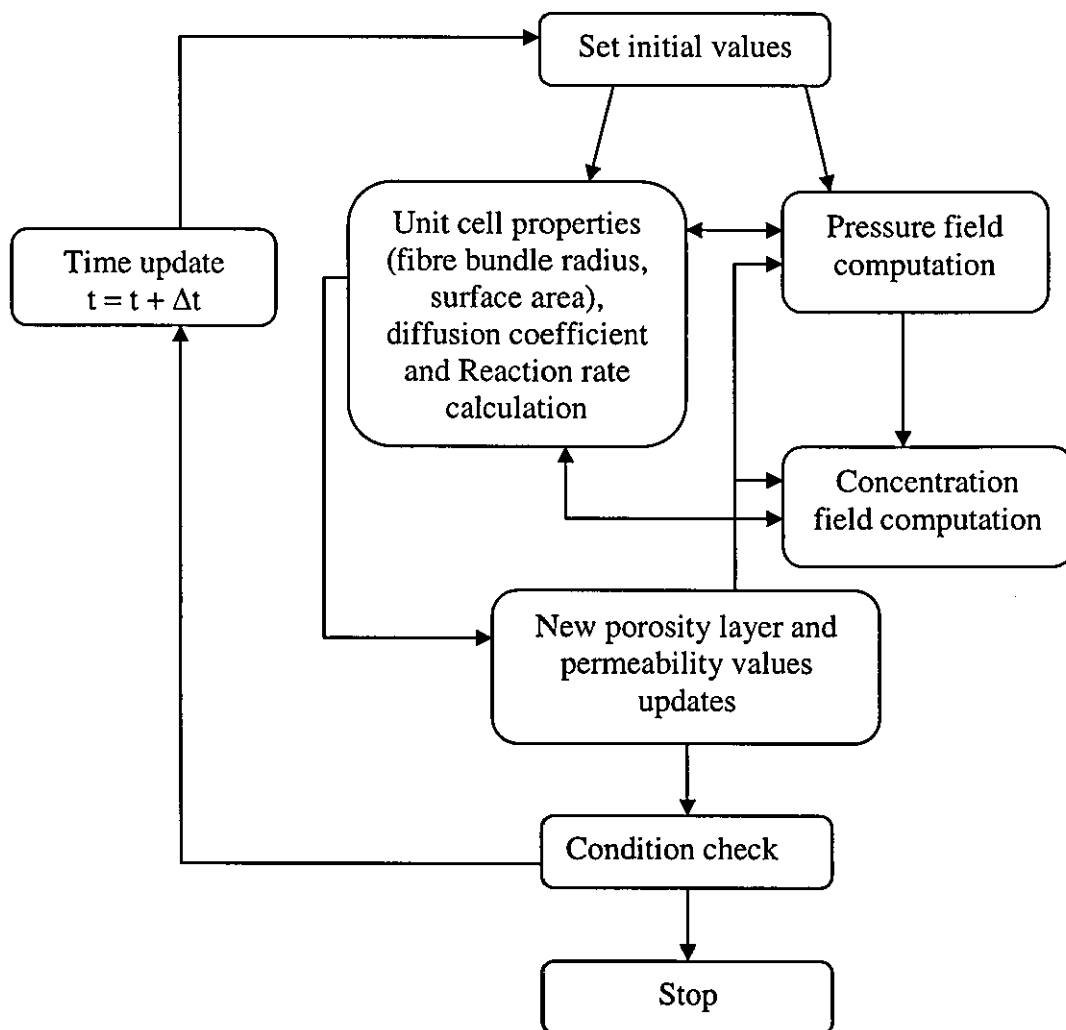
Figure 3.7: Flow chart describing the steps involved in numerically solving the FCVI-Model.

3.3.4 ME-FCVI model

The ME-FCVI model as mentioned earlier is obtained by combining the EM-model and the FCVI-model. The evolution of the temperature distribution during the microwave heating is in fact affected by the forced flow of the gaseous precursor during ME-FCVI, which provides convective losses inside the porous preform. Equation (3.24), which describes thermal diffusion within the preform, does not incorporate the convection term, which is due to the forced-flow of the precursor. This cooling effect inside the perform is in fact controlled by the internal surface area (pores surfaces) available for the gaseous precursor to flow. Thus the EM-model would

become complicated to solve by introducing the convective term in the heat diffusion equation. Hence at this stage the consequences of the convective term on the thermal distribution is ignored. However, convective losses at the boundaries of the preform, controlled by the heat transfer coefficient h_e, are included in the thermal boundary conditions, see equation (3.24). But realistically, the cooling effect Further, the decreasing porosity of the preform during ME-FCVI also affects the temperature field, but in the formulation above, the microstructure of the preform is not considered during the electromagnetic heating to avoid the complication that exist. Taking into account of the above facts, the microwave heating stage and the infiltration stage were thus allowed to be decoupled during the ME-FCVI process. The effects of applying an inverse thermal gradient on the processing variables and deposition profiles are hence analysed. Figure 3.8 shows the flow chart describing the steps involved in the ME-FCVI model. A dynamic one-dimensional model, where the effect of the evolution of porosity on the thermal field is considered, is developed and described in Chapter 4.
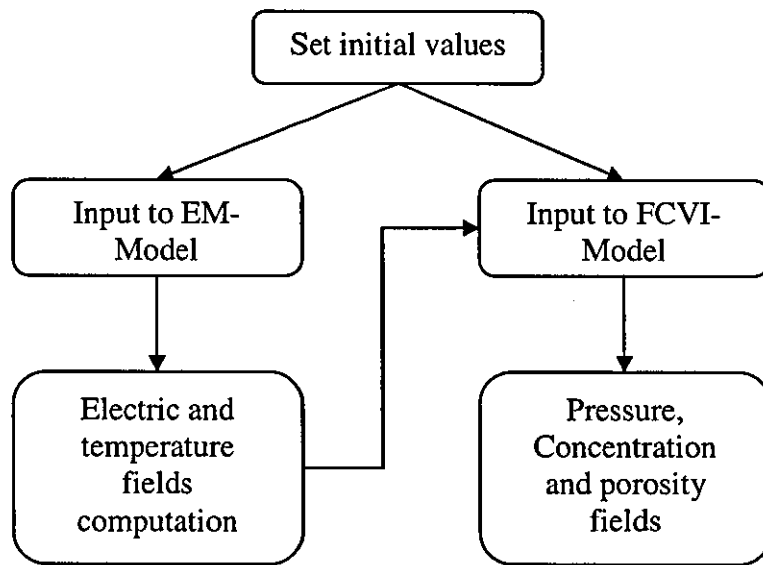
Figure 3.8: Flow chart showing the steps involved in evaluating the ME-FCVI model numerically using the EM and FCVI sub models.

3.4 Numerical results and discussions

Microwave enhanced forced-flow chemical vapour infiltration is dependent on various process conditions such as:

- Temperature and temperature gradient of the preform
- Pressure gradient of the system
- Total gas flow rate
- Gaseous precursor concentration
- Dimensions of the preform
- Porosity of the preform

For a complete understanding of the MEFCVI process, it is necessary to study the effects on the infiltration process when one or more of these parameters are varied. This section is divided into three main sub-sections. In the first one, the effects of adjusting the thermal and electrical parameters on the temperature and temperature gradient of the preform during the heating stage of the sample are studied through the EM-model. This model was also used to investigate the effect of decreasing porosity and sample size on the thermal distribution and consequences of thermal runaway. The simulation results obtained under these investigations are presented and discussed. The system of equations (3.30) and (3.34), was coupled and solved together to obtain these results. In the second sub-section, the effects of the pressure gradient, the gas flow rate and precursor concentration on the infiltration profiles under isothermal conditions were studied using the forced-flow CVI model. Equations (3.39) and (3.36) were coupled together to perform this analysis and the numerical results obtained are presented and discussed. In the final sub-section, the effects of combining the inverse thermal gradient obtained from the EM-model and the forced-flow conditions, on the processing variables, the infiltration profiles and processing times are studied through the MEFCVI model. The corresponding results obtained are presented and discussed therein.

The general operating parameter values and constants used in all the simulations are given in table 3.2, unless otherwise stated. It is recalled here that all the three models are constructed for one half of the sample only, as shown in the diagram below; this assumes a vertical axis of symmetry.
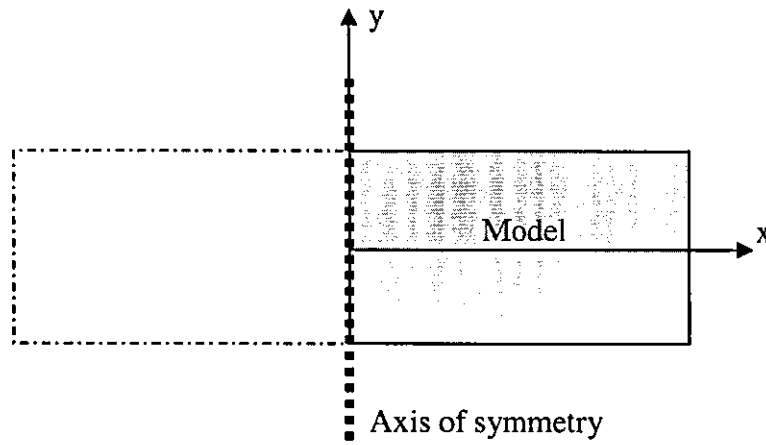
Figure 3.9: Schematic of the SiC preform. The dark section only is being investigated numerically due to symmetry.

Table 3.2: Dimensional parameter values used, unless otherwise stated.

Ambient temperature, T_0	298.15 K
Operating frequency, $f = \omega/2\pi$	2.45 GHz
SiC relative dielectric permittivity, $k_s''(\phi_0, T_0)$	10.0 Fm^{-1}
SiC thermal conductivity, k_{ts}	35.7 W/m K
SiC density, ρ_{ps}	3110 kg/m^3
SiC specific heat, c_{ps}	1100 J/kg K
SiC emissivity, e	0.85
Stefan-Boltzmann constant, s_b	5.67 x 10^{-8} J K^{-4} m^{-2} s^{-1}
SiC molecular mass, M_s	0.04010 kg
MTS molecular mass, M_{MTS}	0.1495 kg
H$_2$ molecular mass, M_{H_2}	0.0020 kg
Heat transfer coefficient, h_e [76]	155 W/m^2 K
Viscosity of mixture, μ	0.013 g/cm^3
Density of Hydrogen, ρ_f	0.0899 Kg/m^3
Diffusion coefficient at STP, D_0	1.0
Length of unit cell, L	500 μm
Reaction constant, k_1 [81]	3.0 m/s
Activation energy, E_a [76]	120 kJ/mole
Universal gas constant, R	8.314 x 10^3 J/K
Lennard-Jones parameter, $\hbar$	0.4414 nm

3.4.1 Microwave heating (EM-model)

Equations (3.30) and (3.34) are solved simultaneously using the LU decomposition method [143] to obtain the electric field and steady state temperature distribution within the SiC preform during microwave heating. In practical microwave heating systems [39], the ceramic preform is placed in a resonant microwave cavity. The equations determining the electric and temperature distributions must then be solved throughout the cavity, and in that case other numerical schemes like the Finite Difference Time Domain (FDTD) must be employed instead to numerically obtain the solutions. Many numerical investigations have been undertaken to describe this interaction, including FDTD [144,145,146], the method of lines, a variation on FDTD which leads to the solution of Maxwell's equations via a system of ordinary differential equations [147,148] and the Finite Element Method [149,150], all of which require discretization of the entire applicator volume and its load. All of these methods are essential for the computation of fields involving arbitrary shaped cavities and loads, however, in cases where the electromagnetic properties of the load vary, these methods often suffer with respect to the large computational time and computer memory required to implement them. Further, more, the results then become cavity specific and the purpose in this present study is to provide some generalizations concerning the ability of microwaves to generate temperature distributions in preforms that are useful in processing CMCs by CVI.

Two issues are important here for a successful simulation of the microwave heating process:

(1) A meaningful model for the microwave absorption by the preform during CVI,

(2) Knowledge of the physical database of the material (SiC), which is involved.

3.4.1.1 SiC dielectric properties models

The results obtained for permittivity measurements, see figure 3.10, of SiC [151] showed that the dielectric properties, k_s' and k_s'', depend critically on temperature. These data are used to obtain the following empirical models describing the behaviour of these properties with respect to the temperature T:

$$k_s' = 0.00001T^2 - 0.0284T + 49.1471,$$ \hfill (3.41a)

$$k_s'' = 0.0001T^2 - 0.0246T + 3.4208. \tag{3.41b}$$

Figure 3.10 shows the graphs obtained when equations (3.41a,b) are plotted together with the experimental data [151]. These two models are used in the EM-model to update the dielectric properties at each time step. The EM-model is constructed in such a way so that other models describing the behaviour of the dielectric properties with temperature can be included.
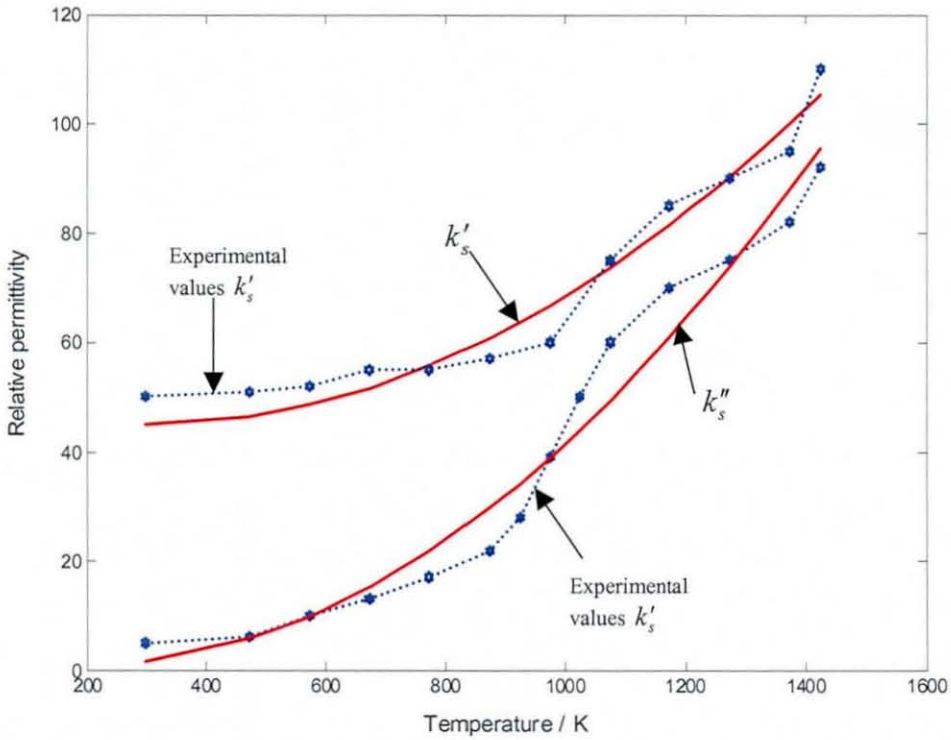
Figure 3.10: The blue graphs represent permittivity data obtained as a function of temperature at 2.45 GHz [147], the red curves represent empirical model describing these data.

3.4.1.2 Unsteady-state analysis

In the simulations, the electric field within the preform, at each time step Δt was determined by solving the complex linear system of equations in (3.30) and then after computing the local heat of generation, the temperature distribution was calculated from (3.34). In this computation, the amplitude of the electric field E_0 incident on the sample was calculated from the instantaneous time average incident power P_{inc} through the relation:

$$|E_0|^2 = \frac{2\eta_0 P_{inc}}{A_s},$$

(3.42)

where A_s is the surface area of the sample and η_0 is the impedance of free space. The physical data of SiC needed as incident for the simulations are listed in table 3.2. The expressions (3.41) were used to update the dielectric properties at each time step during the simulations. The condition $T_{i_c,j}^{n+1} - T_{i_c,j}^{n} \leq 0.05$ (dimensionless value), at a nodal point (i_c, j), was considered as the stopping criteria for most of the simulations. At this point, steady state temperature solutions were basically achieved during the microwave heating process. It is recalled here that the solutions were computed for only half of the sample as mention as shown in figure 3.9.

Figure 3.11 shows the computed isotherms for a SiC preform, with 50% porosity and assumed infinitely long in the z-direction with a cross section of 50 mm × 10 mm, subjected to microwaves of power 1.2 kW from all four sides. The external cooling by convection is characterised by a heat transfer coefficient equal to 155 Wm^{-2}K^{-1}. The contour plot shows that the interior of the sample is hotter than the surface; the centre of the ceramic (0,0) is at 1100 K and the surface (25,0) is at 1000 K.
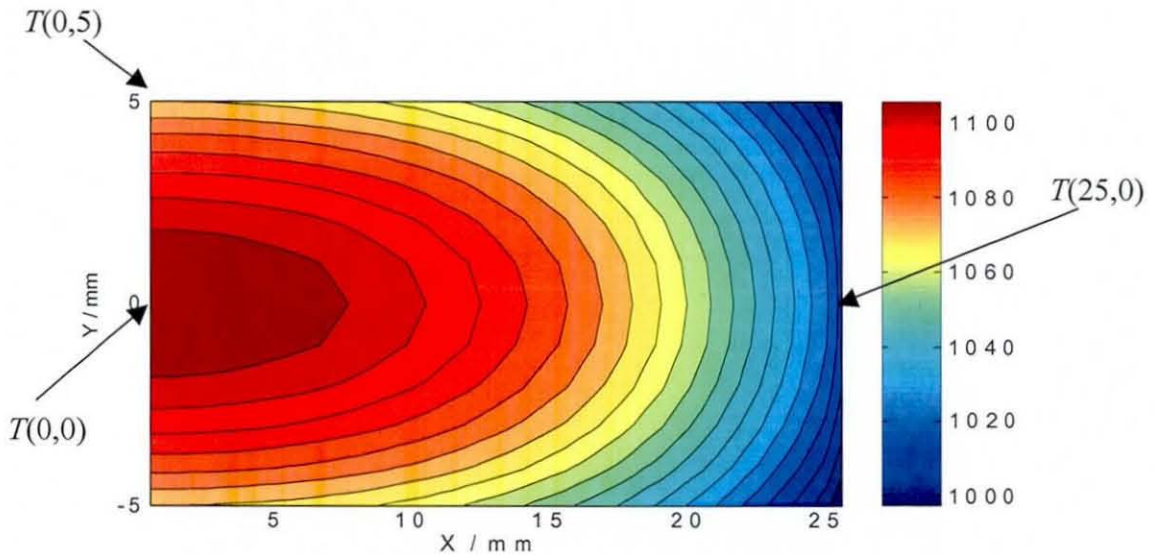
Figure 3.11: Steady-state temperature distributions in a 50% dense SiC subjected to microwaves with $P_{inc} = 1.2\,\text{kW}$. The colour scale on the right defines the temperature in Kelvin.

Furthermore, comparing the temperatures along the x and y axes it is observed that higher thermal difference exists along the x-direction. This is shown in figure 3.12, which represents the evolution of the temperatures differences, $T(0,0) - T(25,0)$ and

91

$T(0,0) - T(0,5)$ with time. It is also observed in the figure that the magnitudes of the electric fields at the centre $E(0,0)$ and the surface $E(25,0)$ decrease nonlinearly with increase in temperature. This is due to the nonlinear increase in the dielectric properties, which causes a decrease in the penetration dept of the electromagnetic field. It is further observed that $|E(0,0)|^2 \approx |E(25,0)|^2$, which says that almost uniform electric field was obtained inside the sample. However, during the heating process, the wavelength of the EM field is reduced[**] since the dielectric properties are increased (see equation 2.17 and 2.18). This could have resulted in multiple hot spots across the sample, but the latter are not observed in figure 3.11. This therefore implies that the dominant effect here is the heat loss across the boundaries that prevents uniform thermal fields and hot spots formation within the sample.
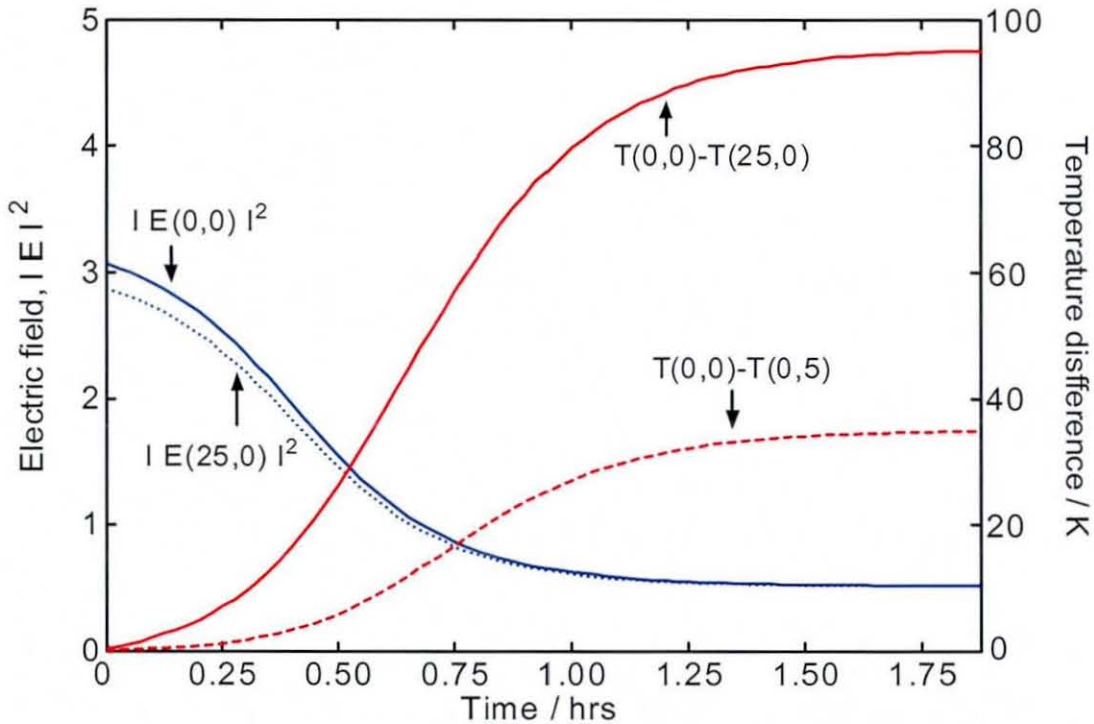
Figure 3.12: Represents the change in the magnitude of the electric field at the centre E(0,0) and the surface E(25,0) with time. Evolution of thermal differences between the temperature at the centre of the preform $T(0,0)$ and the surfaces, $T(25,0)$ and $T(0,5)$ are described as well.

3.4.1.2.1 Effect of incident power and external cooling on the thermal distribution

Figure 3.13 shows the steady state thermal distributions obtained for different incident microwave power. As expected, it is observed that an increase in power input

---

[**] This effect of change in wavelength is importantand should be investigated in the future

elevates the temperature level within the preform. The porosity of the sample and the heat transfer coefficient were kept fixed at 50% and 155 $Wm^{-2}K^{-1}$ respectively. A further increase in the power level would eventually increase the steady state temperature further, however, referring to the S-shaped curve in chapter 2, figure 2.11, a critical power input exits beyond which the steady state temperature would lie on the upper branch of the S-shaped curve, which describes the thermal runaway effect.

Moreover, it is deduced after examining figure 3.14 that an increase in the power input resulted in an increase in the temperature differences across the preform. The figure shows the temperature differences between the centre (0,0) and the surfaces (25,0) and (0,5) for different incident power. The thermal difference increased more along the sample (across the x-axis) than across its thickness (y-axis). Further, it is also seen that steady state thermal solutions is achieved faster with higher power level. This states that a balance between the amount of heat generated inside the sample and the convective and radiative losses at the boundaries is achieved faster for higher P_{inc}. It is noted here that the size of the sample was maintained fixed during this analysis. The effect on the temperature profile when the dimensions of the sample are changed is investigated in section 3.4.1.2.3.
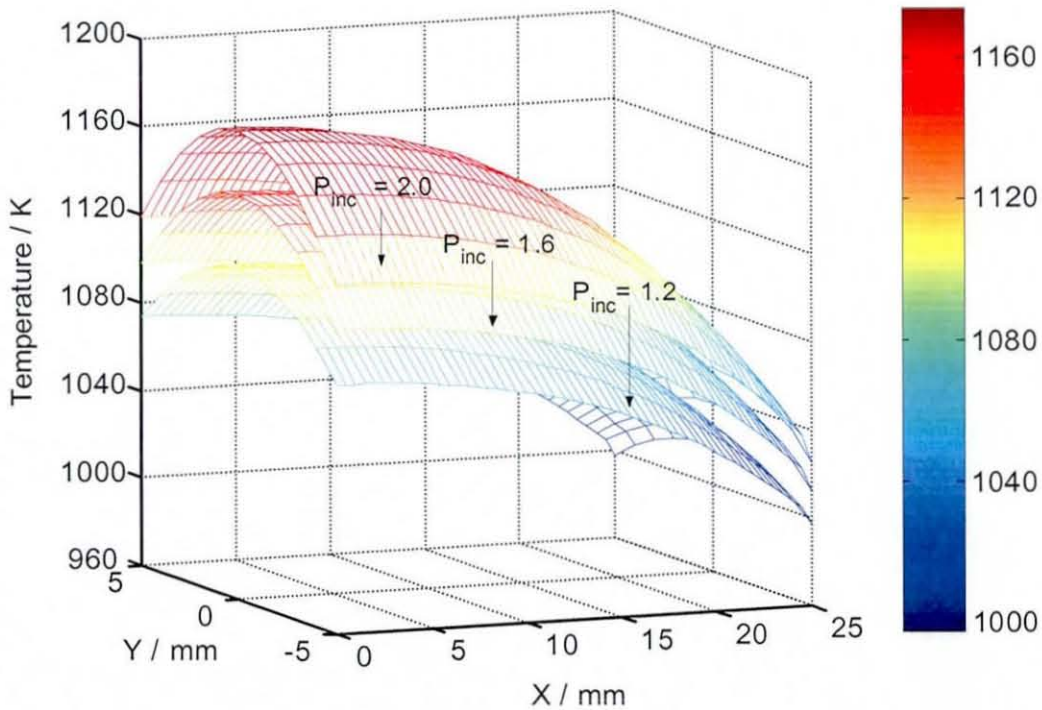
Figure 3.13: Steady state temperature distributions within the preform at different microwave power levels, P_{inc} / kW. The colour bar reflects the temperatures in Kelvin.
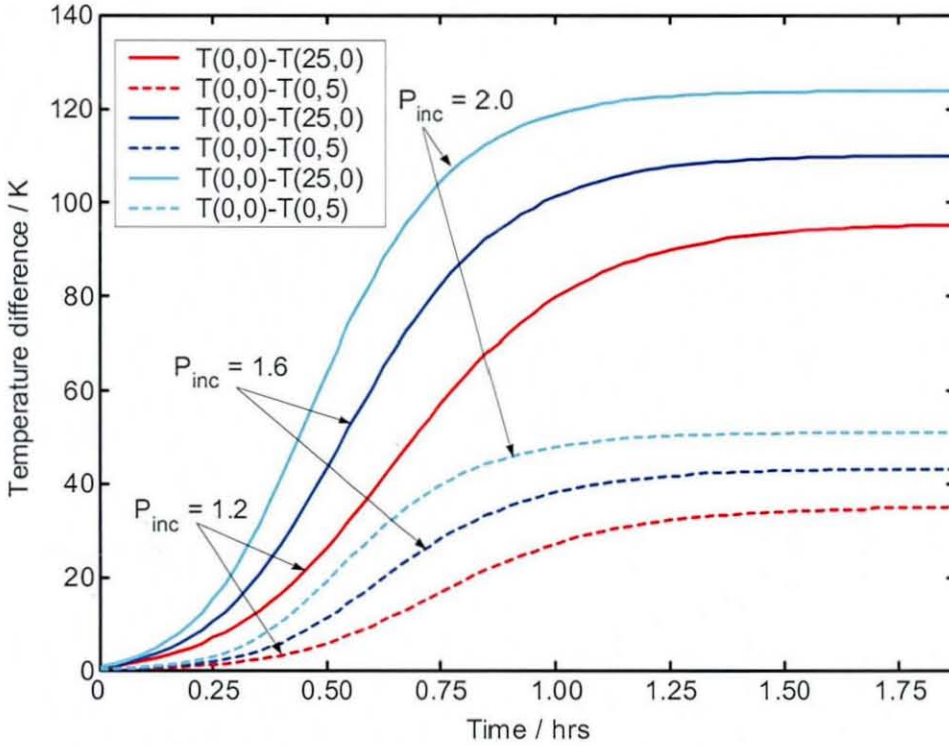
Figure 3.14: Thermal difference evolution with time, with respect to the temperature at the centre $T(0,0)$ for different incident microwave power level, P_{inc} / kW.

As previously stated the external cooling (loss by convection) is characterised by the heat transfer coefficient h_e. Figure 3.15 shows the final steady state temperature distributions obtained for different heat transfer coefficients; $h_e = 135, 155$ and 180 $Wm^{-2}K^{-1}$. It is observed that the temperature levels across the sample decrease with an increase in h_e as expected. The porosity level and the incident power were kept at 50% and 1.6 kW respectively. However, as compared to the change in an increase in incident power level, this variation in the heat transfer coefficient has almost no effect on the temperature gradient as shown in figure 3.16. The figure represent the evolution of the temperature differences with time, between the temperatures at the centre $(0,0)$ and the surfaces $(25,0)$ and $(0,5)$. No change in the thermal differences across the thickness of the sample, $T(0,0)$-$T(0,5)$, is observed. But a slight increase in the thermal gradient along the preform is observed with increase in h_e. However, it is noted here that the effects on the temperature distributions was studied by considering a 66 % increase in the power levels and only a 29% increase in h_e values.
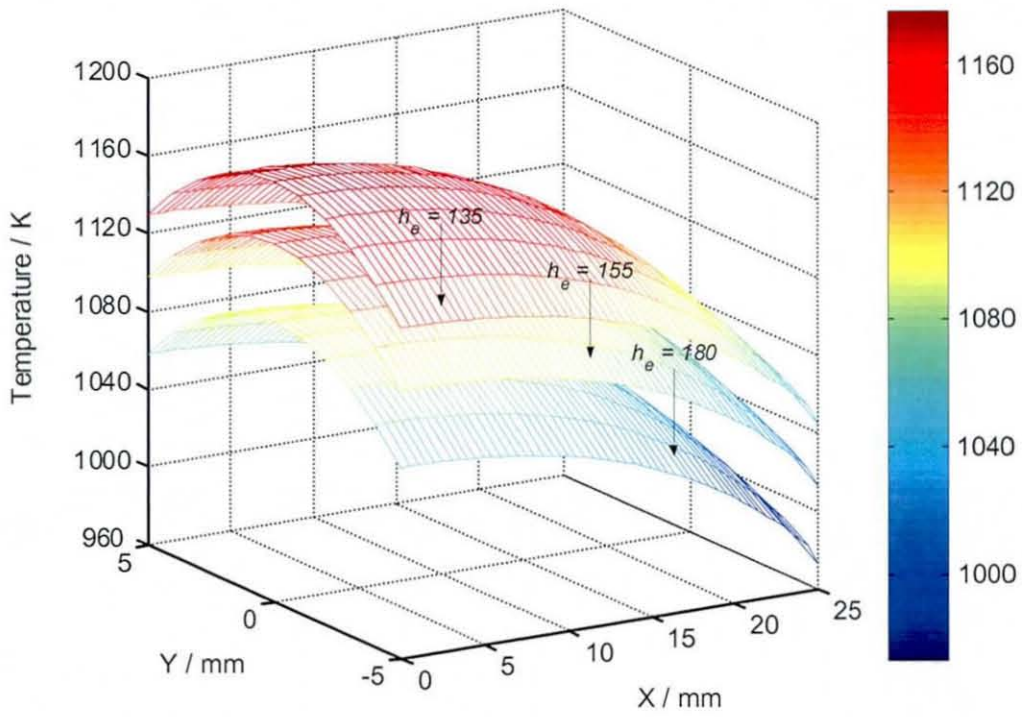
Figure 3.15: Steady state temperature distributions within the preform for different heat transfer coefficient h_e. The colour bar represents the temperature scale.
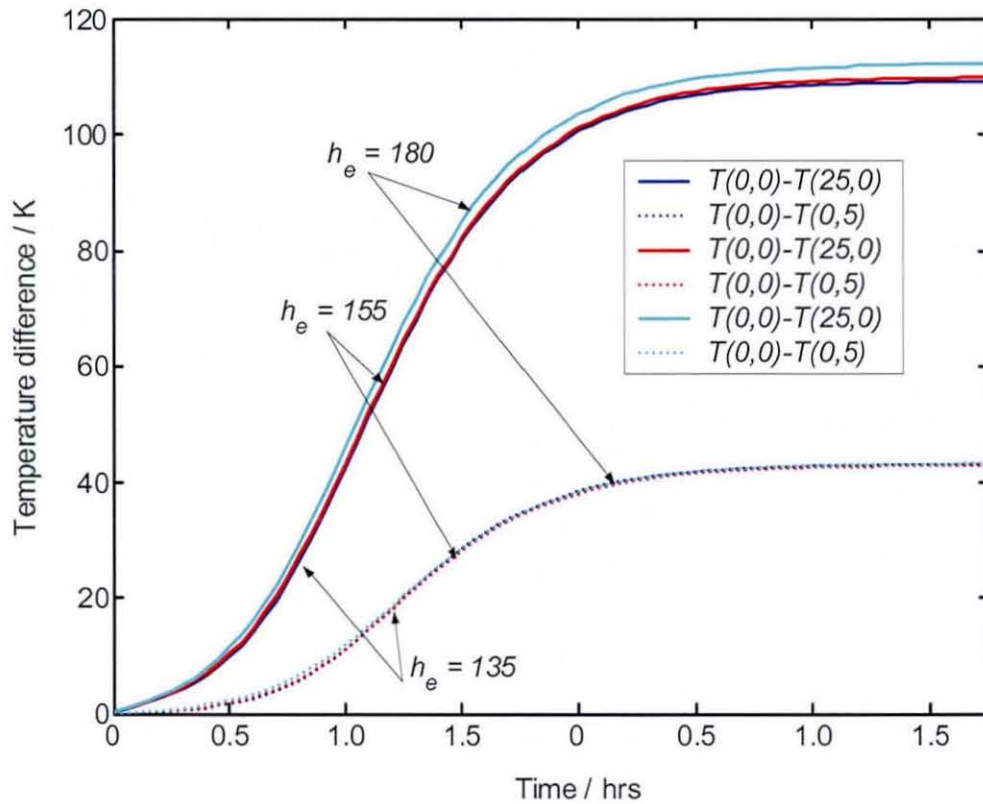
Figure 3.16: Evolution of temperature difference with time between the temperatures at the centre $T(0,0)$ and the surfaces $T(25,0)$ and $T(0,5)$, for different heat transfer coefficient h_e.

95

A practical application of the effect of microwave incident power, P_{inc} and the heat transfer coefficient, h_e is that P_{inc} can be changed accordingly to obtain the required temperature gradient and then independently vary h_e to manipulate the temperature level without affecting the gradient. The heat transfer coefficient, for example, can be increased by flowing gaseous precursors past the sample, as is the case during chemical vapour infiltration, or decreased by insulating it. A large P_{inc} is needed to generate a large temperature gradient. Normally this would result in excessive heating, possibly leading to thermal runaway, unless a large amount of convective losses is also employed, as is the case in figures 3.14 and 3.16. However, for relatively uniform temperatures (small thermal gradient), insulation is necessary, as illustrated in figure 3.17, where P_{inc} and h_e are only 0.8 kW and 25 Wm^{-2}K^{-1} respectively; the difference in temperature between the hottest and coldest part in the ceramic is only 32 K. Moreover, less incident power is required to heat the preform when insulation is used. Thus proper control of the microwave input power, flow of gaseous precursors and the type of insulation used during ME-FCVI can lead to the desired thermal gradient across the preform during infiltration, as demonstrated experimentally by Jaglin [39]
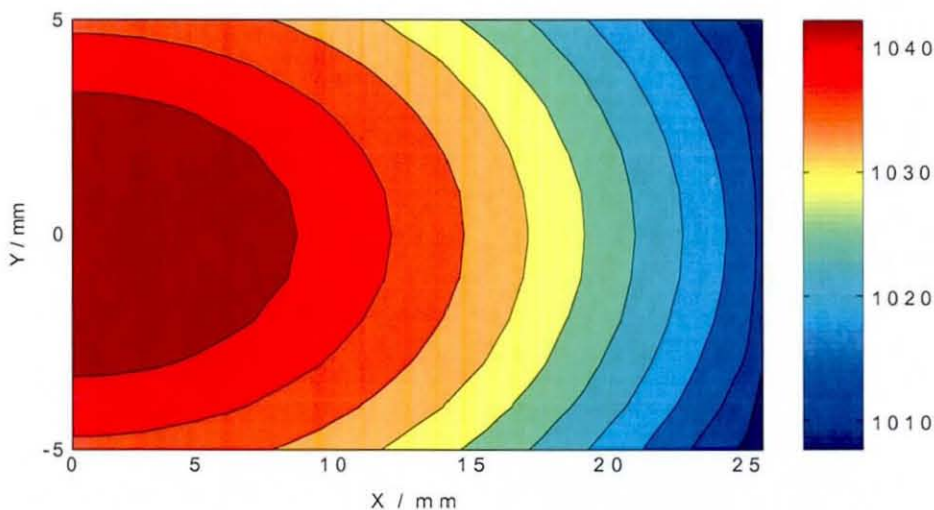
Figure 3.17: Steady state temperature distribution obtained during the microwave heating of a 50% dense insulated SiC sample. The incident power, $P_{inc} = 0.8\,kW$ and the heat transfer coefficient, $h_e = 25\,W/m^2K$. (84% less than the values considered before)

3.4.1.2.2 Effect of decreasing porosity on the temperature levels

During the densification stage in ME-FCVI, the average internal porosity of the preform decreased with time. The analysis above was performed under a constant 50% porosity level. In this section, the effect of changing porosity on the thermal distributions is investigated. Table a-2 in appendix 2 shows the changes in the radius of the fibre bundles to obtain the desired porosity level. Figure 3.18 showed the evolution of the temperature differences between the temperatures at the centre $T(0,0)$ and the surfaces $T(25,0)$ and $T(0,5)$, for different porosity level (ϕ = porosity), during microwave heating of the preform with $P_{inc} = 1.6$ kW and $h_e = 155$ Wm^{-2}K^{-1}. It is observed that the temperature differences across both the radius and thickness of the sample increase with increasing porosity. This means that the temperature levels rise with increase in porosity if a constant input power is employed. This is expected since less material is actually heated as the porosity increases. Moreover, for the case when $\phi = 0.7$, it is seen that the temperature differences rose significantly during the early stage of the heating process, which clearly demonstrates the effect of thermal runaway. Figure 3.19 shows the temperature distribution obtained during the early heating stage of the 70% porosity sample. Referring to the temperature scale in the figure, it is observed that the temperature difference across the sample is more than 350 K, with the temperature at the centre being above 1350 K. This suggested the formation of a hot spot at the centre, which underwent thermal runway during the heating stage. On the other hand, the case for low porosity level, $\phi = 0.1$, more time is needed to achieve steady-state solution. Also, the small increase in the temperature gradient as seen in figure 3.18, suggest that more input power is needed to achieve higher temperature levels.

Thus this model predicts that less incident power is needed to heat a preform of 50 mm by 10 mm initially before ME-FCVI, however, as deposition occurs, more incident power is needed to maintain the required temperature for reaction to occur. It is noted here that during ME-FCVI, the sample is densified in a non-linear fashion, thus the porosity distribution decreases non-uniformly during the process. The results obtained here assumed uniform decrease in the porosity level and the microstructure of the sample was ignored during the formulation of the microwave-heating model.
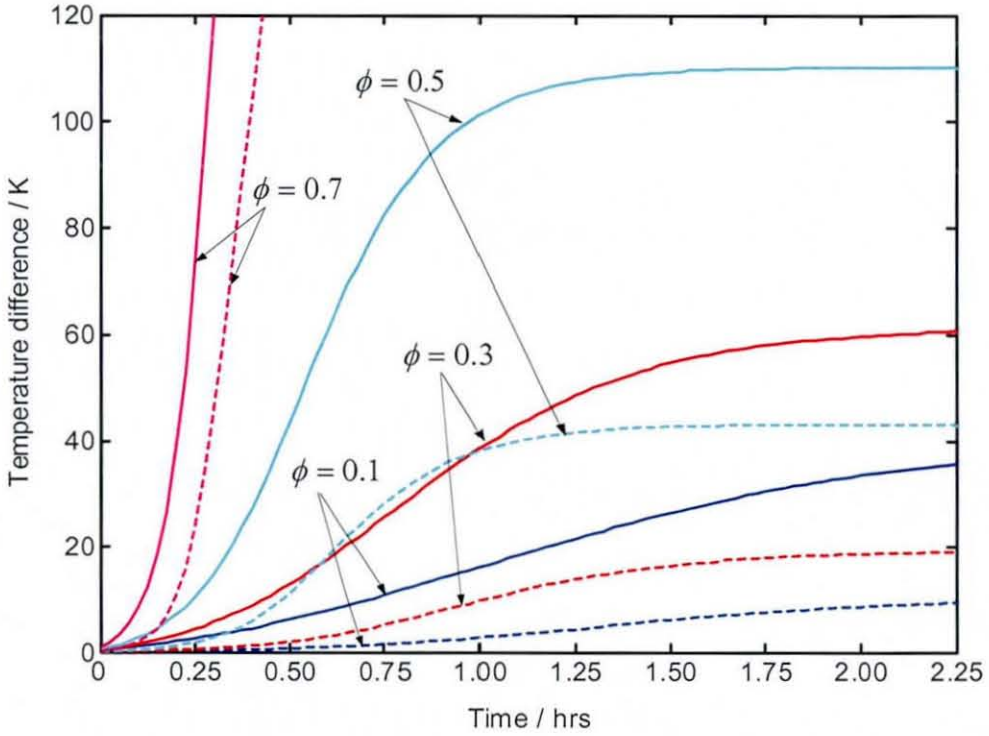
Figure 3.18: Evolution of the temperature differences with time between the temperatures at the centre $T(0,0)$ and the surfaces $T(25,0)$ and $T(0,5)$ for different internal porosity of the preform. The incident power and the heat transfer coefficient were kept fixed at 1.6 kW and 155 $Wm^{-2}K^{-1}$ respectively. The continuous and discontinuous curves represent the temperature gradient $T(0,0)$-$T(25,0)$ and $T(0,0)$-$T(0,5)$ respectively.
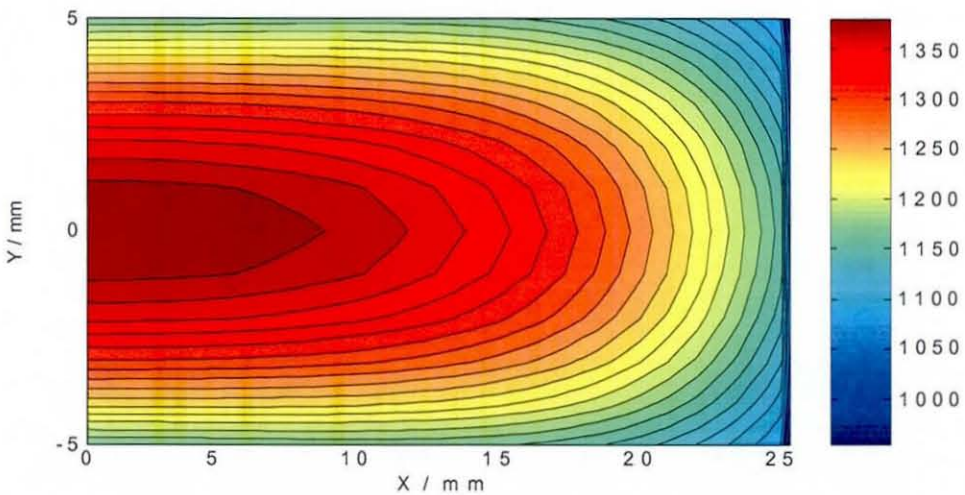
Figure 3.19: Temperature distribution obtained, prior to undergoing thermal runway, during the microwave heating of a 70% dense SiC preform. P_{inc} and h_e were kept fixed at 1.6 kW and 155 $Wm^{-2}K^{-1}$ respectively.

3.4.1.2.3 Effect of sample dimension on the thermal distribution during microwave heating

Along with the incident power, heat transfer coefficient and the porosity level, the size of the ceramic preform also has a significant influence on the temperatures and thermal differences achieved in the sample during microwave heating. Table 3.3 summarizes the numerical simulations carried out under different operating conditions for different preform sizes. Effects of the change in the radius of the ceramic were first studied. When the cross section of the preform was changed from 50×10 mm (figure 3.11) to 100×10 mm, higher temperature differences were obtained, even though the incident power applied was the same. Figure 3.20 shows the evolution with time of the subsequent thermal distributions obtained. It is observed from the distributions that during the early stage of the heating process the sample is heated volumetrically from the inside out, with the highest temperature being at its centre. However, as the temperature increases with time, the hottest zone within the sample moved away from the centre, towards its edge. The reason behind this phenomenon can be explained as follows: the dielectric properties increase with increase in temperature, but the penetration depth of the electromagnetic field decreases with increase in the dielectric properties and this causes the hot-spot to move away from the centre. Similar observations were made when the diameter of the sample was increased to 200 mm, see figure 3.21. However, in this case during the early stages of the process the sample was heated mostly away from the centre, which allowed heat to flow inward. The hot zone eventually moved toward the edges with increase in temperature. This phenomenon is in contrast to the results obtained when an 50×10 mm was heated, where the direction of heat flow was always towards the surfaces. These heat flow patterns and the variations in thermal distributions with a change in the dimensions of the preforms are actually a consequence of inhomogeneous microwave heating power deposition. In most cases of practical importance, the temperature distributions appearing in figure 3.20 and 3.21 would be considered unfavourable. However, during microwave enhanced CVI where densification occurs from the inside out, these thermal distributions could be advantageous for the infiltration process.

In literature [115], is has been shown that during microwave heating of large samples, peaks just in from the edges and dip in the middle of the preforms were seen from the incident microwave power distributions. These peaks were reasonably flat to

produce uniform heating across the sample. However, this depends on the convective losses across the boundaries. These uniform temperature distributions could as well be advantageous during microwave enhanced CVI. But considering the case of isothermal conventional CVI described in Chapter 2, some limitations observed in that case could possibly be produced here.

Preform size / mm radius × thickness	Incident power range, P_{inc} / kW	External cooling, h_e / $Wm^{-2}K^{-1}$	Porosity level ϕ % / 100
50 × 10	1.2, 1.6, 2.0	135, 155, 180	0.1, 0.3, 0.5, 0.7
100 × 10	1.2, 1.6, 2.0	135, 155, 180	0.1, 0.3, 0.5, 0.7
200 × 10	1.2, 1.6, 2.0	135, 155, 180	0.1, 0.3, 0.5, 0.7
200 × 20	1.2, 1.6, 2.0	135, 155, 180	0.1, 0.3, 0.5, 0.7

Table 3.3: Numerical experiments carried out for microwave heating of various sample sizes under different operating conditions.

Figure 3.22 shows the evolution of the thermal gradient between the temperatures at the centre T(0,0) and the surface T(25,0) for different sample sizes and incident microwave power, P_{inc}. From all the curves in the figure, it is seen that the temperature differences increase sharply during the heating process and then decreases smoothly until a steady-state solution is reached. These are due to the movement of the hot zones away from the centre, which relaxes the temperature gradient across the preforms. Further, it is observed that the temperature difference increases significantly with increase in the radius of the preform while its thickness remains fixed. This thermal gradient is further increased with increase in power incident. Also the steady-state temperature distribution is achieved faster with higher P_{inc}.
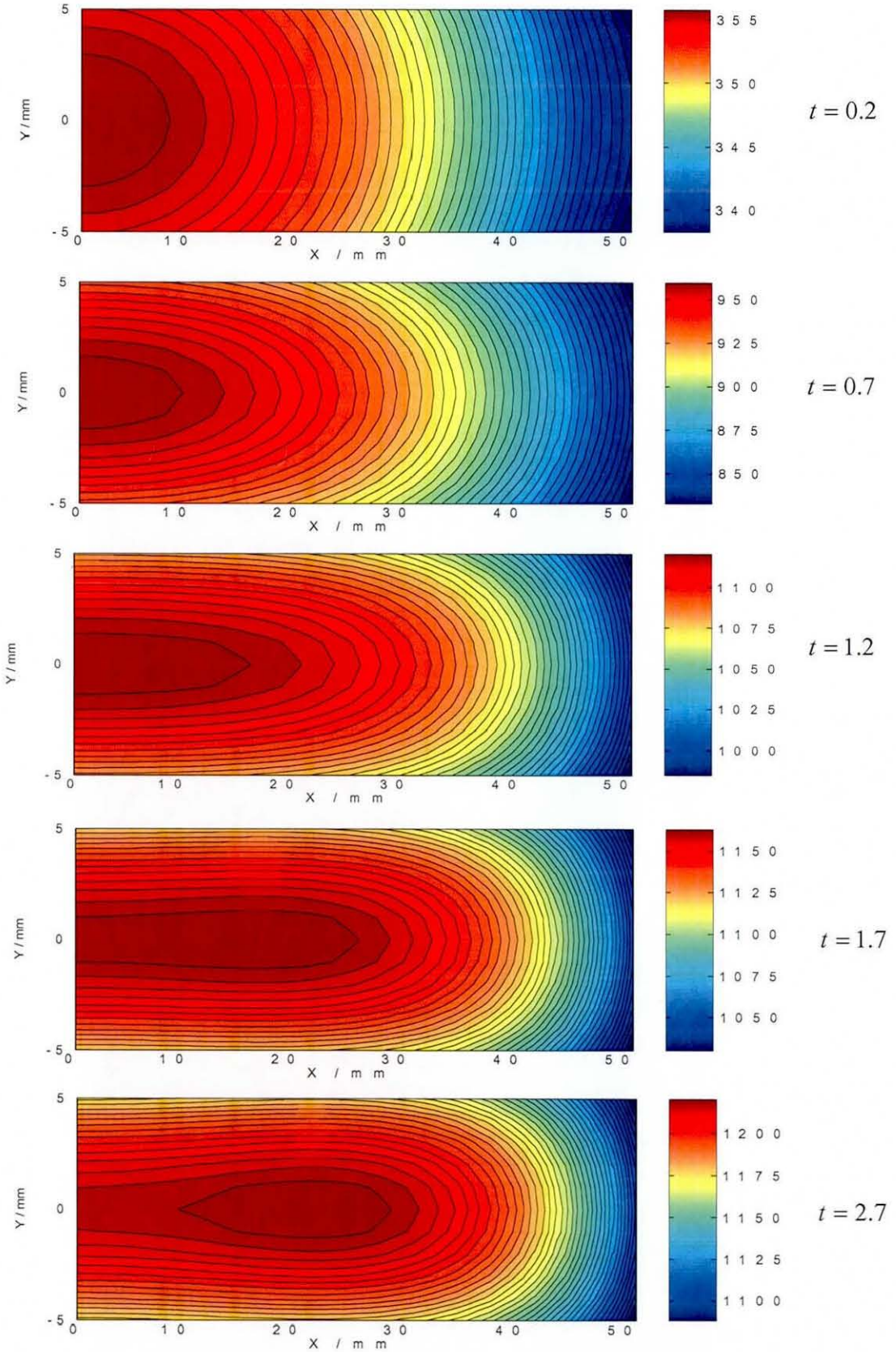
Figure 3.20: Evolution of the thermal distribution with time t obtained when a 50% dense SiC preform, with dimension $100 \times 10 \, \text{mm}$, is heated by microwaves with $P_{inc} = 1.2 \, \text{kW}$ and $h_e = 155 \, \text{Wm}^{-2}\text{K}^{-1}$.
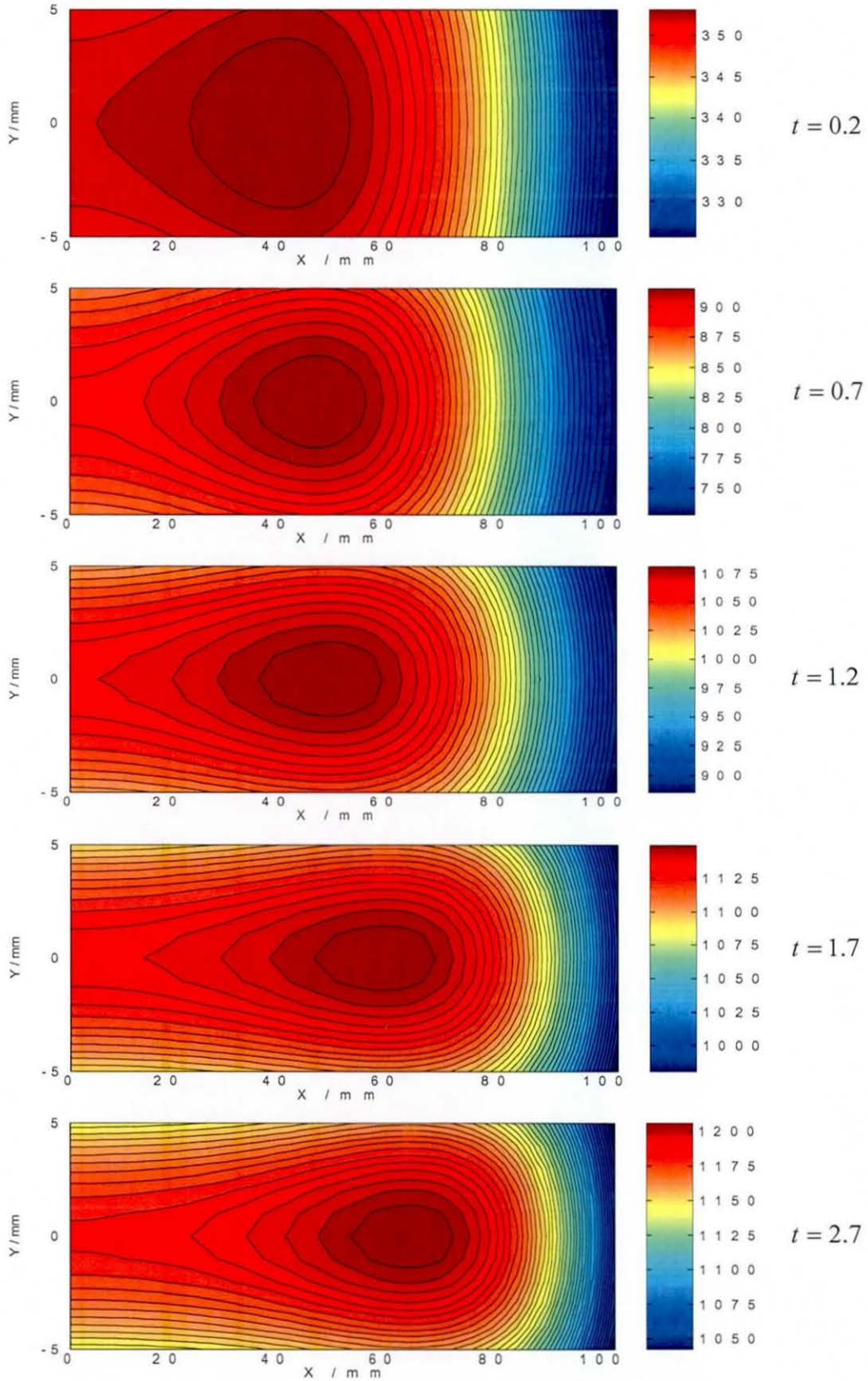
Figure 3.21: Evolution of the thermal distribution with time t obtained when a 50% dense SiC preform, with dimension 200×10 mm, is heated by microwaves with $P_{inc} = 1.2$ kW and $h_e = 155$ Wm^{-2}K^{-1}.

However, comparing the cases where the thickness of the sample is changed from 10 mm to 20 mm while keeping its radius fixed at 100 mm, a considerable drop in the thermal gradient is observed using the same incident power. Also from figure 3.23, which represents the evolution of the thermal distributions with time during the heating of the $200 \times 20\,\text{mm}$ sample, it is seen that the temperature level is low compared to figure 3.22. These changes can be explained by the fact that larger amount of material is heated when the $200 \times 20\,\text{mm}$ sample is considered and this requires higher incident microwave power to reach the same temperature level. It is also seen that the sample is heated initially at its centre before the hot zone is shifted towards the surface. Possibly, this could be due to the fact that with increase in the thickness of the sample, more heat is generated inside the sample while less amount of heat is lost at the surfaces.
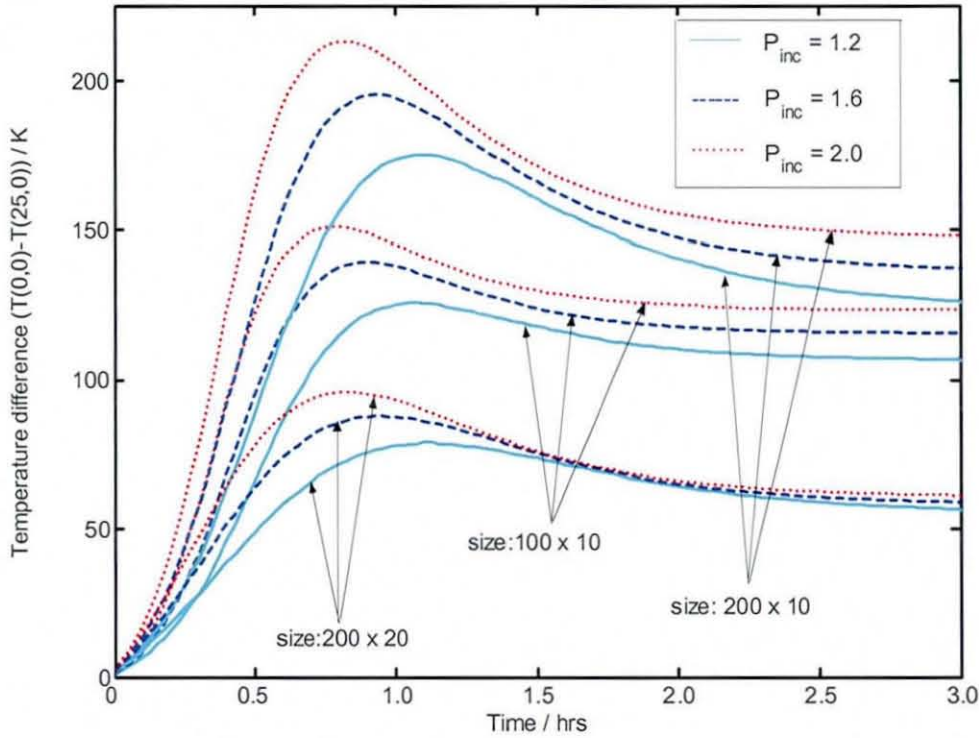
Figure 3.22: Evolution of thermal differences between the temperatures at the centre T(0,0) and the surface T(25,0) of the preform, having different dimensions and under different incident microwave power levels, P_{inc}.

Figure 3.24 shows the evolution of the temperature difference, $T(0,0)$-$T(25,0)$, obtained when $200 \times 10\,\text{mm}$ samples with different porosity levels were heated using an incident power of 1.6 kW. It is observed that the temperature gradient increased with

$P_{inc} = 1.2\,\text{kW}$ and $h_e = 155\ \text{Wm}^{-2}\text{K}^{-1}$.
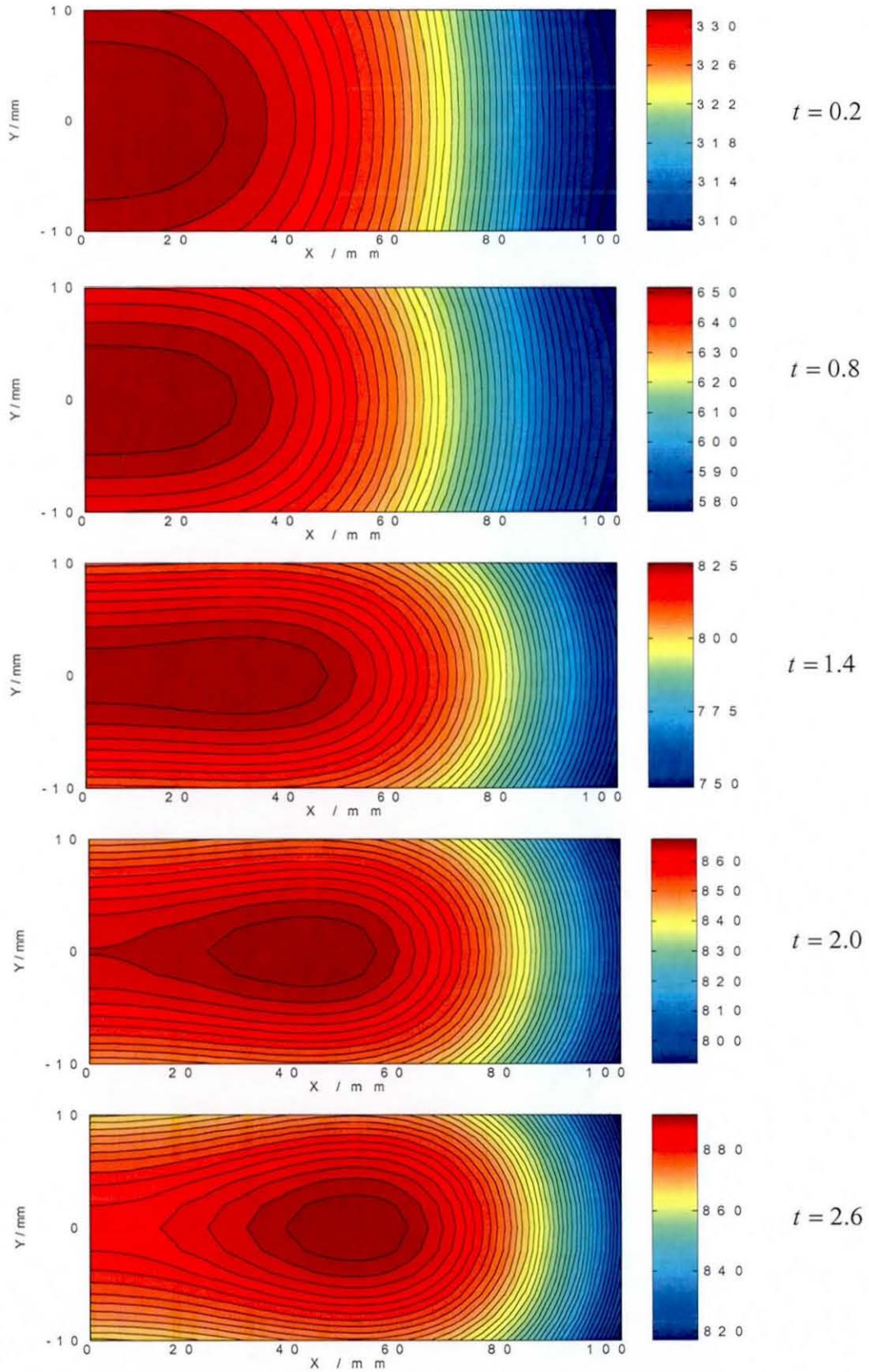
Figure 3.23: Evolution of the thermal distribution with time t obtained when a 50% dense SiC preform, with dimension $200 \times 20\,\text{mm}$, is heated by microwaves with $P_{inc} = 1.2\,\text{kW}$ and $h_e = 155\ \text{Wm}^{-2}\text{K}^{-1}$.

104
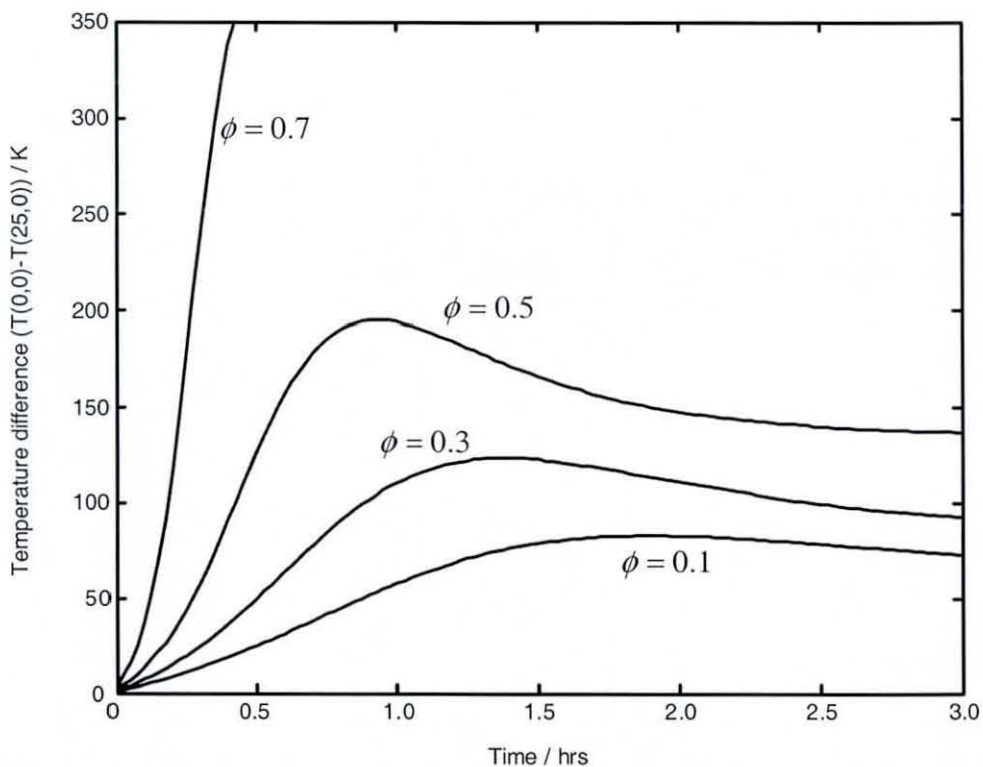
Figure 3.24: Evolution of the thermal difference with time between the temperatures at the centre $T(0,0)$ and the surface $T(25,0)$ for different internal porosity of the preform. The incident power and the heat transfer coefficient were kept fixed at 1.6 kW and 155 $Wm^{-2}K^{-1}$ respectively.

increase in the porosity level. Similar observations were made from figure 3.18, however, in this case higher thermal differences are noted. The latter increased due to the fact that less material was heated as the porosity increased, thus requiring less amount of power to reach the required temperature. In the case when the porosity level was 70%, it was seen again that the temperature underwent thermal runaway during the early stage of the heating process. A good control on the incident power is thus necessary during the heating stage of the ME-FCVI process. It is noted here that the cooling effect which occurred due to the flow of gaseous precursor has not been considered during this analysis; only the effect of the external cooling at the boundary has been investigated. An order of magnitude analysis could be performed to determine the significance of the cooling effect due to the forced flow.

3.4.2 Forced flow chemical vapour infiltration under isothermal conditions

Experimental and theoretical studies of conventional CVI have shown that densification depends on several parameters [47-52]. In summary, it was found that densification was hampered by diffusion limitations even in the case of slower reaction kinetics. Applying thermal differences aligned along the axis of the preform improved overall densification but did not improve the uniformity of the product, and alone it was not sufficient to overcome the diffusion limitations. Also, the processing times were very long, 2 to 3 months. On the other hand, whilst the studies of Forced Flow Chemical Vapour Infiltration have lead to more uniform densification of porous ceramic preforms, due to reduced diffusion limitations [65-72], densification was limited by early termination of the process due to excessive pressure differences being created across the preforms.

The use of inverse thermal differences combined with pressure differences across the preforms have quite satisfactorily overcome diffusion limitations and provided increased control over product quality. However, it is necessary to have proper combinations of these gradients to ensure uniform densification. Thus it is important to study the effects of the varying parameters along with different inlet pressures and flow rates under isothermal conditions on the overall densification, as well as product quality in terms of its uniformity. The case where the pressure gradient is kept fixed is considered first. The case where the flow rate is maintained constant allowing the inlet pressure to vary is investigated in the next sub-section.

3.4.2.1 Constant pressure gradient analysis

During this first analysis, the inlet and outlet pressures of the gaseous precursor were kept fixed at 10 kPa and 1 kPa respectively. The temperature of the preform was maintained at 1250 K and the initial concentration of MTS was taken as 0.005 molm^{-3}. The length of each unit cell and radius of the fibre bundles were considered as approximately 500 μm and 80 μm respectively so that a total of 50% porosity was initially maintained. The diameter and thickness of the sample were taken to be 50 mm and 10 mm respectively. The rest of the operating conditions and parameter values for the process are those given in table 3.2.

As the reaction started, SiC began depositing on the fibre bundles surfaces in each unit cell, which eventually resulted in a decrease in the porosity of the unit cells. The deposition rate can be examined based upon the Arrhenius equation (3.24j), where the activation energy E_a is assumed to be constant throughout the process. Figure 3.25 shows the evolution of the concentration profiles of MTS across the sample during the early stages of the process. It was observed that the concentration remained uniform along the x-axis within the sample; however, a slight increase in the concentration gradient across the thickness of the preform was also observed. Thus, the reaction rate being directly proportional to the concentration of MTS only under isothermal condition caused faster deposition to occur at the inlet rather than inside the sample. This was observed from figure 3.26, which represents the evolution of the porosity profile across the sample for isothermal forced-flow CVI.
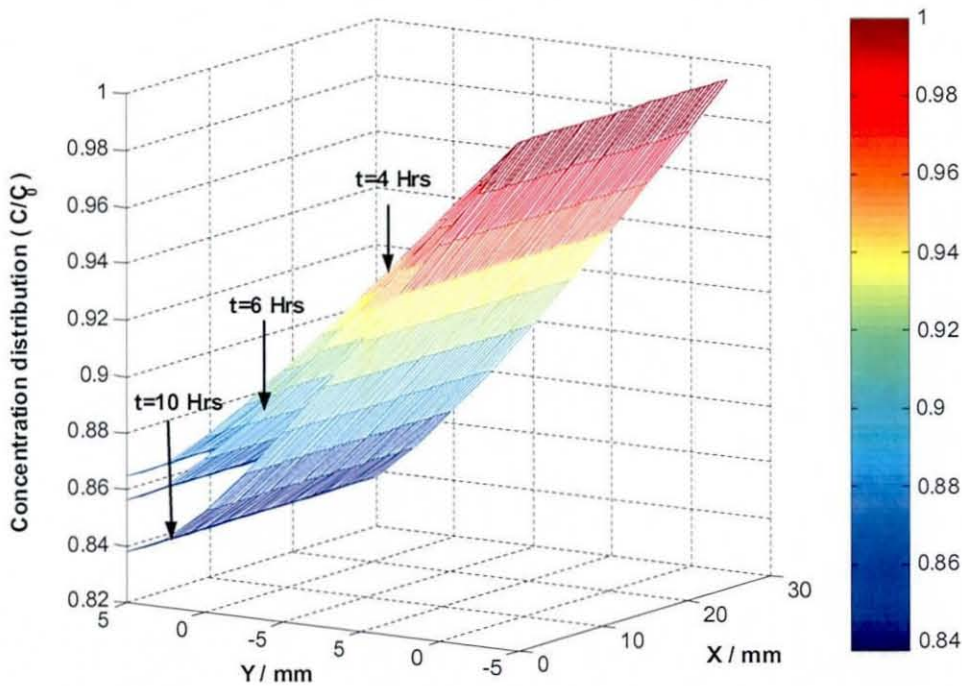
Figure 3.25: Showing the evolution of the concentration distribution profile during the early stage of the process. The inlet pressure applied was 10 kPa. Notice that the concentration gradient increases with time. The initial concentration C_0 was taken to be 0.005 molm^{-3}.

The uniformity of the concentration along the x-axis caused the porosity to be uniform along the same direction. However, the higher reaction rate at the inlet allowed the porosity gradient along the y-axis to increase with time. This resulted in the creation of inaccessible pores, which were not available for mass transport and reaction at the inlet.

Further, because of the matrix deposition, the void size diminished; therefore, since the pressure gradient was kept constant during the process, the flow rate of the gaseous precursors was reduced because of the reduction in the permeability of the preform.
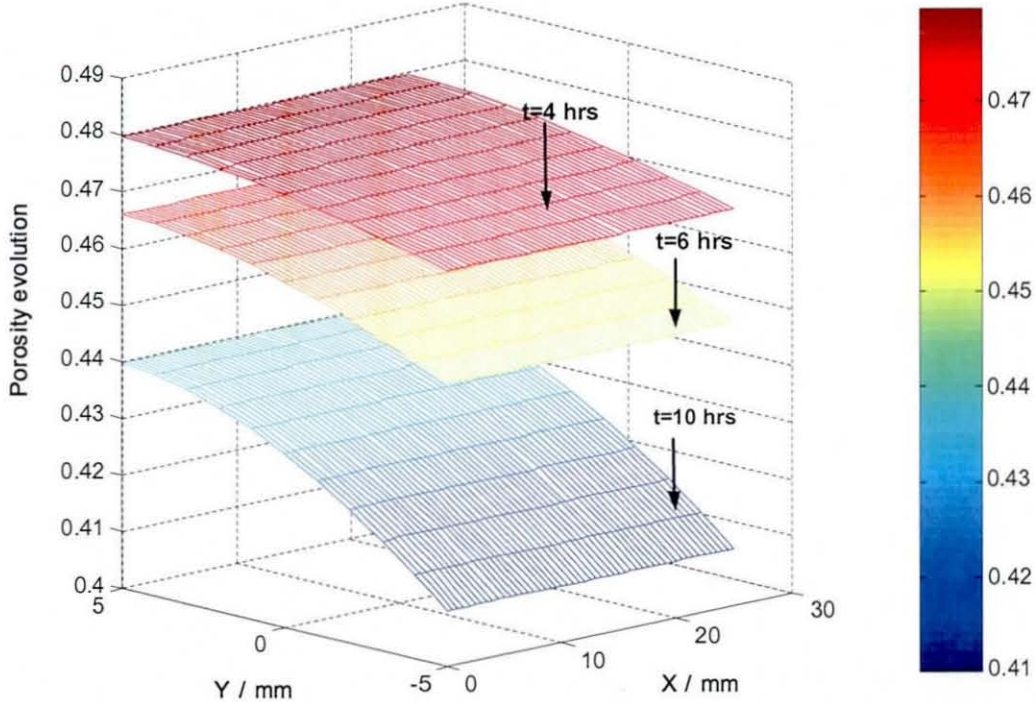
Figure 3.26: Showing the evolution of the porosity profile when $P1=10$ kPa. It is observed here that that the porosity decreased much faster at the inlet boundary than inside the preform. The reason for this is due to the decrease in concentration further inside as observed from figure 3.25.

The pressure distributions obtained during the early stage of the process, for three different inlet pressures, are shown in figure 3.27. It is observed that a constant pressure gradient was obtained instead for each inlet condition across the sample. However, during the process the fact that the porosity of the medium decreased with time, which implied the permeability of the medium decreased, increased the resistance to flow of the gaseous precursor. This resulted in a non-uniform increase in the pressure gradient across the preform. The condition when the value of the pressure gradient was more than half of its initial value during the early stage of the process was chosen as our stopping criterion for the simulation. Figure 3.28 shows the evolution for the pressure profile at the end of the process for the case when the inlet pressure was taken to be 15 kPa. It was seen that there was a sharp increase in pressure gradient at the inlet
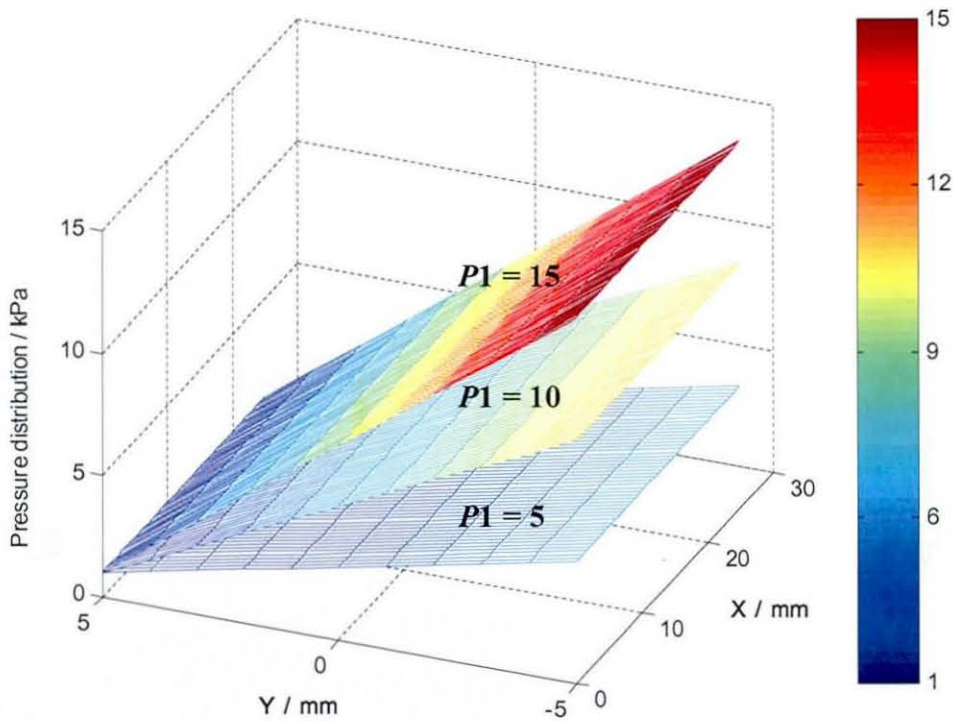
Figure 3.27: Showing the pressure profile for different inlet pressure $P1 = 5, 10, 15\,\text{kPa}$. The outlet pressure was kept fixed during the whole process at 1 kPa. A constant pressure gradient was observed in each case.
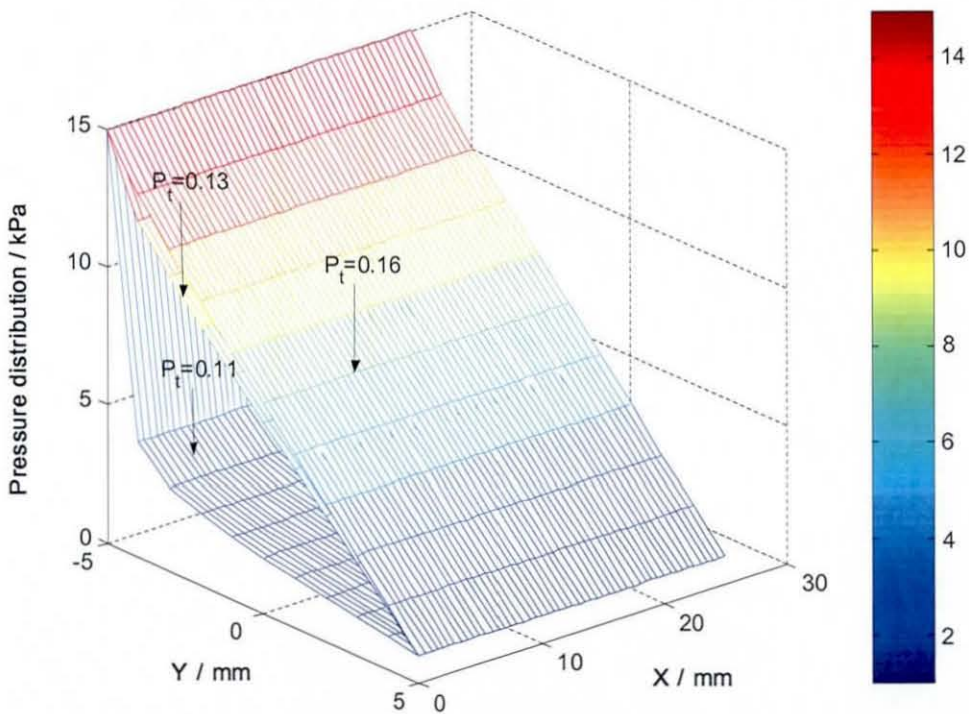
Figure 3.28: Showing the pressure profile at the end of the process for different total porosity of the medium. The inlet pressure was taken to be 15 kPa and P_t represents the total final porosity remained within the sample.

of the preform, which relaxed further inside the latter. This was due to the sharp resistance to flow at the inlet boundary, which tended to close much faster.

3.4.2.1.1 Effect of inlet concentration and pressure on the concentration, pressure, infiltration profiles and total processing times

The concentration evolution at the centre of the sample for three different inlet pressures is shown in Figure 3.29. The figure also shows the concentration profile obtained in the case of diffusion process only. It can be seen that there was a sharp decrease in concentration at the beginning of the process. This was due to the sudden depletion of the MTS when the reaction started. However, the profiles relaxed with time and decreased gradually. This sharp decrease[**] was bigger in the case of the diffusion process, where a slight increase was also seen just after the decrease, where as in the forced flow situations, the depletion of the concentration was expected to be overcome in a small time scale, thus stabilizing the profile quicker. It was also observed that the concentration was much greater when higher inlet pressure is applied compared to the diffusion process only.
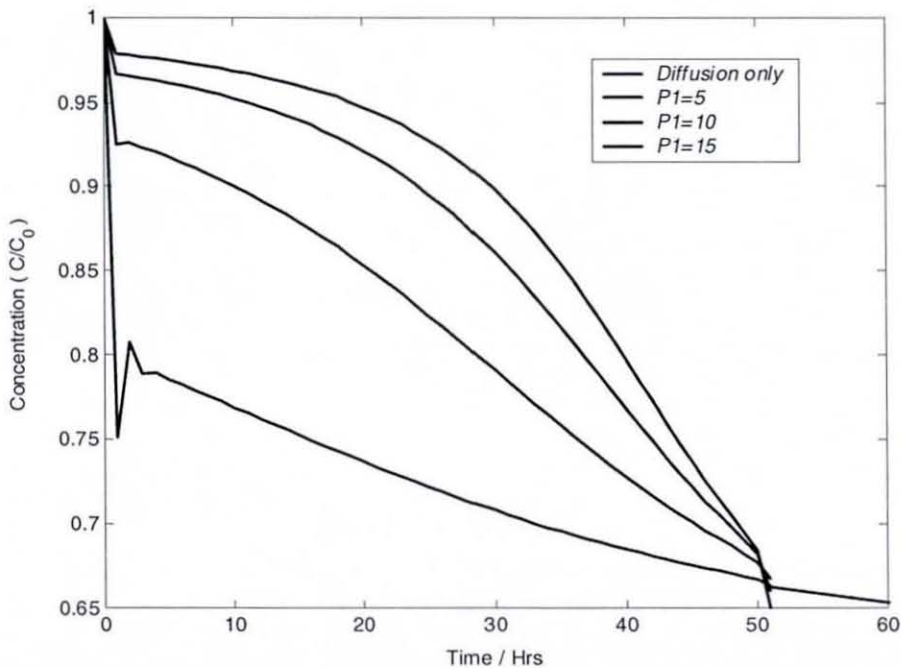
Figure 3.29: Represents the evolution of the concentration profile with time in the middle of the sample for different inlet pressures and the diffusion-only process only. A sharp decrease in concentration may be observed at the beginning of the process.

[**] It is noted here that this observation is thought to be a real effect and could possibly be related to the inverse response phenomena occurring in catalytic reactions, although the possibility that it is a numerical artefact has not been rules out.

In Figure 3.30, the pressure profiles in the middle of the sample at different inlet pressure are shown. It is seen that for higher-pressure inlet, the pressure gradient was greater and also for the case when $P1 = 15 \, kPa$, the pressure decreased even faster inside the sample compared to the case when $P1 = 10 \, kPa$. Thus it can be stated that even though the resistances to flow increased with increase inlet pressure, at the same time the pressure gradient across the sample decreased sharply.
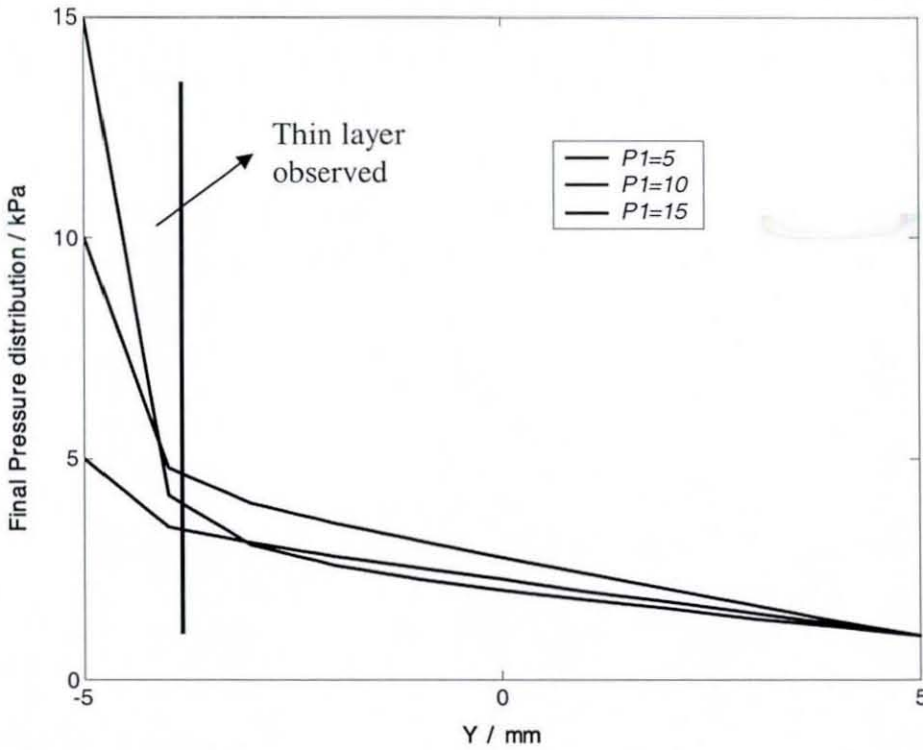
Figure 3.30: Showing the final pressure profile for different inlet pressures, $P1$, across the sample. A thin layer was observed in all cases.

The final porosity profiles for different $P1$ values are shown in Figure 3.31. It can be observed that in the case of the diffusion-only process, where the inlet porosity was zero after the process, the porosity gradient was much greater. This means that the trapped porosity inside the sample after the pore closure at the inlet was very significant, thus resulting in a less densified sample. On the other hand, by applying forced flow conditions, this porosity gradient was significantly reduced, as seen from Figure 3.31. It may be observed that for larger inlet pressure this porosity gradient decreased further, resulting in a more uniformly densified sample. However, this decrease slowed down with further increase in $P1$. The final porosity at the inlet of the preform reached a value approximately 0.05 for each different inlet pressure, P1. This means that the remaining porosity inside the sample is still accessible even though the

reaction is stopped due to the increase in flow resistance. At this stage the inlet pressure could be reduced to allow the diffusion process to become significant, which could further densified the preform until the inlet porosity is closed. However, this might be a time consuming process since the time taken to infiltrate the preform via diffusion process only is much longer compared to forced convection, as seen in Figure 3.32, and at the same time the final densified matrix is expected to contain a certain amount of trapped porosity.

Thus by applying an inverse thermal gradient to the sample via microwave heating this disadvantage could be overcome, since now the reaction rate would depend nonlinearly on the temperature. The temperature of the sample being higher in the middle, as expected, would cause the reaction to be faster inside, thus causing an inside out densification. However, at the same time, the concentration of the precursor in these regions is expected to decrease significantly and this could result in a greater reaction rate at the inlet boundary since the concentration is much larger there. Thus optimal operating conditions for temperature and inlet pressure need to be obtained to optimize the densified matrix. From the set of equations that are solved here under isothermal
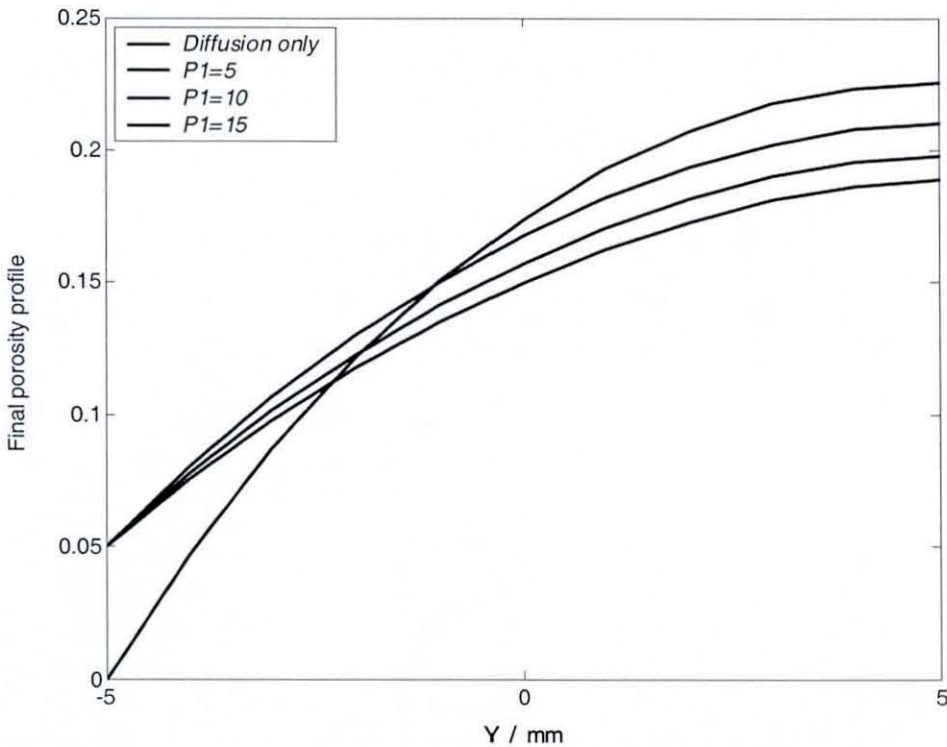
Figure 3.31: Showing the final porosity profile for different inlet pressure P1 and for the diffusion-only process.

conditions, the effect of the inlet MTS concentration was found to be on the total processing times; due to the forced flow conditions, variations in the inlet concentration did not significantly affect the final porosity profiles.

It is observed in Figure 3.32 that the total porosity of the preform decreased linearly with increase in inlet pressure. However, the processing time was almost equal in each case for different inlet pressure. It can also been seen that the processing time for the diffusion process alone was much larger compared to the forced convection processes.
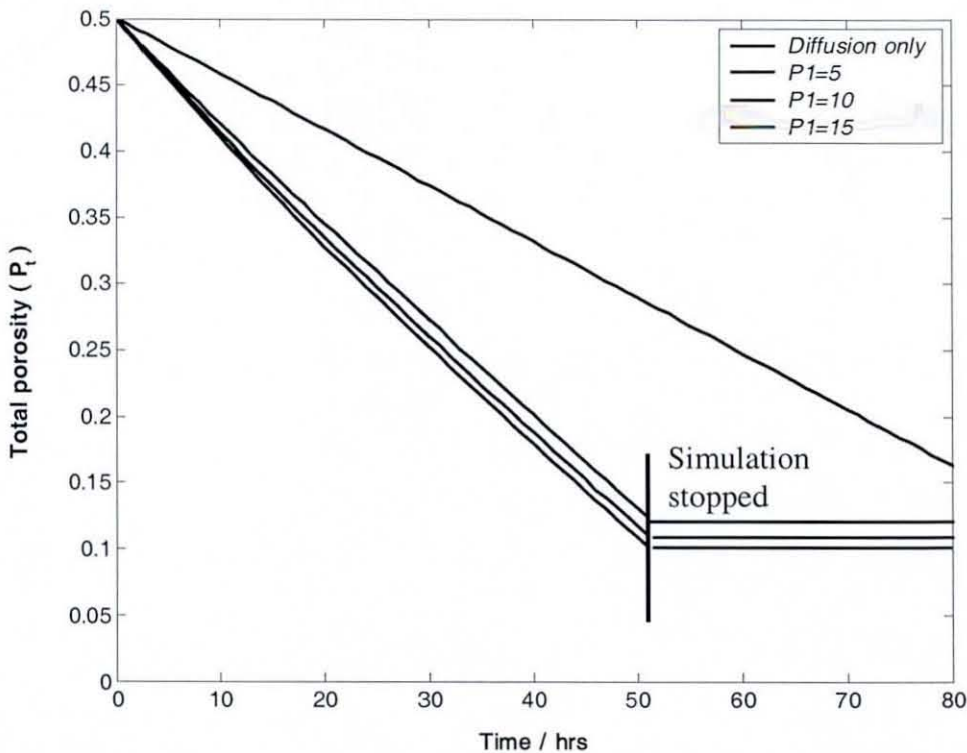
Figure 3.32: Showing evolution of the total porosity of the medium with time for different inlet pressure, $P1$. The simulations was stopped when the pressure gradient within the preform was more than half of its initial value.

3.4.2.2 Constant flow rate analysis

In this analysis, the following results were obtained for the case when the outlet pressure was initially maintained at 1 kPa and the inlet pressure variation was calculated independently so that a constant volume flow rate was maintained at the inlet of the preform. It is recalled here that v is the non-dimensional variable describing the Darcy's velocity of the flow of the precursor and is dependent on the volumetric flow rate. The flow rate is measured in multiples of 10 ml min^{-1} of the gaseous precursor (H$_2$

113

and MTS) at STP. For example, $v = 2$ corresponds to approximately 250 ml min^{-1}. Other operating conditions considered in the previous analysis were maintained as well. Similar observations were made during the early stages of the infiltration process compared to the previous analysis. While deposition continued in the accessible areas within the preform, the resistance to flow of the gaseous precursor kept increasing until the pressure gradient required to maintain the flow of the precursor became very large and exceeded a feasible operating value; densification was stopped at this stage. Compared to the previous analysis, where the pressure gradient was kept constant, in this case the pressure gradient increased during the infiltration process. The value of the inlet pressure, 60 kPa, was considered as the feasible operating value and the stopping criteria for the simulations. Figure 3.33 shows the final pressure profiles obtained for three different inlet flow rates. It is observed that the pressure gradient across the sample became more uniform with increase in the flow rate (increase in v), which implied that greater uniformity in the densification of the preform was achieved. This was due to the fact that with increase in mass flux at the inlet of the preform, further reduced the MTS concentration gradient inside the preform. This in turn allowed a more uniform deposition of SiC inside the preform, which then resulted in an almost uniform pressure gradient across the sample.
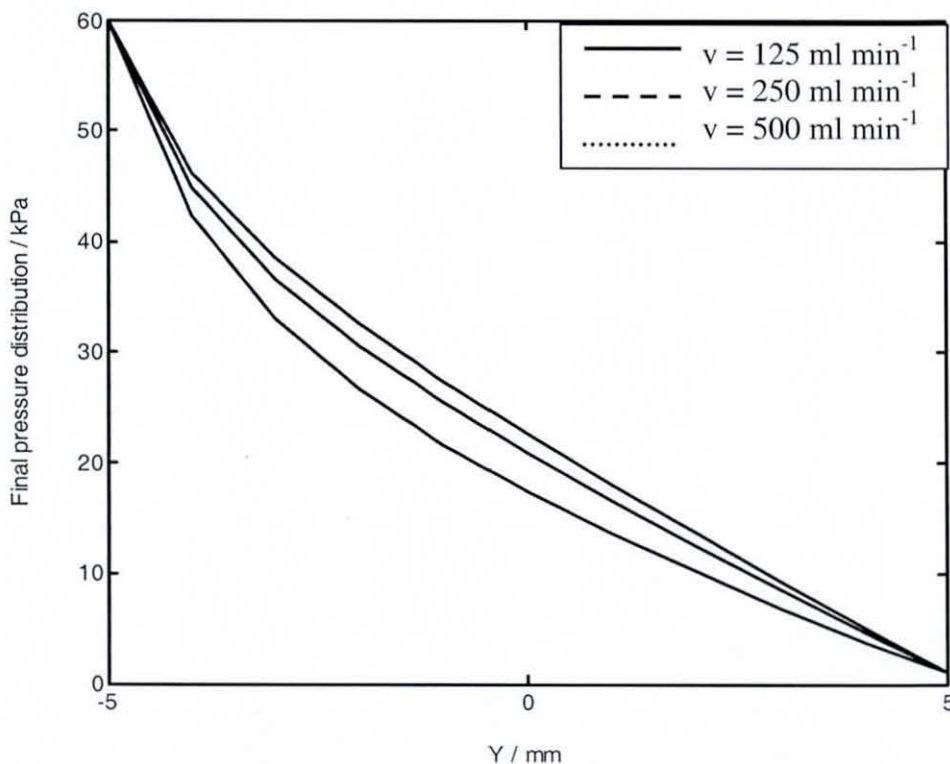
Figure 3.33: Showing the final pressure profile obtained for different inlet flow rate.

The final porosity profile across the sample is shown in figure 3.34. It is observed that a more uniformly infiltrated preform was indeed obtained by increasing the flow rate. However, the change in the final profiles, suggest that an optimum value for v could exist beyond which the profiles would minimally changed. Further, it is observed to this point that the inlet porosity is greater at the end of the process with increase in v. Further, comparing with figure 3.31, it is deduced that the sample is infiltrated more uniformly by keeping a constant flow rate of the precursor. The reason behind this is possibly the decrease in concentration gradient across the sample as seen in figure 3.35, which shows the evolution of the concentration profile inside the sample with time. The sharp decrease in the concentration at the beginning of the reaction was observed here too, which stabilized with time. Also, further increase in the flow rate resulted in a more uniform concentration across the sample.

In general, in spite of the higher and more uniform concentration of reactants throughout the preform, diffusion limitations were not fully overcome. Yet, applying forced-flow significantly reduced the processing times compared to conventional CVI. It was also observed that the process was stopped before the pores at the boundary became inaccessible. This was because even though the pores at the inlet boundary were accessible for flow of the precursor, the resistance to flow was so large that the back-pressure in the system reached the operating limit and densification was stopped. At this stage, further densification of the preform could be achieved by decreasing the flow rate, allowing the diffusion process to become more significant. However, in this case, the concentration gradient was expected to increase across the sample, which would allow faster densification at the boundaries. As already stated in the previous section, this would result in trapped porosity inside the sample due to the complete densification of the preform surfaces.

Linear evolution of the total porosity of the preform for different flow rates may be observed from figure 3.36. It is seen here that the processing time reduced with increase in flow rates. However, the final densification matrix was not significantly changed. This means that the optimal flow rate values must be properly determined to
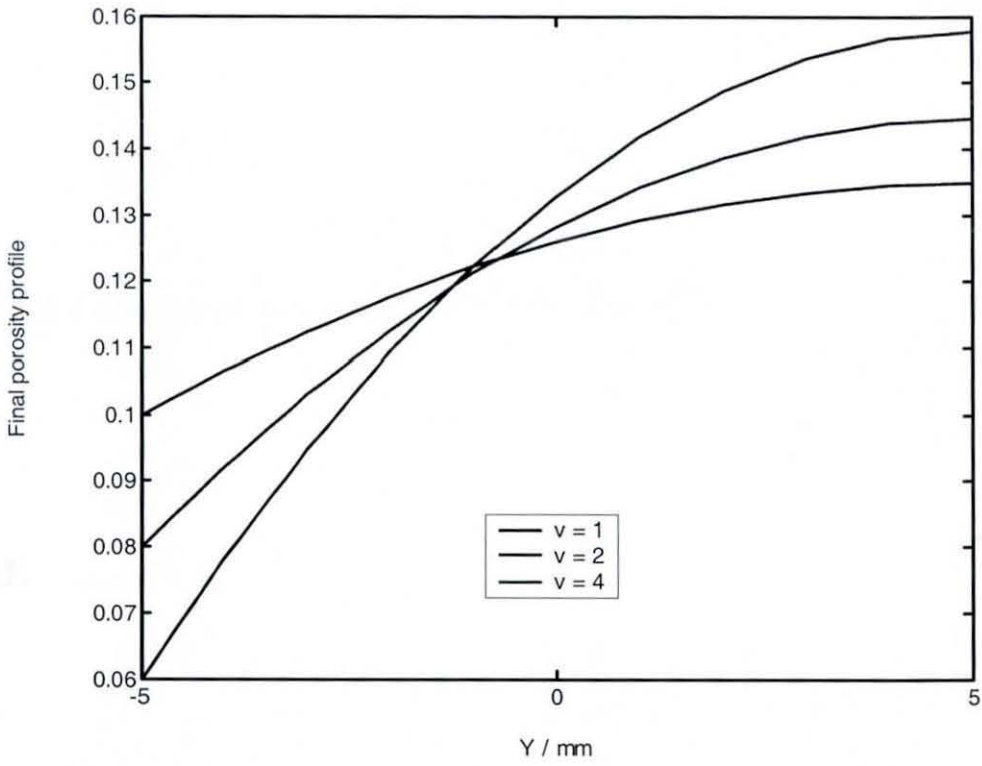
Figure 3.34: Showing the final porosity profile obtained for different inlet flow rate.
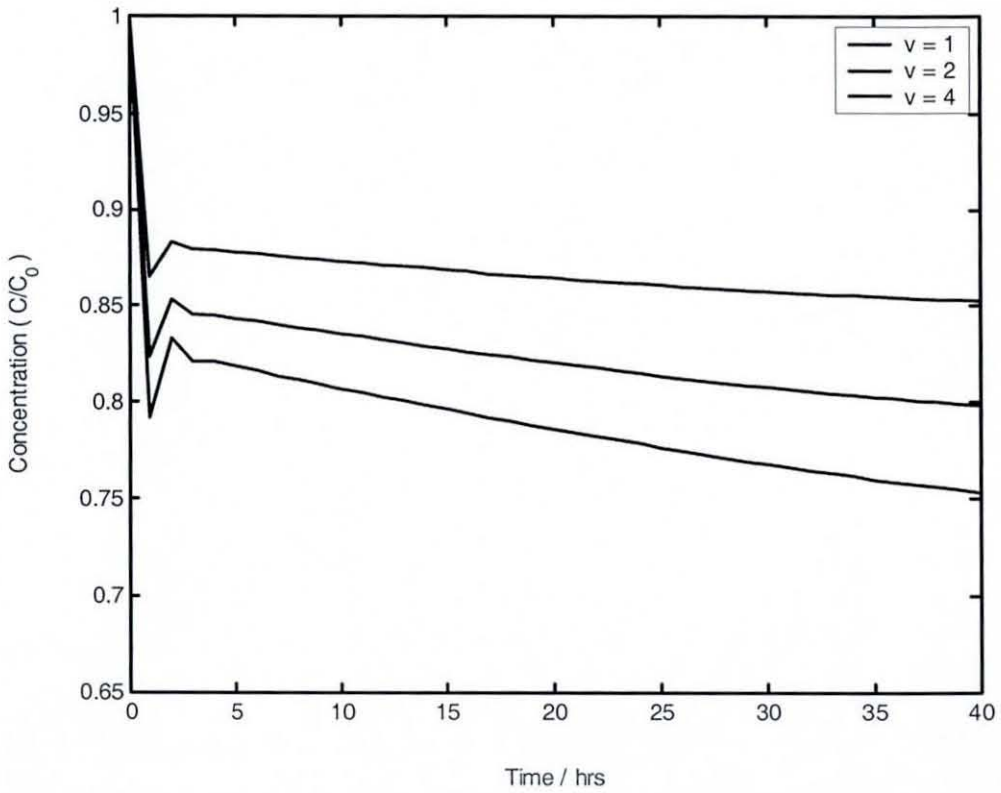
Figure 3.35: representing the evolution of the concentration profiles with time for different v.
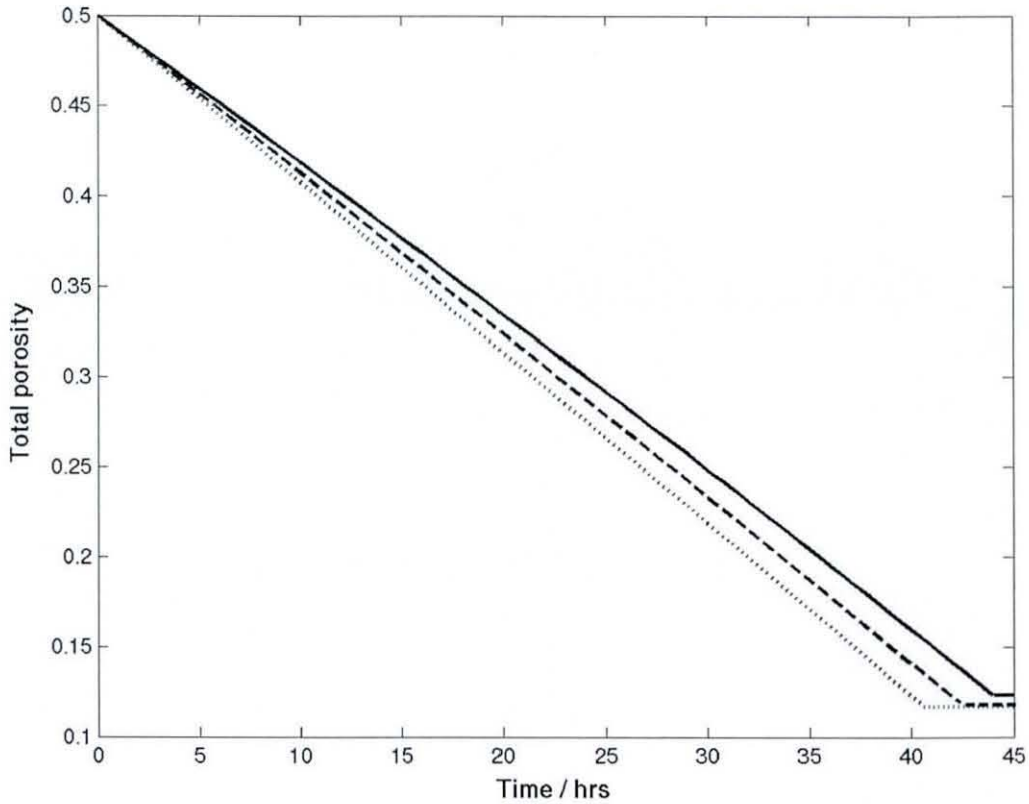
Figure 3.36: Showing the evolution of total porosity of the preform with time.

allow more uniform densification of the sample and whilst reducing the pressure gradient at the same time across the sample. At the same time, it can be concluded that the flow rates can always be varied to achieve the amount of preform densification that is needed.

Since only isothermal conditions were considered in this analysis, the rate of the reaction was directly proportional to the concentration of the precursor. The Arrhenius nonlinear dependence on temperature, as seen from equation (3.36d), was kept constant in the investigation. In the following section, the inverse temperature profiles generated by microwave heating were applied to the constant flow rate analysis to study the combined effects of forced flow and thermal gradient on the infiltration profiles and processing times.

3.4.3 Microwave enhanced forced-flow CVI

It is recalled here that for a good understanding of the Microwave Enhanced Forced-flow Chemical Vapour Infiltration (ME-FCVI) process, it is necessary to study the effects of the following processing variables on the infiltration process and the processing times:

- Temperature level and thermal gradient in the preform
- Total gas flow rate
- Pressure gradient across the preform
- Gaseous precursor concentration
- Dimensions of the preform
- Porosity of the preform

In this section the results obtained from the ME-FCVI model, which is the combination of the EM-model and FCVI-model, are presented and discussed. The inverse temperature profiles were first generated from the microwave heating stage and they were applied to study their effects on the densification pattern and the process variables during the forced flow chemical vapour infiltration process. It is noted here that the evolution of the temperature distribution during microwave heating would in practice be indeed affected by the forced flow of the gaseous precursor during ME-FCVI, providing convective losses inside the preform. However, equation (3.24), which was used to describe thermal diffusion within the preform, did not incorporate a convection term. Thus its consequences on the thermal distribution were ignored. However, convective losses at the boundaries of the preform, controlled by the heat transfer coefficient h_e, were included in the thermal boundary conditions, see equation (3.24). Further, the decreasing porosity of the preform during ME-FCVI also affected the temperature field as presented earlier (see figure 3.18 and 3.24), but in the analysis, the microstructure of the preform was not considered during electromagnetic heating to avoid the resultant complications. By taking into account the above facts, the microwave heating stage and the infiltration stage were allowed to be decoupled during the ME-FCVI process.

Figure 3.37 shows the evolution with time of the densification of a 50×10 mm preform. In this analysis, a 50% dense SiC sample was heated by considering $P_{inc} = 1.6$ kW and $h_e = 155$ Wm^{-2}K^{-1}. A constant mass flux of the gaseous precursors

at the inlet was maintained during the infiltration stage by fixing the non-dimensional velocity $v = 2$ (corresponding to 250 ml min^{-1}), the outlet pressure $P2$ at 1 kPa and the initial MTS concentration C_0 at 0.005 mol m^{-3}. During the early stage of the infiltration process, it was observed that by applying the inverse temperature profile, densification occurred mostly at the centre of the sample. This was due to the fact that the higher temperature at the centre allowed the reaction rate to be faster, which in turn resulted in higher deposition. The Arrhenius nonlinear dependence of the rate of reaction on temperature can be seen from expression 3.36d. However, as the infiltration process continued, the decrease in the porosity at the centre of the preform caused a corresponding decrease in the MTS concentration as shown in Figure 3.38. In addition, the MTS concentration being higher at the inlet also affected the reaction rate, allowing faster deposition to occur at the inlet during the latter stages of the process. This transition is seen from figure 3.37. The red zone represents the region where higher densification is achieved. It is seen that this red zone moves slowly from the centre towards the inlet of the preform during the process. Further, from figure 3.38, it is observed that the MTS concentration gradient increased across the sample, which caused the deposition to increase radially from the inlet of the preform, as shown by the black arrow in figure 3.37. One major factor that hindered this infiltration process however, was the non-linear increase of the back-pressure during the process.

It is recalled here that a constant mass flux was maintained at the inlet of the preform. This caused the pressure gradient across the thickness of the sample to increase during the infiltration process, figure 3.39. It may be observed that whilst deposition continued in the accessible areas within the porous preform, the resistance to flow of the gaseous precursor at the inlet increased until the pressure gradient required became very large and exceeded a feasible operating value. Densification was stopped at this stage. A value 60 kPa was considered as the maximum outlet pressure and hence the stopping criteria for the simulations.
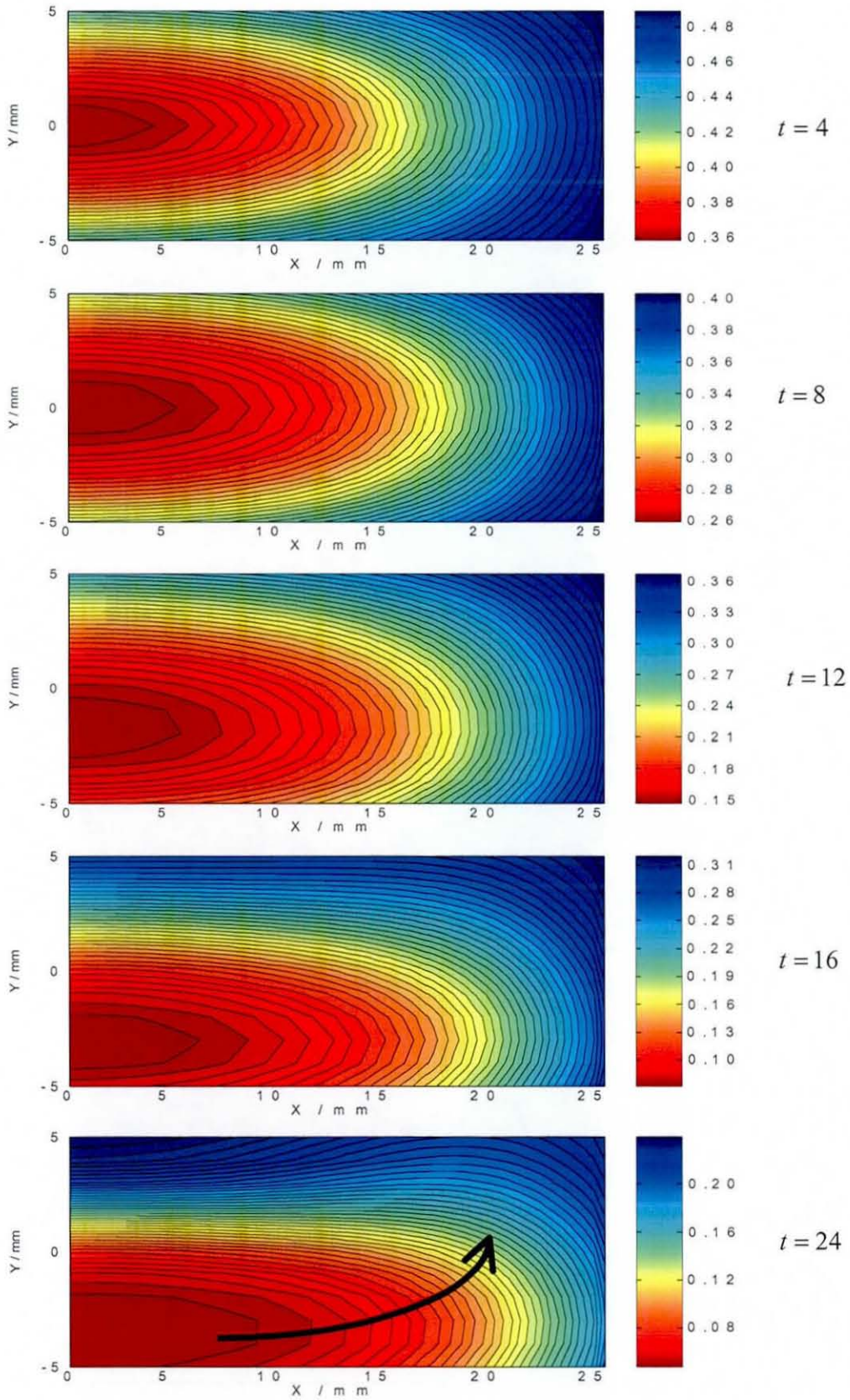
Figure 3.37: Evolution of the densification of a 50×10 mm preform under ME-FCVI. The colour bar reflects the porosity distribution at each time step.
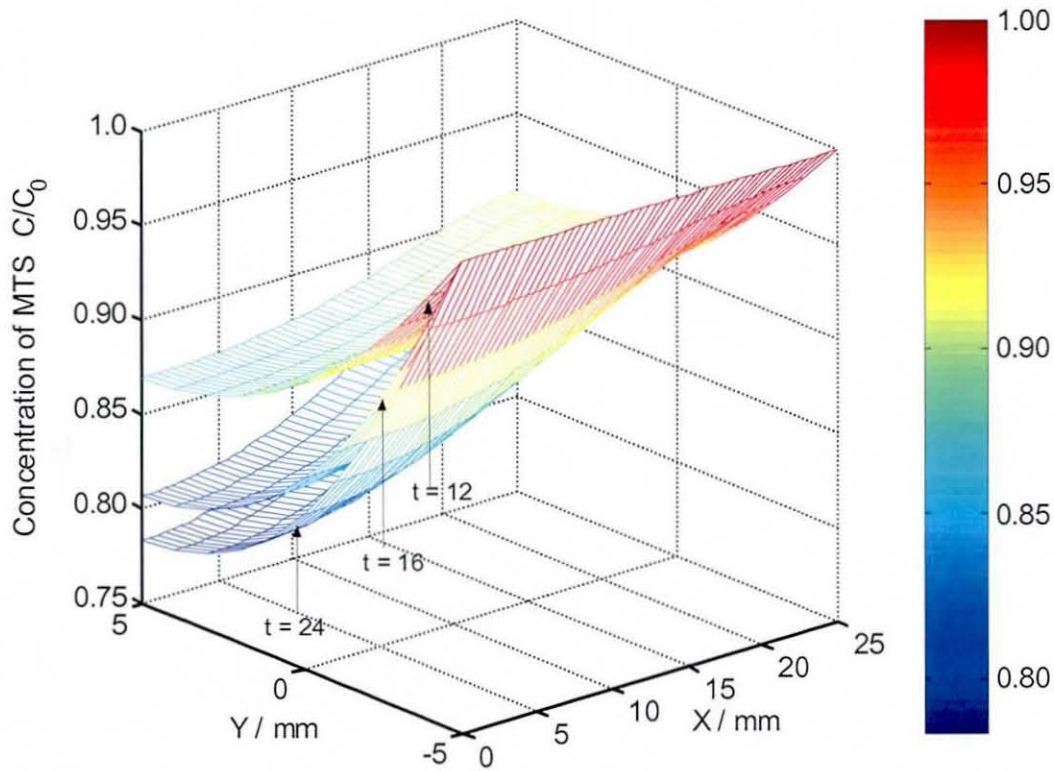
Figure 3.38: Evolution of the MTS relative concentration profile, C/C_0 with time during the densification of a 50×10 mm preform under ME-FCVI.

Figure 3.40 shows the final porosity profile obtained after the process has stopped. Even though the porosity at the inlet is greatly reduced, it is seen that significant porosity remained at the boundaries of the preform and partly inside the preform whilst the use of an inverse temperature profile indeed helped to achieve an inside out densification during the early stages of the process, the decrease in MTS concentration later caused most densification to occur at the inlet, which resulted in a steeper pressure gradient and eventually stopped the process. Variations in the porosity gradient across the sample were studied next by altering the various process variables.

Figure 3.39: Evolution of the pressure profiles with time during the infiltration process of a 50×10 mm preform under ME-FCVI. The colour bar reflects the pressure values in kPa.
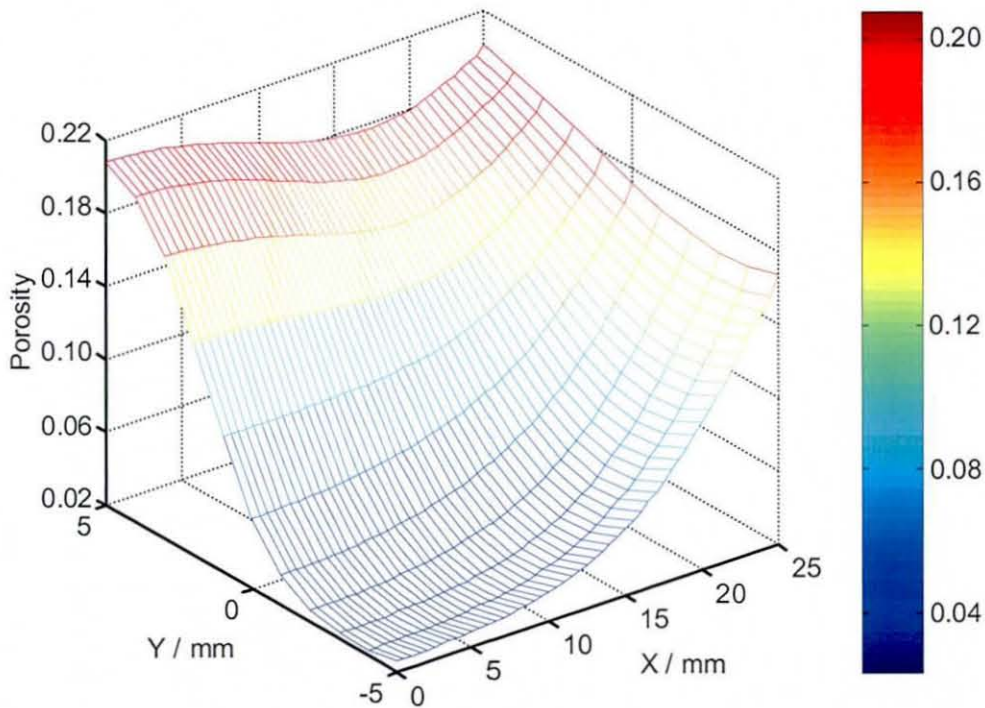
Figure 3.40: Final porosity profile obtained during the infiltration process of an 50×10 mm preform under ME-FCVI. The colour bar represents the porosity level.

3.4.3.1 Effect of applying higher temperature level and temperature gradient on the porosity profiles and processing times

From the results described in section 3.4.1 it was seen that the temperature of the preform could be changed, without affecting the thermal gradient, by modifying the heat transfer coefficient. Figure 3.41 shows the evolution of the total porosity profile when the highest temperature of the preform required for reaction to occur, T_h, was altered. The incident microwave power, P_{inc}, was kept fixed at 1.6 kW. It may be observed that by increasing the temperature, the processing time was greatly reduced, however the total porosity of the preform was hardly changed. Also, a slight increase in the porosity at the outlet of the preform was seen, see figure 3.42. This could be explained by the fact that the faster rate of reaction at higher temperatures caused faster densification at the preform centre. This eventually increased the concentration gradient across the sample, which allowed less densification at the preform outlet of the.
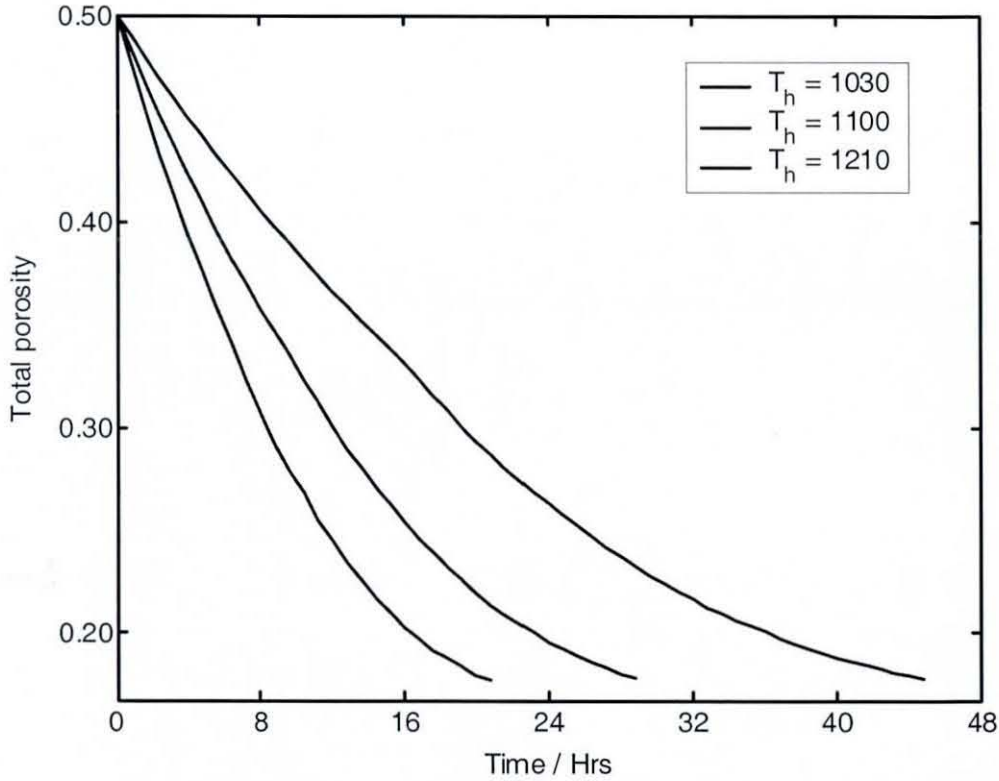
Figure 3.41: Evolution of the total porosity, at different temperatures, during the infiltration process. The preform was initially assumed 50% dense and heated with an incident microwave power of 1.6 kW. h_e was taken to be 155 $Wm^{-2}K^{-1}$. T_h represents the highest temperature of the preform in Kelvin.

The results described in section 3.4.1 also showed that thermal gradient across the sample could be changed by altering the incident microwave power. Figure 3.42 shows the final porosity profile obtained when the incident microwave power was altered. The heat transfer coefficient, h_e, which characterises the external cooling, was maintained at 135 $Wm^{-2}K^{-1}$. It may be observed that when a larger thermal gradient (i.e. higher incident power) is applied, larger porosity gradient is obtained within the preform. The much higher temperature at the centre again resulting in faster deposition compared to the infiltration occurring at the outlet. However, minimal change in the final remaining porosities were observed at the inlet. The overall remaining porosity was thus higher with increase in the incident power level. Thus a proper control of the temperature level and thermal gradient was required to achieve the desired densification of the preforms.
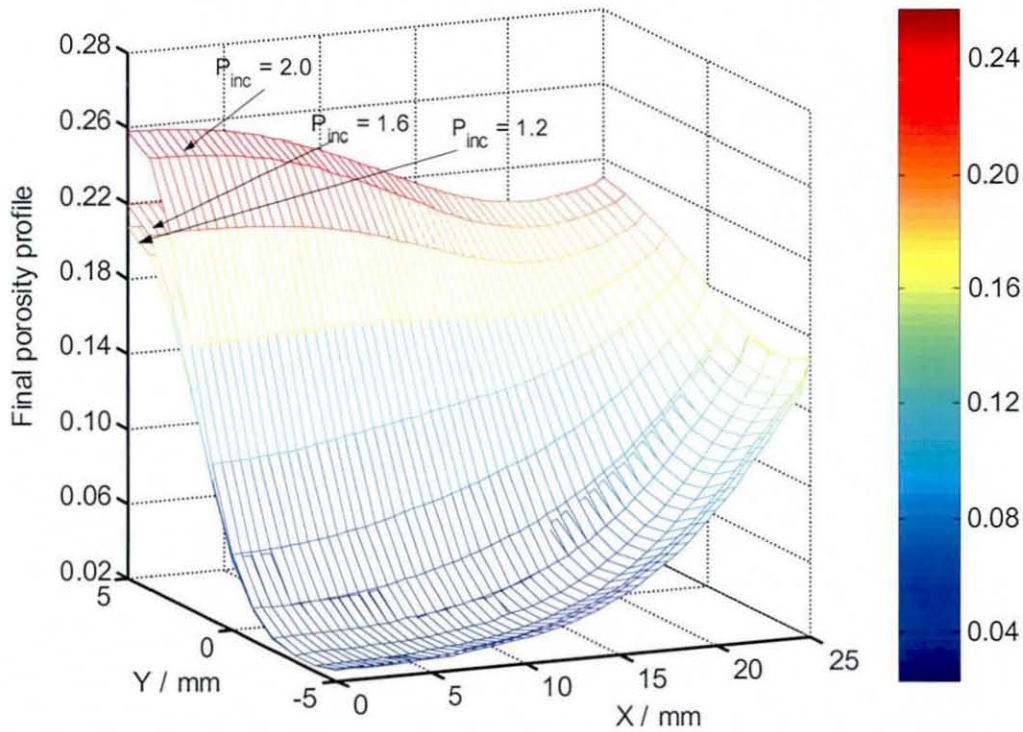
Figure 3.42: Final porosity profiles obtained by applying different incident microwave power, P_{inc} to infiltrate a 50% dense SiC preform.

3.4.3.2 Effect of applying larger flow rates on the final porosity profiles and infiltration times

As explained in section 3.4.2.2, an increase in the flow rate causes a decrease in the MTS concentration gradient inside the preform. When combined with an inverse temperature gradient the reaction rate inside the sample is expected to be higher, thus allowing higher deposition inside the sample. Figure 3.43 shows the final porosity profiles obtained along the y-axis, at the middle of the preform, when different inlet flow rates were applied. It may be observed that the porosities at the outlet decreased further with increase in flow rate, however densification at the inlet surface was reduced. Similar observations are made in figure 3.44, which shows the variation of the final porosity along the x-axis inside the sample. Here it may be is observed that the porosity at the boundaries was further decreased with increased in flow rate. In this analysis, an incident power of 1.6 kW was considered to generate the inverse temperature profile and the outlet pressure was initially maintained at 2 kPa. The two

125
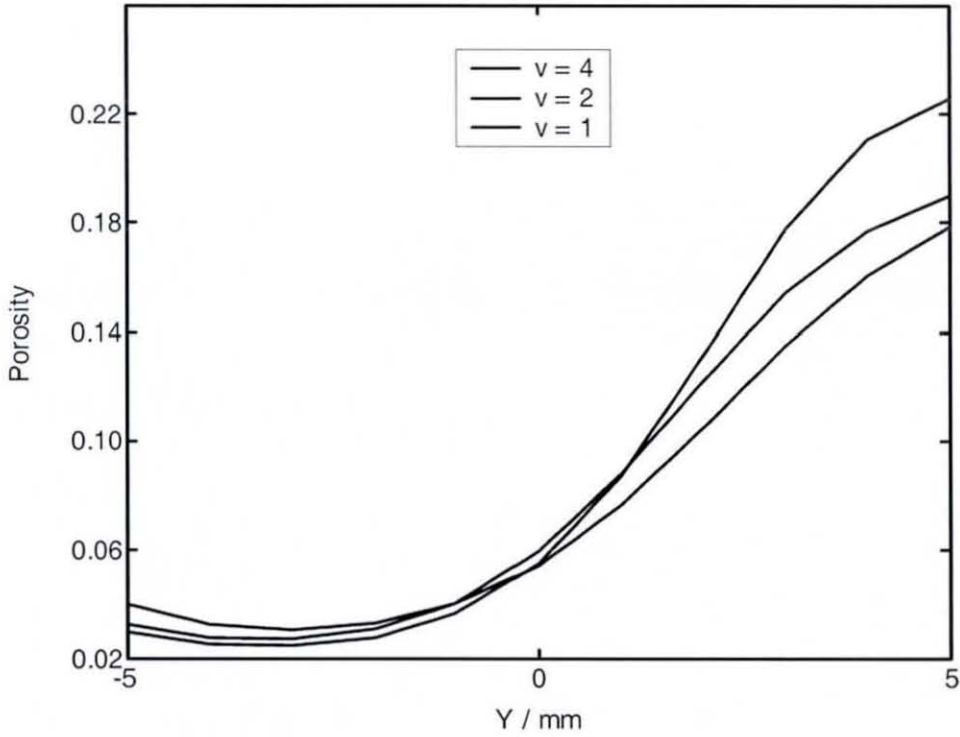
Figure 3.43: Variation of final porosity profile along the *y*-axis at the middle of the preform. *v* is the non-dimensional initial velocity of the flow of the reactants at the inlet.
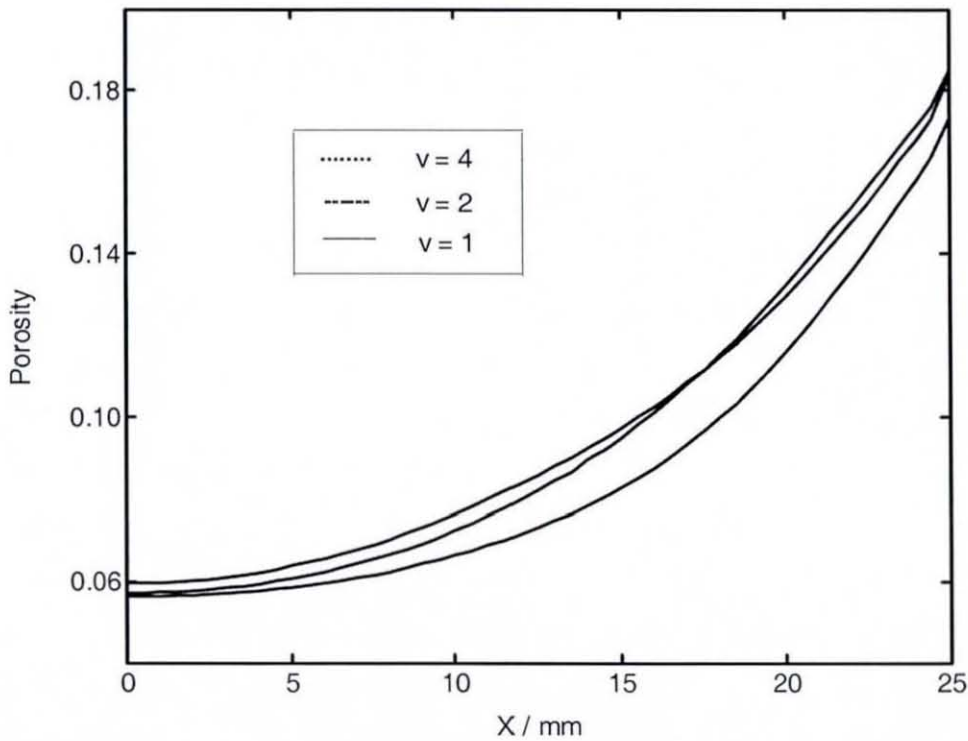
Figure 3.44: Variation of final porosity profiles obtained along the *x*-axis at the middle of the preform under different inlet flow rate.

competing effects of reactant depletion and reaction rate acceleration (due to increase in mass flux and higher temperature) resulted in more densification inside the preform, thus decreasing the porosity gradient across the sample. However, as stated earlier, deposition of the solid product reduced the pore sizes and hence also decreased the local permeability of the preform. Consequently, the pressure gradient required to maintain the flow through these regions of low porosity increased rapidly eventually increasing the back pressure beyond the operating limit and prematurely stopping the process. This caused the elements at the inlet boundary to be less densified in this case. It was also observed in this analysis that the final processing times were reduced with increase in flow rates. This is due to the fact that the back pressure increased faster with increase in flow rate of the gaseous precursors.

3.4.3.3 Effect of the outlet pressure and concentration on the deposition profiles

Figures 3.45 and 3.46 show the final porosity profiles obtained along the y and x-axes respectively at the middle of the preform when different outlet pressure $P2$, were applied. Similar to the previous analysis, at high outlet pressure it was observed that the internal porosity of the preform was further reduced but the inlet boundary of the sample was less densified. However, in this case, it was also observed that further increase in the outlet pressure, for example when $P2 = 8$ kPa, resulted in the interior of the sample being less densified. This analysis was performed by maintaining a constant flow rate ($v = 2$) of the gaseous precursors. According to Darcy's law, see equation (3.17), at high outlet pressure, i.e. at low pressure gradient across the sample, the precursor velocity is expected to be higher during the infiltration process. Consequently this allowed higher mass flow of the reactants inside the preform, which resulted in greater depletion of the MTS inside the sample, thus decreasing the internal porosity. However, densification was limited by the chemical kinetics for much larger gas velocities (higher outlet pressures) since mass transport to the surface was very fast.

It was found that increase of the MTS fraction in the gas mixture had almost no effect on the final composite density. However, the processing time, being inversely proportional with the MTS initial concentration C_0, was reduced due to the increase in precursor concentration.
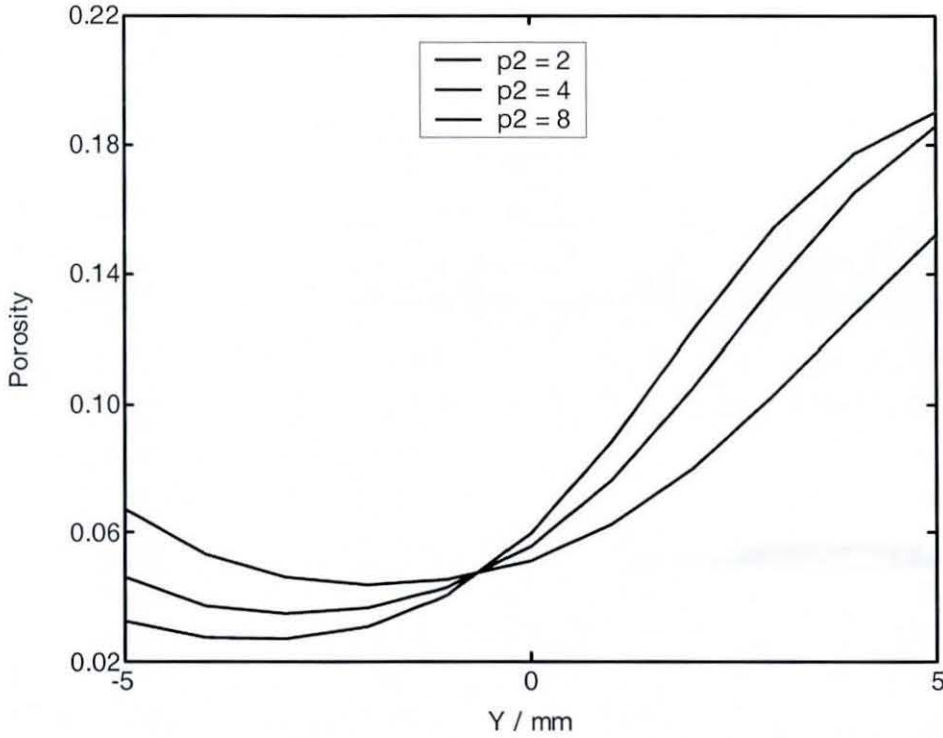
Figure 3.45: Final porosity profile obtained along the y-axis at the middle of the preform by applying different outlet pressure *P2* and maintaining a constant flow rate.
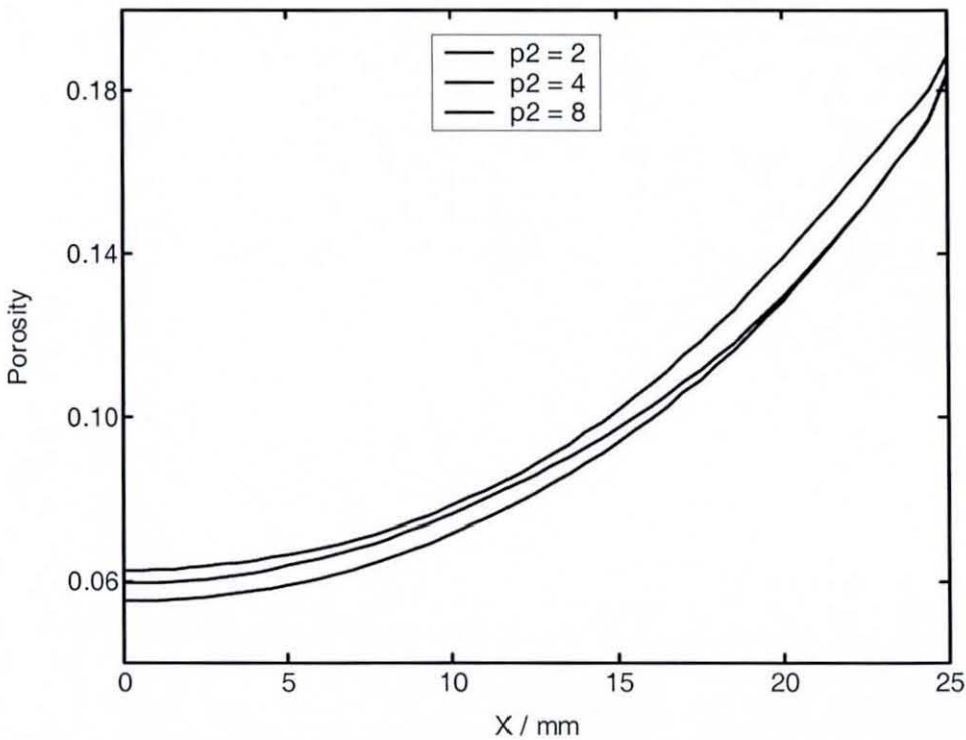
Figure 3.46: Final porosity profile obtained along the x-axis across the middle of the preform by applying different outlet pressure *P2* and maintaining a constant flow rate.

128

3.4.3.4 Infiltration of larger samples

The ME-FCVI model was employed to study the infiltration process of larger preform sizes during microwave enhanced FCVI. The sample sizes stated in table 3.3 were considered during this analysis. Figure 3.47 shows the evolution with time of the porosity profiles obtained when a sample size of 200×10 mm was heated with an incident microwave power of 1.2 kW and then infiltrated with a constant flow rate of $v = 8$. It is observed from the figure that deposition occurred predominantly at a region remote from the centre of the preform as predicted by figure 3.21, which shows that the hottest region was also not at the preform centre. In addition, as occurred previously the region of highest densification moved towards the inlet of the preform during the process. It may be further observed that as deposition continued the region of greatest densification increased in size and at the same time propagated towards the centre of the sample, thus largely infiltrating the interior of the sample. This observation contradicts the expectation that the use of microwaves always results in an inside-out densification from the centre of the preform. The process eventually stopped when the limiting back-pressure was reached, figure 3.48. It is seen from the latter that, as expected, the back pressure gradient started to increase in the region where the highest densification occurred. From figure 3.47, it may also be observed that significant porosity remained at the surfaces of the preform, resulting in a high porosity gradient across the preform. These porosities could possibly be reduced by using larger flow rates and lower temperature gradients. As expected, the processing time in this case was much longer compared to the time taken to infiltrate a 50×10 mm preform. Similar observations were made from simulations results obtained when other large sizes were considered.

This analysis has shown that the microwave heating of a large SiC preform can result in a different infiltration pattern and yielded non-uniform dense composites.
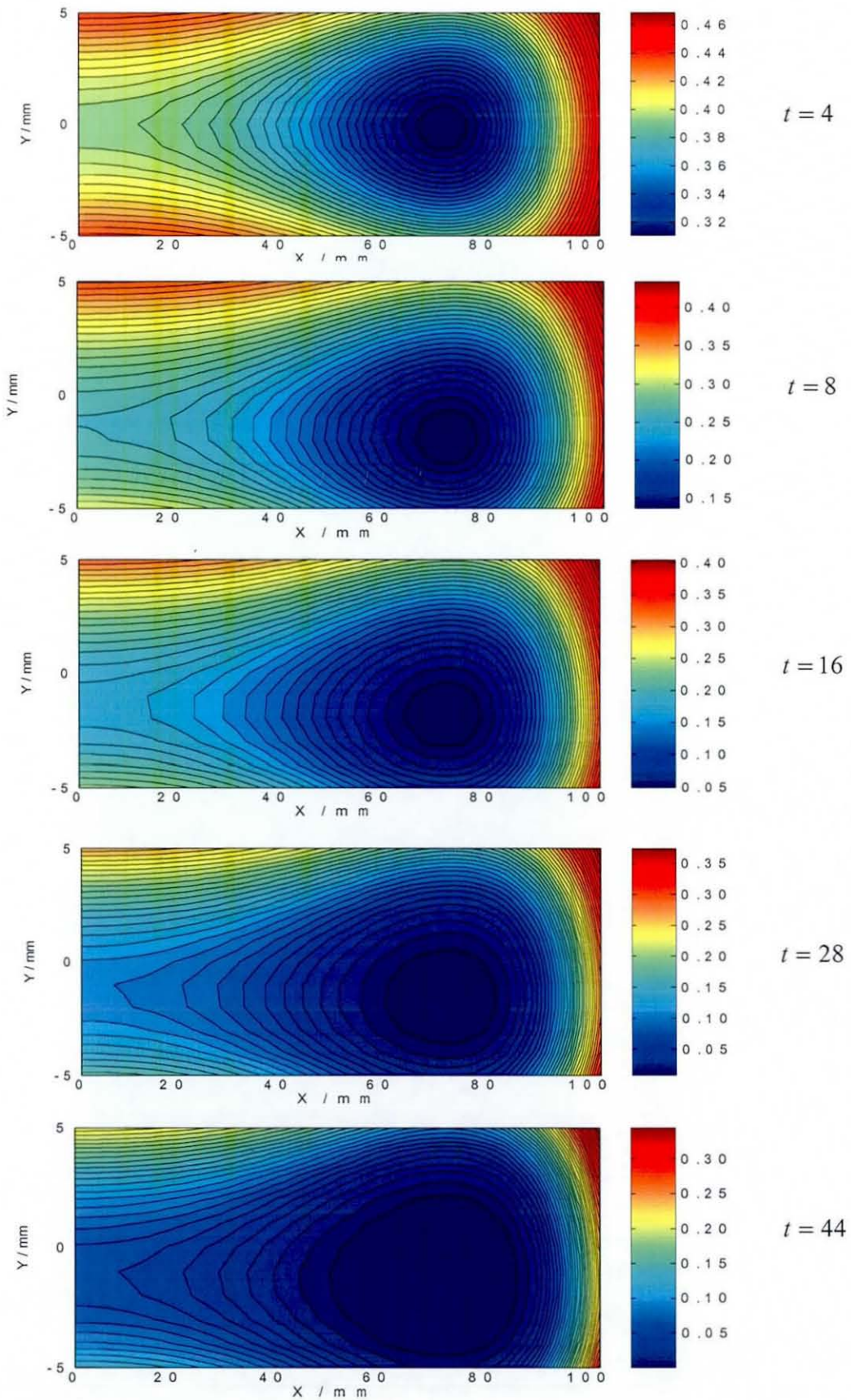
Figure 3.47: Evolution of the densification of a 200×10 mm preform under ME-FCVI. An input power of 1.2 kW was applied to heat the preform whilst maintaining a constant inlet flow rate, $v = 8$, of the precursors for infiltration.

130
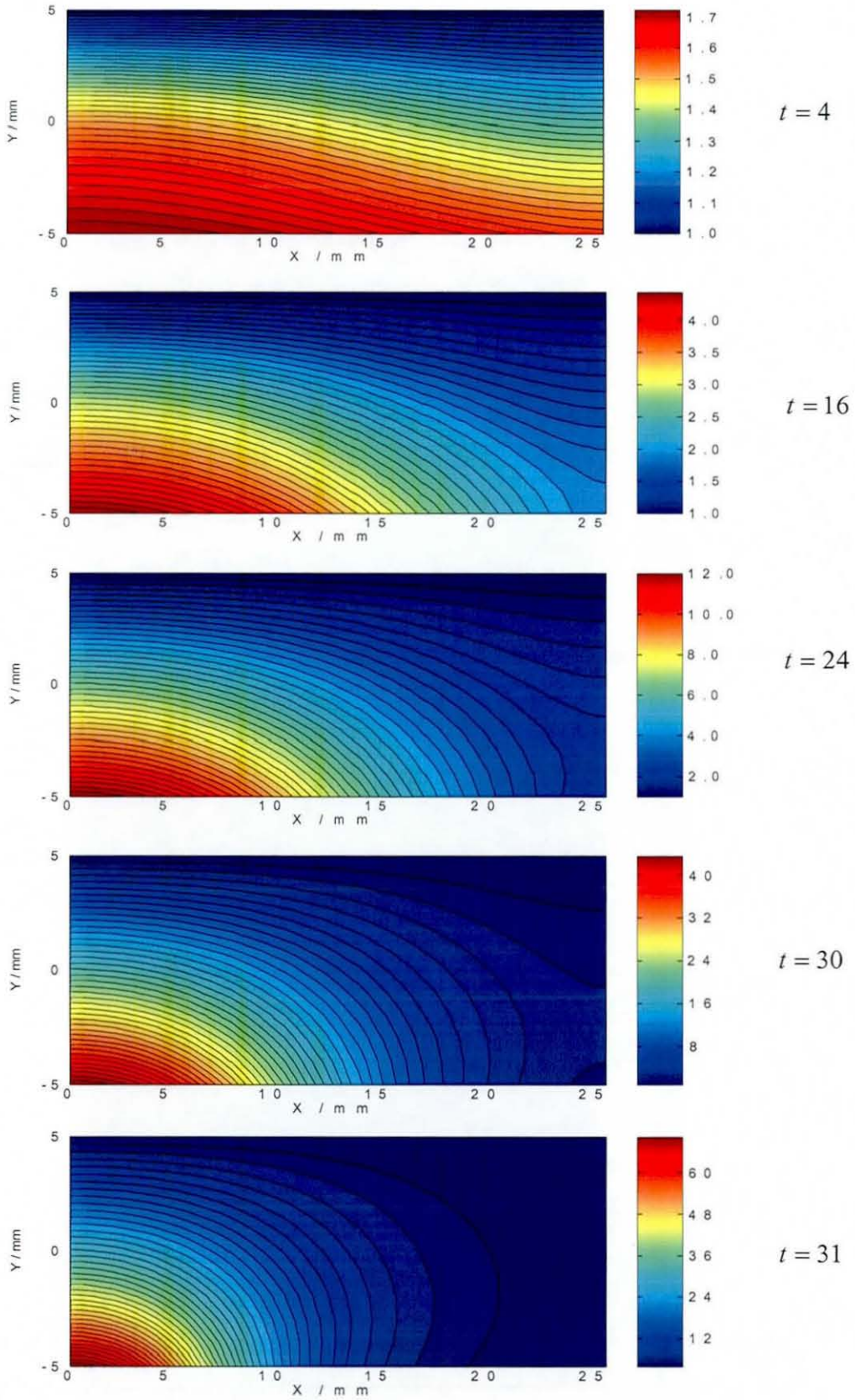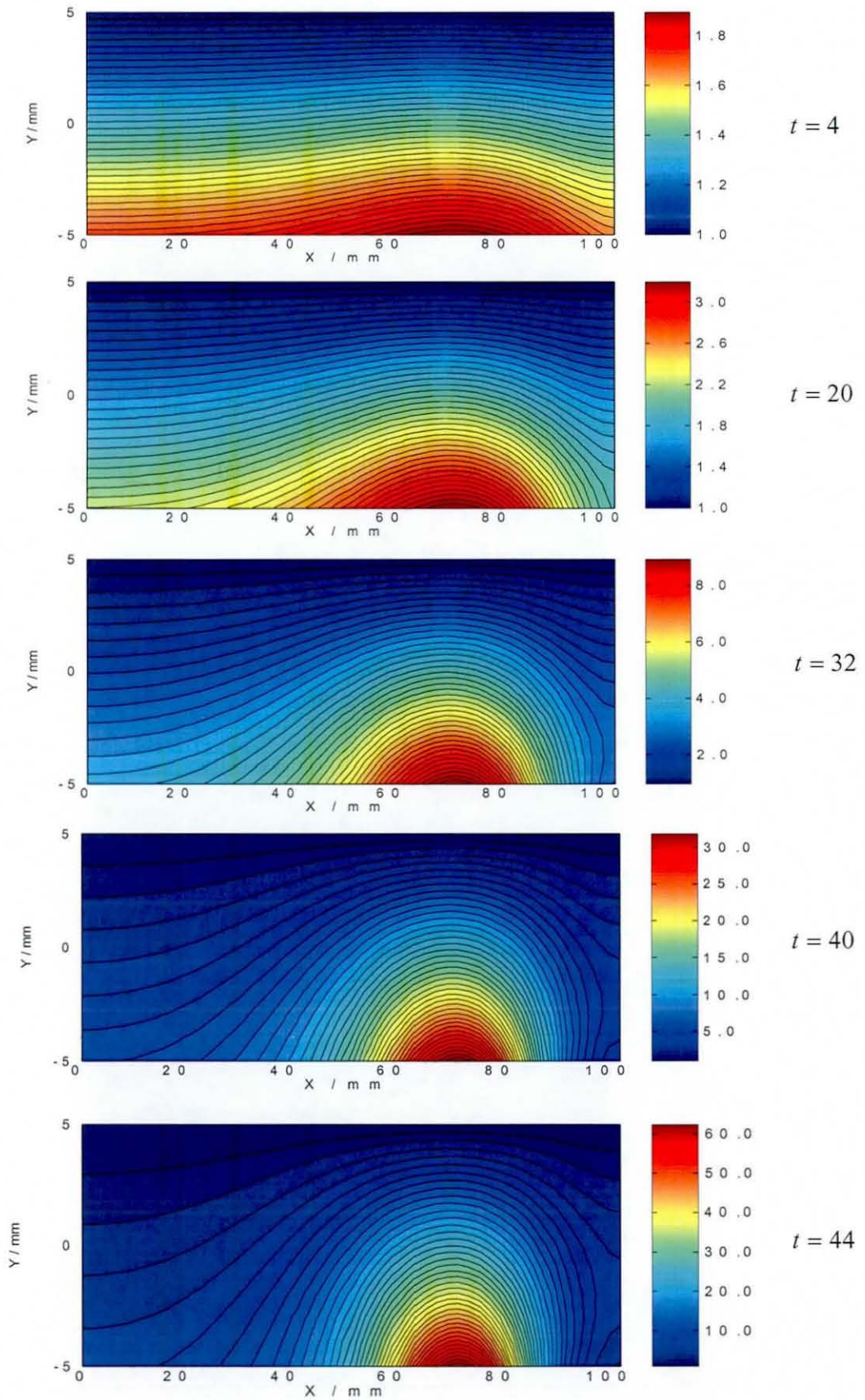
Figure 3.48: Evolution of the pressure profiles during the infiltration of a 200×10 mm preform under ME-FCVI. The colour bar reflects the pressure values in kPa.

3.5 Summary

A mathematical model describing the process of microwave enhanced forced-flow chemical vapour infiltration (ME-FCVI) to produce SiC$_f$/SiC composites has been developed and presented. Due to the complexities involved in developing such model, viz the electromagnetic heating of the ceramic preform, forced-flow of the gaseous reactants and reaction/deposition mechanisms occurring inside the porous preform, two sub-models were first developed. The *EM-model* described the electromagnetic heating of a SiC preform having a constant porosity level and determined the electric field and thermal distribution within the latter. This sub model also investigated the occurrence of thermal runaway with decreasing porosity during ME-FCVI. The *FCVI-model* evaluated the mass balance of the gaseous species and porosity variation during the infiltration process under isothermal conditions. The two sub models were then combined together to study the effects of the processing variables on the infiltration profiles and processing times during ME-FCVI. The function of this model is to predict trends in the composite density distributions and infiltration time that might be expected when the process conditions are varied.

The simulation results have shown that the final density of the preform, as well as the uniformity of the latter, are strongly influenced by the processing variables. The results from the *FCVI model* showed that forcing the gaseous precursor through the porous preform lead to more uniform densification due to reduced diffusion limitations encountered during conventional CVI. However, densification was limited by early termination of the process due to excessive pressure gradients. Also, it was observed that the boundaries of the preform were less densified. The use of inverse temperature gradients, when combined with pressure gradients, quite satisfactorily overcame diffusion limitations and provided increased control over the composite quality. Again it was necessary to have a proper combination of flow rates and thermal gradients to avoid preferential deposition in the region of highest temperatures, thus reducing density gradient across the preform. Together, the microwave incident power and external cooling (controlled by the heat transfer coefficient) could be manipulated to control both the temperature level and thermal gradient during the microwave heating stage. Higher temperature levels could lead to a decrease in the overall processing time with the overall density of the composite being minimally changed. On the other hand, the use of higher inverse temperature gradient resulted in greater non-uniformity and a

decrease in the density of the final composite. However, in all cases it is observed that the boundaries of the preform remained less densified compared to its interior. Further densification was still possible by using inverse thermal gradient combined with diffusion transport of the gaseous precursors.

The results obtained from the *EM-model* showed that the temperature profiles were greatly affected by the decrease in porosity level during the process. The analysis performed by applying constant microwave incident power showed that at larger porosity levels, thermal runaway might occur. However, in this model the cooling effect inside the preform generated by the forced flow of the gaseous precursors was ignored. Also the microstructure of the preform was neglected during the electromagnetic formulation due to the complexities involved in modelling the interaction of microwaves with a porous media.

To overcome some of the limitations and drawbacks described above, a one-dimensional model was developed and analysed. The model describes the process of microwave enhanced chemical vapour infiltration (MECVI) under diffusion transport. This could help to understand the infiltration processes required to further densify the boundaries of the final composites obtained during ME-FCVI. The electromagnetic formulation of this model includes the microstructure of the preform, and a dynamic version of the MECVI process was investigated, where the temperature distribution was allowed to vary as the porosity level changed

CHAPTER 4:

MICROWAVE ENHANCED DIFFUSION BASED CHEMICAL VAPPOUR INFILTRATION – A ONE DIMENSIONAL MODEL

4.1 Introduction

In the previous chapter it was observed that by applying forced-flow, the performs heated with microwaves were less infiltrated at their boundaries as compared to their interiors. By reducing the flow rate of the gaseous precursor, making diffusion the dominant mechanism, it was expected that this effect would be greatly reduced. Thus, in this one dimensional model the infiltration process at the boundaries was considered and investigated by considering the gaseous precursor to flow thorough the performs via diffusion only. The preform was assumed to compose of fibrous silicon carbide sheets stacked together with certain amount of porosity present in between. The effects of allowing the thermal and electrical parameters, which are porosity dependent, to vary during the infiltration process were also investigated. Further, occurrence of thermal runaway during the infiltration process was also studied by considering the effects of decreasing the total porosity on the steady-state solutions of the temperature distributions.

The physical problem is stated in section 4.2 and a general mathematical formulation is presented in sections 4.3 and 4.4. The variables and parameters used here are defined accordingly and in some cases they do not follow the same definitions as in previous chapters. An asymptotic analysis producing homogenized equations describing microwave heating and the transport/reaction processes are performed in the following section. A regular perturbation expansion technique is then applied to the system of two-dimensional equations (in space) to obtain averaged equations with averaged boundary conditions. The numerical techniques applied to solve the system of equations obtained from the perturbation analysis are presented in section 4.6. Finally,

the solutions to this system of equations are simulated numerically and discussed in section 4.7.

4.2   Model formulation

The MECVI system that was investigated is shown in figure 4.1; it consisted of a preform of thickness $2b$ residing in a microwave cavity. The preform was composed of fibrous ceramic sheets stacked together with a void space, of thickness $2\alpha_1 a_1$, present between them, where $a_1 << b$ and α_1 lies between 0 and 1.

The process consisted of allowing gaseous precursors of known composition to flow continuously through the void space keeping a constant species composition at the perform surfaces. Two plane time-harmonic electromagnetic waves of angular frequency ω impinged symmetrically onto both sides of the preform with the same uniform power per unit surface area, P_d.

TM polarization was considered where the electric field was aligned along the z-axis. In the free space regions, $x < -b$ and $x > b$, the electric field was given by:

$$\mathbf{E} = E_0[\exp(ik_2x - i\omega t) + \sum_{m=-\infty}^{\infty} R_m \exp(2\pi i m y)\exp(-i\beta_m x - i\omega t)]\hat{z}, \qquad x < -b \quad (4.1)$$

and

$$\mathbf{E} = E_0[\exp(-ik_2x - i\omega t) + \sum_{m=-\infty}^{\infty} R_m \exp(2\pi i m y)\exp(i\beta_m x - i\omega t)]\hat{z}, \qquad x > b \quad (4.2)$$

where E_0 represents the strength of the incident electric field; R_m the total reflection coefficients, $k_2 = \omega/c_s$; c_s the speed of light in free space and t is the time variable. $\hat{z}$ is the unit vector along the z-axis and x and y represent the distances along the x-axis and y-axis respectively, as shown in figure 4.1. The propagation constant β_m for the m mode was given by:

$$\beta_m = \sqrt{k_2^2 - 4m^2\pi^2} \ . \tag{4.3}$$

The electric field that penetrated the laminate preform and interacted with the material was given by $\mathbf{E}_p = [E_0 V_e(x, y) e^{-i\omega t}] \hat{z}$, where the dimensionless function V_e satisfied:

135

$$\nabla^2 V_e + k^2 [N_1^2(y) + i\frac{\sigma_0}{\omega\varepsilon_0} f_c(-1 + T/T_0, y)]V_e = 0, \qquad -b < x' < b. \qquad (4.4)$$

Here, ∇^2 is the Laplacian operator; N_1^2 the index of refraction; σ_0 the conductivity of the ceramic sheets at ambient temperature T_0; ε_0 the permittivity of free space; T the temperature of the sheets in the presence of microwave radiation and the function f_c is the conductivity of the preform normalized by σ_0. It is noted here that N_1^2 and f_c are both piecewise constant on each ceramic sheet.
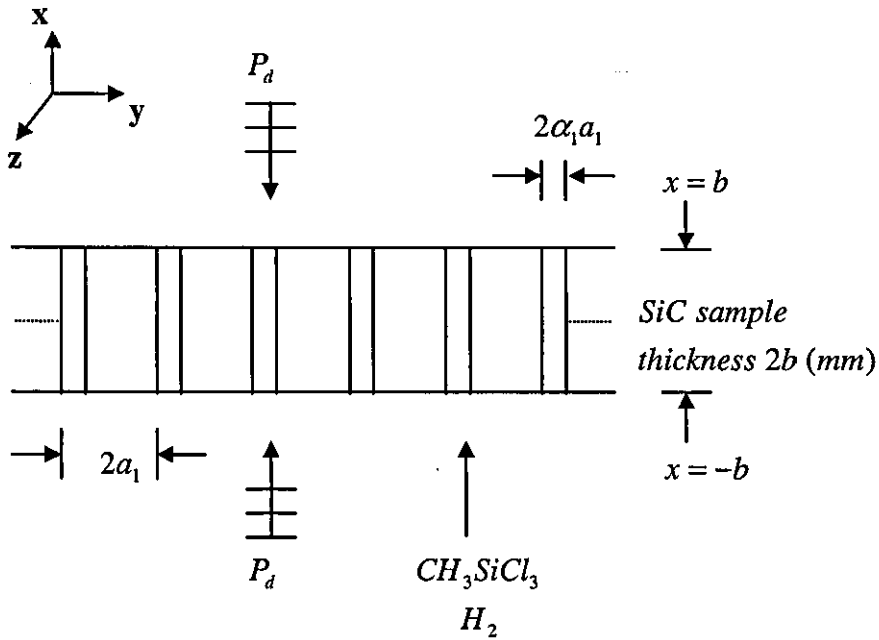
Figure 4.1: Schematic of the microwave assisted CVI of a fibrous preform. The preform is heated symmetrically by electromagnetic waves propagating in the x-direction.

At the interfaces $x = \pm b$, the tangential electric and magnetic fields were continuous, hence V_e and its derivative were also continuous there. Using these as boundary conditions, the electric field within the preform could thus be determined. Hence the power density dissipated in the preform due to microwave heating could be evaluated by:

$$P_d = \frac{1}{2}|E_0|^2 \sigma_0 f_c(-1 + T/T_0, y)|E_p|^2 \qquad (4.5)$$

136

4.3 Chemical kinetics

It is recalled here that in the present work, silicon carbide (SiC) formed the matrix material of the composite with methyltrichlorosilane (MTS) decomposition being used for its deposition, with an excess of hydrogen (H_2) acting as the carrier gas. As mentioned in the literature review, although SiC/SiC composites have been the subject of several investigations in the field of Chemical Vapour Infiltration (CVI), the complete reaction mechanism of MTS decomposition under CVI conditions is still not well established. Hence, it was assumed that MTS decomposed according to an overall heterogeneous reaction, the equation being re-stated here for convenience:

$$CH_3Cl_3Si_{(s)} + n_1 H_{2\,(g)} \longrightarrow SiC_{(s)} + 3HCl_{(g)} + n_1 H_{2\,(g)} \tag{4.6}$$

The reaction rate was assumed to be first order in the precursor concentration and to have an Arrhenius-type dependence on the temperature, given by:

$$\Gamma = k_1 C \exp(-E_a / RT), \tag{4.7}$$

where Γ denotes the reaction rate, k_1 the reaction constant; C the concentration of MTS; E_a the activation energy and R the universal gas constant.

4.4 Conservation equations

As discussed in Chapter 2, a complete understanding of the transport process of the gaseous species that occur during CVI involves a number of complexities. However, the Dusty gas model can be used to describe it. The simplest formulation of the gaseous phase within the preform is obtained by considering one reacting species. Hence, it is assumed here that the gaseous system is dilute, that is, the concentration of MTS is much smaller than that of the carrier gas. Dilute gas systems during CVI have been investigated successfully in the past [55, 65, 66] involving binary and Knudsen diffusion. The Dusty gas model can thus be simplified to obtain an approximate expression for the molar flux. Hence the unsteady state mass balance of the precursor gas that diffuses throughout the accessible part of the preform is given by:

$$\frac{\partial C}{\partial t} = \nabla \cdot (D \nabla C).$$

(4.8)

D is the effective diffusion coefficient given by:

$$\frac{1}{D} = \frac{1}{D_k} + \frac{1}{D_m},$$

(4.9a)

where D_k' is the Knudsen diffusion coefficient due to collision of the molecules with the pore walls given by:

$$D_k^e = 9700 F \left(\frac{T}{M_{TMS}} \right)^{1/2},$$

(4.9b)

where, F represents the characteristic size of the pores and M_{MTS} is the molecular mass of MTS. D_m is the binary diffusion coefficient due to collision of the molecules between themselves given according to kinetic theory [130] by:

$$D_k^e = \frac{0.001858 T^{3/2} \sqrt{\frac{1}{M_{MTS}} + \frac{1}{M_{H_2}}}}{P \hbar^2 \Pi},$$

(4.9c)

where P is the pressure (assumed fixed); $\hbar$ the Lennard-Jones parameter for the pair of gases; Π is the collision integral and M_{H_2} is the molecular mass of H_2.

It should be noted that the term describing the reaction at the solid/gas interface in equation (4.8) has been omitted. This will be considered in section 4.5 when finding the boundary condition across this interface. At the preform/environment interface it is assumed that the concentration of the precursor gas remains fixed, that is, $C = C_0$ at $x = \pm b$, C_0 being the initial inlet concentration.

The energy balance is considered next. A heat source term was required to represent the amount of energy dissipated within the porous body by microwave heating and a sink source term to represent the energy needed for the chemical reaction to take place. It was assumed, however, that the latter was negligible compared to the former. Hence, the unsteady state energy balance equation for the gas-fibre preform was given by:

$$\left(\rho_p c_p \right) \frac{\partial T}{\partial t} = \nabla \cdot (k_t \nabla T) + P_d,$$

(4.10)

where ρ_p, c_p and k_t represent the density, specific heat and thermal conductivity of the fibre preform respectively. These thermal parameters were assumed to be piecewise constant across the material. It was assumed initially that the sample was at ambient temperature T_0. At the interfaces between the preform and the environment heat losses were considered due to convection and radiation:

$$k_t \frac{\partial T}{\partial x} = \mp h_e (T - T_0) \mp s_b e (T^4 - T_0^4) \qquad x = \pm b, \qquad (4.11)$$

where h_e represents the heat transfer coefficient; s_b the Stefan-Boltzmann constant and e the emissivity of SiC.

Finally, the evolution of the preform porosity with respect to the reaction was obtained through a mass balance given by:

$$\frac{\partial F}{\partial t} = -\frac{\Gamma}{\rho_{p_s}}, \qquad (4.12)$$

where F represents the moving solid/gas interface and ρ_{p_s} the density of SiC, respectively. It was assumed initially that the void space was uniform:

$$F(t = 0, x) = \pm \alpha_1 a_1.$$

Next the above system of equations is non-dimensionalised by substituting the following dimensionless variables denoted by the prime letters:

$$x' = x/b, \qquad y' = y/a_1, \qquad T' = -1 + T/T_0, \qquad t' = t/\theta, \qquad k_t' = k_{ts} k_t,$$

$$k_2' = k_2 b, \qquad \beta_m' = \beta_m/b, \qquad (\rho_p c_p) = (\rho_{p_s} c_{p_s})g \qquad E' = E/E_0, \qquad C' = C/C_0,$$

$$D' = D/D_0 \qquad F' = F/a_1 \qquad \Gamma = \Gamma' b/C_0 D_0 \qquad (4.13)$$

where k_{ts} and c_{p_s} are the thermal conductivity and heat capacity of SiC respectively and D_0 is the diffusion coefficient at ambient temperature. It should be noted that the time variable was scaled by θ, which is as yet unspecified.

The electric field in non-dimensional terms after dropping the primes now becomes:

$$\mathbf{E} = [\exp(ik_2 x - i\omega t\theta) + \sum_{m=-\infty}^{\infty} R_m \exp(2\pi i m y a_1) \exp(-i\beta_m x - i\omega t\theta)]\hat{z}, \quad x < -1, (4.14a)$$

$$\mathbf{E} = [\exp(-ik_2 x - i\omega t\theta) + \sum_{m=-\infty}^{\infty} R_m \exp(2\pi im\, y a_1)\exp(i\beta_m x - i\omega t\theta)]\,\hat{z}, \quad x > 1, \quad (4.14b)$$

where the propagation constant was given by:

$$\beta_m = \sqrt{k_2^2 - 4m^2\pi^2 b^2}\,. \tag{4.14c}$$

The function V_e satisfied:

$$\varepsilon_*^2 \frac{\partial^2 V_e}{\partial x^2} + \frac{\partial^2 V_e}{\partial y^2} + \varepsilon_*^2 k_2^2 [N_1^2(y) + iv_c f_c(T, y)] V_e = 0\,, \tag{4.15}$$

and the temperature and concentration distributions became:

$$\frac{\varepsilon_*^2 A_1 g}{\theta} \frac{\partial T}{\partial t} = k_t \left(\varepsilon_*^2 \frac{\partial^2 T}{\partial x^2} + \frac{\partial^2 T}{\partial y^2} \right) + \varepsilon_*^2 P_c f_c(T, y)|\mathbf{E}_p|^2\,, \tag{4.16}$$

and

$$\frac{\varepsilon_*^2 A_2}{\theta} \frac{\partial C}{\partial t} = \varepsilon_*^2 \frac{\partial}{\partial x}\left(D \frac{\partial C}{\partial x} \right) + \frac{\partial}{\partial x}\left(D \frac{\partial C}{\partial y} \right)\,. \tag{4.17}$$

Finally, the evolution of the solid/gas interface was described by:

$$\frac{\varepsilon_*^2 A_3}{\theta} \frac{\partial F}{\partial t} = -\Gamma\,, \tag{4.18a}$$

where,

$$\Gamma = D_a' C \exp(-E_a/RT_0(T+1))\,, \tag{4.18b}$$

From the above equations the following dimensionless parameters arise:

$$\varepsilon_* = a_1/b\,, \qquad B = \frac{h_e b}{k_{ts}}\,, \qquad \beta_r = \frac{s_b e T_0^3}{h_e}\,, \qquad v_c = \sigma_0/\omega\varepsilon_0\,, \qquad P_c = \frac{\sigma_0 b^2}{2T_0 k_{ts}}|E_0|^2\,,$$

$$D_a' = bk_0/D_0\,, \qquad A_1 = \frac{(\rho c_p)_s b^2}{K_s}\,, \qquad A_2 = b^2/D_0\,, \qquad A_3 = \frac{b^2 \rho_{ps}}{C_0 D_0}\,. \tag{4.19}$$

Here ε_* is a parameter for the geometry of the porosity present; B is the Biot number measuring the relative effects of convection and conduction; β_r is the radiation heat loss parameter; P_c is a measure of absorbed power density from the electric field; D_a' is

the Damkohler number representing the ratio of the characteristic diffusion time to the characteristic reaction time and A_1, A_2 and A_3 are respectively the thermal diffusion, gas diffusion and reaction time scales. The equations (4.15-4.18) were only valid within the preform, i.e. $|x| < 1$.

It was further assumed that the filling process of the porous preform occurred in an axis-symmetric fashion. Hence by applying no-flux boundary conditions on the axes of symmetry, the following non-dimensional conditions were obtained:

At $x = 0$,

$$\frac{dV_e}{dx} = 0, \qquad \frac{\partial T}{\partial x} = 0, \qquad \frac{\partial C}{\partial x} = 0. \qquad\qquad (4.20a)$$

At $x = 1$,

$$k_r \frac{\partial T}{\partial x} = -BT - B\beta_r \left[(T+1)^4 - 1 \right], \qquad\qquad (4.20b)$$

and $C = 1$.

The temperature and the electric field distributions were considered to be continuous across the gas/solid interface and their derivatives with respect to y to be zero at the pore axes. The boundary F was assumed to be equal to α_1 initially. The boundary condition for the concentration field is developed in the following section.

4.5 Asymptotic analysis in the limit $\varepsilon_*^2 \to 0$

As a starting point the non-dimensional parameter $\varepsilon_* = a_1 / b$ was considered. It may be remembered that the thickness $2a_1$ of the ceramic fibre layer and the pore, which make up the preform, was much smaller than the total thickness b of the preform, that is $\varepsilon_* \ll 1$. Regular perturbation methods [152,153] were applied to the above governing system of equations to derive homogenized simplified equations describing the microwave heating and the transport/reaction process in the limit $\varepsilon_* \to 0$. The filling process of one pore was considered for convenience and an expansion in powers of ε_*^2 for V_e, T and C was assumed, i.e.,

$$V_e(x,y,\varepsilon_*,t) = \sum_{j=0}^{\infty} \varepsilon_*^{2j} V_{ej}(x,y,t), \qquad (4.21a)$$

$$T(x,y,\varepsilon_*,t) = \sum_{j=0}^{\infty} \varepsilon_*^{2j} T_{aj}(x,y,t), \qquad (4.21b)$$

$$C(x,y,\varepsilon,t) = \sum_{j=0}^{\infty} \varepsilon_*^{2j} C_{aj}(x,y,t), \qquad (4.21c)$$

in the limit $\varepsilon_*^2 \to 0$.

Inserting (4.21a-c) into (4.15-4.17), expanding the nonlinear terms in an asymptotic series, and equating to zero the coefficients of the powers of ε_*^2, yielded an infinite set of equations that sequentially determined V_{ej}, T_{aj} and C_{aj}. The leading order $O(1)$ equations were:

$$\frac{\partial^2 V_{e0}}{\partial y^2} = 0, \qquad k_t \frac{\partial^2 T_{a0}}{\partial t^2} = 0, \qquad \frac{\partial}{\partial y}\left(D\frac{\partial C_{a0}}{\partial y}\right) = 0, \qquad (4.22)$$

and their solutions were:

$$V_{e0} = a_0(x,t) + b_0(x,t)y, \quad T_{a0} = c_0(x,t) + yd_0(x,t), \quad C_{a0} = e_0(x,t) + f_0(x,t)y \quad (4.23)$$

Appendix 5 demonstrates the use of the power expansion series to obtain the leading order equations and their corresponding solutions. At $y = 0$, the derivative of V_{e0}, T_{a0}, and C_{a0} with respect to y was required to be zero. This implied that to the leading order $O(1)$ term these distributions were functions of x and t only. It should be noted that D was dependant on temperature, hence to leading order it was a function of x and t.

The order $O(\varepsilon^2)$ equations were:

$$\frac{\partial^2 V_{e1}}{\partial y^2} = -\frac{\partial^2 V_{e0}}{\partial x^2} - k_2^2[N_1^2(y) + i\nu_c f_c(T,y)]V_{e0}, \qquad (4.24)$$

$$\frac{A_1 g}{\theta}\frac{\partial T_{a0}}{\partial t} = k_t \frac{\partial^2 T_{a0}}{\partial x^2} + k_t \frac{\partial^2 T_{a1}}{\partial y^2} + P_c f_c(T,yb)|E_p|^2, \qquad (4.25)$$

$$\frac{A_2}{\theta}\frac{\partial C_{a0}}{\partial t} = \frac{\partial}{\partial x}\left(D\frac{\partial C_{a0}}{\partial x}\right) + D\frac{\partial^2 C_{a1}}{\partial y^2}, \qquad (4.26)$$

142

Considering the region within the gas phase and integrating (4.24) and (4.25) once with respect to y resulted in:

$$\frac{\partial V_{e1}}{\partial y} = -y \frac{\partial^2 V_{e0}}{\partial x^2} - k_2^2 V_{e0} \int_0^y [N_{1p}^2 + i \nu_c f_{cp}(T)] ds \tag{4.27}$$

$$\frac{y A_1 g}{\theta} \frac{\partial T_{a0}}{\partial t} = k_t y \frac{\partial^2 T_{a0}}{\partial x^2} + k_t \frac{\partial T_{a1}}{\partial y} + \int_0^y P_c f_{cp}(T) |E_p|^2 ds, \tag{4.28}$$

where s is a dummy variable, N_{1p}^2 and $f_{cp}(T)$ are respectively the index of refraction and the conductivity of the gaseous precursor. Also it may be noted that $|E_p|^2$ was a function of x only. Similarly, within the region of the solid material:

$$\frac{\partial V_{e1}}{\partial y} = -(y-1) - k_2^2 V_{e0} \int_1^y [N_{1s}^2 + i \nu_c f_{cs}(T)] ds \tag{4.29}$$

$$\frac{(y-1) A_1}{\theta} \frac{\partial T_{a0}}{\partial t} = (y-1) \frac{\partial^2 T_{a0}}{\partial x^2} + \frac{\partial T_{a1}}{\partial y} + \int_1^y P_c f_{cs}(T) |E_p|^2 ds, \tag{4.30}$$

where this time N_{1s}^2 and $f_{cs}(T)$ are the index of refraction and the conductivity of the solid material respectively.

At the boundary $y = F(x)$, it was required that the normal derivatives of the temperature and the electric field were continuous, that is, $\nabla T^+ \cdot \hat{n} = K \nabla T^- \cdot \hat{n}$ and $\nabla V_e^+ \cdot \hat{n} = \nabla V_e^- \cdot \hat{n}$. The + and - sign denote values slightly above and below the interface F. The normal vector at the boundary F in dimensionless form was given by:

$$\hat{n} = \left(-\varepsilon_* \frac{\partial F}{\partial x}, 1 \right). \tag{4.31}$$

Thus, to leading order $O(1)$ term:

$$\left[\frac{\partial V_{e1}}{\partial y} - \frac{\partial V_{e0}}{\partial x} \frac{\partial F}{\partial x} \right]^+ = \left[\frac{\partial V_{e1}}{\partial y} - \frac{\partial V_{e0}}{\partial x} \frac{\partial F}{\partial x} \right]^-, \tag{4.32a}$$

$$\left[\frac{\partial T_{a1}}{\partial y} - \frac{\partial F}{\partial x} \frac{\partial T_{a0}}{\partial x} \right]^+ = k_t \left[\frac{\partial T_{a1}}{\partial y} - \frac{\partial F}{\partial x} \frac{\partial T_{a0}}{\partial x} \right]^-. \tag{4.32b}$$

Applying these conditions to Equations (4.27-4.30) yielded:

$$\frac{\partial^2 V_{e0}}{\partial x^2} + k_2^2 [\hat{N}_1^2 + i v_c \, \hat{f}_c(T_0)] V_{e0} = 0, \tag{4.33a}$$

$$\frac{A_1 \hat{g}}{\theta} \frac{\partial T_{a0}}{\partial t} = \frac{\partial}{\partial x} \left(\hat{k}_t \frac{\partial T_{a0}}{\partial x} \right) + (1-F) P_c \, \hat{f}_c(T_{a0}) |\mathbf{E}_p|^2, \tag{4.33b}$$

where

$$\hat{N}_1^2 = F N_{1p}^2 + (1-F) N_{1s}^2,$$

$$\hat{f}_c(T_{a0}) = F f_{cp}(T_{a0}) + (1-F) f_{cs}(T_{a0}),$$

$$\hat{g} = (1-F) + Fg,$$

$$\hat{k}_t = (1-F) + F k_t.$$

The $O(\varepsilon_*^2)$ equation for the concentration field was:

$$\frac{A_2}{\theta} \frac{\partial C_{a0}}{\partial t} = \frac{\partial}{\partial x} \left(D \frac{\partial C_{a0}}{\partial x} \right) + D \frac{\partial^2 C_{a1}}{\partial y^2}, \qquad 0 < y < F. \tag{4.34}$$

Considering a simple conservation of mass argument at the boundary $y = F(x)$ yielded the following condition:

$$\hat{\mathbf{n}} \cdot \left(\varepsilon_* D \frac{\partial C}{\partial x}, D \frac{\partial C}{\partial y} \right) = -\Gamma, \tag{4.35}$$

where Γ was given by equation (4.18b). It may be noted that the exponential term in the expression for Γ was on the order $O(\varepsilon_*^2)$ when the temperature reached the critical value T_c at which the reaction started to occur. Thus Γ was written in the form, $\Gamma = \varepsilon_*^2 D_a' C \hat{\Gamma}$, where $\hat{\Gamma}$ was on the order $O(1)$ and was temperature dependent. Substituting for Γ in (4.35) and using equation (4.21c), the leading order $O(1)$ condition was:

$$\frac{\partial C_{a0}}{\partial y} = 0, \tag{4.36}$$

whose solution was again a function of x and t. The leading order $O(\varepsilon^2)$ condition now became:

$$D\frac{\partial C_{a1}}{\partial x} = -D_a'\hat{\Gamma}C_{a0} + D\frac{\partial F}{\partial x}\frac{\partial C_{a0}}{\partial x}. \tag{4.37}$$

Integrating (3.34) once with respect to y and applying condition (4.37), yielded

$$\frac{A_2 F}{\theta}\frac{\partial C_{a0}}{\partial t} = \frac{\partial}{\partial x}\left(DF\frac{\partial C_{a0}}{\partial x}\right) - D_a'\hat{\Gamma}C_{a0}. \tag{4.38}$$

A similar analysis was required to obtain the corresponding boundary conditions for the temperature concentration and electric field distributions, these steps have been omitted here to avoid repetitions, viz:

$$x = 1: \quad \frac{\partial V_{e0}}{\partial x} - ik_2 V_{e0} = -2ik_2\exp(-ik_2),$$

$$\hat{k}_t\frac{\partial T_{a0}}{\partial x} = B\left[T_{a0} + \beta_r\left((1+T_{a0})^4 - 1\right)\right], \qquad C_0 = 1 \tag{4.39a}$$

$$x = 0: \quad \frac{dV_{e0}}{dx} = 0, \qquad \frac{\partial T_{a0}}{\partial x} = 0, \qquad \frac{\partial C_{a0}}{\partial x} = 0. \tag{4.39b}$$

The evolution of the moving solid/gas interface was given by

$$\frac{A_3}{\theta}\frac{\partial F}{\partial t} = -\hat{\Gamma}D_a'C_{a0}. \tag{4.40}$$

where $F = \alpha_1$ initially.

4.6 Numerical experimental

The system of equations (4.33) and (4.39) was investigated by applying numerical techniques to study the thermal runaway effects during the chemical vapour infiltration process. Steady state equations were considered in this first analysis. The dynamic version of the MEFCVI, described by equations (4.33), (4.38), (4.39) and (4.40), was then investigated by applying the finite difference techniques to determine the evolution of the various distributions involved during the process. For convenience, the subscripts defining the leading order terms for the distributions have been omitted.

145

4.6.1 Determining steady-state solution to study thermal runaway effects

This analysis was begun by seeking steady-state solutions for equation (4.33b). Setting the time derivative equal to zero and integrating the resulting ordinary differential equations with respect to the space variable x and applying the boundary conditions (4.39a), yielded the following implicit expression for the latter at the preform/environment boundary:

$$P_c = \frac{B\left(T_s(1) + \beta_r((T_s(1) + 1)^4 - 1)\right)}{\hat{f}_c(T_s)\|V_e\|^2}, \tag{4.41}$$

where $\|V_{e0}\| = \int_0^1 |V_{e0}|^2 \, dx$. $T_s(1)$ represents the steady-state temperature at the preform/environment boundary. In order to pursue the study further, a specific form for the function $\hat{f}_c$ needed to be chosen. Recall that $\hat{f}_c$ was the effective non-dimensional electrical conductivity function of the preform. An analysis of the dielectric properties data for SiC [151,154] and following the same approach performed by Kriegsmann [116] it was found that the function $f_{cs}(T)$ representing the electrical conductivity of SiC could be modelled as:

$$f_{cs}(T) = e^{c_1 T}, \tag{4.42}$$

where c_1 was a constant representing the slope of the line obtained when the natural logarithm of the function f_{cs} was plotted against the temperature T. It was observed that the value of c_1 was greatly dependent on the dielectric property value for the material being investigated, in this case SiC. Analysing the dielectric property data of SiC obtained under different measurements [151,154], it was seen that an enormous degree of scatter existed in the values. Batt et al [151] stated that the more lossy the material was, the more difficult it was to get accurate dielectric property measurements. Hence, after fitting empirical models in the permittivity data from [151,154], particular values of c_1 obtained were 3.0 and 0.8. Assuming the electrical conductivity, f_{cp}, of the gaseous precursor present within the pores to be 1, the function $\hat{f}_c$ was given by:

$$\hat{f}(T) = (1 - F)f_{cs}(T). \tag{4.43}$$

It was observed that the term in the denominator of equation (4.41) coupled the latter with equation (4.33a) describing the electric field. Thus both equations were solved simultaneously at each prescribed point in space using the shooting method [141]. This way, a series of steady state temperature values were finally obtained for different power and porosity levels, which could be used to study the thermal runaway effects.

4.6.2 MECVI – dynamic version

In this analysis, the non steady-state solutions for the temperature, concentration of MTS and porosity distributions were evaluated during the infiltration process. The Finite Difference (FD) techniques (see section 3.3) were applied in space to solve equations (4.33b), (4.38) and (4.40). Updating the model with respect to time was performed using the Crank-Nicholson (CN) scheme [141,142]. Also a regular shooting method [141] was used to determine the electric field distribution within the perform at each time step. Only the equations obtained in dicretizing the heat diffusion equation (4.33b) by using FD techniques and the CN scheme are shown below in order to avoid repetition. Following the same steps involved in section 3.3 the perform was discretized along the x-direction with step size Δx and the time variable t was discretized similarly with time step Δt. Thus the temperature at a typical point (x_m, t_n) at time step n was represented as T_m^n, where,

$$x_m = x_0 + m\Delta x, \qquad m = 0, 1, \ldots \ldots, 2M \qquad x_0 = 0,$$

$$t_n = n\Delta t, \quad n = 0, 1, 2, \ldots \ldots.$$

The differential equation (4.33b) was converted to its equivalent finite difference approximation, given as:

$$\frac{T_m^{n+1} - T_m^n}{\Delta t} = \frac{\hat{k}_t \theta}{2A_1 \hat{g} \Delta x} \left[T_{m-1}^{n+1} - 2T_m^{n+1} + T_{m+1}^{n+1} + T_{m-1}^n - T_m^n + T_{m+1}^n \right]$$
$$+ \frac{2\theta(1 - F_m^n)P_c \hat{f}_c(T_m^n)\left| E_{p_m}^{\ n} \right|^2}{A_1 \hat{g}}$$

(4.44)

It is noted here that the thermal conductivity $\hat{k}_t$ and the variable $\hat{g}$ were considered to be a function of total porosity only at each time step in order to avoid extra

147

complications in the numerical analysis. The above equation was simplified using the substitutions:

$$\lambda_2 = \frac{\hat{k}_t \theta \Delta t}{2 A_1 \hat{g} \Delta x^2} \quad \text{and} \quad E_m^n = \frac{2\theta(1 - F_m^n) P \hat{f}(T_m^n) \left| E_{p_m}^{\ n} \right|^2}{A_1 \hat{g}} \Delta t, \text{ to obtain:}$$

$$-\lambda_2 T_{m-1}^{n+1} + (1 + 2\lambda_2) T_m^{n+1} - \lambda T_{m+1}^{n+1} = \lambda T_{m-1}^n + (1 - 2\lambda_2) T_m^n + \lambda_2 T_{m+1}^n + E_m^n \qquad (4.45a)$$

Similarly the boundary conditions (4.39) were converted to the following finite difference approximations:

$$T_{-1}^n = T_1^n \text{ at } x = x_0,$$

$$T_{M+1}^n = T_M^n - \gamma_2 T_M^n - \beta_2 \left[(1 + T_M^n)^4 - 1 \right] \text{ at } x = x_M, \qquad (4.45b)$$

where, $\gamma_2 = \dfrac{2\Delta x B}{\hat{k}_t}$ and $\beta_2 = \dfrac{2\Delta x \beta_r B}{\hat{k}_t}$.

Finally equations (4.45) were transformed into a set of $M + 1$ linear equations, which were represented in matrix form as:

$$\begin{bmatrix} 1+2\lambda_2 & -2\lambda_2 & & & & \\ -\lambda_2 & 1+2\lambda_2 & \lambda_2 & & & \\ & \ddots & \ddots & \ddots & & \\ & & \ddots & \ddots & \ddots & \\ & & & -\lambda_2 & 1+2\lambda_2 & -\lambda_2 \\ & & & & -2\lambda_2 & \alpha_2 \end{bmatrix} \begin{bmatrix} T_{00} \\ \vdots \\ \vdots \\ \vdots \\ \vdots \\ T_{0M} \end{bmatrix}^{n+1} = \begin{bmatrix} 1-2\lambda_2 & 2\lambda_2 & & & & \\ \lambda_2 & 1-2\lambda_2 & \lambda_2 & & & \\ & \ddots & \ddots & \ddots & & \\ & & \ddots & \ddots & \ddots & \\ & & & \lambda_2 & 1-2\lambda_2 & \lambda_2 \\ & & & & 2\lambda_2 & 2-\alpha_2 \end{bmatrix} \begin{bmatrix} T_0 \\ \vdots \\ \vdots \\ \vdots \\ \vdots \\ T_M \end{bmatrix}^n + \begin{bmatrix} E_0 \\ E_1 \\ \vdots \\ \vdots \\ E_{M-1} \\ E_M + S_M \end{bmatrix}^n$$

$$\ldots\ldots(4.46)$$

where, $S_M = -2\lambda_2 \beta_2 \left[(1 + T_M^n)^4 - 1 \right]$ and $\alpha_2 = 1 + 2\lambda_2 + \lambda\gamma_2$.

This system of linear equations was solved onward using LU Decomposition, see appendix 4.

4.7 Numerical results and discussion

The values of the dimensionless parameters involved in the simulation were obtained by using the values of the dimensional parameters shown in Table 4.1. During the process physical phenomena occurred at different time scales. Using the

dimensional parameter values, the approximate order of magnitude of these time scales A_1, A_2 and A_3 in equations. 4.33b, 4.38 and 4.40 respectively were evaluated and are listed in Table 4.2. It may be seen that the concentration and temperature distributions reached equilibrium much faster than the evolution of the pore.

Table 4.1. Dimensional parameter values used.

Sample thickness, $2b$	0.020 m
Slab+pore width, $2a_1$	$\approx 100 \ \mu m$
Ambient temperature, T_0	298.15 K
SiC thermal conductivity, k_{ts}	35.7 W/m K
SiC density, ρ_{p_s}	3110 kg/m^3
SiC specific heat, c_{p_s}	1100 J/kg K
SiC electrical conductivity, σ_0	4 x 10^6 1/Ω m
SiC emissivity, e	0.85
MTS molecular mass, M_{MTS}	0.1495 kg
H$_2$ molecular mass, M_{H_2}	0.0022 kg
Frequency, $\omega/2\pi$	2.45 GHz
Heat transfer coefficient, h_e	155 W/m^2 K
Reaction constant, k_1	3.0 Kg/m^{2}s
Activation energy, E_a	155 kJ/mole
Initial pressure, P	1.01 x 10^4 Pa
Lennard-Jones parameter, $\hbar$	0.4414 nm
Diffusion coefficient at STP, D_0	1.0

Table 4.2: Time scales of physical phenomena

Time scale	Represented parameter	Order of magnitude
Gas diffusion	A_2	$O(10^{-1})$
Thermal diffusion	A_1	$O(10^{-1})$
Pore evolution	A_3	$O(10^3)$

149

During the early stage of the process, since the gas diffusion time scale was much less than the thermal diffusion time scale, the dilute mixture of gases was able to diffuse into the preform whilst the latter was still moderately cool. This way, the concentration distribution became almost equal throughout the preform. The reaction started to take place when the preform temperature reached the critical temperature $T_c \approx 2.6$, which corresponds to a dimensional temperature of $1080\ K$ from equation (4.13), thus allowing concentration gradients to be established. A threshold power level was needed for the preform temperature to reach T_c. The dimensional time variable θ was taken to be $\theta = A_1$ throughout the next analysis.

4.7.1 Steady-state temperature solutions

The steady-state solutions were investigated for different initial porosity levels. The solutions were obtained by considering the numerical analysis in section 4.6.1. From expression (4.41), it was deduced that if the power parameter P_c was sufficiently small, then the steady state temperature could never reach the critical temperature for the reaction to occur. Figure 4.2 shows the S-shaped response curve obtained when the steady state solutions were plotted against their respective power levels. The constant c_1 in (4.42) was taken to be 0.8 in this case with an initial porosity level $\alpha_1 = 0.5$. The skin effect, which reduced the electric field within the perform (occurrence of thermal runaway) created the steady state temperature values represented by the upper branch. This response curve shows that there are either one or three possible steady state solutions for a given power; the case $P_c = 0.05$ is considered as an example where t_1, t_2 and t_3 are the three solutions. However, numerically only t_1 was obtained as a steady-state solution for $P_c = 0.05$ when the power level is increased monotonically. This was achieved by considering the dynamic version of this heating process. The solutions obtained are represented by the lower branch, the line $s_1 s_2$ and the upper branch. The line $s_1 s_2$ shows that a slight increase in power level at the point s_1 causes the steady-state temperature to evolve on the upper branch at s_2, which corresponds to thermal runaway. The solutions t_2 and t_3, can be obtained in practice by considering a power control heating system [116]. The latter however are quite difficult to produce.
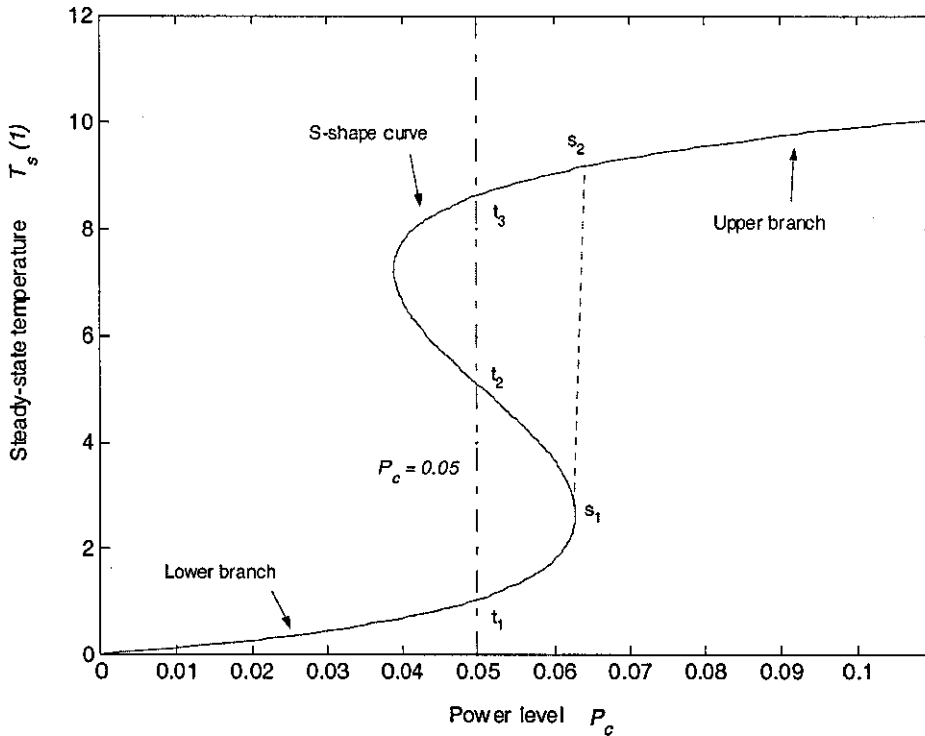
Figure 4.2: Plots of steady-state temperatures $T_s(1)$ for different power levels P_c. The constant c_1 was taken to be 0.8 and the initial porosity level $\alpha_1 = 0.5$

Figure 4.3 shows the numerical results obtained for various initial porosity levels when the constant c_1 in (4.42) was taken to be 3.0. It was observed that for small initial powers, the steady-state solutions for the different porosity levels α was limited well below the threshold temperature T_c (temperature at which the reaction is expected to occur in this analysis). The lower branches of the S-shaped curves represent these solutions. However, for larger power levels the steady state solutions are represented by the upper branches, where the skin effect began to significantly reduce the electric field within the preform as discussed above. It is also seen that these solutions are well below the temperature at which the material breaks down (≈ 6.5) [39], which means that the densification process of the preform can still continue. However, due to the skin effects the temperature of the preform/environment interface was slightly higher than the interior of the preform and . hence, the reaction rates being greater at this interface, the pores closed faster, choking off the reaction.

151
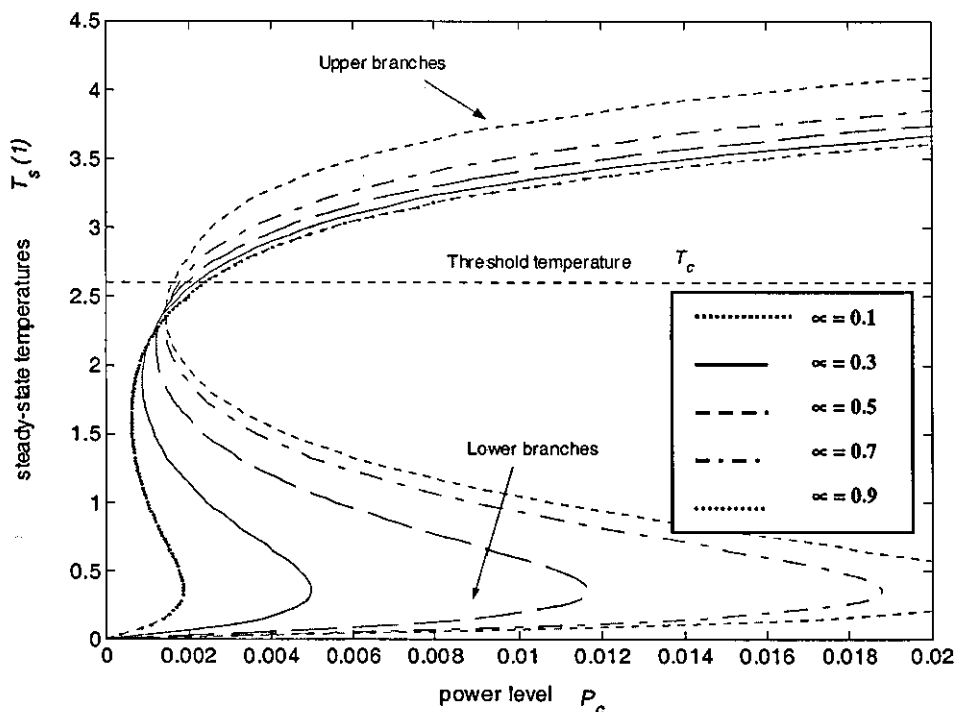
Figure 4.3: Plots of steady-state temperatures $T_s(1)$ for different power levels P_c. The constant c_1 was taken to be 3.0. It is observed that the upper branches of the curves lie below the 4.5 mark on the temperature axis, which is well below the temperature at which the material breaks down (≈ 6.5).

Figure 4.4 represents the corresponding numerical solutions for the steady-state temperatures when c was taken to be 0.8. It should also be noted in this case that higher power levels were needed to reach the threshold temperature for reaction to occur. It is observed from the figure that the critical power needed to reach the threshold temperature lay almost on the lower branches of the S-shaped curves for the different porosity levels. Thus the temperature in the interior of the preform was expected to be higher, allowing the reaction rate to be faster there, hence favouring an inside out densification. However, as the reaction proceeded, the porosity of the preform decreased. This allowed the temperature to increase to reach the upper branch of the response curve, which corresponded, to thermal runaway. It is observed from the figure that these steady state solutions occurred well beyond the temperature at which the material breaks down. A control power theory could thus be applied in this case to ensure rapid heating and proper densification of the preform without destroying the material through thermal runaway. It is also observed that in this case more power was needed to reach the threshold temperature compared to the first case. A similar

152

observation from these two figures is that increasing the amount of SiC in the structure lowered the temperature on the upper branch for a given power level.
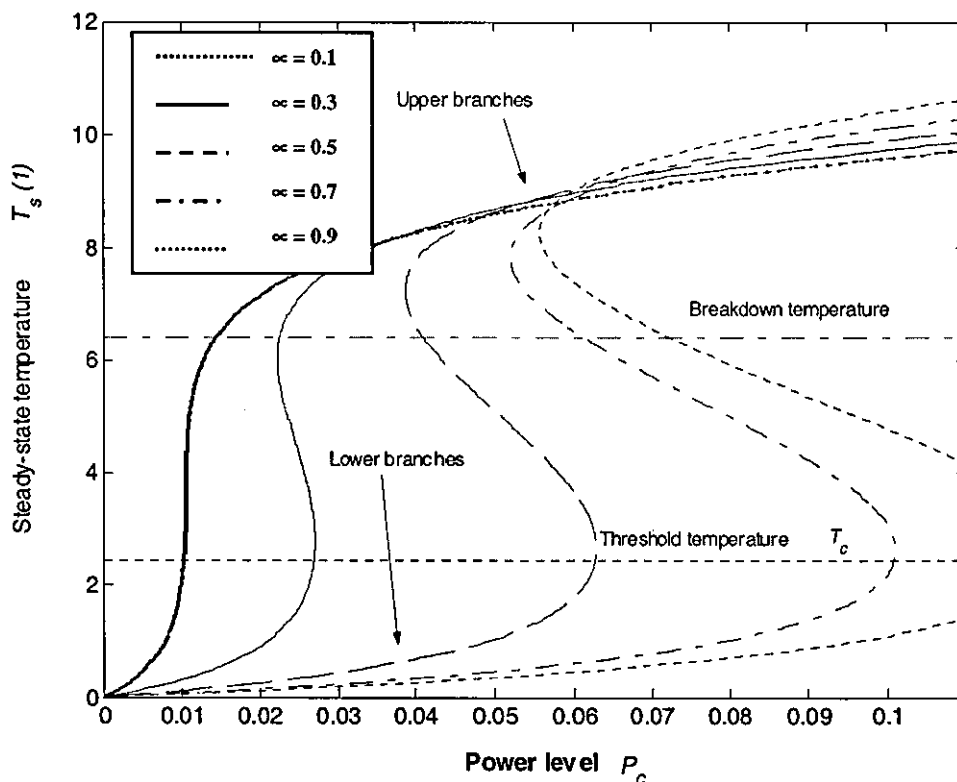
Figure 4.4: Plots of steady-state temperatures $T_s(1)$ for different power levels P_c. the constant c_1 was taken to be 0.8

4.7.2 Dynamic version of the MECVI process

The dynamic system where the pore boundary was allowed to propagate was considered next using the numerical analysis reported in section 4.6.2. The case where the constant $c_1 = 0.8$ was investigated by considering the non-dimensional power parameter $P_c = 0.02$, with an initial porosity level $\alpha_1 = 0.4$ and initial concentration of 0.05. Figure 4.5 shows the evolution of the interior temperature $T(0,t)$ and the perform/environment interface temperature $T(1,t)$ as a function of the time variable t during the early stage of the process. In addition, the magnitude of the electric field at the interior of the preform $|V_e(0,t)|^2$ as a function of t is also shown. Using the dimensional values in Table 4.1, the variable $t = 55$ corresponds to a dimensional time

of approximately 2.3 hours and the parameter $P_c = 0.02$ corresponds to a power density of approximately 50 Wcm^{-2}. It was observed that initially the electric field in the preform remained almost constant as it heated, however, prior to reaching the threshold temperature at which the reaction occurred, the magnitude of the electric field decreased significantly due to the skin effects occurring in the preform, thus the temperature appeared to be in thermal runaway.
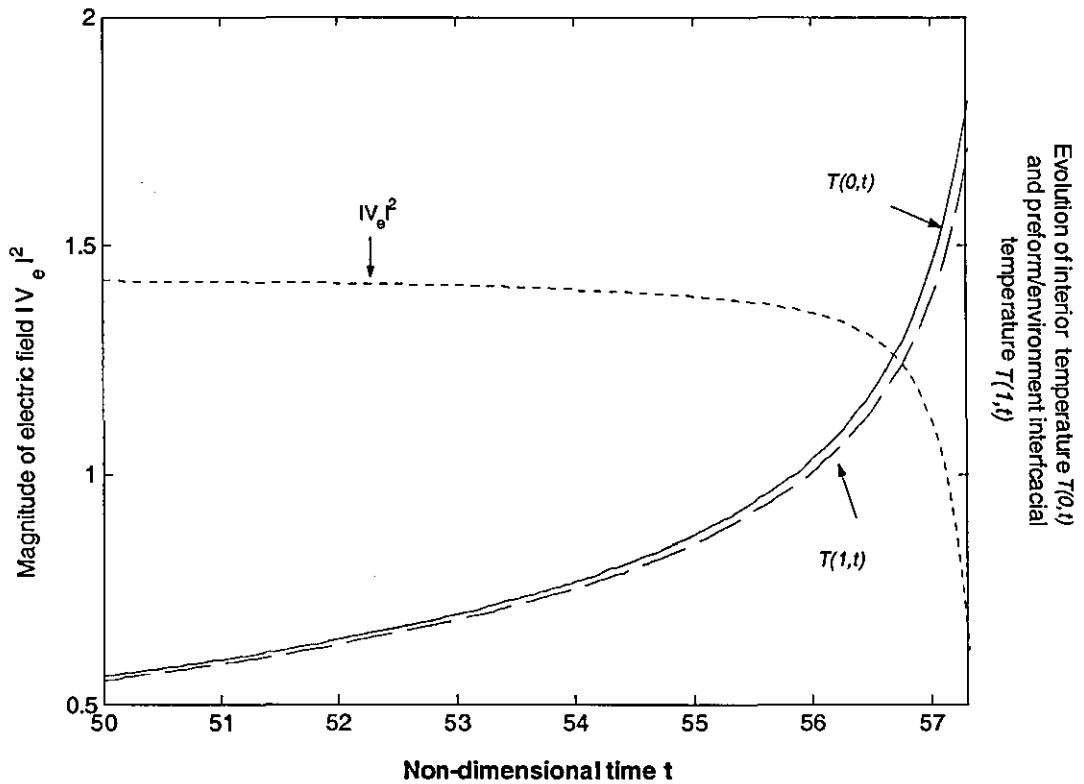
Figure 4.5: Showing the interior temperature $T_0(0,t)$, preform/environment interfacial temperature $T_0(1,t)$ and the magnitude of the electric field in the preform $|V(0,t)|^2$ as a function of time.

When the threshold temperature was reached the MTS gas decomposed within the preform to produce SiC, which was deposited on the pore walls. The interior temperature being slightly higher, figure 4.5, caused the local reaction rate to be faster, hence causing an inside out densification process to occur. However, later during the process when the density of the material increased, the skin effects occurring in the preform allowed the preform/environment interfacial temperature to become higher. This caused the pore mouth to close much faster compared to the interior of the pore

154

and the numerical simulation was terminated when the pore mouth at the preform/environment interface was closed; $F(1,t) = 0.001$ was chosen to represent this.

Figure 4.6 shows the evolution of a single pore wall/precursor gas interface $F(x,t)$ as a function of the distance x from the centre of the preform at various times t, the preform centre and the preform/environment interface being located at $x = 0.0$ and $x = 1.0$ respectively. It can be clearly seen that the pore closes faster at the preform/environment interface as explained earlier leaving behind a small amount of porosity. As will be shown in the coming numerical results, this trapped porosity could be decreased by varying the operating conditions; viz the initial concentration of MTS and the power level.

Figure 4.6: Evolution of the pore boundary $F(x,t)$ at $t = 2.50\,\mathrm{hrs}$, $t = 4.17\,\mathrm{hrs}$, $t = 6.25\,\mathrm{hrs}$ and $t = 8.33\,\mathrm{hrs}$, initial porosity level $\alpha = 0.4$. It can be seen that the pore closes faster at the preform/environment interface where $x = 1$

The evolution of the concentration profiles of the precursor at different times, t, as a function of the distance, x, from the centre of the preform is shown in figure 4.7. As discussed at the beginning of this chapter, the dilute mixture of gases was able to diffuse into the preform whilst the latter was still relatively cool during the early stage of the process, allowing the concentration distribution of the precursor to be uniform throughout the preform, that is $C(x,t) = 1.0$. However, a significant drop in the concentration in the interior of the preform during the early stage of the process was observed when the reaction process started, figure 4.7. The concentration at $t = 2.38$ hrs dropped from 1.0 to a value less than 0.6 at $t = 2.5$ hrs at the preform centre. However, the concentration decreased much more slowly as the reaction process

Figure 4.7: Gas concentration profiles $C(x,t)$ across the preform at the values $t = 2.50$ hrs, $t = 4.17$ hrs, $t = 6.25$ hrs and $t = 8.33$ hrs. It may be seen that there is a large initial drop in the concentration in the interior of the preform at the beginning of the processing stage, which slows down over time.

156

continued. This initial drop was due to the immediate depletion of the precursor gas when the reaction process began, which then relaxed over time through the diffusion process that occurred.

At the beginning of the reaction processing stage, the temperature of the preform $T(x,t)$ continued to increase beyond the threshold temperature until the steady-state solution was attained, with the temperature at the preform/environment interface being slightly higher due to the skin effects discussed earlier. It may be observed from figure 4.8 that as the amount of matrix SiC in the preform increases due to the chemical reactions taking place, the steady state temperature decreases slowly with time. This can be explained as follows: more power is needed to keep the preform temperature at a required level as the latter gets densifies. However, since the preform was being heated by a fixed power P_c in this analysis, the steady state temperature would decrease with increase in densification of the preform. This is also clearly observed from the S-shaped curves shown in Figure 4.3 obtained by considering the steady-state version of the problem.

4.7.3 Control densification of the preform

As discussed above, the temperature being higher at the preform/environment interface together with a higher concentration of the precursor present at that point caused the rate of the reaction to be greater, hence closing the pore mouth much faster compared to the interior of the pore. This allowed the pore width at the preform/environment interface to be smaller than that at the centre of the preform. Figure 4.9 shows a schematic diagram of the filling of one pore during the process, where $F(x,t)$ represents the moving solid/gas interface as the reaction proceeds. The input power level P_c and the initial concentration are the parameters that can be used to control the densification of the preform and the processing times, t_f, at which the simulations terminate.
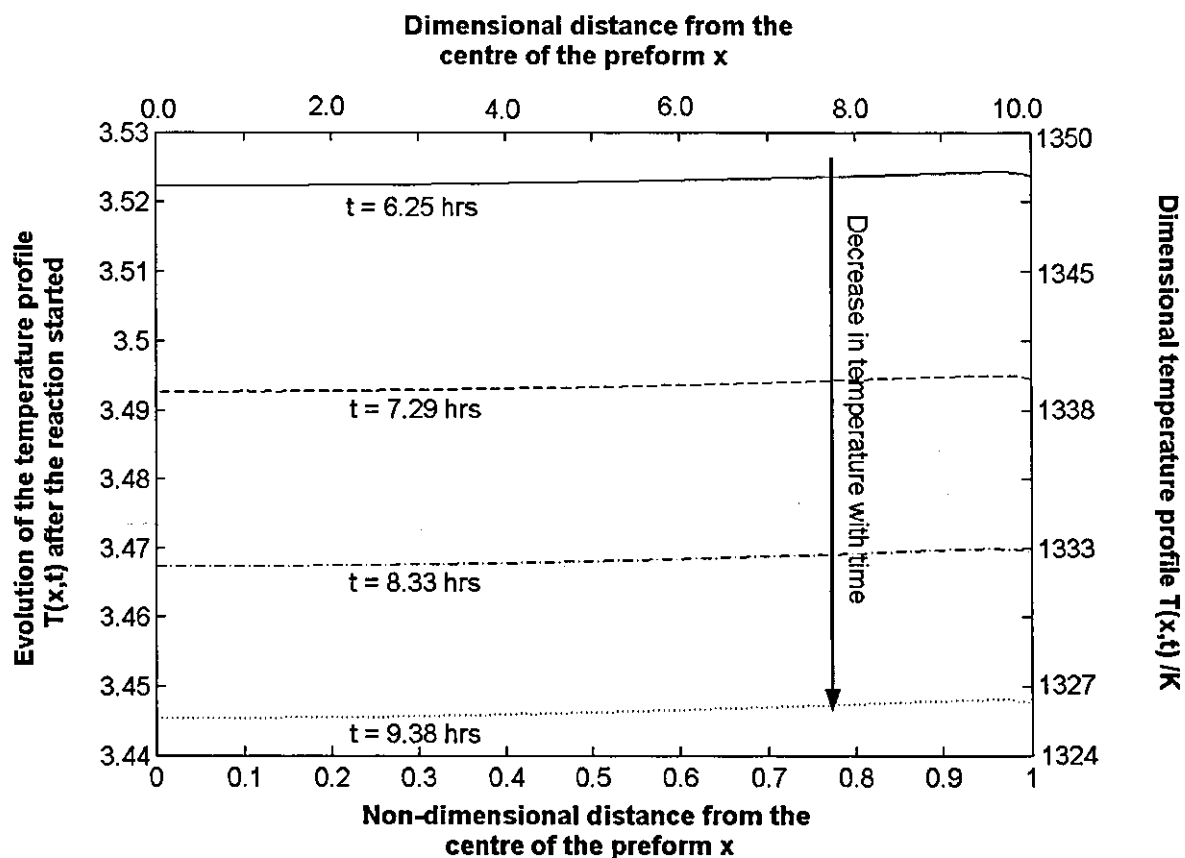
Figure 4.8: Temperature profiles within the preform at the times $t = 6.25\,\text{hrs}$, $t = 7.29\,\text{hrs}$, $t = 8.33\,\text{hrs}$ and $t = 9.38\,\text{hrs}$. It may be observed that the preform/environment interfacial temperature, at $x = 1$, is slightly higher due to the skin effects. Also during the process, the steady state temperature decrease with increase in the amount of SiC in the structure.

As indicated earlier, the stopping criteria for these simulations was when the pore width at the preform/environment interface closed, that is, when the pore wall/precursor gas interface, $F(1,t)$, reaches the axis of the pore; the condition $F(1,t) = 0.001$ was chosen to represent this. From figure 4.9 it may be observed that it was sufficient to control the final position of the pore width $F(0,t)$ at the centre of the preform in order to control the densification of the whole preform; by reducing the final position of $F(0,t)$, a more densified preform was obtained. It is noted that $F(0,t)$ is the position of pore wall/precursor at $x = 0$ at time t.
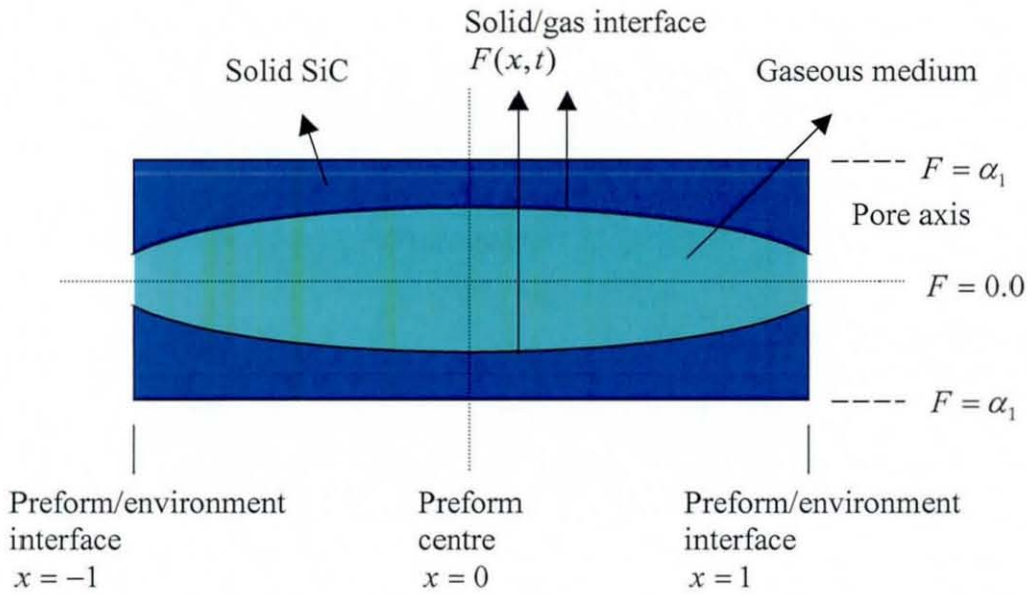
Figure 4.9: Schematic of the filling process of one pore during the MECVI process

Figure 4.10 shows the final position of the pore width $F(0,t)$ for different values of P_c for given initial porosity levels, $\alpha_1 = 0.1, 0.2, 0.4$, and an initial concentration of 0.1. It is seen that larger power levels lead to better densification of the preform. However, for smaller initial porosity levels, for example in the case $\alpha_1 = 0.1$, the final position of $F(0,t)$ didn't improve much with increase in power levels. Thus the final densified preform was not significantly changed by an increase in power level in that case. Further it was observed that for larger initial porosity levels, more trapped porosity remained within the preform. For example in the case $\alpha_1 = 0.4$, the final position of $F(0,t)$ was much higher compared to those obtained when smaller initial porosity levels were considered. This meant that less densified preforms were obtained if samples with larger porosity levels were used.

Figure 4.11, shows the final position of the interior of the preform $F(0,t)$ for various inlet concentrations of the precursor gas, MTS. It was observed that $F(0,t)$ decreased significantly with increase in the concentration. This implied that the

porosity of the preform decreased considerably to produce a denser composite. It was also observed that the final position of $F(0,t)$ was more or less the same for the different initial porosity levels. This meant the final density of the composite was not affected by the initial porosity level in this case. It is also seen that the final position of $F(0,t)$ remained almost constant with further increase in the inlet concentration for each of the porosity levels. This implied the final densified preform was not much improved beyond certain inlet concentration of MTS.
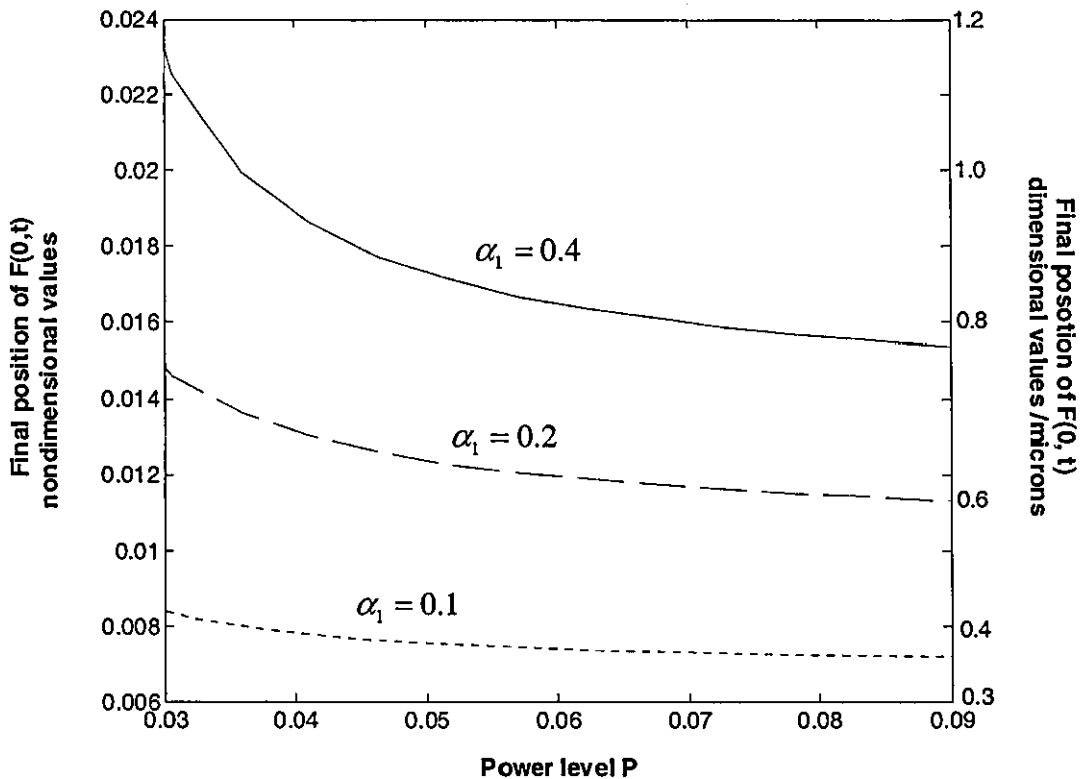
Figure 4.10: Final position of the pore width $F(0,t)$ at the interior of the preform as a function of input power levels for $\alpha_1 = 0.1$, $\alpha_1 = 0.2$ and $\alpha_1 = 0.4$. For larger initial porosity, higher power levels leads to better densification.
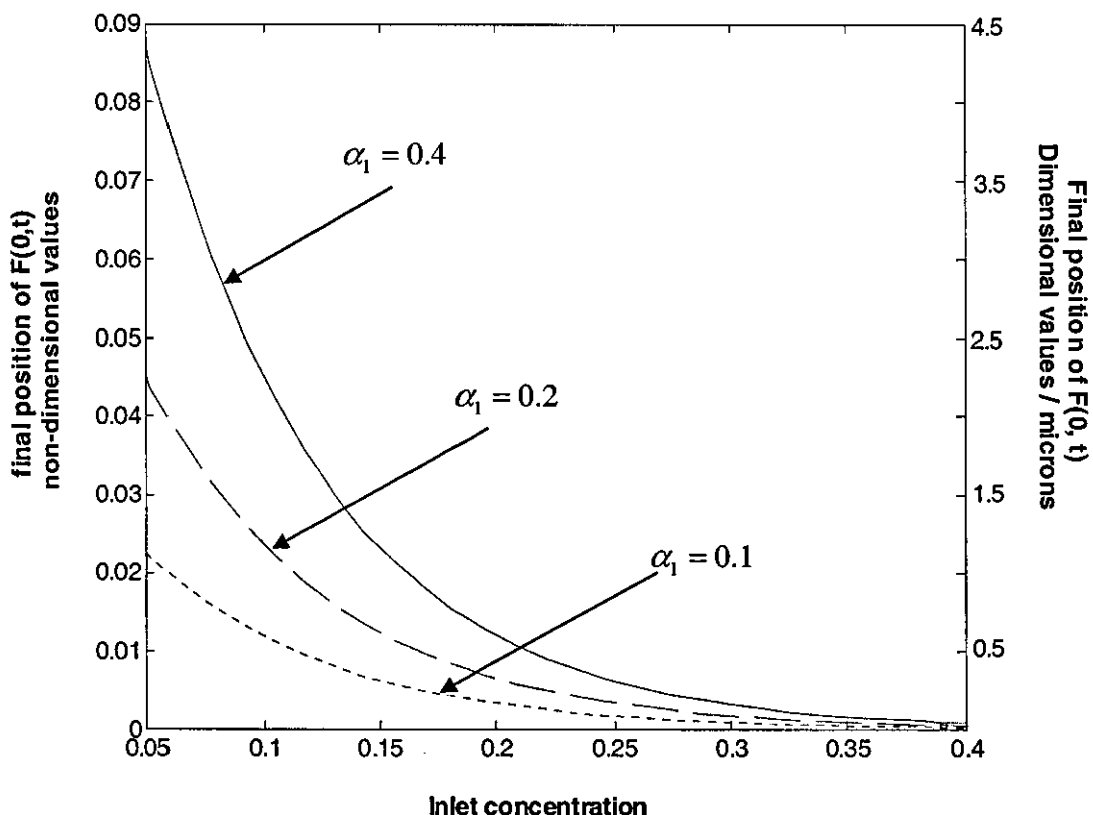
Figure 4.11: Final location of the pore width $F(0,t)$ at the interior of the preform as a function of initial concentration of MTS for $\alpha = 0.1$, $\alpha = 0.2$ and $\alpha = 0.4$. Larger initial concentrations lead to better densification.

Figure 4.12 shows the final processing time, t_f, (time it takes for the pore to close at the preform/environment interface) as a function of input power density for initial porosity levels of $\alpha_1 = 0.1$, $\alpha_1 = 0.2$, $\alpha_1 = 0.4$. These simulations were performed by keeping the inlet concentration fixed at 0.1. It can be seen that increasing the input power density, P_c, decreased t_f for each α_1, however, the effect was relatively small. This observation was also seen when the inlet concentration of MTS was increased, keeping the input power fixed, however the effect was even smaller, figure 4.13. Thus it can be concluded that the final processing time was almost unaffected by the MTS inlet concentration.

161
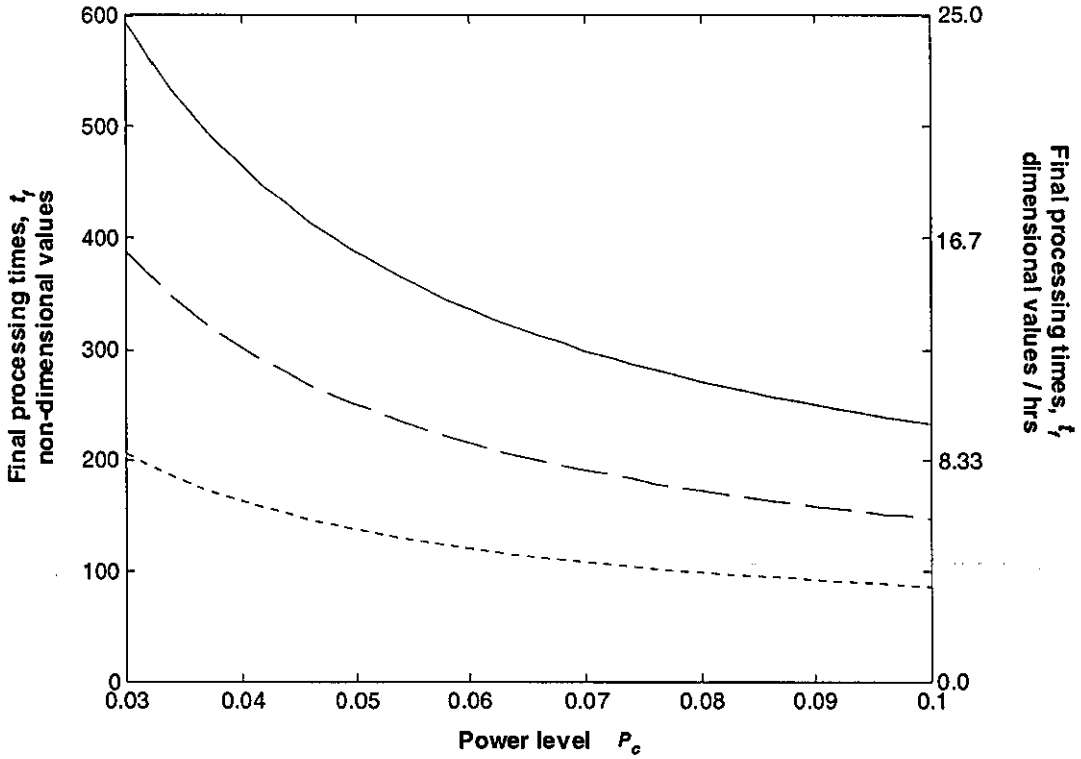
Figure 4.12: Final processing times t_f as a function of input power levels for initial porosity level $\alpha_1 = 0.1$, $\alpha_1 = 0.2$ and $\alpha_1 = 0.4$, with inlet concentration 0.1.
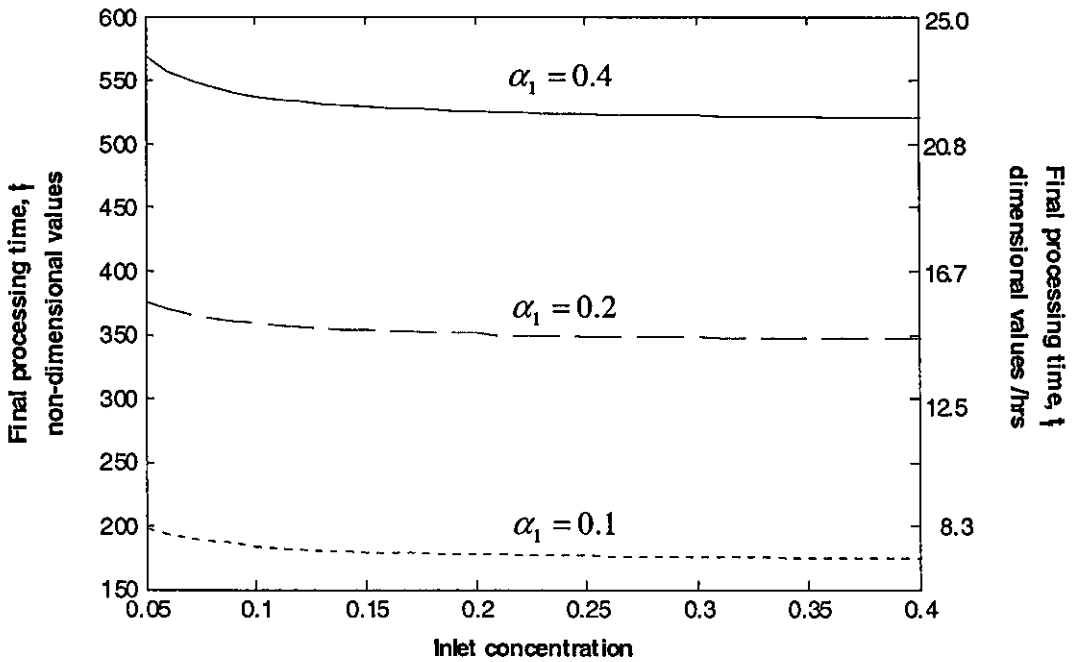
Figure 4.13: Final processing times t_f as a function of initials concentrations of MTS for initial porosity level $\alpha_1 = 0.1$, $\alpha_1 = 0.2$ and $\alpha_1 = 0.4$, with initial power level of 0.02.

4.8   Summary

A one-dimensional mathematical model describing the process microwave enhanced chemical vapour infiltration (MECVI) process has been developed and analysed. The model helped to investigate the infiltration of a porous SiC preform by allowing gaseous reactants to flow through the preform by diffusion transport. An asymptotic analysis producing homogenized equations describing the microwave heating and the transport/reaction processes was performed. The infiltration process of a single pore was considered and the evolution of the pore boundary was numerically obtained by solving the resulting homogenized set of equations. The model took into account the effects of the changing materials properties, the heat of reaction and non-uniformities in the gas concentration within the preform on the infiltration profiles and processing times during the process. It also investigated the important issues of non-uniform heating and thermal runway during microwave heating of the porous SiC preform.

It was found that for a fixed input power, as the amount of porosity in the preform increased the steady state temperature eventually moved to the upper branch of the S-shaped curve that corresponds to thermal runaway. It was seen that the steady-state solutions lying on the upper branch were significantly less than the temperature at which the material breaks down, thus allowing further densification without damaging the material. However, due to the skin effects, the preform/environment interfacial temperature was slightly higher than that of the interior. This allowed the pore to close faster at the boundary, choking off the reaction in the interior of the preform. This caused entrapment of porosity in the interior of the preform that would have unfavourably affected the mechanical properties of the final densified product. This could be overcome by applying a control power theory to prevent thermal runway.

Although the model developed was one dimensional, the numerical results predicted some important trends including the skin effects. This gave a considerable degree of insight in understanding the MECVI process under diffusion driven gaseous precursors. However, it may be concluded here that for better quantitative comparison with experimental data, the dependence of the material properties on porosity and temperature, together with experimental details during this complicated process, are still required.

CHAPTER 5:

GENERAL DISCUSSION

5.1 Introduction

In line with the models developed during this research for Microwave Enhanced CVI (MECVI) and the numerical results obtained from the simulations, this discussion chapter is divided into two main parts. The first section discusses the numerical results obtained and mainly focuses on a comparison between the experimental and literature results. For convenience, a general comparison in the trend of the numerical results obtained with their experimental counterparts is performed here; the results obtained from the experimental work carried out by Jaglin [39] are considered most during this study. Figure 3.1 in Chapter 3 shows the schematic diagram of the MECVI apparatus used during the latter experimental investigation. The second section discusses the mathematical aspects and difficulties faced upon developing the models and examines their consequences on the latter. Previous theoretical models developed in the past by various authors describing the process are also considered here for a comparison.

5.2 Validation of numerical results

5.2.1 Microwave heating of SiC preform before infiltration by CVI

The results of temperature profile measurements made on SiC fibre preforms during the initial microwave heating stage are considered here [39]. In this experimental work, the temperature at the centre of the preforms was controlled using a type-K thermocouple and the input microwave powers needed to heat the samples were dependent on the set temperatures. The plot of the relative temperature difference between the centre and points across the SiC foams for four central control temperatures ranging from 1073 to 1373 K are shown in figure 5.1. The bell-shaped curves are typical of the inverse temperature profiles generated by volumetric microwave heating. Similar results were obtained from the numerical simulations, see figure 3.11. From figure 5.1, it can be seen that when the control temperature was

decreased, the temperature profile flattened across the sample. From figures 3.13 and 3.14, the numerical results demonstrated that both the temperature and the thermal gradient were dependent on the input power; a decrease in the latter caused both temperature and thermal gradient to decrease in agreement with the experimental results.
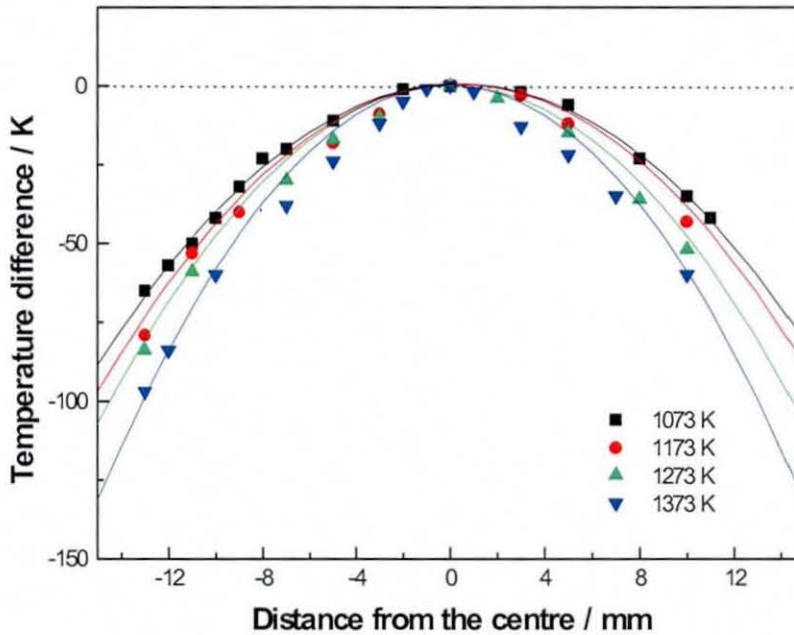
Figure 5.1: Temperature profiles recorded across a SiC preform with dimensions 50×10 mm, in air for central set point temperatures of 1073, 1173, 1273 and 1373 K. The microwave power was allowed to vary in the range 0.36–3.60 kW. Reproduced from reference [39].

The numerical results also showed that the temperature levels could be varied by controlling the degree of external cooling via the heat transfer coefficient, h_e. It was seen that an increase in h_e caused the temperature to decrease without affecting the thermal gradient significantly. Thus a proper control on both the input power and h_e showed that the required temperature and temperature gradient could be achieved, see figure 3.17. In the experimental work, this was performed by using insulating materials to surround the sample, e.g. porous alumina, that were relatively transparent to microwave radiation. In this case it was seen that the use of the alumina allowed the temperature profile to be tailored by maintaining the desired temperature. This was due

to the fact that both radiative and convective heat losses at the boundaries were limited with the use of the insulating foams. This qualitatively validates the numerical results; however the central temperature of the preform was only controlled during the experiment and thus it was impossible to see the quantitative effect of the insulations alone on the temperature level by maintaining a fixed input power.

5.2.2 Densification pattern obtained during infiltration of SiC preform by MECVI

Figure 5.2 represents raw X-ray absorption scans with their colour enhancement for SiC samples obtained at different times during the infiltration process [39]. It can be observed that densification progressed from the inside out, the densifying region at the centre first becoming broader and denser as shown in the figure. After 16 and 24 h of MEFCVI, the densification mainly occurred in the central parts of the sample spreading outwards. The density pattern is modified at this stage as the relative density increased rather non-uniformly across the sample. Standard conditions were used in this experiment; the temperature at the centre, $T = 1273\,\text{K}$, the mixture flow rate, $Q = 300\,\text{ml/min}$ and the total pressure, $P_t = 70\,\text{kPa}$. Similar trends were observed in the numerical results obtained using the MEFCVI model, see figure 3.37. However, the experimental results only accounted for densification variation along the diameter of the sample. The numerical results on the other hand also showed that densification variation existed along the central axis of the preform, which affected the net infiltration of the preform during the process. The results showed that the region with highest densification moved from the centre towards the inlet of the preform before finally propagating radially across the sample. Further analysis would have been required during the experimental work to confirm that this effect really does occur.

5.2.3 Effect of the processing variables during MECVI

5.2.3.1 Temperature and thermal gradient

The experimental results showed that the temperature profile throughout the fibre preform greatly influenced the infiltration. Since only the temperature at the centre of the preform was controlled, the required thermal gradient variation across the

latter was obtained by using different types of insulation thickness. The results demonstrated that higher temperatures promoted faster decomposition of MTS to SiC, hence resulting in higher matrix growth rates. The numerical results on the other hand provided similar observations and the model explained from the standard assumption that the reaction rate is exponentially dependent on temperature. However, it should be

(a) Initial
$\rho_r = 29.0\%$

(b) 2 h
$\rho_r = 32.0\%$

(c) 4 h
$\rho_r = 34.7\%$

(d) 6 h
$\rho_r = 36.8\%$

(e) 8 h
$\rho_r = 38.0\%$

(f) 16 h
$\rho_r = 48.1\%$

(g) 24 h
$\rho_r = 55.4\%$

75%
65%
55%
45%
35%
<25%

Relative
Density ρ_r
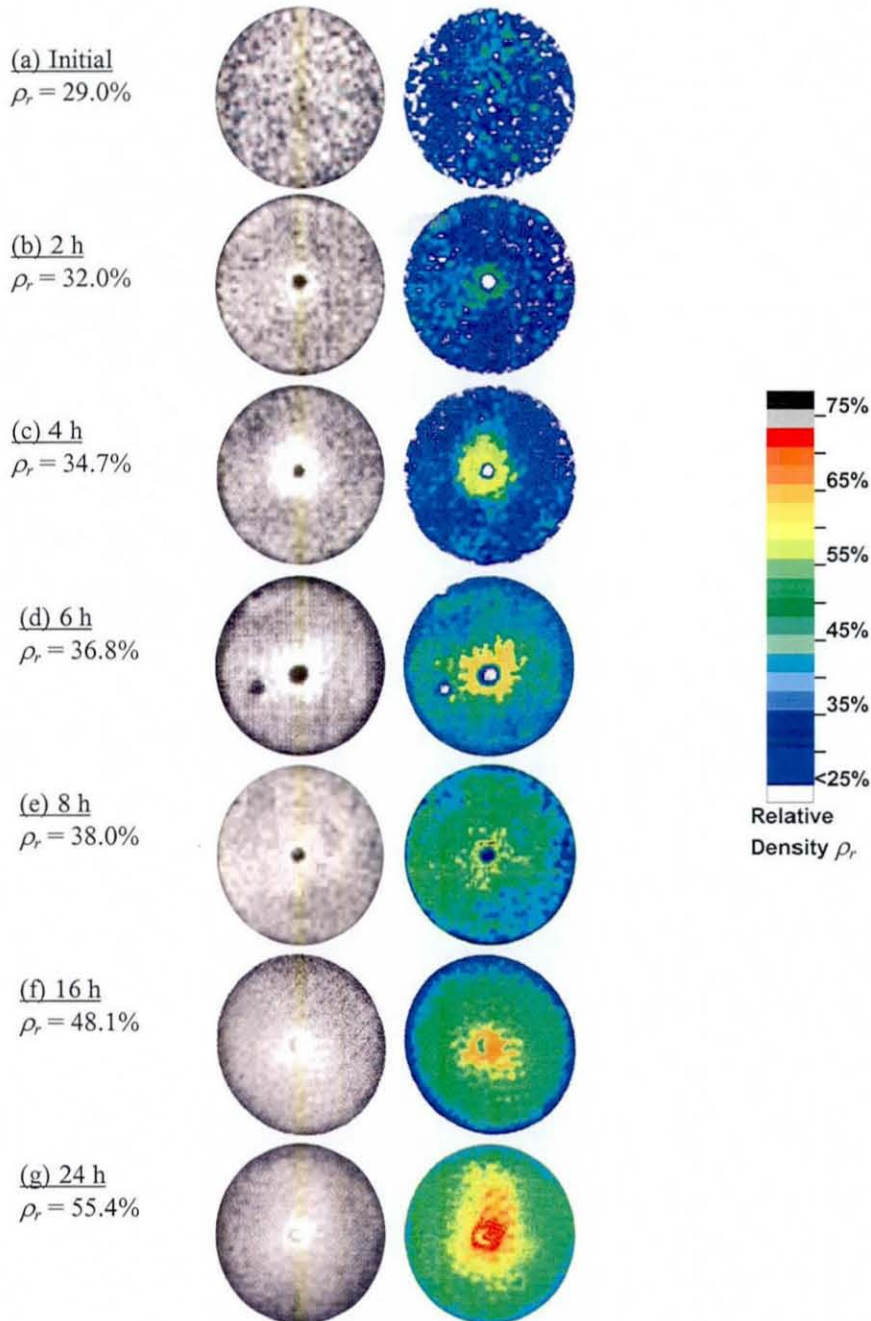
Figure 5.2: (a)-(g) X-ray absorption scans for standard SiC preforms infiltrated by MECVI after 0, 2, 4, 6, 8, 16 and 24 hours. Raw scans (black and white) and enhanced scans (colour) are presented. Reproduced from reference [39].

noted that in the experimental work [39], the stoichiometry of the deposited material the experimental varied with reaction temperature, excess carbon being produced with an increase in temperature. Whilst this further supports the idea of enhanced reactivity, the model had to assume the formation of SiC having constant stoichiometry.

It was also experimentally oberved that the increase in infiltration rates with temperature slowed down above 1273 K. Based on the observations made from the numerical results in the present work, this can be explained as follows. The increase in processing temperature led to a higher depletion of the reacted species, hence decreasing the accessible porosity inside the preform and creating a larger MTS concentration gradient across the sample. The latter combined to decrease the infiltration rate

Both the experimental and numerical results showed that a decrease in thermal gradient across the sample resulted in relatively more uniform infiltration. In the numerical simulations the thermal gradients were altered by changing the input microwave power. However, the 1-D model showed that a slight increase in input power, or even maintaining the same input power during MECVI could cause thermal runaway to occur, where the temperature at the boundary could become higher than that at the centre of the preform. Then the locally higher temperature and MTS concentration cause faster deposition at the boundaries, hence choking off the reaction at the centre of the preform. This scenario is observed experimentally in figure 5.3,
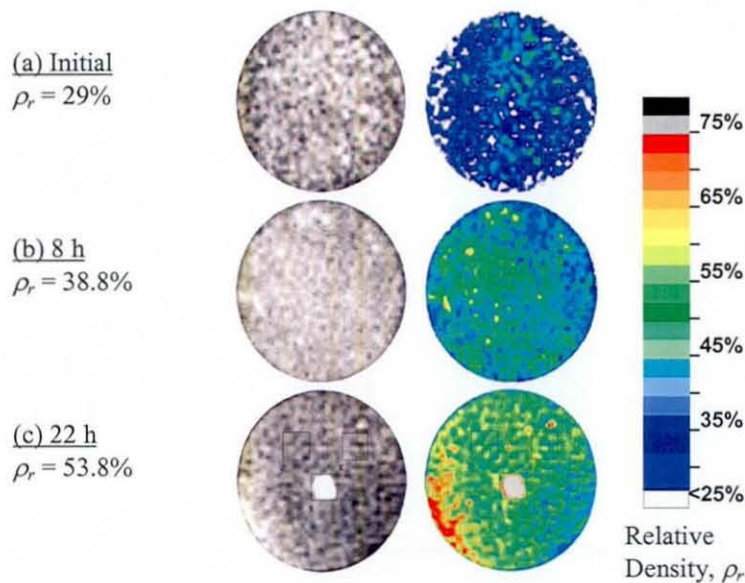

Figure 5.3: (a)-(c): XRA scans for standard SiC sample infiltrated by MECVI after 0, 8 and 22 h. Raw scans (black and white) and enhanced scans (colour) are presented. The preform in this case was insulated using alumina. Reproduced from reference [39].

where a small thermal gradient was created during the infiltration of the sample by increasing the thickness of the porous insulation around the sample (alumina). The latter reduced the degree of heat loss at the boundaries considerably. As the infiltration proceeded, the temperature at the sample edges increased higher than that at the centre resulting in hot-spot formation, causing locally higher deposition, as seen in figure 5.3.

5.2.3.2 Total gaseous precursor flow rate

It is noted here that in the experimental work carried out on MECVI [39], the hydrogen flow rate and the inlet pressure were maintained at constant values. During the infiltration process the outlet pressure was decreased gradually along with a decrease in the MTS flow rate. In the MEFCVI model, the hydrogen flow rate was assumed to be the gaseous mixture flow rate (due to the ratio MTS:H_2 being 1:9) and was kept constant. Further, the inlet pressure was allowed to increase due to the increase in back pressure as infiltration progressed. Thus a complete quantitative comparison between both results is not feasible. Nevertheless, a comparison of the general trend of the results can still be made.

The experimental results showed that both the infiltration rate and the matrix growth rate increased linearly with increase in hydrogen flow rate, see figure 5.4. Also it is observed that larger flow rates resulted in higher gas velocities through the pores, which reduced the residence time of the gases in the preform structure. This in turn resulted in the residence time becoming smaller than the required reaction time. The effect of the hydrogen flow rate on the efficiency of the reaction was seen from the numerical results (section 3.4.3.2), where it was described that the increase in the flow rate decreased the MTS concentration gradient inside the preform, thus allowing a faster reaction rate that eventually resulted in more uniform infiltration. The model also showed the variation in the infiltration across the thickness of the preform with increase in flow rate, see figure 3.44. Higher flow rates produced greater infiltration at the outlet but less deposition was observed at the preform inlet. Similar observations were made in the model developed by Gupte et al [82] where conventional heating was used to produced thermal gradients across the preform during forced flow CVI. Both models showed that the back pressure increased faster with increase in flow rate, thus reducing the processing time slightly. However, the model developed by Gupte et al also showed

that a limiting flow rate existed beyond which overall densification was decreased. No such limit was found in the present work. Such high flow rates were not investigated here.
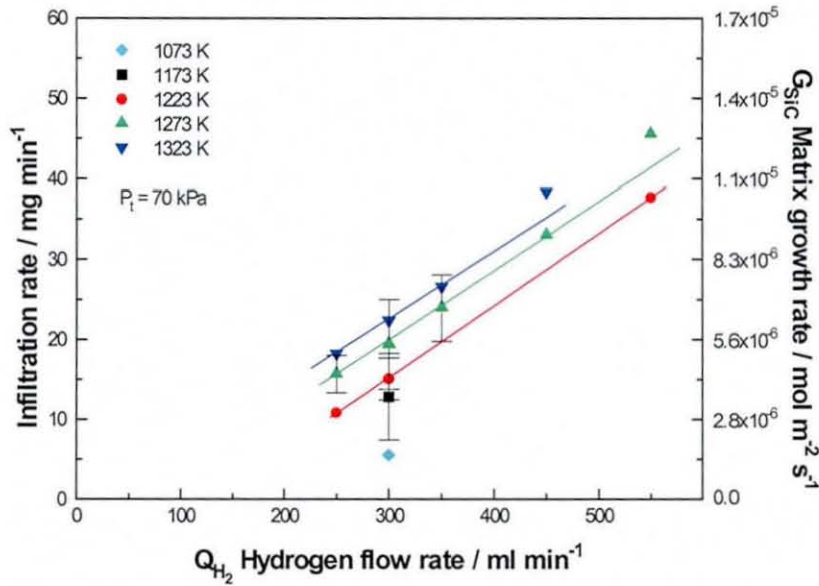
Figure 5.4: SiC matrix growth rate on SiC fibre preforms as a function of the hydrogen flow rate for infiltration temperatures between 1073 and 1323 K at total pressure, P_t = 70 kPa. Reproduced from reference [39].

5.2.3.3 Total pressure and MTS concentration

The SiC matrix generated by MECVI displayed different morphologies when the "total pressure" of the system was modified [39]. It is noted here that the total pressure, P_t, defined in [39] was actually the pressure difference across the sample and the MTS:H_2 molar ratios varied with the pressure. At low pressure, supersaturation was high, that is, the molar ratio was low. Infiltration rate variation with the system pressure during the experiment is shown in figure 5.5. It is observed that a maxima was observed, with the highest value occurring at about 70 kPa. This effect was also observed in the numerical results, see figure 3.45 and 3.46. In the latter, the inlet pressure was allowed to vary independently whilst the outlet pressure and the molar ratio were maintained constant. The numerical results showed that an initial increase in outlet pressure caused more uniform infiltration across the preform, however, further increases resulted in an increase in the final porosity gradient and total porosity across the sample. Thus an optimum outlet pressure existed beyond which the sample remain less densified.
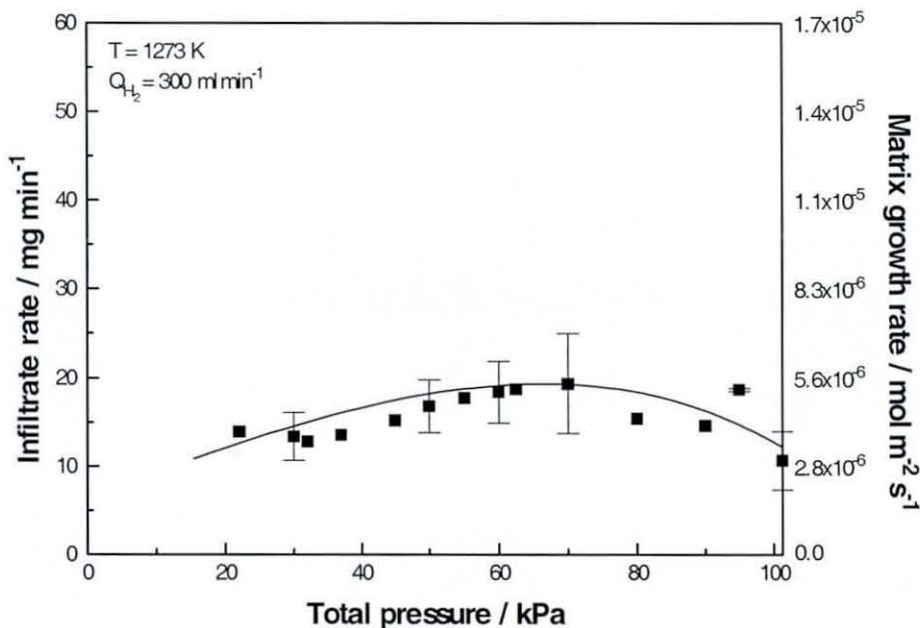
Figure 5.5: SiC matrix growth rate on SiC fibre preforms (insulated using porous alumina) against the "total pressure" (temperature, $T = 1273$ K, hydrogen flow rate, $Q = 300$ ml min^{-1}). Reproduced from reference [39].

The effect of the initial MTS concentration could not be accounted during the experimental work since the flow rate of the latter was dependent on the total pressure of the system. However, comparing the results of the present work with theoretical models developed earlier [37,38,73], similar conclusions were found. An increase in the concentration has almost no effect on the overall infiltration profile when forced flow condition is applied, through minor changes are observed in the final processing time. During diffusion transport however, the internal porosity is decreased with increase in inlet MTS concentration, see figure 4.13.

5.3 Mathematical aspects and difficulties of microwave enhanced CVI modelling

As mentioned in the literature survey, microwave enhanced CVI is a complex process, which is affected significantly by the process variables such as temperature, pressure, flow rate, reactant concentration and their gradients. The mathematical models developed during the course of this research can help to understand the effects of altering those variables. Similarly, the better their effects are understood

experimentally, the more accurately they can be incorporated into the models allowing their optimization. This will eventually result in performing real-time simulation of the evolving structure inside the process to produce both qualitative and quantitative numerical results, which would then significantly reduce the cost of fabricating composites by MECVI. But, at the same time, knowing the effects of the mathematical aspects that contributed to the models and the difficulties faced in developing the latter are essential. This section describes some of these important features.

5.3.1 Fibre preform structure modelling

In the two-dimensional model described in Chapter 3, the fibre preform was discretized into a finite number of unit cells, see figure 3.3. The edges and the diagonals of each unit cell represented part of the fibre bundles present in the preform. During microwave enhanced CVI under forced flow, SiC was deposited on the surfaces of these fibre bundles, allowing the matrix to grow radially with respect to the axes of the bundles. In the one-dimensional model, the preform was assumed to be composed of fibrous ceramic layers stacked together with a void space present in between them. During MECVI, the gaseous reactant diffused through the void spaces and decomposed to form the matrix on the layers. This caused the layers to grow, thereby reducing the porosity inside the preform. However, in these two types of ceramic porous structure modelling, the intratow porosities that existed within the fibretows themselves were neglected. In the 2-D model, the fibre bundles were assumed completely dense and only the porosities present between the bundles (intertow) were considered during the infiltration process. Similarly, in the 1-D model, the intratow porosities inside each fibrous layer were neglected.

5.3.1.1 Influence of intratow and intertow porosities on densification pattern during MECVI

The experimental work carried out by Jaglin [39] showed that both the infiltration of the intertow and intratow porosities contributed significantly to the overall densification pattern, depending on the process conditions during microwave enhanced CVI. It was found that when the temperature, temperature gradient of the preform and precursor flow rates were controlled appropriately, the intratow porosity

was infiltrated before the matrix started to grow significantly within the intertow porosity. However, under certain process conditions, it was also seen that the intertow porosities began to fill substantially before the intratow porosities were infiltrated completely. This created inaccessible intratow pores within the final densified composite. During forced flow chemical vapour infiltration, the gaseous precursor flows through the intertow porosity inside the preform by the applied pressure gradient and then diffuses though the intratow porosities. Thus diffusion transport predominantly caused infiltration of these intratow porosities. The 1-D model, which accounts for diffusion transport during MECVI, can be used here to understand the infiltration process.

A complete model, however, where both the intertow and intratow porosities are considered during microwave enhanced CVI, would be fairly complex to investigate. This is mainly due to the complexities involved in heating a porous ceramic preform with microwaves. One needs to account for the fact that only the solid parts of the fibre preform, which also have irregular shapes, interact with microwaves to generate heat. During this development, a scattered electromagnetic (EM) field would be created around and within the sample. In the 2-D model where the internal porosity was neglected during the analysis, only the presence of a scattered EM field around the sample needed to be considered.

5.3.2 Electromagnetic heating modelling

In the practical microwave heating system seen in figure 3.1, the SiC sample was placed in a resonant microwave cavity. It was observed that the dimensions of the cavity were much larger than the size of the preform. To determine the electromagnetic and thermal distribution within the preform, the equations for electric and magnetic fields would have to be solved throughout the cavity and the numerical techniques described in sections 3.4.1 employed. However, since the electrical and thermal properties of the preform vary during MECVI, large computational time and computer memory would be needed to obtain numerically the distributions. During the development of the models, considering the dimensions of the sample and the cavity, the preform was assumed to be in free space occupying an arbitrary cross section. This allowed the fields' equations to be solved inside the sample only, hence avoiding the

time and memory constraints. In the 2-D model, four identical electromagnetic plane waves were allowed to propagate through the sample from its four sides as shown in figure 3.2. This generated a scattered EM field around the sample, which was not calculated in the numerical study. The results obtained from the EM-model have demonstrated that the temperature distributions within the preforms are sensitive to the dimensions of the materials. In line with this analysis, methods such as periodical shifting of phase of microwaves [31] are required to reduce the sensitivity. In the 1-D model, two incident EM plane waves were impinged symmetrically onto both sides of the preform as shown in figure 4.1. This resulted in two reflected fields outside the sample whose effects were neglected since the sample was assumed to reside in free space. Considering the microwave cavity during the EM heating, however, would have incorporated the effects of the scattered and reflected fields in the 2-D model and 1-D model respectively.

5.3.2.1 Influence of SiC matrix on dielectric properties

It has been shown that the dielectric properties of the deposited matrix material can have significant impact on the absorption of microwave energy and hence thermal profile evolution during MECVI [39]. In the 2-D model, during the heating stage the dielectric properties were modelled as quadratic functions based on the experimental data [147]. Considering the analysis performed with the EM-model, where the input microwave power, P_{inc} was maintained constant, it was found that the temperature gradient across the preform increased as the overall porosity of the medium decreased. This implied that less input power was needed to reach the set temperature for more porous preforms and that as the porosity decreased during the infiltration process more power would be required to maintain the set temperature. Similar observations were made during the experimental work [39], where it was observed that the temperature of the infiltrating preform decreased during the infiltration process. The deposition of the SiC on the fibres (that is increase in the amount of material) was considered responsible for this; it was speculated that the matrix absorbed microwave energy less efficiently than the initial fibre preform. If correct, this meant that the matrix formed and fibre preform had different dielectric properties. The experimental work by Devlin et al [149] also showed that stoichiometric variations influenced the microwave absorption

174

distribution, however they found that the deposition of a Si-rich SiC matrix dissipated microwave energy as well as the fibre preform reinforcement. In the 2-D model the effect of the deposited SiC on the temperature profile was not considered, since the EM and FCVI model were decoupled. Conversely, in the 1-D model this effect was taken into account, however the dielectric properties of both the deposited matrix and the fibre preform were considered to be the same due to a lack of experimental data. The dielectric properties were modelled as exponential functions based on the data obtained from Batt et al and Baeraky [147,148] for different types of SiC materials and also following the analysis performed by Kriegsmann [116]. It was found that maintaining a constant input power could cause the steady state temperature to evolve on the upper branch of the S-shaped curve during the infiltration process, see figure 4.3 and 4.4. It was also seen that the steady-state temperature decreased with a decrease in the net porosity. Rather than controlling the input microwave power, a control theory could be developed instead to maintain the set temperature in the models, hence controlling the reduction in temperature during the infiltration process.

5.3.2.2   Influence of the SiC matrix on thermal properties

The heat transfer during the electromagnetic heating of the SiC preform is governed by its thermal conductivity, its relative volume fraction and its geometrical arrangement with respect to porosity, which acts as a barrier to heat flow. Thus the decrease in porosity of the medium results in an increase in its thermal conductivity, hence decreasing thermal inhomogeneities in regions where sufficient densification has occurred during MECVI. Further, experimental and theoretical studies performed by Youngblood et al [150,151] have shown that the matrix and fibres in SiC_f/SiC composites have different thermal conductivity values, which depend moderately on temperature. Similar observation was made by Taylor et al [153], who found that the heat conduction in fibre composites was dominated by the conductivity of the SiC matrix whilst the contribution of the fibres was secondary. However, the dependence of the effective thermal conductivity of SiC_f/SiC composites on the porosity during MECVI is hardly mentioned in the literature. In the models developed here, in line with previous literature models on CVI, the effective thermal conductivity of the preform was modelled as a linear function of the overall porosity only. Following the observation made from the experimental work, [39], where it was seen that thermal

conductivity was not primarily involved in the temperature variations occurring in the sample, its dependence on temperature was neglected.

5.3.3 Reaction kinetics

As previously stated, MTS decomposes at high temperatures according to equation (3.20), yielding solid SiC and HCl gas. H_2 is used as the carrier gas not only for its lightness, reactant diffusion is faster, but its presence is also necessary for reaction with chemical constituents such as chlorine [39]. The deposition of SiC from MTS is in fact a very complex reaction. This resulted in an incomplete understanding of the kinetics of the silicon carbide deposition reaction, which complicated both the experimental and theoretical realization of the MECVI process. The deposition sequence probably involved multiple steps, or competing forward and reverse reactions, which were endothermic overall [24,39,97,133,134]. A first order reaction has often been selected for modelling purposes. In the models developed here, this first order reaction hypothesis has been considered only, with the production of HCl as a by-product not being taken into account.

Several authors have reported the inhibitory effect of HCl [46,52], particularly at large temperatures. Considerable evidence also suggested that the presence of HCl-rich waste gas during the infiltration process damaged the fibres in the preform [39]. The experimental work carried out by Jaglin [39] showed that at higher temperatures a higher infiltration rate resulted that caused greater depletion of the reacted species, thus producing more HCl-based byproduct. The net effect of using higher temperatures was thus to both inhibit the reaction and cause etching of the fibres. Hence, the inclusion of HCl during theoretical modelling would be beneficial.

5.3.3.1 Activation energy

Activation energies, E_A, found in the literature [24,46,73,97] relating to the decomposition of the MTS gas lie between 120 and 170 kJ mol⁻¹. However, calculations of E_A during the experimental work carried on MECVI [39] resulted in values of 53 ± 4 kJ mol⁻¹. These calculations were performed according to both the matrix growth across the whole preform undergoing a temperature profile and the

coating thickness variations with temperature. Due to the large differences observed in both these values, the author suggested that the chemistry involved might have been altered during the process and also the differences could be attributed to the lack of thermal stability across the sample [39]. Further work is needed to elucidate on the effect of microwave radiation on the decomposition of MTS to SiC in an H_2 atmosphere, hence, in the mathematical models developed in the present work, the activation energy was considered to be 120 kJ mol^{-1}.

CHAPTER 6:

GENERAL CONCLUSION

The primary goal of the modelling of microwave enhanced chemical vapour infiltration (CVI) modelling is the real time simulation of the evolution of the matrix during infiltration allowing the effect of variables to be determined. Understanding these relationships could significantly reduce the cost and processing times required for fabricating composites by microwave enhanced CVI.

In this thesis two main models have been developed for macrostructure evolution during the chemical vapour infiltration process under microwave heating:

- The *ME-FCVI two-dimensional model* – which describes CVI under both microwave heating and forced flow of the gaseous reactants.

- The *MECVI one-dimensional model* – which describes microwave enhanced CVI under diffusion transport of the gaseous precursor.

The *ME-FCVI model* was built upon the successive development of two sub models due to the complexities involved during the process: the *EM sub model* investigated the electromagnetic heating of a SiC preform having constant porosity level and the occurrence of thermal runaway under decreasing porosity during the process. The *FCVI sub model* evaluated the mass balance of the gaseous species and porosity variation during the infiltration process under isothermal conditions. The capability of the final ME-FCVI model was to predict trends in the composite density distribution and infiltration time that might be expected when the process conditions were varied. This model has shown that the final density of the preform was strongly influenced by the processing variables as follows:

- The microwave incident power and external cooling, controlled by the heat transfer coefficient, could be manipulated to control both the temperature level and thermal gradient developed during the microwave heating stage. Whilst higher temperatures can lead to a decrease in the overall processing time, the overall density of the composite was minimally affected. On the other hand, the use of a higher inverse temperature

gradient could result in greater non-uniformity and a decrease in the density of the final composite.

• Forcing the gaseous precursor through the porous preform lead to more uniform densification, due to a reduced dependency on diffusion. However, densification was limited by the early termination of the process due to excessive pressure gradients. Also it was observed that the edges of the preform were less densified.

• When combined with appropriate pressure gradients, the use of inverse temperature gradients via microwave heating quite satisfactorily overcame diffusion limitations and provided increased control over the composite quality. Again it was necessary to have a proper combination of gaseous precursor flow rates and thermal gradients to obtain the desired matrix composite.

• The results have also shown that the temperature distributions developed were greatly affected by the decrease in porosity level during the process. The analysis performed by applying constant microwave input power showed that at higher porosity levels, thermal runaway could occur.

• However, it should be noted that in this model the cooling effect inside the preform generated by the forced flow of the gaseous precursors was ignored. Also the microstructure of the preform was neglected during the electromagnetic formulation due to the complexities involved in modelling the interaction of microwaves with a porous media.

• Finally, it was observed from all the results that the edges of the preform remained less densified compared to its interior. However, further densification was still possible by combining the inverse thermal gradient with diffusion transport of the gaseous precursors.

The *MECVI model* helped to investigate the infiltration of a porous SiC preform under microwave heating by allowing gaseous reactants to flow through the preform by diffusion transport. The model took into account the effects of the changing materials properties, both during the heating and infiltration stages, the heat of reaction and non-uniformities in the gas concentration within the preform, on the infiltration profiles and processing times during the process. It also investigated the important issues of non-uniform heating and thermal runway during microwave heating of the porous SiC preform.

- An S-shaped curve was produced when the steady-state thermal distribution was plotted against the input microwave power. The curve was significantly affected by the dielectric properties of the SiC preform. It was found that as the amount of porosity in the initial preform increased, the steady state temperatures within the preform eventually moved to the upper branch of the S-shaped curve, which corresponded to thermal runaway. This caused the interfacial temperature to be slightly higher than the interior.

- Since the MTS concentration was higher at the preform/environment interface, in addition to the temperature being greater, the pores closed faster at the boundary choking off the reaction in the interior of the preform. This resulted in the entrapment of porosity in the interior of the preform that would unfavourably affect the mechanical properties of the final densified product.

- Finally, the numerical results also predicted some important trends observed in experiments including the skin effect. This gave a considerable amount of insight in understanding this microwave enhanced CVI process under diffusion driven gaseous precursors.

However, as shown earlier, microwave enhanced CVI is a very complex process, that is affected by many process variables. Whilst the *ME-FCVI* and *MECVI* models developed during the course of this research can help to understand the effects of altering those variables, the better their effects are understood experimentally, the more usefully they could be incorporated into extending and optimizing the models.

CHPATER 7:

FUTURE WORK

In order to achieve the goal mentioned in Chapter 6, the microwave enhanced CVI process has to be understood well and the models have to be improved to describe the latter better and more accurately. Along the way to the ultimate goal and considering the models developed during the course of this research works as a fundamental background, more research work can be performed.

- Due to the extremely complicated geometry of the SiC fibre preform microstructure, more accurate and efficient fibre structure models can be used where both the intertow and intratow porosities are included. Numerical techniques like the Level Set Method (LSM) and the Fast Marching Method (FMM) have been developed and successfully used in the past couple of years to follow the evolution of interfaces in problems related to fluid mechanics, combustion, image processing and structure of snowflakes. These techniques can be employed to model the geometry of the microstructure of the fibre preform and track its changes during the CVI process. The latter can also detect the formation of inaccessible pores and adjust the deposition inside these pores to make the fibre growth stop there.

- In line with the above point, forced-flow and diffusion mechanisms can thus be used for mass transport inside the intertow and intratow porosities respectively. However, the partial differential equations describing the gas transport within the fibre preform of complex geometry can impose numerical difficulty. To solve them efficiently, other techniques like the Immersed Interface Method can be used accordingly.

- The microwave heating of the SiC porous sample can be performed inside a resonant microwave cavity using numerical techniques like Finite Element Method and Finite Difference Time Domain, where the effects of the cavity walls on the electromagnetic field are considered. This can be followed by considering the microstructure of the fibre preform with higher dimensions. However, these will

increase computation cost significantly. And more, the computation is in microscopic level, so a full-scale process simulation would require huge computation power.

- More accurate models describing the thermal and electrical data can be produced for SiC samples having different porosity levels. However, proper experimental data on the latter are needed to be able to investigate such models.

- Proper control on the input microwave power and the set temperature can be done by including a control power theory. This could help to control the effect of thermal runaway during the infiltration process.

- The cooling effect of the forced-flow of the gaseous precursor on the thermal profiles during microwave heating of the preform can be investigated by coupling the necessary set of equations and introducing the convective term in the heat diffusion equation.

- The formation of HCl as a by-product during the decomposition of MTS can be studied by considering the convection and diffusion of a multicomponent mixture of three gaseous species: hydrogen, MTS and HCl. This multicomponent diffusion in the presence of significant pressure gradients can be described using a "three-parameter" variant of the Dusty–Gas model, which accounts for the viscous flow using Darcy's law. Mass conservation equations for each species can thus be obtained using this model. The formation of HCl can help to study its inhibitory effect on the deposition kinetics.

- Further, as explained in the literature survey the deposition of SiC from MTS is very complex, which involve multi-steps decomposition reactions having different order-reactions. The better the mechanism of the reaction is understood, the better it can be incorporated into the model.

APPENDICES

Appendix 1

Mathematical description of converting equation (3.6) to (3.7) using a Green's function approach [140]

Equation (3.6) is restated here for convenience:

$$\nabla^2 \overline{E}_s + k_2^2 \overline{E}_s = \underbrace{k_2^2 (1 - N^2)(\overline{E}_{inc} + \overline{E}_s)}_{F(\underline{x})} \tag{3.6}$$

This equation is solved by considering the Green's function $G(\underline{x})$, which satisfies:

$$\nabla^2 G + k_2^2 G = \delta_f (\underline{x} - \underline{x}_1), \tag{a1.1}$$

where, δ_f is the delta function and the point $\underline{x}_1$ can be both inside and outside the 2-D SiC preform as shown in figure a1.1. By multiplying equations (3.6) and (a1.1) by $G(\underline{x})$ and $\overline{E}_s$ respectively and subtracting the resulting expressions, the following equation is obtained:

$$\nabla \cdot \left(\overline{E}_s \nabla G - G \nabla \overline{E}_s \right) = -FG + \delta \overline{E}_s \tag{a1.2}$$

Now, integrating the above equation over the whole domain, within the circle of radius R_r, the corresponding expression is achieved:

$$\int_0^{2\pi} \left(\overline{E}_s \frac{\partial G}{\partial r} - G \frac{\partial \overline{E}_s}{\partial r} \right) R \, d\theta = - \iint_{x^2+y^2 \le R} F(\underline{x})G + \overline{E}_s (\underline{x}_1) \, dxdy \tag{a1.3}$$

In the far field away from the sample, the scattered electric field and the Green's functions satisfy the radiation conditions and are given by:

$$\left. \begin{aligned} E_s &\sim \frac{A_c e^{ik_2 r}}{\sqrt{r}} \\ G &\sim H_0^{(1)} \sim \frac{e^{ik_2 r}}{\sqrt{r}} \end{aligned} \right\} \longrightarrow 0 \quad \text{as } r \longrightarrow \infty. \tag{a1.4}$$

Here, A_c is a damping constant and $H_0^{(1)}$ is Hankel function of the first kind of order zero. Applying these conditions in (a1.3), the following expression for the scattered field is thus obtained:

$$\overline{E}_s(\underline{x}_1) = \iint\limits_{x^2+y^2 \le R^2} \mathbf{F G}\, dxdy$$

$$= k_2^2 \iint\limits_{SiC\,sample} (1 - N^2)\mathbf{G}\underline{E}\, dxdy \qquad ,$$ (a1.5)

$$= k_2^2 \iint\limits_{SiC\,sample} (1 - N^2(\underline{x}_1))\underline{E}(\underline{x}) H_0^{(1)}(k_2|\underline{x} - \underline{x}_1|)\, dxdy$$

From equation (3.5), the scattered field is also given by $\overline{E}_s = \overline{E} - \overline{E}_{inc}$. Also, since $\underline{x}_1$ is any arbitrary point within the closed region, exchanging $\underline{x}_1$ by $\underline{x}$, expression (3.7) in finally obtained.
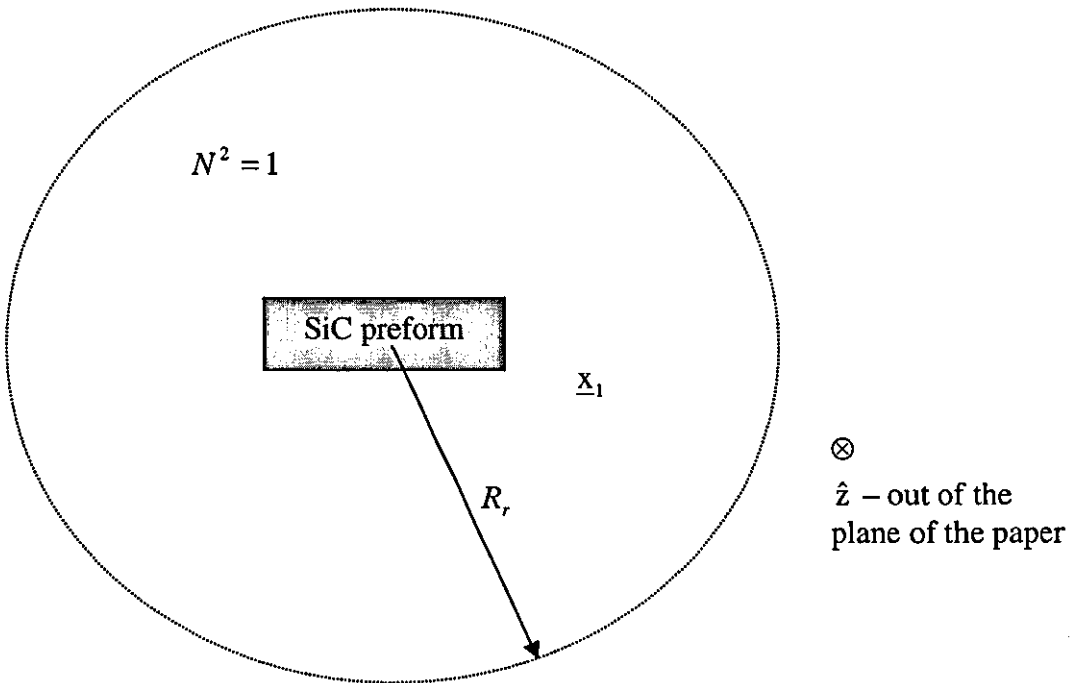

Figure a1.1: Region of propagation of electromagnetic plane waves on a SiC preform in free space.

Appendix 2

Determining the increase in volume content of SiC during deposition of solid material in a unit cell

During the infiltration process, SiC solid is deposited on the fibre tows, causing the matrix to grow radially from the bundles surfaces. The idea that the matrix grew radially from the surface of a sphere was adopted to model the matrix deposition at the corners of the unit cell. This growth is idealized in figure a2.1. The triangle depicts a cross section of a unit cell, with the corners indicating the crossover points. l_2 and l_3 denote the radii of the spheres associated with the matrix growth at the centre corner respectively. The mathematical expressions relating the volume content of SiC in the unit cell is developed next:

$$l_4 = L_1 / \sqrt{2} \qquad \text{(a2.1)}$$

$$\tan \varphi_2 = 2l_4 / L_1 = \sqrt{2} \qquad \text{(a2.2)}$$

$$\cos \varphi_2 = 1 / \sqrt{3} \qquad \text{(a2.3)}$$

$$\varphi_1 = 90 - \varphi_2 \qquad \text{(a2.4)}$$

$$\sin \varphi_1 = \cos \varphi_2 = 1 / \sqrt{3} \qquad \text{(a2.5)}$$

From the figure below,

$$\sin \varphi_1 = r / l_2 \implies l_2 = r / \sin \varphi_1 = \sqrt{3} r \qquad \text{(a2.6)}$$

$$\sin(\varphi_2 / 2) = r / l_3 \implies l_3 = r / \sin(\varphi_2 / 2) = \sqrt{\left(18 - 6\sqrt{3}\right)} r / 6 \qquad \text{(a2.7)}$$

Therefore, during the deposition process, the increasing volume of the sphere at the centre of the unit cell is given by:

$$c_{v1} = 4\pi l_2^3 / 3 \qquad \text{(a2.8)}$$

Similarly, the volume of the sphere at the corner of the unit cell is:

$$c_{v2} = 8(1/8)(4\pi l_3^3 / 3) \qquad \text{(a2.9)}$$

The volume of the fibre tow and matrix deposited on the edge of the unit cell is:

$$c_{v3} = 12(1/4)(L_1 - 2l_3)\pi r^2 \tag{a2.10}$$

Thus, the volume of the fibre tow and the deposited matrix in a unit cell excluding c_{v3}, c_{v2} and c_{v3} is:

$$c_{v4} = 4\pi r^2 \left(\sqrt{3L_1} - 2l_2 - 2l_3 \right) \tag{a2.11}$$

Hence the total volume of solid content in a unit cell during the infiltration process is given by:

$$
\begin{aligned}
c_s &= c_{v1} + c_{v2} + c_{v3} + c_{v4} \\
&= \left((\sqrt{3} + 4)L_1 + \left(((3 - \sqrt{3})/27 - 14/6)(6 - 2\sqrt{3}) - 4 \right) r \right) \sqrt{3}\, \pi r^2
\end{aligned}
\tag{a2.12}
$$

The mathematical expressions relating the volume content of SiC in the unit cell is developed next:

The surface area of the sphere at the centre of the unit cell during densification is:

$$A_{s1} = 4\pi d_2^2 \tag{a2.13}$$

Similarly, the surface area of the sphere at the corner of the unit cell is:

$$A_{s2} = 8(1/8)(4\pi d_3^2) \tag{a2.14}$$

The surface area of the fibre tow and deposited matrix on the edge of the unit cell is

$$A_{s3} = 12(1/4)(L_1 - 2l_3)2\pi r \tag{a2.15}$$

Thus, the surface area of the fibre tow and matrix in a unit cell excluding A_{s1}, A_{s2} and A_{s3} is:

$$A_{s4} = 8(2\pi r)\left(\left(\sqrt{3L_1} - 2l_2 - 2l_3 \right) / 2 \right) \tag{a2.16}$$

Hence, the total surface of the solid content in a unit cell during infiltration is

$$A_{st} = A_{s1} + A_{s2} + A_{s3} + A_{s4} \tag{a2.17}$$

Therefore the corresponding effective surface area in a unit cell is:

$A = A_{st}$ / *bulk volume of unit cell*

$$= \frac{\left((6+8\sqrt{3})L_1 - \left((14/3)\sqrt{18-6\sqrt{3}} + 50\sqrt{3}/3 + 14\right)r\right)\pi r}{L_1^3}$$

(a2.18)
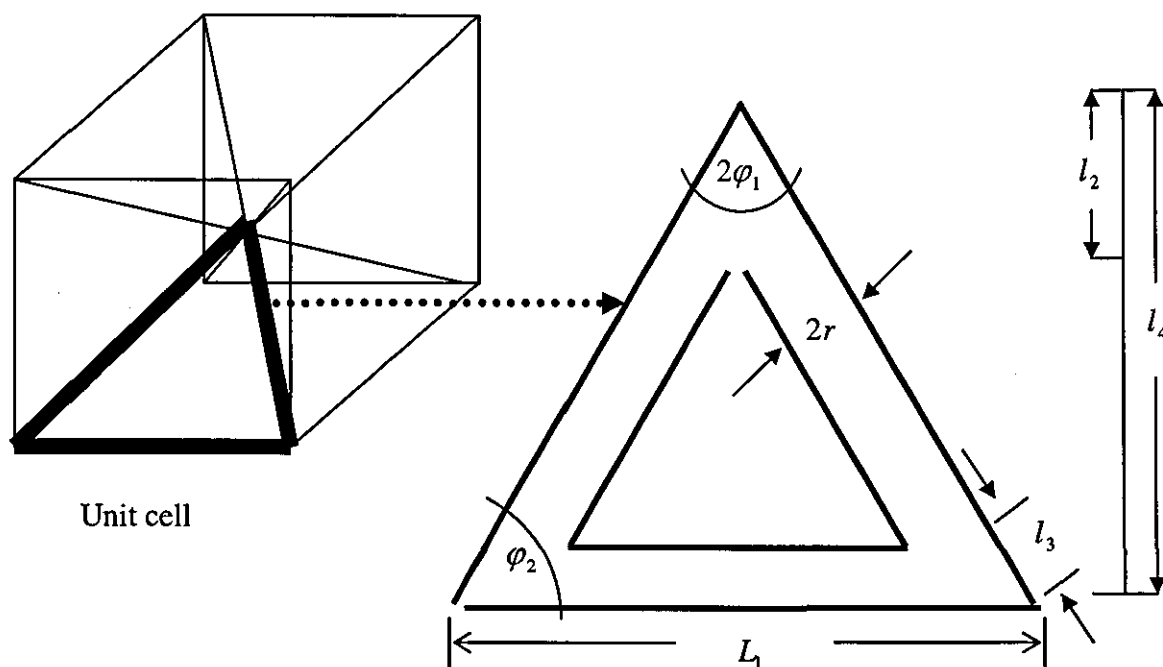
Figure a2.1: Schematic of the unit cell, whose edges and diagonals represent fibre tows. The triangular part characterizes the dark cross section of the unit cell.

Appendix 3

Approximate expression for the Hankel function of the first kind of order zero

The Hankel function of the first kind of order ς is given by [159]:

$$H_{\varsigma}^{(1)}(u_c) = J_{\varsigma}(u_c) + iY_{\varsigma}(u_c) \tag{a3.1}$$

where, $J_{\varsigma}(u_c)$ is the Bessel function of the first kind and $Y_{\varsigma}(u_c)$ is the Bessel function of the second kind. For small argument u_c ($u_c \longrightarrow 0$), these Bessel functions are approximated by:

$$J_{\varsigma}(u_c) \approx \frac{1}{2^{\varsigma}\varsigma!} u_c^{\varsigma}$$

$$Y_{\varsigma}(u_c) \approx \frac{2}{\pi} \ln u_c$$

Thus for order zero ($\varsigma = 0$), the above expressions can be reduced to:

$$J_0(u_c) \approx 1$$

$$Y_0(u_c) \approx \frac{2\ln u_c}{\pi}$$

Hence, the corresponding Hankel function is given by:

$$H_0^{(1)}(u_c) = 1 + \frac{2i}{\pi} \ln u_c$$

Appendix 4

Solving a linear system of equation using LU decomposition

The evolution of the electromagnetic, temperature, pressure and MTS concentration distributions during the infiltration process are determined at each time step by solving linear systems of equations. In general, these linear systems can be written in the form:

$$A_m \mathbf{x}_v = \mathbf{b}_v \qquad (a4.1)$$

where, A_m is a matrix whose entries are written as, $a_{i,j}$, $\mathbf{x}_v = (x_j)$ is a column vector representing the particular distribution being solved and the vector $\mathbf{b}_v = (b_j)$ normally consist of the previous time step data for that distribution. The size of the matrix A_m is considered to be $mn \times mn$, thus, $i_c = 1, 2........., mn$ and $j = 1, 2,........., mn$. Equation (a4.1) is solved using the LU decomposition method, where A_m is factorized into two matrices as follows:

$$A_m \mathbf{x}_v = L_m U_m \mathbf{x}_v = \mathbf{b}_v \qquad (a4.2)$$

$L_m = (l_{i,j})$ and $U_m = (u_{i,j})$ are known as the upper and lower triangular matrices, where the main diagonal of either L_m or U_m consist of all ones. They are found numerically by considering the steps in the following algorithm:

Algorithm: **LU decomposition**

Step 1: Select l_{11} and u_{11} satisfying $l_{11}u_{11} = a_{11}$.

If $l_{11}u_{11} = 0$, then OUTPUT ('factorization impossible')
STOP

Step 2: For $j = 2,........., mn$, set $u_{1j} = a_{1j}/l_{11}$; (First row of U_m)

$$l_{j1} = a_{j1}/u_{11} \text{ ; (First column of } L_m \text{)}$$

Step 3: For $i_c = 2,........., mn - 1$ do Steps 4 and 5

Step 4: Select $l_{i_c i_c}$ and $u_{i_c i_c}$ satisfying $l_{i_c i_c} u_{i_c i_c} = a_{i_c i_c} - \sum_{k_c=1}^{i_c-1} l_{i_c k_c} u_{k_c i_c}$.

If $l_{i_c i_c} u_{i_c i_c} = 0$ then OUTPUT ('factorization impossible')

STOP

Step 5: For $j = i_c + 1, \ldots\ldots, mn$

$$\text{Set } u_{i_c j} = \frac{1}{l_{i_c i_c}} \left[a_{i_c j} - \sum_{k_c=1}^{i_c-1} l_{i_c k_c} u_{k_c j} \right]; \quad (i_c \text{th row of } U_m)$$

$$l_{j i_c} = \frac{1}{u_{i_c i_c}} \left[a_{j i_c} - \sum_{k_c=1}^{i_c-1} l_{j k_c} u_{k_c i_c} \right]; \quad (i_c \text{th column of } L_m)$$

Step 6: Select $l_{mn\,mn}$ and $u_{mn\,mn}$ satisfying $l_{mn\,mn} u_{mn\,mn} = a_{mn\,mn} - \sum_{k_c=1}^{mn-1} l_{mn k_c} u_{k_c mn}$

Step 7: OUTPUT ($l_{i_c j}$ for $j = 1, 2, \ldots\ldots, mn$ and $i_c = 1, 2 \ldots\ldots, mn$)
OUTPUT ($u_{i_c j}$ for $j = 1, 2, \ldots\ldots, mn$ and $i_c = 1, 2 \ldots\ldots, mn$)
STOP

Once the factorization of matrix A_m is complete, the solution to the linear system is found (a4.2) is found by first letting $\mathbf{y}_v = U_m \mathbf{x}_v$ and determining $\mathbf{y}_v = (y_j)$ from the equations:

$$y_1 = \frac{b_1}{l_{11}} \tag{a4.3}$$

and for each $j = 2, \ldots\ldots, mn$

$$y_j = \frac{1}{l_{jj}} \left[b_j - \sum_{k_c=1}^{j-1} l_{jk_c} y_{k_c} \right] \tag{a4.4}$$

Once $\mathbf{y}_v$ is found, the upper triangular system $U_m \mathbf{x}_v = \mathbf{y}_v$ is solved for $\mathbf{x}_v$ to finally determine the corresponding distribution.

190

Appendix 5

Finding the leading order equations during the asymptotic analysis

The perturbation method is applied to the set of partial differential equations (4.15)-(4.18) and the corresponding boundary conditions (4.20) to obtain averaged simplified equations. The expression describing the temperature distribution within the 1-dimensional preform is considered here as an example to demonstrate the method used to obtain the leading order terms. For convenience, equation (4.16) is restated here:

$$\frac{\varepsilon_*^2 A_1 g}{\theta}\frac{\partial T}{\partial t} = k_t\left(\varepsilon_*^2 \frac{\partial^2 T}{\partial x^2} + \frac{\partial^2 T}{\partial y^2}\right) + \varepsilon_*^2 P_c f_c(T, y)|E_p|^2 \tag{4.16}$$

The power series expression employed in the limit $\varepsilon_*^2 \to 0$ is given as:

$$T(x, y, \varepsilon_*, t) = \sum_{j=0}^{\infty} \varepsilon_*^{2j} T_{aj}(x, y, t) \tag{4.21b}$$

By inserting the above expression in (4.16) and expanding the power series, the resulting equation is obtained

$$\frac{\varepsilon_*^2 A_1 g}{\theta}\left(\frac{\partial T_{a0}}{\partial t} + \varepsilon_*^2 \frac{\partial T_{a1}}{\partial t}\right) = k_t\left(\varepsilon_*^2\left(\frac{\partial^2 T_{a0}}{\partial x^2} + \varepsilon_*^2 \frac{\partial^2 T_{a1}}{\partial x^2}\right) + \left(\frac{\partial^2 T_{a0}}{\partial y^2} + \varepsilon_*^2 \frac{\partial^2 T_{a1}}{\partial y^2}\right)\right)$$
$$+ \varepsilon_*^2 P_c f_c(T, y)|E_p|^2 \tag{a5.1}$$

It is noted here that the values for $j = 0$ and 1 is considered only during the expansion, since these are enough to produce the leading order $O(1)$ and $O(\varepsilon_*^2)$ terms. Equation (a5.1) can be re-written as:

$$\frac{A_1 g}{\theta}\left(\varepsilon_*^2 \frac{\partial T_{a0}}{\partial t} + \varepsilon_*^4 \frac{\partial T_{a1}}{\partial t}\right) = k_t\left(\varepsilon_*^2 \frac{\partial^2 T_{a0}}{\partial x^2} + \varepsilon_*^4 \frac{\partial^2 T_{a1}}{\partial x^2} + \frac{\partial^2 T_{a0}}{\partial y^2} + \varepsilon_*^2 \frac{\partial^2 T_{a1}}{\partial y^2}\right)$$
$$+ \varepsilon_*^2 P_c f_c(T, y)|E_p|^2 \tag{a5.2}$$

Thus by comparing the coefficients of each term in the above expression, the leading order $O(1)$ equation is given by

$$k_t \frac{\partial^2 T_{a0}}{\partial y^2} = 0 \tag{a5.3}$$

The general solution of this expression is obtained by performing double integration with respect to y and is given by:

$$T_{a0} = c_0(x,t) + d_0(x,t)y \qquad (a5.4)$$

where $c_0(x,t)$ and $d_0(x,t)$ are constants. Similarly, by comparing the coefficients of the term in (a5.2) and retaining the terms containing ε_*^2, the following order $O(\varepsilon_*^2)$ equation is obtained:

$$\frac{A_1 g}{\theta}\frac{\partial T_{a0}}{\partial t} = k_t\frac{\partial^2 T_{a0}}{\partial x^2} + k_t\frac{\partial^2 T_{a1}}{\partial y^2} + P_c f_c(T,yb)|E_p|^2 \qquad (4.25)$$

The solution of this equation is described in section 4.5 using the boundary conditions.

REFERENCES

[1] K.K Chawla, "*Ceramic matrix composites*", 2nd edition, Kluwer Academic Publishers, 2002.

[2] D.W. Richerson, "*Modern ceramic engineering: properties, processing and use in design*", 2nd edition, New York: M. Dekker, 1992.

[3] S.C. Sharma, "*Composite materials*", Narosa Publishing House, 2000.

[4] http://www.ms.ornl.gov/programs/energyeff/cfcc/doe2076.htm.

[5] I.J. McColm and N.J. Clark, "*Forming, shaping and working of high-performance ceramics*", Blackie, Chapman & Hall, 1988.

[6] M.H. Van de Voorde and M.R. Nedele, "*CMC's research in Europe and the future potential of CMC's in industry*", Ceram.Eng.Sci.proc., **17**, 4, pp3-21, 1996.

[7] A.P. Majidi, J.M. Yang, R.B. Pipes and T.W. Chou, "*Mechanical behaviour of the three-dimensional woven fibre composites*", Conference Proceedings of the 5th Int. Conf. on Composite Materials, San Diego, Metallurgical Society, Inc, pp1247-1265, 1985.

[8] K. Ko and G.W. Du, "*Advanced composites manufacturing*", T.G. Gutowski, Wiley-interscience Publications, John Wiley & sons, Inc, Chap. 5, pp157-205, 1997.

[9] N.P. Bansal, J.P. Singh, H.-T. Lin, "*Advances in ceramic matrix composites*" VII proceedings of the Ceramic Matrix Composites, Indiana, USA, 2001

[10] W. Krenkel, R. Naslain, H. Schneider, "*High temperature ceramic matrix composites*", New York, Wiley-VCH, 2001.

[11] E.R. Generazio, "*Advanced ceramic matrix composites: design approaches, testing, and life prediction methods*", Pa, USA, Technomic Pub. Co., 1996.

[12] *RGB-110N Ceramic Matrix Composites* (www.bccresearch.com), Business Communication Company, Inc. 2000.

[13] Y-W Kim, J-G Lee, M-S Kim, J-H Park, "*Effect of multilayer coating on mechanical properties of Nicalon-fibre-reinforced silicon carbide composites*", J.Mater.Sci., **31**, pp335-338, 1996.

[14] D. Lewis, "*Continuous fibre-reinforced ceramic matrix composites: A historical overview*", Handbook on continuous fibre-reinforced ceramic matrix composites, ed. Lehman R.L., El-Rahaiby S.K., Watchman J.B., Chap. 1, pp1-34, 1995.

[15] A. Muhlratzer, "*Production, properties and applications of ceramic matrix composites*", cfi / Ber. DKG, **4**, pp30-35, 1999.

[16] K.R. Vaidyanathan, J. Sankar, A.D. Kelkar, D.P. Stinton, M.H. Headinger, "*Investigation of mechanical properties of chemically vapour infiltrated ceramic matrix composites under pure tension*", 17th Annual Conference on Composites and Advanced Ceramic Materials, American Ceramic Society, Ceram.Eng.Sci.Proc., pp1016-1027, 1993.

[17] J.H. Kinney, T.M. Breunig, T.L Starr, D. Haupt, M.C. Nichols, S.R. Stock, M.D. Butts, R.A. Saroyan, "*X-ray tomographic study of chemical vapour infiltration processing of ceramic composites*", Science, **260**, pp789-791, 1993.

[18] Vaidyanathan K.R., Sankar J., Kelkar A.D., Narayan J., "*Investigation of mechanical properties of chemically vapour infiltrated (CVI) ceramic matrix composites*", Ceram.Eng.Sci.Proc., **15**, 4, pp281-291, 1994.

[19] Sheppard L.M., "*Progress in composites processing*", Ceram.Bull., **69**, 4, pp666-673, 1990.

[20] Besmann T.M., Lowden R.A., Stinton D.P., "*Overview of chemical vapour infiltration*", High Temperature Ceramic Matrix Composites: 6th Eur. Conf. on Composite Materials, Bordeaux, Woodhead Publishing Limited, pp215-229, 1993.

[21] Park H.D., Jeong H.J., Choi Y.M., Lee J.D., "*Processing parameters of pulse CVI in C / C composites*", Ceram.Trans., **46**, pp155-163, 1994.

[22] D.P. Stinton, A.J. Caputo and R.A. Lowden, "*Synthesis of Fibre-Reinforced SiC composites by Chemical vapour infiltration*", Am. Ceramic. Soc. Bull., **65**, 2, pp347-350, 1986.

[23] T.L. Starr, "*Deposition Kinetics in Forced Flow/Thermal Gradient CVI*", Ceram. Eng. Sci. Proc., **9**, 7, pp803-812 1988.

[24] Naslain, F. Langlais, and R. Fedou, "*The CVI-Processing of Ceramic Matrix Composites*", J. Phys. Colloq. C5, suppl., **50**, 5, c5-191-c5-207, 1989.

[25] N.H. Tai and T.W. Chou, "*Analytical Modelling of Chemical Vapour Infiltration in Fabrication of Ceramic Composites*", J. Am. Ceram. Soc., **72**, 3 pp414-420, 1989.

[26]   Nyan-Hwa Tai and Tsu-Wei Chou, *J. Am. Ceram. Soc.*, **73** [6], pp1489-98, 1990.

[27]   I. J. McColm and N.J. Clark, *"Forming, shaping and working of high-performance ceramics"*, ed. Blackie, Chapman & Hall, pp301-304, 1988.

[28]   Y. Yin , J.G.P. Binner & T.E. Cross, Ceram. Trans., **80,** pp349-356, 1997.

[29]   D. Jaglin, J.G.P Binner, C. Prentice, R. Shatwell, L. Timms, W. Westby, *"SiC$_f$/SiC fabrication via vacuum bagging, electrophoretic infiltration and microwave enhanced CVI"*, ECCM9, Conf. Proceedings., 2000

[30]   D. Jaglin and J.G.P. Binner, *"Densification of woven fibre SiC/SiC composites by microwave enhanced chemical vapour infiltration"*, 7th International Conference on Microwave and High Frequency Heating", pp283-286, 1999.

[31]   D. Gupta and J.W. Evans, *"A mathematical model for chemical vapour infiltration with microwave heating external cooling"*, J. of Materials Res., **40,** pp810-818, 1991.

[32]   J. Morell, D.J. Economou and N.R. Amundson, *"A Mathematical Model for Chemical Vapour Infiltration with Volume Heating"*, J. Electrochem Soc.,**139,** 1, pp328-336 1992.

[33]   J. Morell, D.J. Economou and N.R. Amundson, *"Pulsed-power volume-heating chemical vapour infiltration"*, J. Mater. Res., **7,** 9, pp2447-2457, 1992.

[34]   J. Morell, D.J. Economou and N.R. Amundson, *"Chemical vapour infiltration of SiC with microwave heating"*, J. Mater. Res., **8,** 5, pp1057-1067, 1993.

[35]   D. Gupta and J. W. Evans, *"Mathematical model for chemical vapour infiltration in a microwave-heated perform"*, J. Amer. Ceramic Soc., **76,** pp1924-1929, 1993

[36]   D.J. Skamser, J.T. Thomas, H.M. Jennings, and D.L. Johnson, *"A model for microwave processing of compositionally changing ceramic systems"*, J. of Material Res, **10,** pp3160-3178, 1995.

[37]   B.S. Tilley and G.A. Kriegsmann, *"Microwave-enhanced chemical vapour infiltration: a moving interface model"*, Second World Congress on Microwave and Radio-Freqency Processing, 2000.

[38]   B.S. Tilley and G.A. Kriegsmann, *"Microwave-enhanced chemical vapour infiltration: a sharp interface model"*, J. Eng Math., **41,** 2, 2001.

[39]   D. Jaglin, *"Densification of SiC$_f$/SiC composites via microwave enhanced chemical vapour infiltration"*, Thesis, Nottingham University, UK, 2002.

[40] C.V. Burkland, W.E. Bustamante and J.M. Wang, "*Whisker and Fibre Toughened Ceramic*", ASM Intl., Materials Park, Ohio, USA, 1988.

[41] Starr T.L., Smith A.W., Vinyard G.Y., "*Model-assisted control of chemical vapour infiltration for ceramic composite fabrication*", Ceram.Eng.Sci.Proc., **12**, 9-10, pp2017-2028, 1991.

[42] T. Noda et al, "*Microstructure and mechanical properties of CVI carbon fibre/SiC composites*", Journal of Nuclear Materials, 191-194, pp539-543, 1992.

[43] B. Reznik et al, "*Microstructure of SiC deposited from methyltrichlorosilane*", Journal of the European Ceramic Society, **23**, pp1499-1508, 2003.

[44] W.J. Lackey, T.L. Starr, "*Fabrication of fiber-reinforced ceramic composites by chemical vapour infiltration: Processing, structure and properties*", Fibre-reinforced ceramic composites: Materials, processing and technology, ed. Mazdiyasni K.S., Noyes Publications, Chap. **14**, pp397-450, 1990.

[45] S.V. Sotirchos, "*Dynamic modelling of chemical vapour infiltration*", AIChE J, **37** 1365-1378 1991.

[46] Starr T.L., Smith A., Besmann T.M., McLaughlin J., Sheldon B., "*Modelling of chemical vapour infiltration for composite fabrication*", High Temperature Ceramic Matrix Composites: 6th Eur. Conf. on Composite Materials, Bordeaux, ed. Woodhead Publishing Limited, pp231-239, 1993.

[47] Sasaki M., Suzuli T., Hirai T., "*Chemical vapour infiltration of silicon carbide using the SiCl$_4$-CH$_4$-H$_2$ reagent system*", Journal of Materials Processing Technology, **2**, 2, pp109-115, 1994.

[48] T.Noda, H.Araki, H. Suzuki and F. Abe, "*Processing of carbon fibre/SiC composite for low activation*", Materials Transactions, JIM, 34, 11, pp1122-29, 1993.

[49] S. Middleman, "*The interaction of chemical kinetics and diffusion in the dynamics of chemical vapour infiltration*", Journal of Material Research, **4**, 6, pp1515-1524, 1989.

[50] R.R Melkote and K.F. Jensen, "*Gas diffusion in random-fibre substrates*", AIChE Journal, **35**, 12, pp1942-1952, 1989.

[51] S.V. Sotirchos, "*Multicomponent diffusion and convection in capillary structures*", AIChE Journal, **35**, 12, pp1953-1961, 1989.

[52] B.W. Sheldon and T.M. Besmann, "*Reaction and diffusion kinetics during the infiltration stages of isothermal chemical vapour infiltration*", Journal of the American ceramic society, **74**, 12, pp3046-53, 1991.

[53] G.Y. Chung and B. J. McCoy, "*Modelling of chemical vapour infiltration for ceramic composites reinforced with layered, woven fabrics*", Journal of the American ceramic society, **74**, 4, pp746-51, 1991.

[54] R.P. Currier, D.J. Devlin and J. Morzinski, "*Dynamics of chemical vapour infiltration in carbon fibre bundles*", Journal of advanced materials, **4**, 1, pp13-24, 1996.

[55] H.C. Chang et al, "*Mathematical Analysis and optimization of Infiltration process*", Journal of scientific computing, **13**, 3, pp303-321, 1998.

[56] W. Zhang, K.J. Huttinger, "*Chemical vapour infiltration of carbon – revised Part I: Model simulations*", Carbon, **39**, pp1013-22, 2001.

[57] A. Ditkowski, D. Gottlieb and B.W. Sheldon, "*Optimization of chemical vapour infiltration with simultaneous powder formation*", Nasa/CR-2000-210620 ICASE report No. 2000-44, 2000.

[58] S. Jin, X. Wang, T.L. Starr and X. Chen, "*Robust numerical simulation of porosity evolution in chemistry vapour infiltration I: Two space dimension*", Journal of Computational Physics, **162**, pp467-482, 2000.

[59] T.A. Langhoff and E. Shnack, "*Modelling chemical vapour infiltration of pyrocarbon as moving boundary problem*", Institute of Solid Mechanics, Karsruhe University, Kaiserstr, Karlsruhe, Germany, 2002.

[60] N. Yoshikawa and J.W Evans, "*Modelling of chemical vapour infiltration rate considering a pore size distribution*", Journal of the American ceramic society, **85**, 6, 1485-91, 2002.

[61] T.A. Langhoff and E. Shnack, "*Modelling chemical vapour infiltration of pyrolytic carbon*", Fifth World Congress on Computational Mechanics, 2002.

[61] S. Jin and X. Wang, "*Robust numerical simulation of porosity evolution in chemical vapour infiltration II: Two Dimension Anisotropic Fronts*", Journal of Computational Physics, **179**, pp557-577, 2002.

[62] S. Jin and X. Wang, "*Robust numerical simulation of porosity evolution in chemical vapour infiltration II: three space dimension*", Journal of Computational Physics, **186**, pp582-595, 2003.

[63]   T. Noda et al, *"Preparation of carbon fibre/SiC composite by chemical vapour infiltration"*, ISIJ International, **32**, 8, pp926-931, 1992.

[64]   T. Tago, M. Kawase, Y. Ikuta and K. Hashimoto, *"Numerical simulation of the thermal-gradient chemical vapour infiltration process for production of fibre-reinforced ceramic composite"*, Chemical Engineering Science, **56**, pp2161-2170, 2001.

[65]   S.M. Gupte and J.A. Tsamopoulos, *"Densification of porous materials by chemical vapour infiltration"*, Journal of Electrochemical Society, **136**, 2, pp555-561, 1989.

[66]   S.M. Gupte and J.A. Tsamopoulos, *"An effective medium approach for modelling chemical vapour infiltration of porous ceramic materials"*, Journal of Electrochemical Society, **137**, 5, pp1626-38, 1990.

[67]   J.Y. Ofori and S.V. Sotirchos, *"Multidimensional modelling of chemical vapour infiltration" application to Isobaric CVI*", Ind. Eng. Chem. Res, **36**, pp357-367, 1997.

[68]   D.J. Skamser, H.M. Jennings and D.L. Johnson, *"Model of chemical vapour infiltration using temperature gradients"*, Journal of Material Research, **12**, 3, pp724-737, 1997.

[69]   K. Nakano, K. Suzuki and T. W. Chou, *"Pulse CVI-slurry joint process for manufacturing of small and medium size parts"*, Adv. Composite Materials, **8**, 1, pp117-126, 1999.

[70]   Y.G. Roman et al, *"The preparation of carbon reinforced silicon carbide composites using the isothermal forced flow chemical vapour infiltration technique"*, J. de Physique IV Colloque C2, pp1190-1198, 1993.

[71]   E. Walasek et al, *"Chemical vapour infiltration of SiC in porous graphite materials"*, Key Engineering Materials, **206**, pp567-570, 2002.

[72]   Y.G. Roman, M. de Croon and R. Metselaar, *"Analysis of the isothermal forced flow chemical vapour infiltration process. Part II: Experimental Study"*, Journal of the European Ceramic Society, **15**, pp887-898, 1995.

[73]   Y.G. Roman, J.F. Kotte and M. de Croon, *"Analysis of the isothermal forced flow chemical vapour infiltration process. Part I: Theoretical aspects"*, Journal of the European Ceramic Society, **15**, pp875-886, 1995.

[74] G.L. Vignoles, C.Descamps and N. Reuge, "*Interaction between a reactive preform and the surrounding gas-phase during CVI*", J. Phys. IV France, **10**, 2, pp9-17, 2000.

[75] M. Jones, T.L. Starr, "*Enhancements to the Georgia Tech. chemical vapour infiltration process model for ceramic matrix composites*", Ceram.Eng.Sci.Proc., **16**, 5, pp829-836, 1995.

[76] T.M. Besmann, J.C. McLaughlin, T.L. Starr, "*Scale-up and modelling of forced chemical vapour infiltration*", Proceedings of the Conference on Composites and Advanced Ceramic Materials-B, Cocoa Beach, American Ceramic society, Ceram.Eng.Sci.Proc., pp897-907, 1994.

[77] Y.G. Roman, R.A. Terpstra, "*Ceramic Technology International: Chemical vapour infiltration*", ed. by London Sterling Publications, Ltd., pp113-116, 1996.

[78] K.J. Probst, T.M. Besmann, D.P. Stinton, Lowden R.A., Anderson T.J., Starr T.L., "*Recent advances in forced-flow, thermal-gradient CVI for refractory composites*", Surface and Coatings Technology, **120-121**, pp250-258, 1999.

[79] Roman Y.G., Stinton D.P., Besmann T.M., "*Development of high density fibre reinforced silicon carbide FCVI composites*", J.Phys IV, c2, suppl.J.Phys.II, **1**, pp689-695, 1991.

[80] Z. Hu, K.J. Huttinger, "*Chemical vapour infiltration of carbon – revised Part II: Experimental results*", Carbon, **39**, pp1023-32, 2001.

[81] T.L Starr and A.W. Smith, "*3-D Modelling of forced-flow thermal-gradient CVI for ceramic composite fabrication*", Mat. Res. Soc. Symp. Proc, **168**, pp55-60, 1990.

[82] S.M. Gupte and J.A. Tsamopoulos, "*Forced-flow chemical vapour infiltration of porous ceramic materials*", J. Electrochemical Soc., **137**, 11, 3675-82, 1990.

[83] N.H. Tai, T.W. Chou and C.C. Ma, "*Effects of deposition mechanisms in the modelling of forced-flow/temperature-gradient chemical vapour infiltration*", Journal of the American Ceramic Society, **77**, 3, 849-51, 1994.

[84] J.Y. Ofori and S.V. Sotirchos, "*Investigation of the potential of forced-flow chemical vapour infiltration*", J. Electrochemical. Soc., **144**, 1, pp274-289, 1997.

[85] J.Y. Ofori and S.V. Sotirchos, "*Multidimensional transport effects on forced-flow chemical vapour infiltration*", Ind. Eng. Chem. Res, **36**, pp1921-31, 1997.

[86]   T.L. Starr and D.Y. Chiang, *"Kinetics of silicon carbide deposition in forced flow chemical vapour infiltration"*, Ceram.Eng.Sci.Proc., **12**, 2, 281-287, 1999.

[87]   Chiang Y-M., Haggerty J.S., Messner R.P., Demetry C., *"Reaction-based processing methods for ceramic-matrix composites"*, Ceram.Bull., **68**, 2, pp420-428, 1989.

[88]   R.V. Decareau and R.A. Peterson, *"Microwave processing and engineering"*, Chichester: Ellis Horwood, c1986.

[89]   S.C. Harsany, *"Principles of microwave technology"*, Upper Saddle River, N.J: Prentice Hall, 1997.

[90]   P.R. Karmel, G.D. Colef and R.L. Camisa, *"Introduction to electromagnetic and microwave engineering"*, New York, Chichester: Wiley, 1998.

[91]   W.H. Sutton, M.H. Brooks and I.J. Chabinsky, *"Microwave processing of materials"*, Materials research society symposium proceedings, 124, 1988.

[92]   I.J. Chabinsky, *"Application of microwave energy, past, present and future: Brave new world"*, In Sutton et al [91], pp17-32, 1988.

[93]   W.B. Snyder, W.H. Sutton, M.F. Iskander and D.L. Johnson, *"Microwave processing of Materials II"*, Material research society symposium proceedings, **189**, 1990.

[94]   Ahmad I., Paquette L, Silberglitt R., *"Microwave energy-assisted chemical vapour infiltration"*, United States Patent 5 238 710, 24 August 1993.

[95]   Skamser D.J., Thomas J.J., Jennings H.M., Johnson D.L., *"A model for microwave processing of compositionally changing ceramic systems"*, J.Mater.Res., **10**, 12, pp3160-3178, 1995.

[96]   Metaxas A.C., Binner J.G.P, *"Microwave processing of ceramics"*, Advanced Ceramic Processing & Technology, vol.1, ed. Binner J.G.P., Noyes Publications, Chap. 8, pp285-367, 1993.

[97]   Metaxas A.C., Meredith R.J., *"Industrial microwave heating"*, ed. Peter Peregrinus Ltd., Chap. 2-3, pp5-25; 26-69, 1983.

[98]   Binner J.G.P., *"Applications of microwave heating to ceramic processing"*, Proceedings of a seminar organised by the Materials and Microwave Processing Group, ed. Binner J.G.P., Abington Publishing, 1991.

[99]   Metaxas A.C., Binner J.G.P, *"Microwave processing of ceramics"*, Advanced Ceramic Processing & Technology, vol.1, ed. Binner J.G.P., Noyes Publications, Chap. 8, pp285-367, 1993.

[100] Pozar D., "*Microwave engineering*", 2nd edition, ed. John Wiley & Sons, Inc., Chap. 1, pp1-55, 1998.

[101] S.Meier and D.Gupta, Trans. of the ASME, **116**, 250, 1994.

[102] K. Sheffler and D.Gupta, Journal of Eng. for Gas Turbines and power, **110**, 605, 1988.

[103] R. Botsco, R. McMaster, "*Nondestructive Testing Handbook*", ASNT, 4, 1986.

[104] A. V. Hippel, "*Dielectric Materials and Applications*", John Wiley & Sons, 1954.

[105] P. Harrop, "*Dielectrics*", John Willey & Sons, 1972.

[106] R. Fletcher, "*Investigation into microwave heating of uranium dioxide*", Ph.D., University of Nottingham, pp1-26; 49-60; 122-142, 1995.

[107] J.D Jackson, "*Classical Electrodynamics*", *Willey, New York*, 1962.

[108] National Research Council, "*microwave processing of materials*", Publication NMAB-473, National Academy Press Washington, USA, 1994.

[109] A.H. Pincombe and N.F.Smyth, "*Microwave heating of materials with low conductivity*", Proc. Roy. Soc., **433**, pp479-498, 1991.

[110] G.A. Kriegsmann, D. Watters and M.E. Brodwin, "*Microwave heating of a ceramic half-space*", SIAM J. Appl. Math., **50**, pp1088-1098, 1990.

[111] N.F. Smyth, "*Microwave heating of bodies with temperature dependent properties*", Wave Motion, **12**, pp171-186, 1990.

[112] T.R. Marchant and N.F. Smyth, "*Microwave heating of materials with non-ohmic conductance*", SIAM J. Appl. Math., **53**, 1993.

[113] J.M. Hill and A.H. Pincombe, "*Some similarity temperature profiles for the microwave heating of a haf-space*", J. Austral. Math Soc., pp290-320, 1992.

[114] J.R. Thomas et al, "*Mathematical Model of thermal spikes in microwave heating of oxide ceramic fibres*", Mat. Res. Soc. Symp. Poc., **347**, pp363-pp368, 1994.

[115] Deepak and J.W. Evans, "*Calculation of temperature in microwave heated two dimensional ceramic bodies*", Journal of the American Ceramic Society, **76**, 8, pp1915-23, 1993.

[116] G.A. Kriegsmann, "*Thermal runaway in microwave heated ceramic: one-dimensional model*", Journal of Applied Physics, **71**, 4, pp1960-66, 1992.

[117] G.A. Kriegsmann, "*Cavity effects in microwave heating of ceramics*", SIAM Journal of Applied Math, **57**, 2, pp382-400, 1997.

[118] M.R. Booty and G.A.Kriegsmann, *"Microwave heating and joining of ceramic cylinders: A mathematical model"*, Methods and Applications of Analysis, **1**, 4, pp403-414, 1994.

[119] G.A. Kriegsmann, *"Hot-spot formation in microwave heated ceramic fibres"*, IMA Journal of Applied Mathematics, **59**, pp123-148, 1997.

[120] G.J.Vogt and W.P. Unruh, *"Microwave hybrid heating of alumina filaments"*, Microwaves: Theory and Applications in Material Processing II, The American Ceramic Society, 1993.

[121] J.A. Pelesko and G.A. Kriegsmann, *"Microwave heating of ceramic laminates"*, Journal of Engineering Mathematics, **32**, pp1-18, 1997.

[122] laminate panel paper of kriegsmann

[123] G. Roussy and J. A. Pearce, *"Temperature runaway of microwave heated materials: Study and control"*, Journal of Microwave Power, **20**, 1, pp47-51, 1985.

[124] X.L. Zhang et al, *"Microwave dielectric heating behaviour of supported mos$_2$ and pt catalysts"*, Industrial and Engineering Chemistry Research, **40**, 13, pp2810-17, 2001.

[125] H.W. Jackson, M. Barmatz and P. Wagner, *"Transient temperature behaviour of a sphere heated by microwaves"*, Microwaves: Theory and Application in Materials Processing II, Ceramic Transaction, **36**, 1993.

[126] N. Gupta, V. Midha, V. Balakotaiah and D.J. Economou, *"Bifurcation analysis of thermal runaway in microwave heating of ceramics"*, Journal of the Electrochemical Society, **146**, 12, pp4659-65, 1999.

[127] Y.L. Tian, *"Practices of ultra-rapid sintering of ceramic using single mode applicators in microwave: Theory and Applications in Materials Processing"*, Ceramic Transactions., 21ed by D.E. Clark, F.D. Gac, and W.H. Sutton, *Am. Ceram. Soc.*, 283-300, 1991.

[128] G.O. Beale and M. Li, *"Robust Temperature Control for Microwave heating of Ceramics"*, *IEEE Transactions on Industrial Electronics*, **44**, 1, 1997.

[129] E.A. Mason and A.P. Malinauskas, *"Gas Transport in Porous Media: The Dusty Gas Model"*, Elsevier Science Publishers *B.V.*, 1983.

[130] R.B. Bird, W. E. Stewart, and E.N. Lightfoot, *"Transport Phenomena"*, Wiley, New York, 1960.

[131] http://www.mas.ncl.ac.uk/~sbrooks/book/nish.mit.edu/2006/Textbook/Nodes/

[132] J.Y. Ofori and S.V. Sotirchos, "*Dynamic convection-driven thermal gradient chemical vapour infiltration*", J. Mater. Res., **11**, 10, pp2541-55, 1996.

[133] T.M. Besmann, B.W. Sheldon, T.S. Moss and M.D. Kaster "*depletion effects of silicon carbide deposition from methyltrichlorosilane*", J. Am. Ceram. Soc., **75**, 10, pp2899-2903, 1992.

[134] M.D. Allendorf and T.H. Osterheld, "*Modelling the gas phase chemistry of silicon carbide formation*", Mat. Res. Soc. Symp. Proc., **363**, pp39-44, 1995.

[135] H.C. Yu and S.V. Sotirchos, "*A generalized pore model for gas-solid reaction exhibiting pore closure*", AIChE Journal, **33**, 382-393, 1987.

[136] S. Sotirchos and S. Zarkanitis, "*A distributed pore size and length model for porous media reacting with diminishing porosity*", Chemical Engineering Science, **48**, 1487-1502, 1993.

[137] T.L. Starr, "*Gas transport model for chemical vapour infiltration*", J. Mater. Res., **10**, 9, pp2360-66, 1995.

[138] B.J. Matkowsky and G.I. Sivashinsky, "*Propagation of a pulsating reaction front in solid fuel combustion*", SIAM J. Appl Math. **35** 465-478 1978.

[139] B.J. Matkowsky and G.I. Sivashinsky, "*An approach derivation of two models in frame theory associated with the constant density approximation*", SIAM J. Appl Math. **37** 686-699 1979.

[140] I. Stakgold, "*Green's functions and boundary value problems*", 2nd ed, New York, Willey, 1998.

[141] R.L. Burden and J.D. Faires, "*Numerical analysis*", 7th ed, U. K. Brook/Cole Pacific Grove, Australia, 2001.

[142] K.W. Morton and D.F. Mayers, "*Numerical solution of partial differential equations: an introduction*", Cambridge University Press, 1994.

[143] H. William, "*Numerical recipes in FORTRAN: the art of scientific computing*", 2nd ed, Cambridge University Press, 1992.

[144] F. Liu, I. Turner and M. Bialkowski, "*A finite difference time domain simulation of power density distribution in a dielectric loaded microwave cavity*", Journal of Microwave Power and Electromagnetic Energy, **29**, 3, pp138-148, 1994.

[145] M.F. Iskander, M. Subirats, M.J. White, J.O. Kiggans, Jr., "*FDTD simulation of microwave sintering in large (500/4000 litres) multimode cavities*", Journal of Microwave Power and Electromagnetic Energy, **32**, 3, pp161-170, 1997.

203

[146] M.J. White, M.F. Iskander, Z. Huang and H.D. Kimrey, "*A three dimensional multigrid FDTD code for modelling microwave sintering of materials*", IEEE Antennas and Propagation International Symposium, MD, USA, **1**, pp120-122, 1996.

[147] W.Fu and A. Metaxas, "*Numerical solution of Maxwell's equation in three dimensions using the method of lines with applications to microwave heating in a multimode cavity*", International Journal of Applied Electromagnetics and Mechanics, **6**, pp165-186, 1995.

[148] H.Zhao, I. Turner and F. Liu, "*Numerical simulation of the power density distribution generated in a multimode cavity by using the method of lines technique to solve directly for the electric field*", IEEE Transactions on Microwave Theory and Techniques, **44** (12), pp2185-94, 1996.

[149] D. Rodger, "*Finite element method for calculating power frequency 3-D electromagnetic field distributions*", IEEE Proc, **130** part A (5), pp233-38, 1983.

[150] X. Jia and P. Jolly, "*Simulation of microwave field and power distribution in a cavity by a three dimensional finite element method*", Journal of Microwave Power and Electromagnetic Energy, **27**, pp11-22, 1992.

[151] J. Batt et al, "*A parallel measurement program in high-temperature dielectric property measurements: an update*", Ceram Trans, Am Ceram Soc, **59**, pp243-250, 1995.

[152] C.M. Bender and S.A. Orszag, "*Advanced mathematical methods for scientists and engineers I: asymptotic methods and perturbation theory*", New York, Springer, 1999.

[153] A. Georgescu, "*Asymptotic treatment of differential equations*", Chapman and Hall, London, 1995.

[154] T.A. Baeraky, "*Microwave Measurements of the dielectric properties of silicon carbide at high temperature*", Egypt. J. Sol, **25**, 2, pp263-273, 2002.

[155] D.J. Devlin, R.P. Currier, R.S. Barbero, B.F. Espinoza and N. Elliot, "*Microwave assisted chemical vapour infiltration*", Mat.Res.Soc.Symp.Proc., 250, pp245-250, 1992.

[156] G.E. Youngblood, D.J. Senor and R.H. Jones, "*Optimizing the transverse thermal conductivity of 2D-SiC$_f$/SiC composites. I. Modelling*", Journal of Nuclear Materials, **307-311**, pp1112-19, 2002

[157] G.E. Youngblood, D.J. Senor, R.H. Jones and W. Kowbel, *"Optimizing the transverse thermal conductivity of 2D-SiC$_f$/SiC composites. II. Experimental"*, Journal of Nuclear Materials, **307-311**, pp1120-25, 2002

[158] R. Taylor, J.R. Brandon and V. Piddock, *"Thermal transport in SiC fibre-SiC matrix composites"*, British Ceramic Transactions, **92**, 3, pp97-100, 1993

[159] http://mathworld.wolfram.com/HankelFunction.html